

ABSORPTION SPECTRA AND PHASE
TRANSFORMATIONS OF MINERALS
AT PRESSURES UP TO 200 KILOBARS

by

RATEB M. ABU-EID

B.Sc. (Hons), Alexandria University
1968

SUBMITTED IN PARTIAL FULFILLMENT
OF THE REQUIREMENTS FOR THE
DEGREE OF DOCTOR OF
PHILOSOPHY

at the

MASSACHUSETTS INSTITUTE OF
TECHNOLOGY

January, 1975

Signature of Author _____
Department of Earth and Planetary Sciences, January 27, 1975

Certified by _____ Thesis Supervisor

Accepted by _____
Chairman, Departmental Committee on Graduate Studies

~~Lindgren~~
WITHDRAWN
APR FROM
MIT LIBRARIES

ABSTRACT

HIGH PRESSURE ABSORPTION SPECTRA AND PHASE
TRANSFORMATIONS OF MINERALS AT PRESSURES
UP TO 200 KILOBARS

by

Rateb M. Abu-Eid

Submitted to the Department of Earth and Planetary Sciences
on January 27, 1975 in partial fulfillment of the
requirements for the Degree of Doctor of Philosophy

The absorption spectra of minerals containing a variety of transition metal ions were investigated at pressures ranging from 1 atm. to 200 kb. using the Cary 17 spectrophotometer with a newly designed optical microscope attachment and the diamond anvil pressure cell. The general results indicate that with increasing pressure, spin-allowed crystal field bands shift to higher energies, whereas charge transfer bands shift to lower energies; spin-forbidden bands, on the other hand, did not show any significant shift. The rate of the energy shift ($\text{cm}^{-1}/\text{kb.}$) varies from one band to the other depending on the nature of the transition metal ion and the coordination site symmetry. From the high pressure spectra, energy level diagrams were constructed at elevated pressures. Such diagrams provided the energy values of the crystal field splitting, $10Dq$, and the crystal field stabilization energy, CFSE, parameters at various pressures. The site compressibilities of Fe^{2+} , Mn^{3+} , and Cr^{3+} contained in orthoferrosilite, piemontite, and uvarovite were estimated at various pressures and correlated with the compressibilities of the bulk mineral phases containing them. It appears that the SiO_4 tetrahedra are the least compressible sites, whereas the 8-fold coordination sites (Ca site) are the most compressible ones.

The degree of covalency of the metal-ligand bond was estimated in uvarovite and Fe^{3+} -bearing minerals. There is a very slight decrease in Racah parameter B with increasing pressure ($6-10 \text{ cm}^{-1}/100 \text{ kb.}$), indicating that the ionic character of the M-L bond may not be changed significantly under pressures of up to 200 kb.

The d-energy levels constructed at high pressures provided information on the degree of regularity or distortion of the transition metal ion site. In most cases, it appears that distorted sites tend to be more regular at elevated pressures,

and the longer M-O bond is shortened substantially more than the shorter one as pressure increases.

No evidence has been obtained for any pressure-induced spin-pairing in Fe^{2+} in gillespite mineral or in any other minerals. Nevertheless, from the rates of band energy shifts with pressure, it appears that spin-pairing may take place in the lower mantle in the FeO phase.

Pressure-induced reduction of Cr^{6+} , V^{5+} , Mn^{7+} , and Cu^{2+} ions contained in crocoite, vanadinite, KMnO_4 , and Egyptian-blue, occurs at pressures ranging from 50-120 kb.. On the other hand, no reduction was detected in the other cations such as Fe^{3+} , Cr^{3+} , and Mn^{3+} with increasing pressure up to 200 kb..

The high pressure spectra were used to distinguish crystal field bands from charge transfer bands, (e.g. Ti^{3+} in lunar pyroxene), and to give appropriate assignments to many of the observed absorption features in the spectra of minerals.

In the course of this study, many high pressure polymorphs were identified from the high pressure spectra. Some of those were studied intensively using other techniques, such as x-ray and Mössbauer, and others remained to be investigated further. From the high pressure spectra, the minerals gillespite, azurite, crocoite, and vanadinite are believed to transform to other structures. In all of these minerals, discontinuous changes in their colors and spectra were observed at various pressures. High pressure x-ray studies are warranted to identify the crystal structures of the new polymorphs.

THESIS SUPERVISOR: Roger G. Burns
TITLE: Professor of Mineralogy and Geochemistry

TABLE OF CONTENTS

	<u>page</u>
TITLE PAGE	1
ABSTRACT	2
TABLE OF CONTENTS	4
INDEX OF FIGURES IN THE TEXT	7
INDEX OF TABLES IN THE TEXT	13
ACKNOWLEDGMENTS	14
Chapter I: INTRODUCTION.	15
Chapter II: THEORETICAL BASIS	19
II-1. Introduction.	19
II-2. Crystal Field Theory.	20
II-3. Ligand Field Theory and Racah Parameters.	24
II-4. Molecular Orbital Theory and Charge Transfer Spectra.	31
II-5. Effect of Pressure On Crystal Field and Charge Transfer Bands.	36
Chapter III: APPARATUS AND EXPERIMENTAL METHODS	44
III-1. Spectral Apparatus.	44
III-2. High Pressure Instruments.	54
III-3. Sample Preparation For Spectral Studies.	62
III-4. Pressure Calibration	72
III-5. Experimental Difficulties.	78
Chapter IV: EFFECT OF PRESSURE ON CRYSTAL FIELD BANDS.	86
IV-1. Introduction.	86
IV-2. Pyroxenes	87
IV-2.1 Orthoferrosilite.	91
IV-2.2 Bronzite	111
IV-2.3 Lunar Ti-augite.	116
IV-2.4 Blue Omphacite	131
IV-2.5 Rhodonite.	141
IV-3. Olivine	148
IV-4. Garnets	165
IV-4.1 Almandine.	168
IV-4.2 Andradite.	182
IV-4.3 Uvarovite.	189

	<u>page</u>
IV-5. Epidotes	193
IV-5.1 Fe ³⁺ -Epidotes	196
IV-5.2 Mn ³⁺ -Epidotes	201
IV-6. Miscellaneous Minerals	214
IV-6.1 Staurolite	214
IV-6.2 Lusakite	220
IV-6.3 Melilite	230
IV-6.4 Glaucothane	246
IV-6.5 Dioptase	255
IV-6.6 Gillespite	263
 Chapter V: EFFECT OF PRESSURE ON CHARGE TRANSFER BANDS	 264
V-1. Introduction	264
V-2. Band Energies, Intensities and Influence of Pressure	 265
V-3. Effect of Pressure On M-M Charge Transfer Bands	 268
V-3.1 Glaucothane	269
V-3.2 Blue-Omphacite	276
V-3.3 Vivianite	281
V-3.4 Fayalite and Orthoferrosilite	 290
V-4. Effect Of Pressure On M-L and L-M Charge Transfer Absorption	 291
V-4.1 Crocoite	293
V-4.2 Vanadinite	307
V-4.3 KMnO ₄	315
V-4.4 Hematite	324
V-4.5 Silicates	330
 Chapter VI: PRESSURE INDUCED PHASE TRANSFORMATIONS IN: GILLESPIITE, EGYPTIAN BLUE AND AZURITE	 333
VI-1. Introduction	333
VI-2. Gillespite	335
VI-2.1 Introduction	335
VI-2.2 Experimental Methods	336
VI-2.3 Results	337
VI-2.4 Discussion	363
VI-3. Egyptian Blue	377
VI-4. Azurite	384
 Chapter VII: DISCUSSION	 396
VII-1. Energy Shifts Of Spectral Bands With Pressure	 396
VII-2. The Degree of Covalency and Racah Parameter B at Elevated Pressures	400

	<u>page</u>
VII-3. Site Compressibilities From 10Dq Values	408
VII-4. Crystal Field Stabilization Energies (CFSE)	412
VII-5. Pressure Induced Reduction	421
VII-6. Pressure Induced Spin- Pairing	428
VII-7. The Trend Of Pressure Induced Changes In The Structure Of Silicate Minerals	437
VII-8. Absorption Spectra And Radia- tive Heat Transfer	443
References	446
Vita	474

INDEX OF FIGURES IN THE TEXT

(Page numbers refer to figure captions, the figures will be found on the page immediately following.)

FIGURE		PAGE
II-1.	Octahedral array of ligands and position of electron at point P described in spherical coordinates	21
II-2.	Energy levels of the free cation, free ligands, and molecular unit (ML ₆)	33
II-3.	Schematic representation of conduction and valence bands	38
II-4.	Potential energy wells of ground and excited states	41
III-1.	Photograph showing Cary 17 spectrophotometer	45
III-2.	Photograph showing reference and sample microscopes	47
III-3.	Reflecting focusing system	50
III-4.	Spectrophotometer optical attachment	52
III-5.	Light path in the new optical system	55
III-6.	Photograph of UP style pressure cell mounted on universal x-ray table	58
III-7.	Photograph of UXP type pressure cell mounted inside Debye-Scherrer powder x-ray camera	60
III-8.	Photograph of PP type diamond cell mounted on eucentric goniometer head	63
III-9.	Gasketing method	66
III-10.	Photograph of silver iodide (AgI) powder between two diamond anvils	71
III-11.	Geometries of x-ray reflections from NaCl between the anvil faces	76
III-12.	Visible spectra of a pair of diamond anvils used in the pressure cell	79
III-13a.	Pressure distribution in ungasketed sample of powdered NaCl in diamond anvil cell	83
III-13b.	Pressure contours for sample of nickel dimethylglyoxime in NaCl (1:3) in diamond-anvil cell	83
IV-1.	The crystal structure of diopside on z-axis	88
IV-2.	Views of M1 and M2 sites in orthoferrosilite	92
IV-3.	Crystal structure of orthoferrosilite	94
IV-4.	α -spectra of orthoferrosilite at 1 atm. and 20 kb.	98

FIGURE	PAGE
IV-5. γ -spectra of orthoferrosilite at 1 atm. and 20 kb.	101
IV-6. Energy level diagrams for M1 and M2 sites in orthoferrosilite constructed at 1 atm. and 20 kb.	104
IV-7. α -spectrum of bronzite, $Fs_{14.5}$, at 1 atm. and 20 kb.	112
IV-8. Energy level diagram of M2 site in bronzite at 1 atm. and 20 kb.	114
IV-9. Views of M1 and M2 polyhedra in lunar pyroxene	120
IV-10. Polarized absorption spectra of pyroxene single crystals in rock 74275	124
IV-11. Energy level diagrams of Fe^{2+} cation in M1 and M2 sites, and Ti^{3+} ion in M1 site	126
IV-12. α -spectra of 74275 pyroxene at 1 atm. and 50 kb.	129
IV-13. Crystal structure of omphacite projected along (100)	133
IV-14. Absorption spectra of blue-omphacite single crystal at 1 atm. and 40 kb.	139
IV-15. Absorption spectrum of rhodonite in visible and i.r. regions	143
IV-16. Portion of octahedral serrated band in olivine projected on (100)	150
IV-17. M_1 and M_2 polyhedral symmetries in olivine	152
IV-18. γ and α spectra of olivine [Fa_{96}] at normal pressure	155
IV-19. d-energy level diagrams for Fe^{2+} in M_1 and M_2 sites in olivine	157
IV-20. α -spectra of fayalite single crystal at 1 atm., 20 and 40 kb.	160
IV-21. Energy level diagrams of M_1 site in fayalite at 1 atm. and 40 kb.	163
IV-22. Garnet crystal structure along z-axis	166
IV-23. a) Coordination polyhedra of oxygen atoms about Si, Al, and Fe^{2+} atoms in almandine	169
b) Interatomic distances (X-O and O-O) of XO_8 triangular dodecahedron	169
IV-24. Energy level diagrams illustrating splitting of d-energy levels in octahedral, cubic, and dodecahedral symmetries	172
IV-25. Absorption spectrum of almandine garnet at normal pressure	174
IV-26. Absorption spectra of almandine garnet at 1 atm., 50 kb., 100 kb., and 200 kb.	180
IV-27. Absorption spectra of Fe^{3+} in andradite garnet	184
IV-28. Absorption spectra of synthetic uvarovite at 1 atm., 95 kb., and 177 kb.	191

FIGURE	PAGE
IV-29.	Structure of epidote along b-axis 194
IV-30.	α and β spectra of Fe^{3+} -epidote at 1 atm. 197
IV-31.	a) Very distorted octahedral site of Mn^{3+} in piemontite and M-O distances 202 b) Energy level diagram of Mn^{3+} ion at 1 atm. 202 c) Energy level diagram of Mn^{3+} from spectra at 200 kb. 202
IV-32.	Absorption spectra of Mn^{3+} in powdered Mn^{3+} sample of piemontite at 1 atm. and 197 kb. 205
IV-33.	Pressure-induced energy shift of Mn^{3+} absorption bands in piemontite at 18170 cm^{-1} , 22000 cm^{-1} 207
IV-34.	Energy level diagrams of Mn^{3+} orbitals at 1 atm., 75 kb., 92 kb., 135 kb., 180 kb., and 190 kb. 209
IV-35.	Rate of pressure-induced energy changes in CFS and CFSE parameters 212
IV-36.	View of Fe^{2+} tetrahedral site in staurolite 215
IV-37.	Polarized absorption spectra of staurolite at 1 atm. 218
IV-38.	Spectra of lusakite single crystal at 1 atm. and 30 kb. 221
IV-39.	Energy level diagrams of Co^{2+} in lusakite at 1 atm., 20 kb., and 120 kb. 225
IV-40.	Spectra of lusakite powder at 1 atm. and 20 kb. 228
IV-41.	Crystal structure of melilite projected on (001). 231
IV-42.	Mössbauer spectrum of melilite I at room temperature 235
IV-43.	Absorption spectra of melilite I, melilite II, and melilite III 239
IV-44.	i.r. polarized spectra of melilite I at 1 atm., c-spectrum, a-spectrum 241
IV-45.	a) Energy level diagram of Fe^{2+} in melilite I for curve-fitted c-spectrum. 244 b) View of tetrahedral site of Fe^{2+} in melilite I 244
IV-46.	a) View of glaucophane structure along a-axis. 247 b) View of glaucophane structure along c-axis 247
IV-47.	M1, M2, and M3 polyhedra in glaucophane 251
IV-48.	Polarized spectra of glaucophane at normal pressure 253
IV-49.	a) Structure of dioptase along c-axis 256

FIGURE	PAGE
IV-49.	b) Schematic diagram showing edge and corner sharings between Cu^{2+} polyhedra 256
	c) Cu^{2+} distorted octahedron and Cu-O and Cu-OH distances 256
IV-50.	Absorption spectra of diopside at 1 atm. and 50 kb. 259
IV-51.	Cu^{2+} energy level diagrams in O_h and C_{4v} symmetries 261
V-1.	β and γ spectra of glaucophane measured at 1 atm. and 50 kb. 271
V-2.	M1H - M1(1)H direction relative to x, y, and z axes 278
V-3.	Fe_I and Fe_{II} site symmetries and M-L distances in vivianite 282
V-4.	a) Absorption spectra of vivianite at 1 atm. 285
	b) M-M charge transfer spectra of vivianite at 1 atm. and at 300 kb. 285
V-5.	Clinographic projection of the crocoite structure 294
V-6.	a) The visible spectrum of crocoite at 1 atm. 299
	b) Absorption spectrum of crocoite powder at pressure around 20-30 kb. 299
	c) Absorption spectrum of crocoite powder at pressure around 60 kb. 299
V-7.	The molecular orbital energy level diagram of the tetrahedral chromate ion 301
V-8.	a) A photograph of crocoite sample subjected to 100 kb. 304
	b) A photograph of crocoite sample after lowering the pressure to 60 kb. 304
V-9.	Projection of vanadinite structure on the c-axis 308
V-10.	a) Absorption spectra of vanadinite at 1 atm. 311
	b) Spectra of vanadinite at pressure 30-40 kb. 311
	c) The spectrum of vanadinite at pressure around 80 kb. 311
V-11.	a) A photograph of vanadinite sample subjected to about 80 kb. 313
	b) Photograph of crocoite subjected to high pressure and quenched rapidly in the diamond cell 313

	PAGE
V-12. Crystal structure of KMnO_4 projected on (001)	316
V-13. A photograph of KMnO_4 subjected to about 60 kb.	320
V-14. The spectra of KMnO_4 at elevated pressures	321
V-15. M.O. energy level diagram for FeO_6^{9-} ionic cluster	325
V-16. Optical absorption spectra of hematite sample subjected to 100 kb.	328
VI-1. a) Polarized spectra of a gillespite crystal at 1 atm. and 26 kb.	338
b) The visible spectra of a gillespite crystal above the transition pressure	340
VI-2. a) A photograph of gillespite crystal in polarized light, the electric vector E-W	343
b) Photograph of the same crystal above the transition pressure	343
VI-3. a) A photograph of the same crystal as in (VI-2a) rotated 90° (E c)	345
b) Photograph of the same crystal as in (VI-3a) subjected to pressure above 26 kb.	345
VI-4. Polarized spectra of a gillespite crystal mounted in the diamond cell such that the c-axis is perpendicular to the anvil faces.	347
VI-5. Mössbauer spectra of synthetic gillespite at 1 atm. and above the transition pressure	350
VI-6. Cone axis x-ray photograph of a gillespite crystal at 1 atm.	353
VI-7. Cone axis x-ray photograph of the same gillespite crystal above 26 kb.	355
VI-8. O-level precession x-ray photograph of a gillespite crystal without the diamond cell	357
VI-9. O-level x-ray photograph of a gillespite crystal mounted in the diamond cell with the pressure below 26 kb.	359
VI-10. O-level x-ray photograph of the same crystal at pressure above 26 kb.	361
VI-11. a) Energy level diagrams of $\text{Fe}_{h.s.}^{2+}$ in square planar site.	366

VI-11.	b) Energy level diagram showing the increases in the splitting energies	366
	c) Energy level diagram of $Fe_{1.s.}^{2+}$ in square planar site	366
VI-12.	a) Energy level diagram of Fe^{2+} in D_{4h} symmetry	370
	b) Energy level diagram constructed from the spectra of gillespite measured at pressure above 26 kb.	370
VI-13.	Two diagrams illustrating the sites of Fe^{2+} in the low pressure phase and the high pressure phase of gillespite	372
VI-14.	The fluorescence spectrum of ruby crystal fragment contained in the diamond cell at 12.6 kb.	375
VI-15.	a) Absorption spectrum of $BaCuSi_4O_{10}$ measured at normal pressure	379
	b) Energy level diagram showing the electronic transitions of Cu^{2+}	379
VI-16.	The spectra of $BaCuSi_4O_{10}$ measured at 1 atm., 50 kb., and 200 kb.	381
VI-17.	The site symmetries and coordinates of Cu_I and Cu_{II} atoms in azurite	386
VI-18.	a) Spectrum of azurite crystal mounted in the diamond cell at normal pressure	389
	b) Spectrum of azurite crystal above 60 kb.	389
VI-19.	Energy level diagram of Cu^{2+} in O_h and D_{4h} symmetries.	
VII-1.	Variation of B value with Cr-O interatomic distances in a suite of Cr-bearing minerals	404
VII-2.	a) The splitting of the d-energy levels in a regular octahedral symmetry	414
	b) Energy levels of Fe^{2+} in an octahedral site compressed along the z-axis.	414
VII-3.	a) Energy level diagram showing the spin-allowed transitions in $Fe_{h.s.}^{2+}$ and $Fe_{1.s.}^{2+}$	431
	b) Energy level diagram showing the spin-allowed transitions in $Fe_{h.s.}^{2+}$ and $Fe_{1.s.}^{2+}$	431

INDEX OF TABLES IN THE TEXT

TABLE	PAGE
II-1. The energies of some electronic transitions of d^n configurations in octahedral field	27
IV-1. M1-O and M2-O interatomic distances in orthoferrosilite	96
IV-2. Energy values of CFS and CFSE parameters for M1 and M2 sites in orthoferrosilite at 1 atm. and 20 kb.	110
IV-3. Electron microprobe analyses of Apollo 74275 pyroxene	118
IV-4. M1-O and M2-O interatomic distances in lunar pyroxene	122
IV-5. a) Site occupancies of M1, M(1), M1H, and M1(1)H sites in omphacite	136
b) M-O interatomic distances in M1, M1(1)H, M1(1), and M1H sites	136
IV-6. Electron microprobe analysis of blue omphacite .	138
IV-7. Assignments of spectral bands in rhodonite . . .	147
IV-8. Electronic transitions of Fe^{2+} in almandine garnet	178
IV-9. Co^{2+} crystal field band energies at 1 atm., 5 kb., 20 kb., and 30 kb.	226
IV-10. M-O and O-O interatomic distances in staurolite..	216
IV-11. Electron microprobe analyses of melilite I, II, and III	234
IV-12. Mössbauer parameters of various minerals containing Fe^{2+} and Fe^{3+} cations in octahedral, tetrahedral, and square planar sites	238
IV-13. M1-O, M2-O, and M3-O interatomic distances in glaucophane	251
V-1. a) The positional parameters of the M_1 , M_2 , and M_3 sites	274
b) M-M interatomic distances in glaucophane. . . .	274
c) Bond angles MMM in glaucophane	274
V-2. a) Atomic parameters of the Fe ions in the four octahedral sites in omphacite	277
b) M-M distances in omphacite	277
V-3. a) The intensities and d-values of the x-ray diffraction lines for the monoclinic form of $PbCrO_4$	296
b) The intensities and d-values of the x-ray diffraction lines for the orthorhombic form of $PbCrO_4$	296
c) Intensities and d-values of x-ray diffraction lines of the crocoite sample used in this study (1 atm.)	296
d) Intensities and d-values of x-ray diffraction lines of a crocoite sample subjected to 60 kb. and then quenched to normal pressure	297

ACKNOWLEDGMENTS

It is a pleasure to express my gratitude to Professor Roger G. Burns, my advisor, for his guidance, encouragement, and complete support to this study throughout its duration. His ideas and constructive criticisms solved many problems and improved the thesis. Professor Burns kindly provided me with many of the mineral specimens used in this study.

I would also like to thank Drs. Ho-Kwang Mao and Peter Bell, of the Geophysical Laboratory, for allowing me to use their laboratory during the summer of 1972. Dr. Mao spent a lot of his valuable time explaining to me the techniques involved in the usage of the diamond cell. Dr. Gasper Piermarini, of the N.B.S., helped me to measure the transition pressure of gillespite, using the ruby-fluorescence method, and explained many of the techniques involved in the high pressure single crystal x-ray studies. Professor William Bassett of the University of Rochester, provided me with the new modification of the diamond cell (UXP type) and showed me how to use it.

I would particularly like to thank Dr. Frank Huggins for providing me with many stimulating ideas and for useful discussion. Dr. Earl Whipple kindly provided me with two analyzed garnet samples.

I am indebted to Mr. Chien-Min Sung for many helpful discussions and for his assistance. Mr. Bruce Loeffler read some parts of the thesis and critically reviewed Chapter V. I also wish to thank Professor Charles Burnham and Mr. Robert Hazen for the cooperative high pressure x-ray work on gillespite.

Professor Patrick Hurley's advice and encouragement are deeply appreciated. Professor John Dickey provided free time to use the microprobe lab. to analyze mineral specimens.

Mrs. Virginia M. Burns helped me in the bibliographic research and in the preparation of the thesis. I would like to express my appreciation to Ms. Roxanne Regan for typing this thesis; her skills and fast typing saved me a lot of time and improved the thesis.

Last, but not least, I am indebted to my wife, Maria Letizia Abu-Eid, who typed all of the rough draft of the thesis. In the last four months, the first four months of our married life, she accepted, with good spirit, to live alone most of the time while I was working on the thesis; in addition, she provided me with all of her moral support.

Chapter I

INTRODUCTION

Metals of the first transition series are often significant constituents of natural minerals so that the physical and chemical properties of many mineral phases are closely related to the nature and state of transition metal ions contained in their structures.

The electronic absorption spectral technique is one of the most powerful tools employed to study the crystal chemistry of transition metal ions. Most transition metal ions absorb energy in the visible and nearby u.v. and i.r. regions as a result of electronic transitions between 3d orbital energy levels. In the past decade, these crystal field spectra have been used successfully in mineralogy for such studies as determining cation valence state, interpreting cation site symmetries, explaining the cause of color and pleochroism of minerals, and estimating the degree of covalency of the metal-ligand bond. For a detailed review of these applications in mineralogy and geochemistry, the reader is referred to Burns (1966, 1969a, 1970a); Manning (1967a,b, 1969a,b,c, 1970); Faye et al. (1968); and White and Keester (1966). Obtaining the spectra of minerals at elevated pressures should reveal such properties at greater depths in the earth, and may provide valuable information relevant to the nature and composition of the Earth's interior.

The nature of the chemical bond in mineral phases at elevated pressures, whether it has more ionic or covalent character,

is not well understood yet. Racah parameters, B and C, have been used as indicators of the degree of covalency of the chemical bond (Manning, 1970; Moore and White, 1972). Since energies of many crystal field bands depend on such parameters, a study of the pressure effect on absorption bands could reveal information on the nature and character of the bonds between transition metal ions and the ligands in mineral phases existing under elevated pressure conditions in the mantle.

The crystal field stabilization energy parameter (CFSE) has been used to estimate the site preferences of transition metal ions in crystal structures. Obtaining similar parameters from the high pressure spectra of minerals could be of considerable importance for understanding ordering and enrichments of transition metal ions in crystal structures during mineral crystallization.

At elevated pressures, electronic transitions such as spin-pairing (Fyfe, 1960; Strens, 1969; Burns, 1969a; and Gaffney, 1972 a,b) and pressure induced reduction (Drickamer et al., 1969; Burns et al., 1972a,b) of transition metal ions to lower oxidation states are expected to occur when sufficient pressures are applied to the samples. Using high pressure spectral techniques, such transitions should be easily identified. In addition, structural phase transformations in mineral phases may also be detected when significant changes in the site symmetries or the coordination numbers of transition metal ions take place at the phase boundary (Abu-Eid et al., 1973; Hazen and Abu-Eid, 1974; Abu-Eid and Hazen, 1975; and Suchan and Drickamer, 1959).

Since the volumes of the polyhedra containing transition metal ions are closely related to the spectral parameter, $10Dq$, the variation of this parameter with pressure can provide information on the site compressibilities (Tischer and Drickamer, 1962).

In addition to applications to geochemical and mineralogical problems, high pressure absorption spectroscopy has also been used in geophysics for studies of radiative conductivities and the variation of thermal conductivity within the Earth (Pitt and Tozer, 1970a,b; Fukao et al., 1968; and Shankland, 1970, 1972).

Many ambiguities concerning the assignments of a number of spectral bands to either charge transfer or crystal field transitions have been the subject of controversy and debate in the mineralogical literature (Dowty and Clark, 1973a,b; Burns and Huggins, 1973; Burns et al., 1972b,c,d,; and Burns et al., 1973). Since crystal field and charge transfer bands are expected to show opposite energy shifts with pressure, high pressure spectra of minerals can be used for distinguishing crystal field from charge transfer bands.

There is obviously a large scope of spectral data of minerals containing T.M. ions at high pressures. The present investigation is aimed at measuring the crystal field and charge transfer spectra of minerals at pressures ranging from 1 atm. to 200 kilobars, and then employing the obtained experimental results, with some theoretical consideration, to explain or predict the chemical and physical behavior of transition elements at various depths in the Earth.

In the following chapter, crystal field and molecular orbital theories are reviewed briefly since they represent the theoretical basis for interpreting both crystal field and charge transfer bands.

The apparatus and experimental methods are described in chapter III. This is followed by the core of the thesis in chapters IV and V, in which the effect of pressure on crystal field and charge transfer bands for various minerals is discussed in some detail. Chapter VI discusses high pressure polymorphic transitions in some minerals. Finally, applications of the high pressure spectral studies to the Earth's interior are outlined in chapter VII.

Chapter II

THEORETICAL BASIS

II-1. Introduction

The spectra of mineral phases bearing transition metal ions are dominated in general by two types of features. Firstly, there are crystal field bands which are related to electronic transitions between the d-levels of transition metal ions and generally appear in the energy region 4,000-30,000 cm^{-1} . These bands are characterized by their relative low intensities and narrow widths. Secondly, there are charge transfer bands which are of two categories: first, ligand \rightarrow metal or metal \rightarrow ligand, and second, metal \rightarrow metal charge transfer transitions (Phillips and Williams, 1966). The first category, charge transfer bands, arise from electron transfer between energy levels of highly ligand character and levels of mostly metal character, and vice versa (McClure, 1959; Lever, 1968). These, in general, are very intense and usually occur at energies higher than those of crystal field bands above 25,000 cm^{-1} . The second category of charge transfer transitions, metal \rightarrow metal charge transfer bands, arise from transfer of electrons between the d-levels of adjacent metal ions having different oxidation states, e.g. $\text{Fe}^{2+}\rightarrow\text{Fe}^{3+}$ (Hush, 1967).

In this study, crystal field bands will be treated using the models of crystal field and ligand field theories, whereas charge transfer bands will be explained using molecular orbital models.

II-2. Crystal Field Theory

Crystal field theory has been remarkably successful in explaining most spectral bands observed in the spectra of transition metal ions contained in many silicate minerals.

In this model, the negative and positive ions are represented as point charges and the electrostatic potential, V_1 , associated with an electron at a point, P, (Fig. 1) at a distance, d , from ligand (1) and, r , from the central metal ion is given by

$$V_1 = + \frac{Ze^2}{d} \quad (1)$$

where Z is the charge on the ligand.

Considering the particular case of an octahedral array of six negative point charges each at distance, R , from the central ion, the total potential, V , at, P, arising from the six ligands has been calculated by Dunn et al. (1965) and Hutchings (1964), and is expressed as:

$$V = \frac{6Ze^2}{R} + \frac{35Ze^2}{4R^5} (x^4 + y^4 + z^4 - \frac{3}{5}r^4) \quad (2)$$

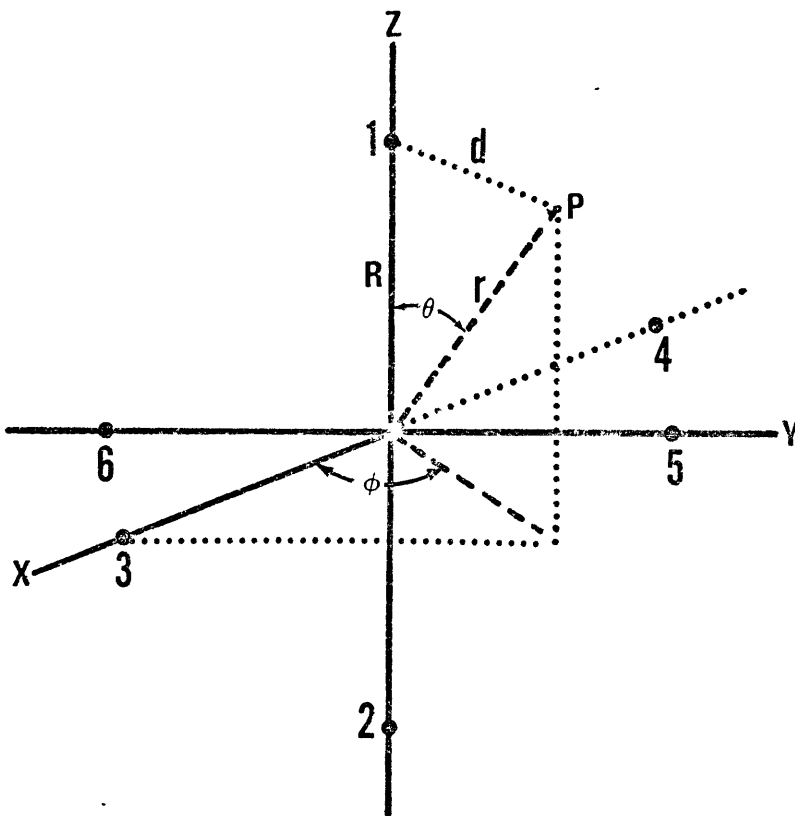
The first term, $\frac{6Ze^2}{R}$, is usually neglected in the crystal field approximation since it is spherically symmetrical and does not participate in the splittings of d orbitals. The quantity, $\frac{35Ze^2}{4R^5}$, is usually denoted by D ; it follows then that the potential at any point at $\leq R$ distance from the central ion can be expressed as :

$$V = D (x^4 + y^4 + z^4 - \frac{3}{5} r^4) \quad (3)$$

After establishing the potential, V , the perturbations of this potential on the wave functions of d electrons are taken into account. This is done by integrating the radial and angular

FIGURE II-1

Octahedral array of ligands and the position of an electron at point P described in spherical coordinates in three dimensional space.



wave function pairs to obtain integrals of the form:

$\int_0^\infty \int_0^\pi \int_0^{2\pi} R_{nl}(r) \Theta_{lm}(\theta) \Phi_m(\phi) V R_{n'l'}(r) \Theta_{l'm'}(\theta) \Phi_{m'}(\phi) r^2 \sin\theta \, dr \, d\theta \, d\phi$
 (Dunn et al., 1965), where $R_{nl}(r)$ is the radial part of a d wave function and $\Theta_{lm}(\theta) \Phi_m(\phi)$ are the angular parts or spherical harmonics.

The perturbation secular determinant can be constructed from solving the above integrals. In case of a d^1 electron, a square matrix 5x5 could be established from the five M_L values for a d electron. Solution of the part of the integral dependent on ϕ will reduce the 25 elements of the secular determinant to seven. However, solutions of the θ integral for different values of m and m' need tedious mathematical treatments and have been given in many references (Dunn et al., 1965; Figgis, 1966; Hutchings, 1964); thus, for example, for $m = m' = 0$, the solution of Θ_{lm} and Φ_m integrals is given as:

$$\langle 0 | (x^4 + y^4 + z^4) | 0 \rangle = \frac{5}{7} r^4 \quad (4)$$

The radial part integral $\int_0^\infty R_{nl}^2(r) r^4 r^2 dr$ cannot be solved (Dunn et al., 1965; Figgis, 1966), and it is replaced by the parameter q where:

$$q = \frac{2}{105} \int_0^\infty R_{nl}^2(r) r^4 r^2 dr \quad (5)$$

Considering the rest of the M_L values, the secular determinant can be formulated from the solution of which the energies of the different sets of d-levels could be evaluated.

This method of calculation represents the basis for constructing energy level diagrams for transition metal ions of various d-electronic configurations. These are frequently called

Orgel energy level diagrams (Orgel, 1966). The splitting energies between these levels are expressed as multiples of Dq and the relations among the Dq values for octahedral, tetrahedral, and cubic symmetries are:

$$Dq \text{ (oct.)} = -\frac{9}{4} Dq \text{ (tet.)} = -\frac{9}{8} Dq \text{ (cubic)}$$

From the above outline of the theoretical basis of crystal field theory, we should keep in mind the important equivalence:

$$Dq \equiv \frac{35Ze^2}{4R^5} \left[\frac{2}{105} \int_0^\infty R_{nl}^2(r) r^4 r^2 dr \right] \quad (6)$$

From this relation, it is evident that Dq is inversely proportional to the fifth power of the average metal-ligand band distance, R .

For qualitative spectroscopic studies, crystal field theory is quite successful. However, for quantitative work it is inadequate, primarily because it does not take into account the possibility of some covalent character of the metal-ligand bond. Because of this inadequacy, ligand field theory has been developed from crystal field theory.

II-3. Ligand Field Theory (LFT) and Racah Parameters

Ligand field theory is a modification of crystal field theory which takes into account the various degrees of overlap between the d-orbitals of the transition metal ion and the ligand orbitals. When there is an excessive degree of mixing between the metal and ligand electrons, LFT will have essentially a molecular orbital formulation; however, in the case of small to moderate amounts of overlap, it will be basically an adjusted crystal field model (Cotton and Wilkinson, 1966).

For the purposes of this study, greater emphasis is placed on crystal field and ligand field models, since the degree of covalency of the metal-ligand bond in most mineral phases under investigation is small to moderate.

The major modifications of crystal field theory that take into account mixing of cation and ligand orbitals involve using the parameters of 3d interelectronic interaction as variables rather than constants (equal to the values for the free ion). Of these parameters, the most significant are the interelectronic repulsion parameters which are frequently known as Racah parameters, B and C.

Racah parameters, B and C, are related to the covalency or the ionicity of the metal-ligand bond. They are derived from calculations of the radial wave functions of the electrons involved in the bonding between transition metal ions and the surrounding ligands (Racah, 1942a,b, 1943, 1949). B and C energy values are inversely proportional to the spatial extent of the ligand and cation orbitals. Hence the larger their values, the more ionic is the metal ligand bond.

The perturbation of the ligand orbitals on the d-wave functions of the central ion, using ligand field models, is mathematically expressed in a secular determinant or energy matrix. The elements of that matrix are given in terms of the crystal field parameter, Dq , and Racah parameters, B and C.

In two classic papers (1954a,b), Tanabe and Sugano derived such secular determinants and from the solutions, they obtained the energies of electronic transitions from the ground state to

the higher energy states. The results of calculations by Tanabe and Sugano have been used by many workers in this line of study.

Some of the important electronic transitions for various d^n configurations in octahedral fields are given in Table 1; their energies in terms of Dq , B , and C are also quoted from different references. Tanabe and Sugano (1954b) also constructed energy level diagrams which show the dependence of energy levels upon both interelectronic repulsion parameters and crystal field of medium strength. In these diagrams, the energies of the levels of a d^n system are plotted in B units as vertical coordinates, and the horizontal coordinate is Dq/B . These diagrams are useful for recognizing the type of electronic transition, forbidden or allowed, and for rough estimation of the energy of each transition in various d^n systems.

In order to apply the above theoretical aspects to assignments of crystal field spectra of transition metal ions in natural minerals, the following procedure will be followed in this thesis:

1. Determine the chemical composition of each mineral phase and especially the concentrations of transition metal ions.
2. Obtain all the accessible information on the crystal structure of each individual mineral with emphasis on the site symmetries of the central ions.
3. Identify spectral bands and assign them to the appropriate electronic transitions.
4. Evaluate the energies of these transitions expressed in terms of Dq and/or B and C .

Table 1: Energies of Some Common Electronic Transitions of d^n Configurations in an Octahedral Field

Number of 3d electrons	Ion	Ground State	Excited State	Energy of Electronic Transition	References
d^1	Ti^{3+}	$2T_{2g}$	$2E_g$	$10Dq$	Dunn et al. (1965), Hutchings (1964), Figgis (1966)
d^2	V^{3+}	$3T_{1g}$	$3T_{2g}$	$\frac{1}{2}(10Dq-15B) + \frac{1}{2}[(10Dq+15B)^2 - 12B \cdot 10Dq]^{1/2}$	Lever (1968), König (1971), Tanabe and Sugano (1954a,b)
			$3T_{1g}$	$[(10Dq+15B)^2 - 12B \cdot 10Dq]^{1/2}$	
			$3A_{2g}$	$\frac{1}{2}(30Dq-15B) + \frac{1}{2}[(10Dq+15B)^2 - 12B \cdot 10Dq]^{1/2}$	
d^3	Cr^{3+}	$4A_{2g}$	$4T_{2g}(F)$	$10Dq$	Tanabe and Sugano (1954a,b), Poole (1964), König (1971), Lever (1968), Reiner (1969)
			$4T_{1g}(F)$	$\frac{1}{2}(15B+30Dq) - \frac{1}{2}[(15B-10Dq)^2 + 1/2B \cdot 10Dq]^{1/2}$	
			$4T_{1g}(P)$	$\frac{1}{2}(15B+30Dq) + \frac{1}{2}[(15B-10Dq)^2 + 12B \cdot 10Dq]^{1/2}$	
d^4	Mn^{3+}	$5E_g$	$5T_{2g}$	$10Dq$	Lever (1968), Orgel (1966), Dunn <u>et al.</u> (1965)

Table 1: (Cont'd - page 2)

Number of 3d elec- trons	Ion	Ground State	Excited State	Energy of Electronic Transition	References
d ⁵	Fe ³⁺ Mn ²⁺	⁶ A _{1g}	⁴ T _{1g}	$-10Dq + 34B - 26B^2/10Dq$	Lever (1968), Ballhausen (1962), Tanabe and Sugano (1954a,b), Figgis (1966)
			⁴ T _{2g}	$-10Dq + 42B - 39B^2/10Dq$	
			⁴ A _{1g} ;	10B + 5C	
			⁴ E _g (G)		
			⁴ E _g (I)	17B + 5C	
d ⁶	Fe ²⁺	⁵ T _{2g}	⁵ E _g	10Dq	Figgis (1966), Dunn et al. (1965), Lever (1968), McClure (1959), Hutchings (1964)
			¹ A _{1g}	$-20Dq+5B+8C-120B^2/10Dq$	
			³ T _{1g}	$-10Dq+5B+5C-70B^2/10Dq$	
			³ T _{2g}	$-10Dq+13B+5C-106B^2/10Dq$	
			¹ T _{1g}	$-10Dq+13B+7C-34B^2/10Dq$	
			¹ T _{2g}	$-10Dq+21B+7C-118B^2/10Dq$	

Table 1: (Cont'd - page 3)

Number of 3d electrons	Ion	Ground State	Excited State	Energy of Electronic Transition	References
d ⁷	Co ²⁺	⁴ T _{1g} (F)	⁴ T _{2g} (F)	$\frac{1}{2}(10Dq-15B)+\frac{1}{2}[(10Dq+15B)^2 - 12B \cdot 10Dq]^{1/2}$	König (1971), Lever (1968), Tanabe and Sugano (1954a,b), Ballhausen (1962)
			⁴ A _{1g} (F)	$\frac{1}{2}(30Dq-15B)+\frac{1}{2}[(10Dq+15B)^2 - 12B \cdot 10Dq]^{1/2}$	
			⁴ T _{1g} (P)	$[(10Dq+15B)^2 - 12B \cdot 10Dq]^{1/2}$	
d ⁸	Ni ²⁺	³ A _{1g}	³ T _{2g} (F)	10Dq	König (1971), Lever (1968), Tanabe and Sugano (1954a,b)
			³ T _{1g} (F)	$\frac{1}{2}(15B+30Dq)-\frac{1}{2}[(15B-10Dq)^2 + 12B \cdot 10Dq]^{1/2}$	
			³ T _{1g} (P)	$\frac{1}{2}(15B+30Dq)+\frac{1}{2}[(50B-10Dq)^2 + 12B \cdot 10Dq]^{1/2}$	
d ⁹	Cu ²⁺	² E _g	² T _{2g}	10Dq	Dunn et al. (1965). Ballhausen (1962)

This procedure may be easily followed for interpreting the spectra of simple mineral phases. However, in complicated systems, i.e. minerals containing more than one transition metal ion and having different oxidation states in distorted and multiple sites, the interpretation needs more careful study and some experience.

The energies of spectral bands may also be calculated and then compared with the experimentally determined energy values (Ilse and Hartmann, 1951a,b; Ballhausen, 1954; Wood and Strens, 1972; and Gaffney, 1972a). This may be done when the site symmetry of the central ion is known and the interatomic bond distances (metal-ligand) are available. The methods of calculating the energies of crystal field transitions are useful, especially whenever there are uncertainties in the assignments of spectral bands.

In natural minerals, transition metal ions are frequently contained in distorted sites. Consequential to the site distortion, the degeneracy of the d-levels will decrease and multiple electronic transitions are obtained for each distorted symmetry. To obtain the values of $10Dq$ in a distorted symmetry, energy level diagrams should be constructed empirically from the energy values of each transition. The baricenters of energy for each set of d-levels are then determined and $10Dq$ or Δ will be the energy separation between the baricenters of energy.

In the present study, we shall follow the above procedure wherever it applies and then calculate the values of $10Dq$ and B at various pressures.

Other complications arise in interpreting the spectra of transition metal ions in natural minerals when other types of absorption bands appear in the spectra. These are the charge transfer bands, the theoretical basis of which is outlined briefly in the next section.

II-4. Molecular Orbital Theory and Charge Transfer Spectra

Crystal field models cannot explain all the observed spectral features, and there is a great deal of experimental evidence demonstrating the limits of its usefulness (McClure, 1959; Cotton, 1971). This limitation is mainly due to the neglect of the overlap of metal and ligand orbitals. To take this into account, molecular orbital theory has been modified from crystal field theory.

In the molecular orbital model, the ligand orbitals of appropriate symmetries are mixed with the d orbitals. As an example, let us consider a strong octahedral crystal field in which the d orbitals are split into e_g and t_{2g} . Of the p orbitals of each ligand in the molecule, one orbital is directed along the bond and gives rise to a σ orbital when combined with a cation orbital. The other two p orbitals, which are perpendicular to the bond, give rise to π orbitals when combined with cation orbitals. These two types of orbitals, σ and π , may also be classified into e_g and t_{2g} .

To form molecular orbitals, the atomic orbitals of the ligand and cation should have similar symmetries, e.g. p orbitals of e_g symmetry will combine with e_g d orbitals, and p orbitals

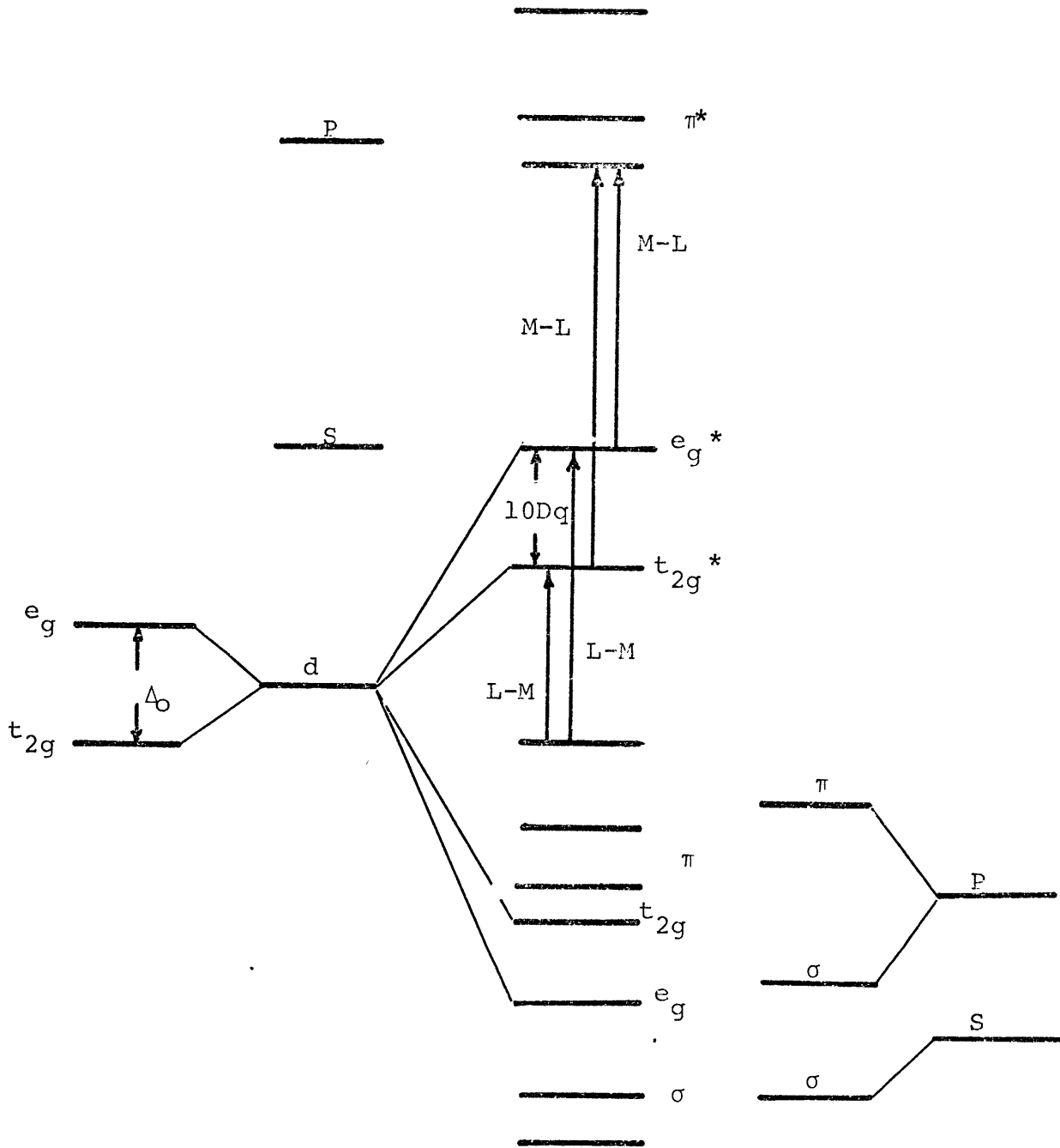
of t_{2g} symmetry will combine with t_{2g} d orbitals (McClure, 1959; Lever, 1968). Since π orbitals are not directed along the ligand bond whereas σ orbitals are so directed, then the former, π , will generally form weaker bonding and antibonding orbitals than do σ .

In both crystal field theory and molecular orbital theory, the difference in energy between e_g and t_{2g} orbitals is a result of the same geometrical factor, the octahedral ligand field, which arises from an electrostatic effect in the former and an antibonding effect of σ -ligand orbitals in the latter (McClure, 1959; Cotton, 1971).

To understand the origin of the charge transfer bands and how they are related to those of crystal field, Fig. 2 is drawn schematically to illustrate both types of transitions for an octahedral complex. In this diagram, the energy levels of the free cation and the free ligand are shown on both sides. Also shown is how the d-orbitals split into two sets of levels, e_g and t_{2g} as a result of placing the cation in a regular octahedral electrostatic environment. The central portion of the diagram shows the energy levels of the molecular units (ML_6) as a consequence of combining ligand and cation orbitals. Molecular orbitals marked by an asterisk are those of antibonding character, whereas others are either bonding or non-bonding. The levels below t_{2g}^* are filled with electrons and the levels above e_g^* are empty. However, these two levels, t_{2g}^* and e_g^* , could be completely filled, or empty, or partly filled depending on the number of d electrons of the transition metal ion. The e_g^* and t_{2g}^* levels have mostly metallic character, whereas the levels

FIGURE II-2

The energy levels of the free cation, the free ligands, and the molecular unit (ML_6), drawn schematically, based on the molecular orbital model.



Cation Orbitals

Molecular Orbitals

Ligand Orbitals

immediately above and below them have mostly ligand character. Transfer of electrons from the ligand orbital to either t_{2g}^* or e_g^* will give rise to ligand-to-metal (L→M) charge transfer bands and from t_{2g}^* or e_g^* to the above levels will produce metal-to-ligand (M→L) charge transfer bands (Phillips and Williams, 1966).

Tails of charge transfer bands, due to electron transfer from the orbitals of primarily ligand character to higher energy levels having mostly metallic character (e_g^* or t_{2g}^*) are always observed in the ultraviolet spectra of silicate minerals bearing transition metals.

Another type of electron transfer is that between the t_{2g}^* and e_g^* levels of one cation to that of another neighboring cation of different oxidation state. This is called a metal-to-metal electron transfer (M→M) or intervalence transfer (Hush, 1967). Metal-metal electron transfer can occur either between the energy levels of cations of the same element but of different oxidation states, e.g. $Fe^{2+} \rightarrow Fe^{3+}$, $Ti^{3+} \rightarrow Ti^{4+}$, which is called homonuclear intervalence transfer; or between d-levels of cations of different elements, e.g. $Fe^{2+} \rightarrow Ti^{4+}$, which is known as heterogeneous intervalence transfer (Hush, 1967).

The intensities and energies of charge transfer bands arising from metal-metal electron transfer are dependent on the extent of delocalization of electrons between metal nuclei. This delocalization will lead either to direct overlap of the orbitals of the two metal atoms or to metal-ligand-metal overlap through σ or π metal-ligand bonding. Overlap orbitals for the former are designated ΔMM , and those for the latter as ΔMLM

(Hush, 1968). The values of the overlap integrals Δ_{MM} or Δ_{MLM} are also dependent on the interatomic distances, the nature of the ligand, and the crystal geometry.

Since it is the purpose of this thesis to examine the effect of pressure on the spectra of minerals, we need to examine how the effect of pressure on absorption phenomena may be described by these theories.

II-5. Effect of Pressure on Crystal Field and Charge Transfer Bands

The most significant spectral parameters that concern this study are the band energies, shapes, and intensities and their interrelationships.

The energies of most significant crystal field transitions are given for d^n (where $n=1,2,\dots,9$) electronic configurations in Table 1. Some of these transitions are dependent solely on Dq , others on B , and still others on both B and Dq . The relation between Dq and the metal-anion distance, R , in equation (6) can be given as:

$$Dq \propto \frac{1}{R^5} \quad (7)$$

With increasing pressure, assuming a typical hydrostatic condition, R is expected to decrease and results in an increase of Dq . Therefore, we expect significant energy increases to be observed for those bands dependent only on Dq . However, bands which are dependent on B and C are expected to show very small negative energy shifts (i.e. red shift). This is because B and C are inversely proportional to the spatial extent of the ligand and

cation orbitals. At elevated pressures, this extent is expected to increase due to shortening of interatomic distances and increased overlap of ligand and cation orbitals.

Decreasing B with pressure will lead to an increase in the degree of covalency which is usually expressed in terms of β which equals B/B_0 , where B and B_0 are the values of Racah parameter in the complex and the free ion respectively; β is sometimes called the "nephelauxetic ratio" (König, 1971; Reiner, 1969; Lever, 1968).

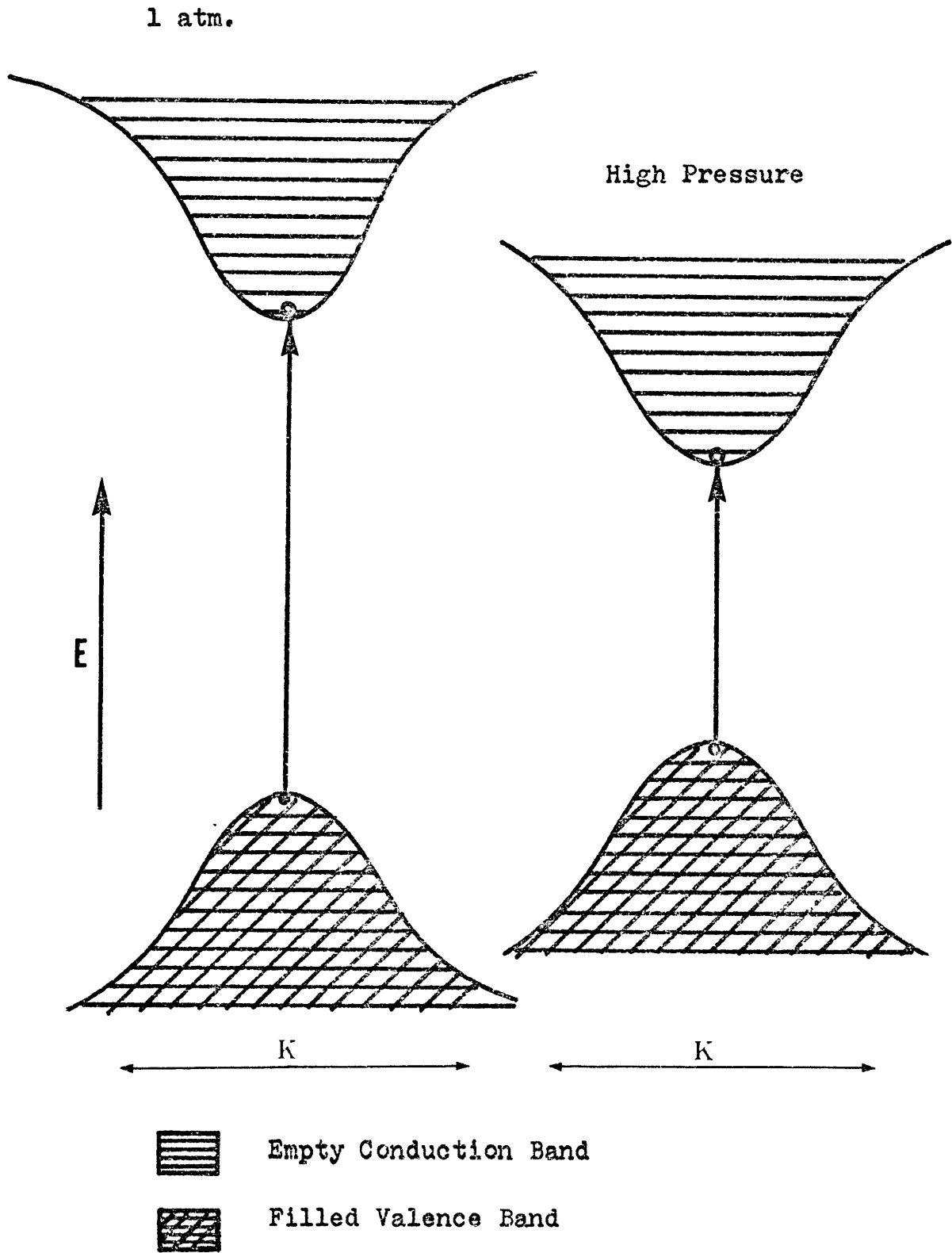
Spectral bands whose energies depend on both B and Dq need careful treatment since B and Dq are expected to show opposite trends with increasing pressure; however, such bands will usually show a blue shift because Dq is more sensitive to the shortening of metal-ligand bond distances than B .

On the other hand, effect of pressure on charge transfer bands could be envisaged in three ways: Firstly, assuming that the d orbitals (e_g and t_{2g} in C.F.T. or e_g^* and t_{2g}^* in M.O.T.) are the major orbitals affected by pressure, then the increase in crystal field splitting parameter $10Dq$ is due mostly to raising e_g^* energy level relative to t_{2g}^* (Fig. 2). As a result of this shift, energies of charge transfer transition, $M \rightarrow L$ and $L \rightarrow M$ are expected to decrease with pressure.

Secondly, using the band model, the effect of pressure on charge transfer bands may be related to closing the energy gap between valence and conduction bands (Drickamer and Frank, 1973). Drickamer (1965) has indicated that with increasing pressure the general tendency is to broaden the energy bands and to lower the

FIGURE II-3

Schematic representation of conduction and valence bands at 1 atm. and high pressure for a direct transition (K is the propagation vector of the wave function).



energy of the conduction band since it is more sensitive to compression than the valence band. The net effect will be a shift of the absorption edge or the charge transfer band to lower energy. This is often true, especially for direct transitions illustrated in Fig. 3 for which $\Delta K=0$. Reducing the energy gap with pressure may also lead to overlap of the highest filled band with the empty conduction band, and may lead to a metallic behavior of the solids. Band theory also predicts decreasing resistivities of metals with pressure, and hence increasing electrical conductivities (Drickamer and Frank, 1973). This is due mostly to the reduced amplitude of lattice vibrations.

Thirdly, using the schematic representation of the potential energies of the ground and excited state (Fig. 4), Hush (1968) and Drickamer et al. (1972) have expressed the energy of the maximum optical absorption as:

$$h\nu_{\max} = E_0 + 1/2 \Delta \Omega^2 \Delta \quad (8)$$

where E_0 is the overall energy difference between the ground and excited state, Δ is the vector difference of equilibrium positions of atoms in the final and initial state of the system, and Ω is the frequency tensor associated with the vibration of all atoms in the medium.

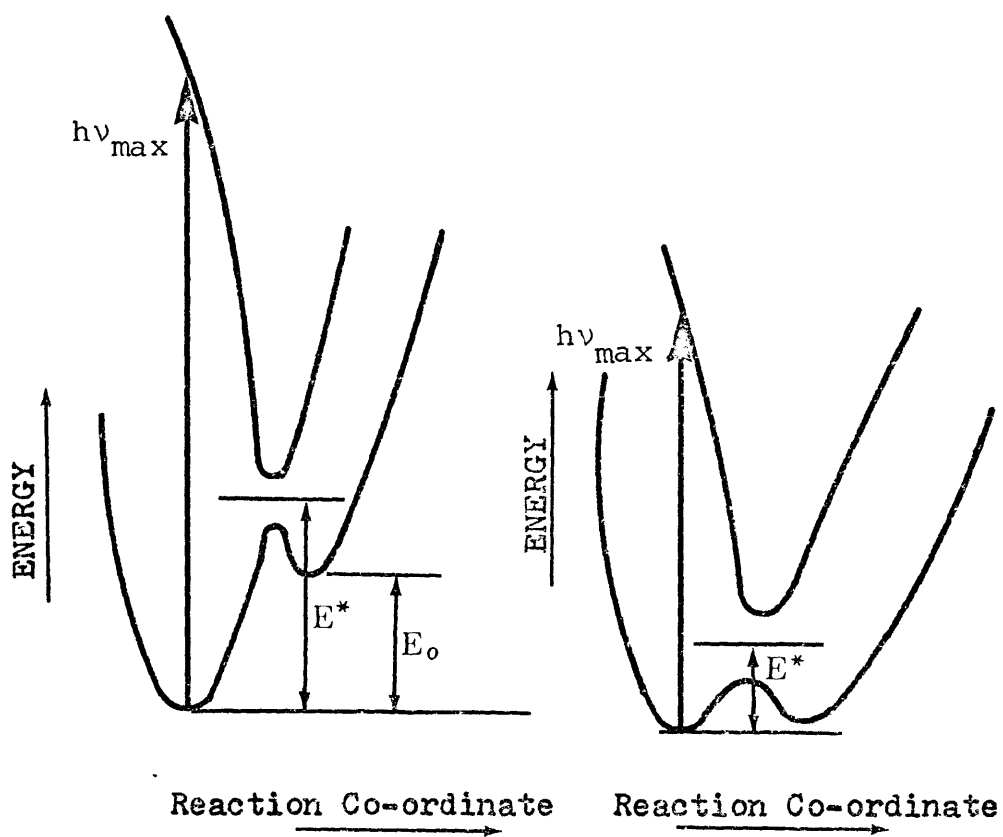
Drickamer et al. (1972) have shown that there is a vertical displacement of the potential wells with pressure (i.e. decreasing E_0) and Δ is expected to decrease due to the horizontal displacement of the configuration coordination. The frequency, Ω , will obviously decrease with pressure due to inhibition of atoms' vibrations, so that the net effect is to decrease the energy of

FIGURE II-4

The potential energy wells of the ground and excited states at 1 atm. and high pressure are shown schematically [modified from Hush (1968) and Drickamer et al. (1972)].

1 atm.

High Pressure



the maximum optical absorption $h\nu_{\text{max}}$, i.e. the energy of charge transfer band.

Chapter III

APPARATUS AND EXPERIMENTAL METHODS

III-1. Spectral Apparatus

The apparatus employed to study the spectra of mineral samples at elevated pressures consisted of a standard Cary 17 spectrophotometer (Fig. III-1). This instrument provides a source of monochromatic radiation from 2200 to 360 nm and measures the ratio of the intensity of the transmitted monochromatic light through the sample to that transmitted through a standard.

The optical system of the spectrophotometer has been modified to enable measurements to be made of the spectra of small crystal fragments (diameter $>50\mu$) and of micro-powdered specimens subjected, simultaneously, to pressures up to 250 kilobars. To obtain the spectra of such small samples at these elevated pressures, it was necessary to place two microscopes (Fig. III-2) in the path of the two beams emerging from the cell compartment openings. It was required also that the two microscopes be in a vertical position, i.e. their axes are at right angles to the horizontal paths of the reference and sample beams. Having the two microscopes in this position enabled the high pressure diamond to be mounted conveniently on the stage of the microscope. This geometry facilitated the viewing and focusing of the sample while it is subjected to high pressures. To achieve the above conditions, it was necessary to add the following parts to the microscopes:

- 1) A reflecting-focusing system (Fig. III-3) which reflects

FIGURE III-1

A photograph showing the Cary 17 spectrophotometer (a), the newly constructed optical attachment (b), and the detector (c).

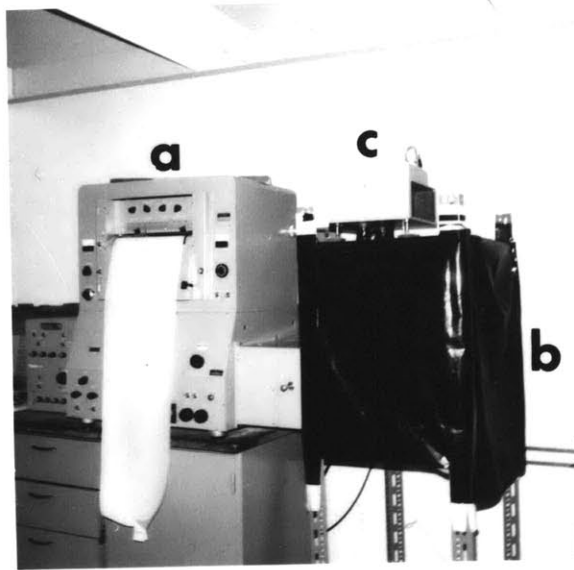
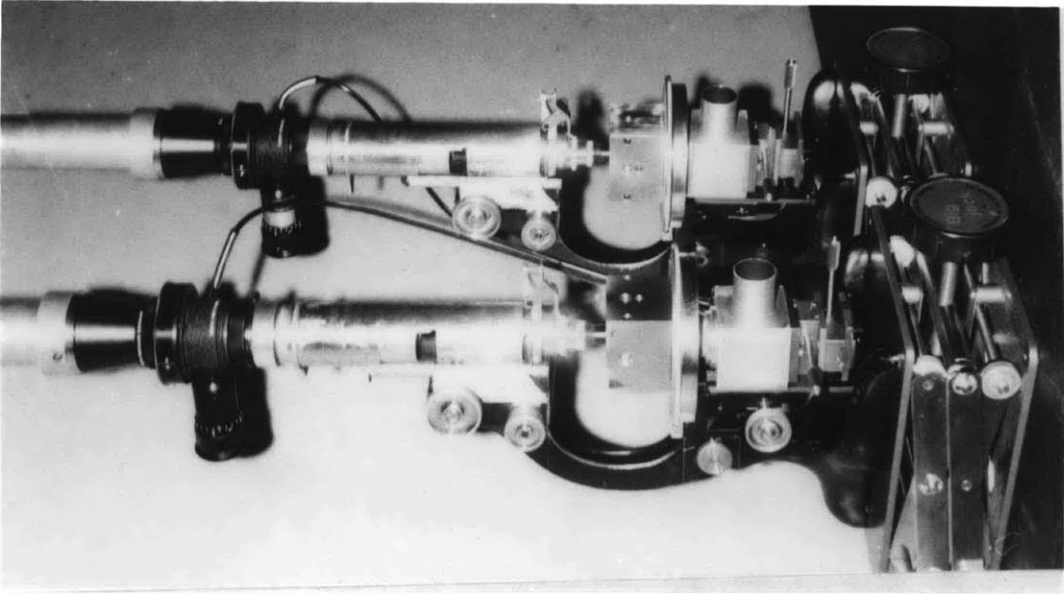


FIGURE III-2

A photograph shows the reference and sample microscopes, the diamond cell placed on the stage of the microscope and the reflecting-focusing system below the stage.



the light beam and focuses it to about 50 μ in diameter. It consists of an aluminum box coated inside with a dull black paint to prevent reflections from the metal surface. The box contains an aluminum mirror placed at its body diagonal to reflect more than 95% of the impinging light; the reflected light from the mirror surface is then focused to about 50 μ in diameter by means of a UMK50 objective fitted in a circular opening at the center of the upper face of the box.

2) A mini-transfer stage: this has been designed to allow travel of the reflecting-focusing box in the x and y directions. It consists of two pairs of mini-gears that are placed perpendicular to each other. Each gear system is attached to an adjusting screw allowing transfer of the substage in the horizontal plane. The substage could also travel vertically along the z axis using another gear system perpendicular to the plane of the transfer stage.

3) Micro-camera attachment: this was added to each microscope to enable viewing and focusing the sample. Each attachment consists of a lateral eyepiece with lower and upper adapting tubes that are used to fit the lateral eyepiece to the microscope tube and to the detector. The detector was rotated 90° from its original position and placed at the top of the upper shelf (Fig. III-4). Leveling screws were used to keep the detector in a horizontal position and other connecting tubes were attached to its two openings in order to receive the light beams emerging from the reference and sample microscopes. Each microscope is placed on a jack which moves the whole microscope system in a vertical

FIGURE III-3

The reflecting focusing system which consists of:

- a) Aluminum box coated with a dull black paint,
- b) Aluminum coated mirror which reflects more than 95% of the impinging light,
- c) UMK50 objective.

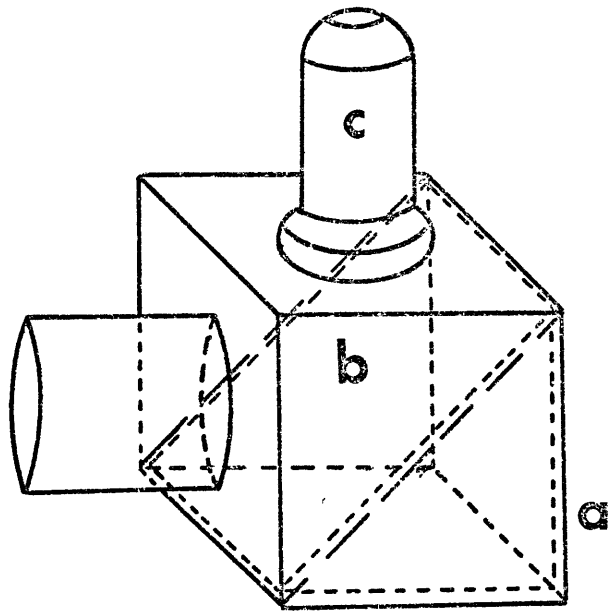
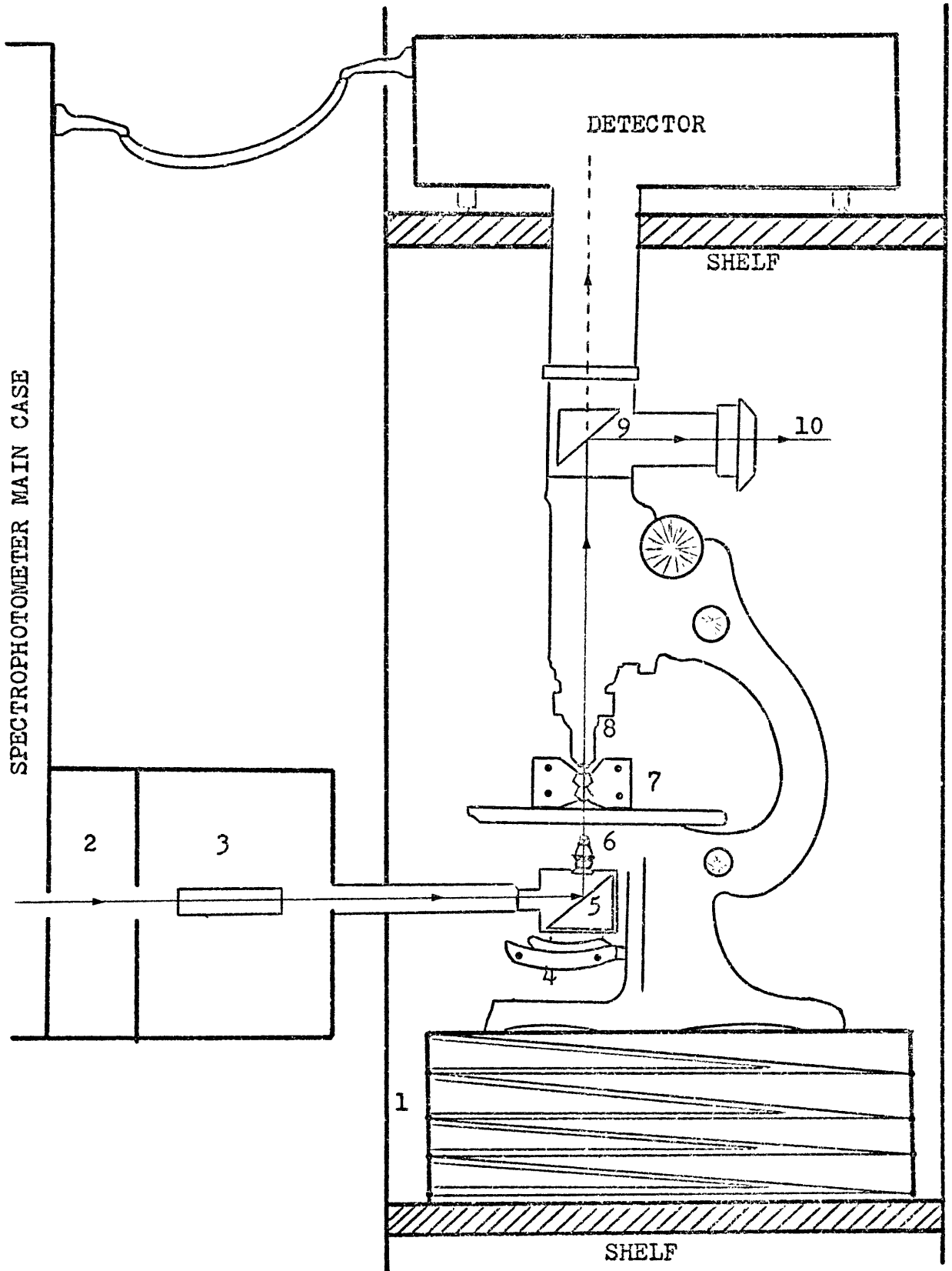


FIGURE III-4

The spectrophotometer optical attachment designed to enable the measurement of the spectra of micro-samples ($>50\mu$): 1. Jack, 2. Beam divider, 3. Polarizer, 4. X-Y mini-transfer stage, 5. Aluminum mirror, 6. Focusing lense(UMK50), 7. Diamond cell, 8. UMK50 objective lense, 9. Mirror-shutter combination, 10. lateral eye piece.



direction. The system as a whole, which is called here the optical attachment, is covered very tightly with a black plastic cloth to prevent interference by light from outside.

The reference and sample beams, before being reflected from the mirror surface, are polarized by means of two calcite prisms placed in the cell compartment. When the spectra of powdered specimens are measured, the polarizers are removed because they cause noise in the spectrum due to the randomly oriented grains of the powdered samples.

The light path of the new optical system is illustrated in Fig. (III-5). Each light beam is reflected and then focused by means of a UMK50 objective. After the beam has been focused on the sample in the diamond cell, it diverges and is converged again by another UMK50 objective. The beam is then either reflected horizontally to the eyepiece or allowed to travel vertically into the detector. A similar light path exists for the reference beam except that it does not pass through the sample.

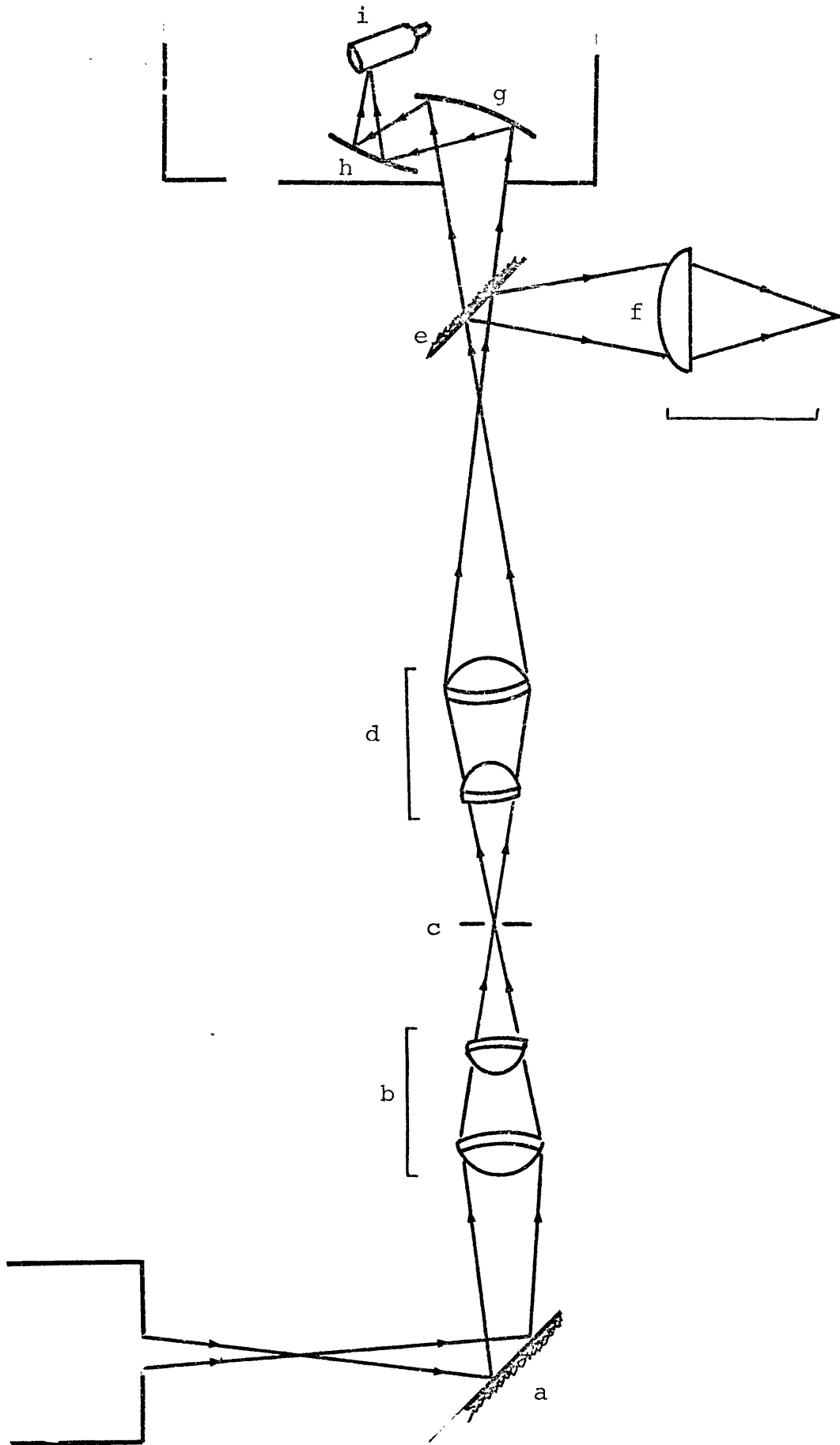
III-2. High Pressure Instruments

The pressure instruments used for generating pressures up to 250 kilobars were diamond pressure cells. Three modifications have been used in this study: UP, UXP, and PP types (Mao, 1967; Bassett et al., 1967; Merrill, 1973; and Bassett, 1974). All of these pressure cells were designed and made by Professor W.A. Bassett at the University of Rochester; however, they were modified at the Machine Shop at M.I.T. so that they could be used in the high pressure spectral measurements.

FIGURE III-5

The light path in the new optical system:

- a) Reflecting mirror
- b) Focusing lower objective
- c) Sample
- d) Upper objective (beam diverges and then converges)
- e) Reflecting prism (it allows the beam either to be reflected horizontally to the eye piece or to travel vertically to the detector system)
- f) Lateral eye piece for viewing the sample and focusing the light beam.
- g,h) Concave mirrors for focusing the beam on the photomultiplier
- i) Photomultiplier tube



The UP style diamond pressure cell (Fig. III-6) consists of two diamond anvils placed on two pistons. One is stationary and the other is driven by means of a driver screw. The powdered sample is placed between the anvil faces and the collimated light travels along the compression axis. To calibrate the pressure, the sample is usually mixed in a 1:2 ratio with NaCl powder, and a lead glass collimator is attached to the diamond cell to collimate the x-ray beam to about 100 μ . The diffracted x-rays are recorded on a film cassette attached to the other end of the cell; the exposure time required to collect x-ray lines of reasonable intensities for each pressure measurement is about 300 hours. The advantage of using this type of pressure cell is that the x-ray is collimated on the central region of the sample (about 100 μ), where the pressure inhomogeneity is minimal. This type of diamond cell was used frequently in the early stages of this research.

The UXP style pressure cell is a modification of UP type which has been reduced significantly in size so that it can fit easily inside a Debye-Scherrer powder x-ray camera (Fig. III-7). The x-rays in this design travel along the anvil faces across the sample. Although the required exposure time in this method is reduced to about 48 hours, it has the disadvantage of broadening the diffraction lines due to the non-uniformity of the pressure across the sample. Using this type of diamond cell requires more careful work to distinguish the low pressure diffraction lines from the high pressure lines of the sample. Some corrections also have to be made to take into account the widths and intensities of the diffraction lines.

FIGURE III-6

A photograph of the UP style pressure cell mounted on a universal x-ray table (note the lead glass collimator at the center of the diamond cell).

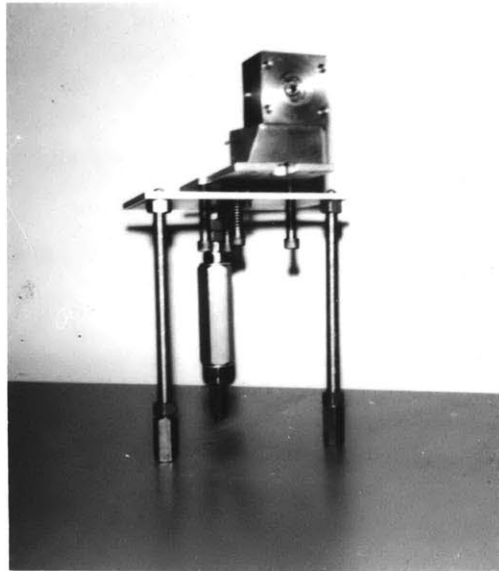
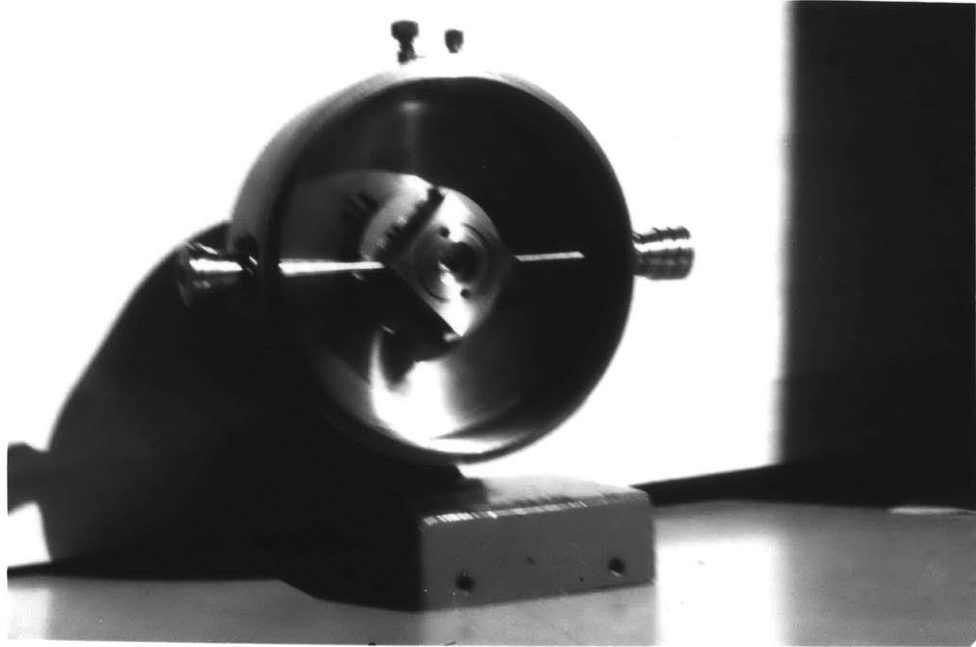


FIGURE III-7

A photograph of the UXP type pressure cell
mounted inside a Debye-Scherrer powder x-ray
camera.



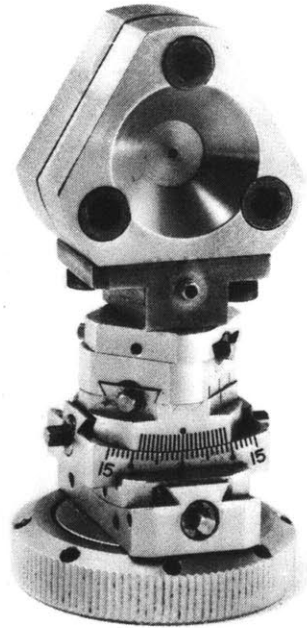
The third type of diamond anvil cell is designated as PP (Merrill, 1973). It is mostly used for x-ray crystallographic studies of single crystals and was employed in this project for the optical absorption measurements of single crystals at elevated pressures. The cell simply consists of two diamond anvils placed on two platens that are driven against each other by means of three screws (Fig. III-8). The maximum pressure that can be achieved using this cell is about 80-100 kilobars. The limitation of this assembly is discussed later in this chapter.

III-3. Sample Preparation for Spectral Studies

The samples used in this research were either powders or single crystals. The process of mounting the powdered specimen is fairly easy; in most cases, gem quality single crystals are selected and crushed in an agate mortar for about three hours, until the grains are hardly recognized under the X45 magnification microscope. The average grain size is usually less than 2μ in diameter. A fine ultra-pure NaCl powder is then added (2:1 weight ratio), mixed and ground thoroughly with the sample. The reason for grinding the sample and NaCl to this size ($1-2\mu$) is to obtain a similar pressure distribution on the sample and the standard, NaCl, and to minimize the shear stress on the sample. A few milligrams of the mixture of NaCl and the sample are placed on the tip of a sharp needle and transferred to the upper face of the lower anvil. The pressure is generated on the sample by driving the lower piston against the stationary upper one. When the two anvils are close enough to each other, although some of

FIGURE III-8

A photograph of the PP type diamond cell mounted on an eucentric goniometer head (Merrill, 1973).



the sample is extruded, the remainder is squeezed between the two anvil faces. The maximum pressure that can be achieved depends on the surface area of the anvil faces and the force applied on the two diamonds. To obtain a pressure of about 300 kilobars a force of about 270 kilograms should be applied on an anvil face of about 0.3 mm in diameter (Bassett, personal communication).

Preparing oriented single crystal fragments for high pressure spectral studies requires more care. A crystal fragment of the sample (150-200 μ in diameter) is oriented by means of spindle and transfer stages and then is mounted on a glass using Duco cement. Without changing the orientation, the crystal is then polished on both sides until flat parallel faces are obtained.

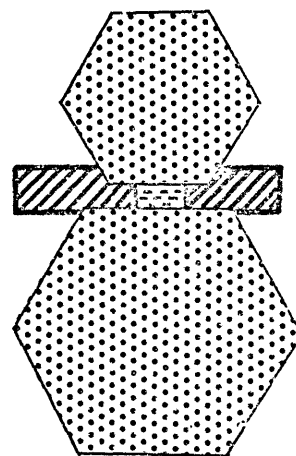
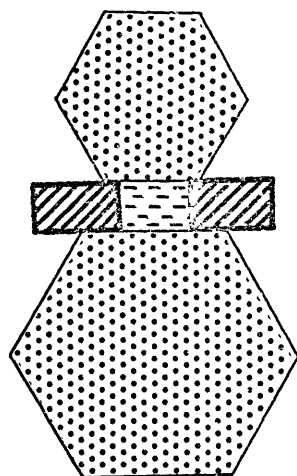
The gasketing technique developed by Van-Valkenberg (1965) was used, in which a crystal is mounted in liquid in the cell, thereby obtaining hydrostatic pressure conditions on the sample. Thus, a stainless steel gasket, having a cylindrical hole (about 0.35 mm in diameter) at its center, is placed on the flat face of the lower anvil (Fig. III-9). After the hole is adjusted so as to be at the center of the face of the lower anvil, it is cemented to both the diamond and the sliding piston in order to prevent movement of the gasket and extrusion of the liquid. The hole in the gasket is then filled with a pressure fluid, and the crystal is placed in the liquid with the known axes parallel to the diamond anvil faces. Pressure is obtained by driving the two diamonds against the metal gasket which in turn transfers the pressure through the liquid to the sample. The ultimate

FIGURE III-9

The gasketing method: A stainless steel gasket between the two diamond anvils at 1 atm. and at high pressure.

1 atm.

High Pressure



Diamond



Stainless Steel Gasket



Pressure Fluid

pressure that can be reached using this method is 80-100 kilobars. This limit results from the gasket's yield strength and the solidification of the liquid.

In the high pressure spectral studies, it is preferable for the sample under investigation to be a single crystal rather than a powder, for the following reasons:

1) The pressure condition in the single crystal method is completely hydrostatic, as long as the pressure transmitting fluid does not solidify in the required pressure range.

2) The high pressure polarized spectra can be measured for at least three different orientations.

3) The single crystal, being much thicker than the powdered sample, produces enough absorption to characterize the weak bands at elevated pressures.

4) The pressure calibration in the single crystal method is easier and more accurate.

III-4. Alignment Procedures and Pressure Calibration

A. Alignment Procedure

In the high pressure experiments, three types of alignments are required before applying pressure to the sample. First, it is necessary to align the two faces of the opposed diamond anvils in a way to make them parallel to each other and perpendicular to the axis of pressure. This alignment is necessary to minimize the possibility of cracking the diamonds and to obtain a uniform pressure distribution across the sample. Alignment of the diamond can be accomplished by employing materials that transform

easily into new phases as a consequence of subjecting them to elevated pressures. These high pressure polymorphs should be easily identified (e.g. from their color changes) and should be sensitive to the pressure. The most commonly used material is silver iodide (AgI), which undergoes several phase transitions at various pressures (Fig. III-10). The most conspicuous of these transitions were reported by Bassett and Takahashi (1965); these are:

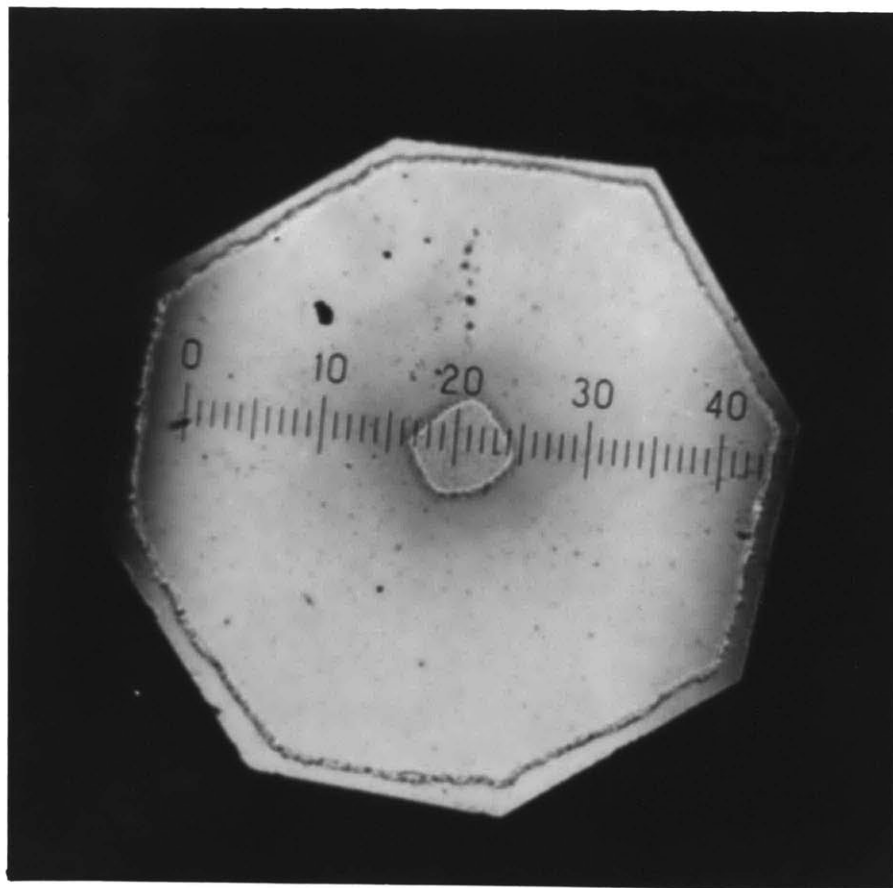
AgI (IV) \rightarrow AgI(III) at 4 Kb. and room temperature,
and AgI (III) \rightarrow AgI(IV) at 100 Kb. and room temperature.

When the anvils are out of alignment, the 4 Kb. phase of AgI will appear off-center on the diamond faces. The alignment can be achieved then by altering the pair of rockers, on which the diamonds are seated, and then centering the high pressure phase.

Secondly, after aligning the diamond faces, the x-ray collimator must be aligned with the diamond anvils. This alignment is essential for the x-rays to impinge only on the central region of the anvil faces where the pressure gradient is minimal. This alignment is achieved by placing a piece of photographic film between the two anvils and applying pressure to cause indentation of the anvil faces on the film. The collimator is then attached to the front side of the diamond cell, and the pressure cell assembly is transferred to a universal table for further alignment of the x-ray beam with the collimator. The latter alignment is achieved by employing a Geiger counter at the other end of the cell and measuring the intensity of the x-rays passing through the collimator and the two diamonds. The x-rays can be aligned

FIGURE III-10

A photograph of silver iodide (AgI) powder between the two diamond anvils. The central region shows the boundary of the high pressure phase, AgI(IV), indicating that the pressure is ≥ 100 kb.. Near the periphery of the anvil face, note the boundary of the AgI(III) phase where the pressure is ≥ 4 kb.. Note also that the AgI(IV) phase is at the center of the diamond face, indicating that the two diamond anvils are in good alignment.



further with the collimator by adjusting the universal table in various angles until maximum x-ray radiations are detected by the Geiger counter. After exposing the photographic film to x-rays for about a minute and developing the film, a black spot should be observed at the center of the indentation on the film caused by the anvil faces. However, if the spot is off center, realignment of the collimator has to be done by slight movement of the collimator and further optical observations under the microscope.

Finally, an alignment of the film cassette is necessary to obtain a geometry similar to that of Debye-Scherrer camera. It is essential that the sample be at the center of the film curvature. This condition is achieved by means of cassette mounting rods, translating bars, and two transparent plastic plates connecting the film cassette with the pressure cell. The center of the curvature of the film is marked on each plate and the sample is aligned so that it is co-linear with the two marks on the plates. For additional information on the alignment procedures see Bassett et al. (1967).

III-4. B. Pressure Calibration

Depending on the nature of the sample (i.e. single crystal or powder), two methods of pressure calibration were used in this study. For powdered specimens, NaCl powder may be used as an internal standard, and the pressure scale is determined from variations of the unit cell parameter "a" versus pressure.

Using the Mie-Gruneisen equation of state, Decker (1965, 1966) calculated the variations of the lattice parameter "a" for NaCl

as a function of pressure over a pressure range 0 to 500 kilbars. Similar calculations have also been done by Weaver et al. (1968).

NaCl was chosen as an internal standard for pressure calibration because:

1) It is transparent in the i.r. and visible spectral regions. This property makes NaCl an excellent internal standard for high pressure spectral studies.

2) NaCl has a very low shear stress (Kinsland, 1974) that minimizes the pressure inhomogeneity on the sample.

3) The isometric nature of the NaCl structure causes minimum interference of its x-ray diffraction lines with those of the sample; in addition, each x-ray reflection yields a value for the molar volume.

4) NaCl has a small bulk modulus, i.e. any changes in pressure could yield large changes in volume.

5) The P-V relation for NaCl has been extensively studied, theoretically and experimentally, and is well documented.

As mentioned previously in the NaCl powder method, a mixture of sample and NaCl is mounted on the anvil face, as was mentioned earlier in this chapter, and the mixture is subjected to high pressure. A pellet of NaCl powder is placed on the rear face of the diamond which faces the film cassette, and the sample and standard are then exposed to x-rays for about 300 hours.

The geometries of x-ray reflections from NaCl between the anvil faces and from NaCl on the outside face of the anvil are illustrated in Fig. III-11 . The x-ray diffraction lines produced from the NaCl platelet, at zero pressure, should be cor-

rected, since the platelet is not placed at the center of the film curvature. In fact, the NaCl sample (in this case at 1 atm.) is at a distance less than R_f , the film curvature radius.

To obtain the corrected NaCl reflection at 1 atm., the following equation is employed (Mao, personal communication):

$$R_c = R + t \sin 2\theta \quad (1)$$

where; R is the arc length corresponding to the angle 2θ of the hkl reflection; R_c is the corrected value of R ($t \sin 2\theta$ corrects for the displacement of the NaCl platelet from the center of the film curvature); t is the diamond thickness; and 2θ is the angle of x-ray reflection from the hkl plane. Since R and t are directly measurable and since θ may be determined from Bragg's Law:

$$\theta = \sin^{-1} \frac{n\lambda}{2d_{hkl}} \quad (2)$$

R_c may be calculated. Then, since θ and R_c are known, the correction factor, c , may be determined from equation (3):

$$C = 2\theta/R_c \quad (3)$$

This, in turn, is used to determine, $2\theta_a$, the high pressure angle of x-ray reflection from the hkl plane, using the directly measurable high pressure arc length of the same hkl reflection, R_a :

$$2\theta_a = C \times R_a \quad (4)$$

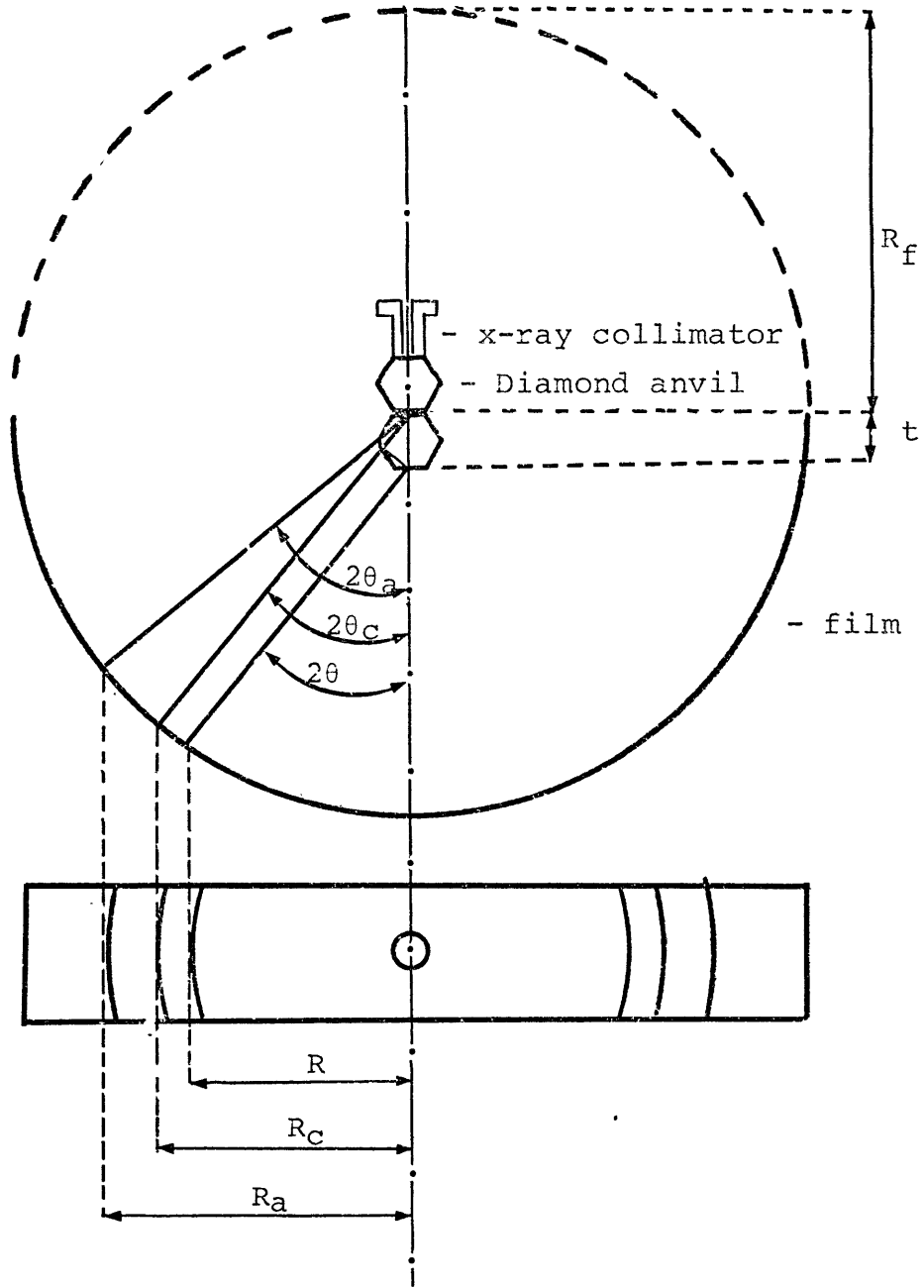
Then, again, employing Bragg's Law, the d_{hkl} of NaCl at elevated pressure can easily be obtained:

$$d_{hkl} = \frac{\lambda}{2\sin\theta_a} \quad (5)$$

and hence, the lattice parameter, "a", at elevated pressure is determined:

FIGURE III-11

The geometries of x-ray reflections from NaCl between the anvil faces and from NaCl platelet mounted on the outside face of the anvil. R , R_c , and R_a are related to reflections corresponding to (200) line. R_c is not observed, but it is calculated from R .



$$"a" = d_{hkl} \sqrt{h^2 + k^2 + l^2} \quad (6)$$

Now, the ratio $(a_0 - a)/a_0$ or $\Delta V/V$ can be obtained and the pressure estimated easily using Decker's Table (1965).

The pressure in the single crystal cell is calibrated by employing different liquids of known freezing pressure (Forman et al., 1972; Piermarini et al., 1973). These liquids are listed in the following table:

Material	Phase Transition	Pressure (Kb.)
CCl ₄	L - I	1.3
H ₂ O	L - VI	9.6
n-C ₇ H ₁₆	L - I	11.4
C ₂ H ₅ Br	L - I	18.3
2-Methyl Alc.	L - S	25.0
Methanol	L - S	35.8
Isoamyl Alc.	L - S	37.0
(1:1) Pentane: Isopentane	L - S	70.0
(4:1) Methanol: Ethanol	L - S	100.0

The solid-solid phase transformation of KCl(I) to KCl(II) which takes place at 19.3 Kb. is also a useful pressure indicator in the liquid cell.

Another method of pressure calibration is the pressure shift of the sharp R-line fluorescence spectrum of ruby. Forman et al. (1972) observed a consistent shift of the two ruby lines R₁ and R₂ of an average -0.77 and -0.84 cm⁻¹/Kb., respectively. Since

the fluorescence instruments are not available at our laboratory, this method was only used to calibrate the phase transition of gillespite during experiments performed by the author at NBS. However, this method can be used if the light source of the Cary spectrophotometer is replaced by a YAG laser, which emits radiations of wavelengths appropriate to cause the fluorescence of the ruby crystal fragment contained in the liquid cell with the sample.

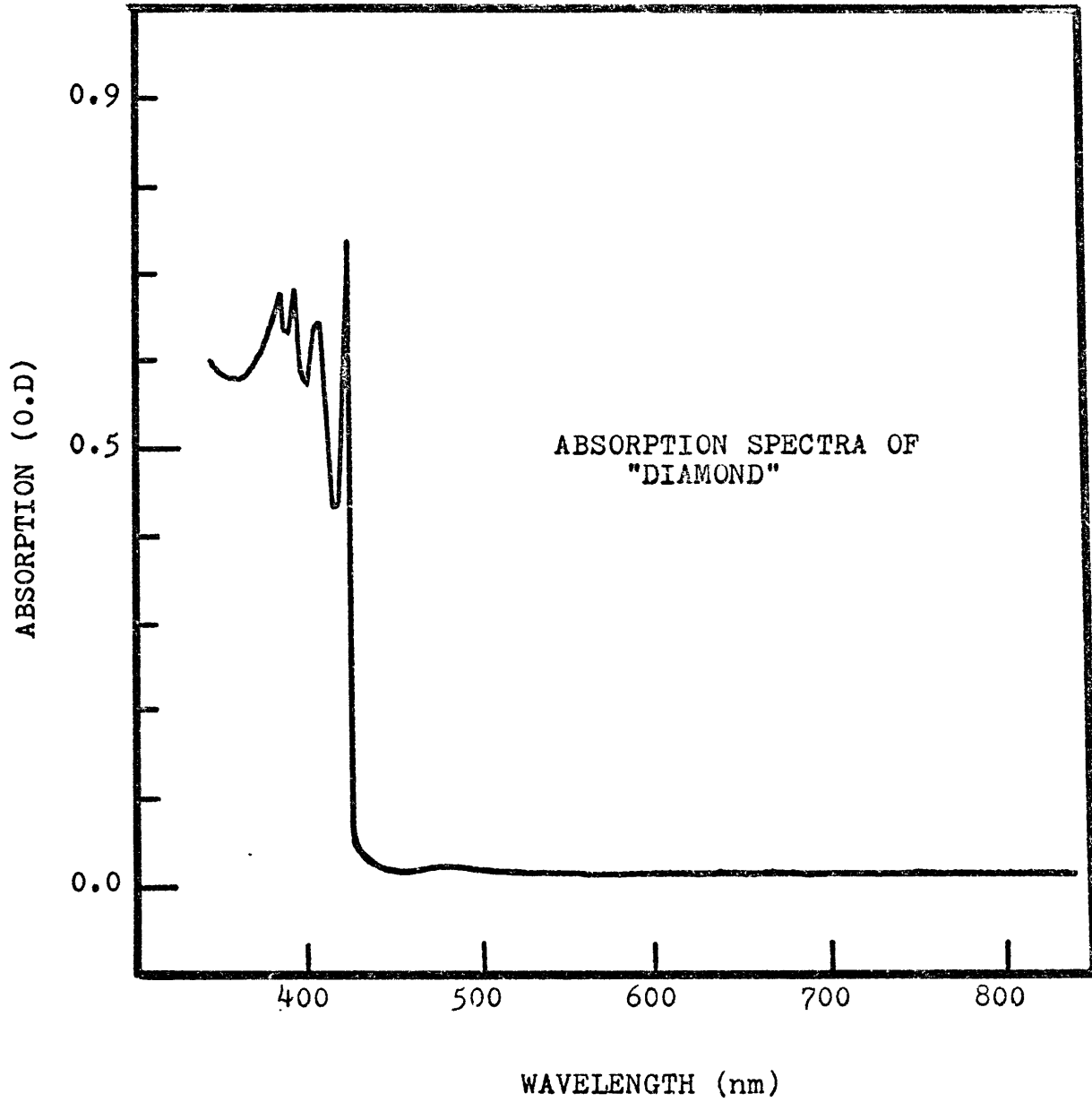
III-5. Experimental Difficulties

Many difficulties have been encountered in performing the experimental part of this project. Some of these have been solved, but others remained unsolvable. Such problems confined the nature of this investigation to be somewhat semiquantitative than quantitative in many cases. These difficulties are:

1) Interference of the diamond absorption in the visible region: Figure III-12 shows the spectra of a pair of diamond anvils used in the pressure cell. The sharp peaks in the visible region around 415, 403, 394, and 384 nm are related to defect centers in the diamond structure containing trapped nitrogen in various forms (Clark et al., 1956; Raal, 1959). The diamond absorption bands overlap bands of certain transition metal ions (e.g. Mn^{2+} , Fe^{3+}) in the visible region and obscure them. To reduce the diamond absorption, another pressure cell containing diamond anvils of similar thicknesses as those in the sample beam was employed in the reference beam. The reference diamond anvils then absorb similarly and may offset the absorption of those used in the sample beam.

FIGURE III-12

The visible spectra of a pair of diamond anvils
used in the pressure cell.



2) Sample thickness and size: The small size of the sample (50-100 μ in diameter and 5 μ thick) used in the high pressure study presents another problem. Working with such small samples will not permit the resolution of the broad and weak bands and will reduce the intensities of many bands significantly. Because of this difficulty, only sharp and intense bands are investigated, especially when powdered specimens are being used.

3) Pressure inhomogeneity across the sample: The pressure gradient across the anvil faces has been recognized by many workers as a serious problem in the opposed anvils high pressure cell. Many attempts have been made to evaluate the pressure distribution across the surface of the sample in the anvil type press. A formula has been derived by Jackson and Waxman (1963) which gives the magnitude of pressure at any point on the surface of the anvil:

$$P = P_0 \cdot G(r) \cdot \exp(2f/h) (r_0 - r)$$

where P is the pressure at radius r from the center of the anvil, P_0 is the pressure at the center of the sample, $G(r)$ is a function of (r) or unity, f is the coefficient of friction, and h is the distance between the two anvils or sample thickness. The above formula depends on many factors that limit its usefulness; however, it shows clearly that the pressure is expected to increase towards the center of the anvil face.

Nevertheless, the magnitude and the shape of pressure distribution in the diamond pressure cell have been investigated experimentally by Lippincott and Duecker (1964), using the high pressure spectral studies of nickel dimethylglyoxime. This

compound has an intense band at $19,000 \text{ cm}^{-1}$ which is very sensitive to pressure. From measurements of samples of nickel dimethylglyoxime located at various radial distance across the diamond anvil face, the shape of pressure distribution was determined (Fig. III-13b).

Further, the pressure distribution in the diamond cell was investigated more accurately by Piermarini et al. (1973) using the line broadening and line shift measurements of the R ruby fluorescence line. Figure III-13a illustrates the pressure gradient across an ungasketed sample of powdered NaCl. Since the average radial position of the sample (sample diameter is about 75 microns), it is obvious then that there is an average error of $\pm 5 \text{ Kb.}$ in the determined pressure.

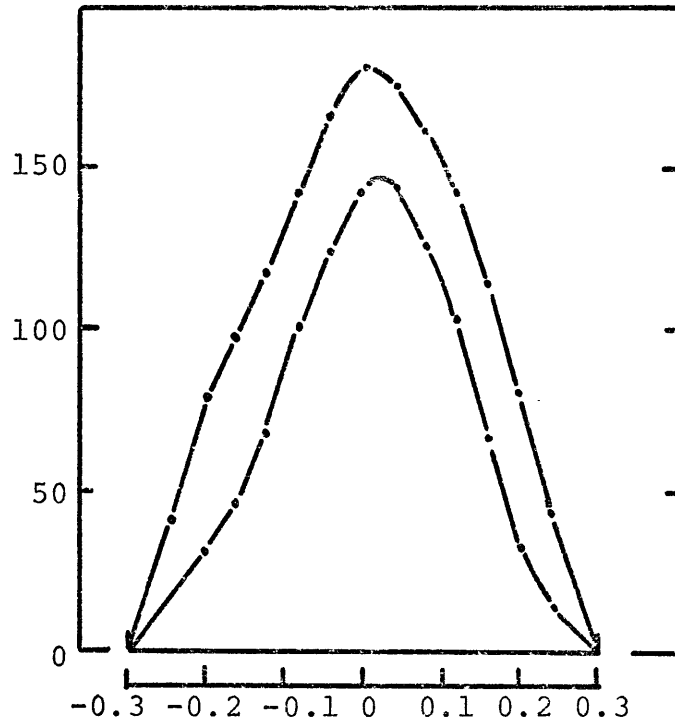
The use of an encapsulating fluid as pressure transmitting medium, however, gives a true hydrostatic pressure condition on the sample. Piermarini et al. (1973) studied the pressure gradient across the sample using a 4:1 by volume liquid mixture of methanol and ethanol. They observed zero pressure gradient across the surface area of the diamond anvil up to 100 Kb. However, above this pressure, the liquid mixture solidified and the shear stress became a significant factor in causing a non-hydrostatic pressure environment around the sample.

4) Problems of pressure calibration: It was mentioned earlier in this chapter that the powdered sample has to be mixed with an internal standard, NaCl. However, dilution with NaCl decreases the relative concentration of the absorbing material and reduces the spectral band intensities. In addition,

FIGURE III-13

- (a) Pressure distribution in an ungasketed sample of powdered NaCl in the diamond-anvil cell at two different applied loads. [From Piermarini, G.J., Black, S., and Barnett, J.D., 1973.]
- (b) Pressure contours for sample of nickel dimethylglyoxime in NaCl (1:3) in the diamond-anvil cell. [From Lippincott, E.R. and Deucker, C.D., 1964.]

FIGURE IV-13(a)



Radial position along sample diameter (mm).

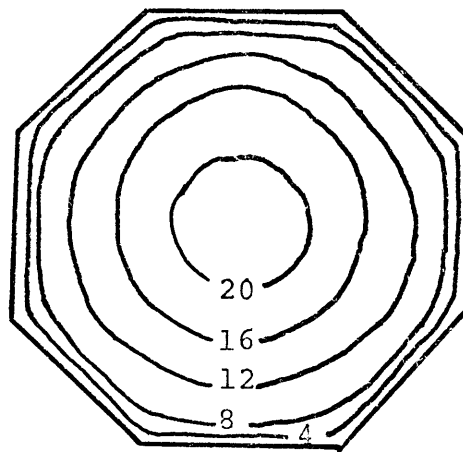


FIGURE IV-13(b)

pressure calibration itself, using the NaCl method, is tedious and time consuming, since, for each pressure measurement, the mixture of sample and NaCl has to be exposed to x-rays for about 300 hours, in order to obtain diffraction lines of reasonable intensities. Errors in pressure calibration may also be significant, because of misalignment of the diamond cell with the x-ray beam could easily happen from any movement of the diamond cell or the x-ray table.

Inadequate x-ray equipment, notably not having an Mo radiation source, was another factor limiting and delaying pressure calibrations.

Chapter IV

EFFECT OF PRESSURE ON CRYSTAL FIELD BANDS

IV-1. Introduction

The objective of this chapter is to present the results of optical absorption spectral measurements performed on mineral samples at various pressures. Then, these results, coupled with other spectral data in the literature, will be used as a basis to discuss the variations of spectral parameters with pressure.

The spectra of natural minerals are usually complicated by multiplicities and distortions of sites containing the transition metal ions, by the occurrences of more than one type of transition metal ion, and by mixed valence states in each individual mineral.

To reduce such complexities, an attempt was made to select mineral samples which contained one transition metal ion in one oxidation state. However, in certain cases, this was not possible, so that the spectra of more than one cation type were investigated in the individual mineral.

The results of this chapter are reported in five sections according to the crystal structures of the minerals studied. The minerals are classified into the following groups: a) pyroxenes; b) olivines; c) garnets; d) epidotes; and e) miscellaneous. The last group includes minerals of significant interest in this investigation which could not be classified under the first four mineral groups.

In each section, a brief review of the crystal chemistry and crystallography of the mineral group is given first. This

is followed by a description of the crystal structure and the spectral properties of each individual mineral, with emphasis on the site occupancies of transition metal ions at 1 atm and at elevated pressures.

The spectra of each mineral species are presented at 1 atm. and at high pressures. From these spectra, crystal field energy level diagrams are constructed, and then crystal field parameters are evaluated at various pressures. Other useful information, such as the variation of the site symmetry with pressure and an estimation of the crystal field stabilization energies, is gained from constructing d-orbital energy levels at various pressures.

IV-2. Pyroxenes

The pyroxene structure consists of alternating tetrahedral and octahedral layers. Each tetrahedral layer consists of silicate chains extending parallel to the c-axis, and each chain consists of SiO_4 tetrahedra sharing corners.

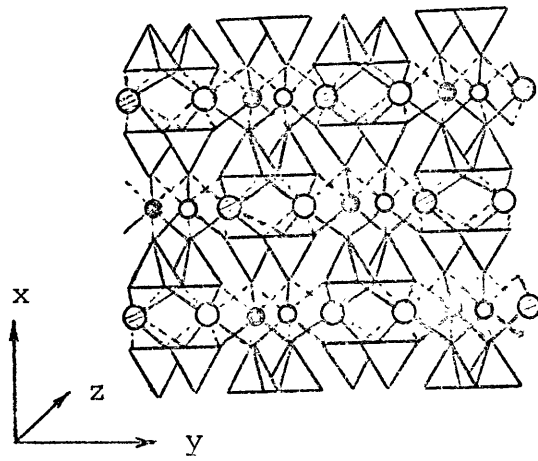
The oxygen atoms on the upper surface of one tetrahedral layer and the oxygens on the lower surface of the next tetrahedral layer together form oxygen polyhedra that surround the larger cations such as: Ca, Na, Mg, Fe, in at least two crystallographically distinct positions (Figure IV-1). These edge-shared groups form the octahedral layer.

The simplest structure in the pyroxene group is that of diopside, which crystallizes in space group $C2/c$. This structure is discussed in some detail to illustrate the crystal chemistry of the pyroxene minerals involved in this project. The

FIGURE IV-1

The crystal structure of diopside projected along the z-axis. Note the 6-fold coordination site of the Mg cation and the 8-fold coordination site of the Ca cation. This figure also shows the octahedral and the tetrahedral layers stacked along the b-axis.

[From Evans, R.C., 1966.]



- Mg at height 0
- Mg at height 1/2
- Ca at height 0
- ⊗ Ca at height 1/2

octahedral layer in diopside contains two crystallographically distinct sites, referred to as M_1 and M_2 (Evans, 1966). The M_1 sites are usually occupied by cations smaller than those in the M_2 sites, and the cations in the M_1 site are coordinated to 6 oxygen atoms in a nearly regular octahedron. The M_1 octahedra share edges to form zig-zag chains parallel to the c-axis, and each M_1 chain is bordered on both sides by M_2 polyhedra, forming octahedral bands referred to as the octahedral layer (Figure IV-1).

In some pyroxenes, the M_2 sites are occupied by large cations such as Ca in diopside and Na in jadeite which are coordinated to 8 oxygens. In this case, the M_2 polyhedra, from two adjacent octahedral bands, share edges leaving a row of discontinuous vacant octahedral sites between the bands (Appleman, 1966).

However, when small cations such as Mg in enstatite and Fe in ferrosilite occupy the M_2 site, they are coordinated to six oxygen atoms in distorted octahedral sites. The M_2 polyhedra from two adjacent bands then do not share edges, and a continuous rift of vacant sites separates the two octahedral bands. In both cases, the octahedral bands are connected by the tetrahedral chains above and below them (Appleman, 1966).

The above crystallographic features are constant in most pyroxene minerals; however, the major variations, as a consequence of variation in chemical composition, occur in the M_2 polyhedra and the relative arrangement of octahedral and tetrahedral layers.

The pyroxene, or pyroxenoid, minerals that were used in this study are: orthoferrosilite, bronzite, lunar Ti-angite, blue-omphacite, and rhodonite. The crystal chemistry of the above minerals will be studied with emphasis on the transition metal site symmetries and metal-oxygen bond distances.

IV-2.1 Orthoferrosilite

The crystal structure of synthetic, end member (Fs_{100}) orthoferrosilite was reported by Burnham (1966). The ferrous ions in this structure occupy both M_1 and M_2 sites, and each Fe ion is coordinated to six oxygen atoms. The M_1 site is nearly a regular octahedron, whereas the M_2 site is very distorted (Figure IV-2). The Fe-O bond distances are given in Table IV-1, and the crystal structure, projected on (010), is shown in Figure IV-3. In the M_1 octahedron, each oxygen atom is coordinated to one silicon atom which is referred to as non-bridging; however, in the M_2 site there are, in addition to four non-bridging oxygens, two oxygens each linked to two silicon atoms, which are referred to as bridging.

As a consequence of the inhomogeneity in the type of the oxygen atoms coordinated to Fe, the M_2 site is significantly more distorted than the M_1 site. This is manifested in Table IV-1, which shows that Fe-O bond distances in the M_1 site depart a maximum of 0.06A from the mean, whereas Fe-O distances in the M_2 site depart a maximum of 0.2A from the mean. Burnham (1966) related the short bond distances in the M_2 site, (Fe-02A and Fe-02B), to the excessive negative charge of (-1/3) on both oxygens

FIGURE IV-2

Pictorial views of the M1 and M2 sites in
orthoferrosilite.

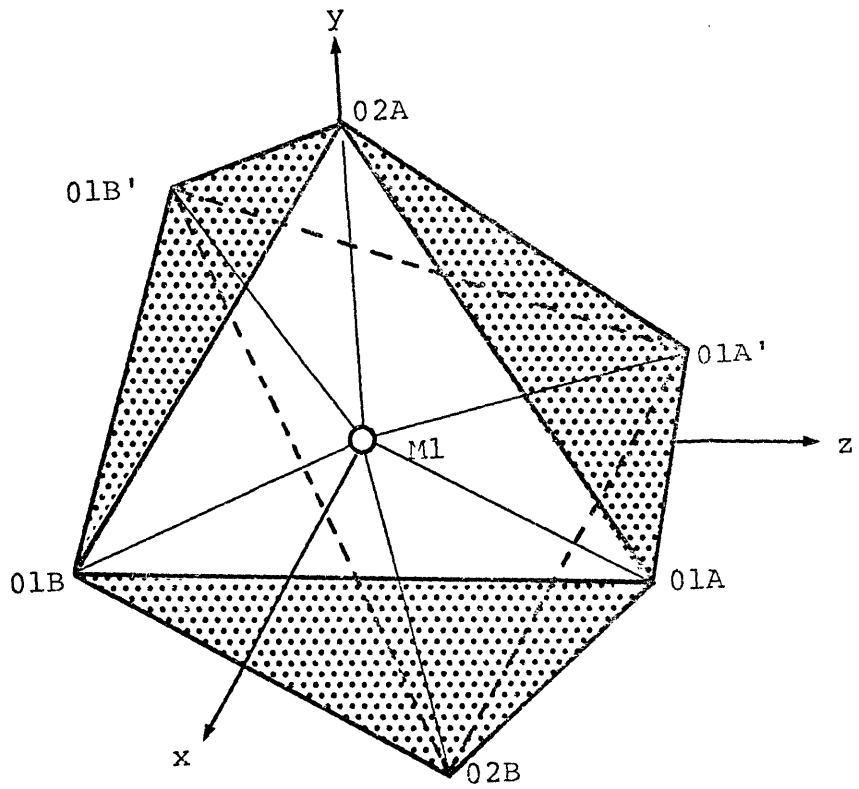
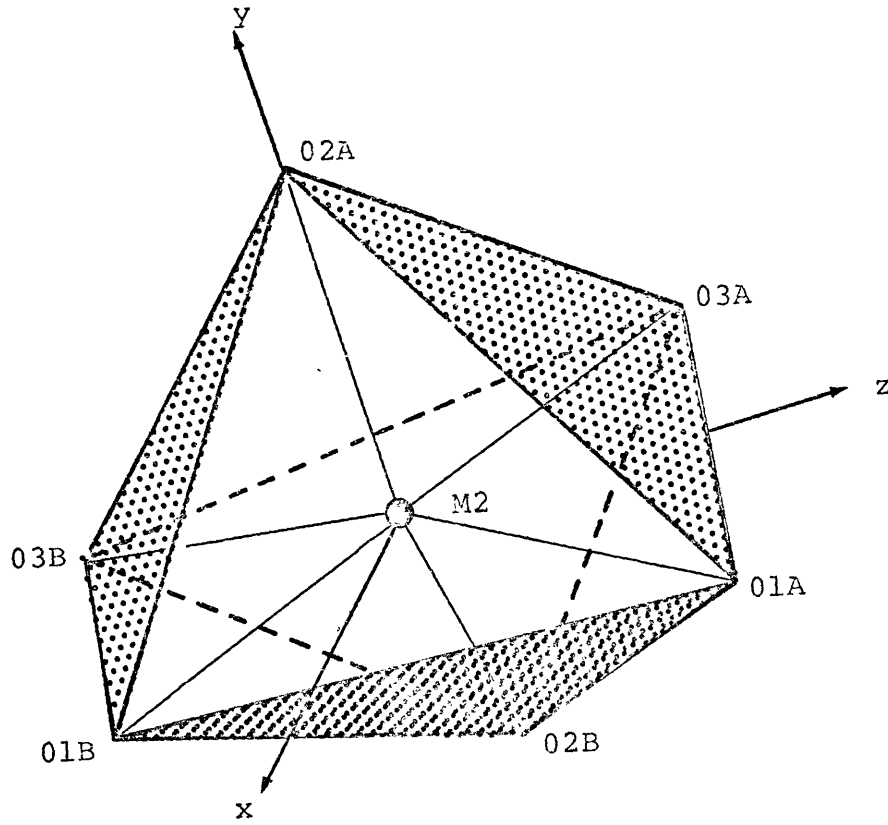


FIGURE IV-3

The crystal structure of orthoferrosilite projected on (010) showing the M1 and M2 polyhedral chains extending along the c-axis. Note the edge sharing between M1 and M2 sites. [From Burnham, C.W., 1966].

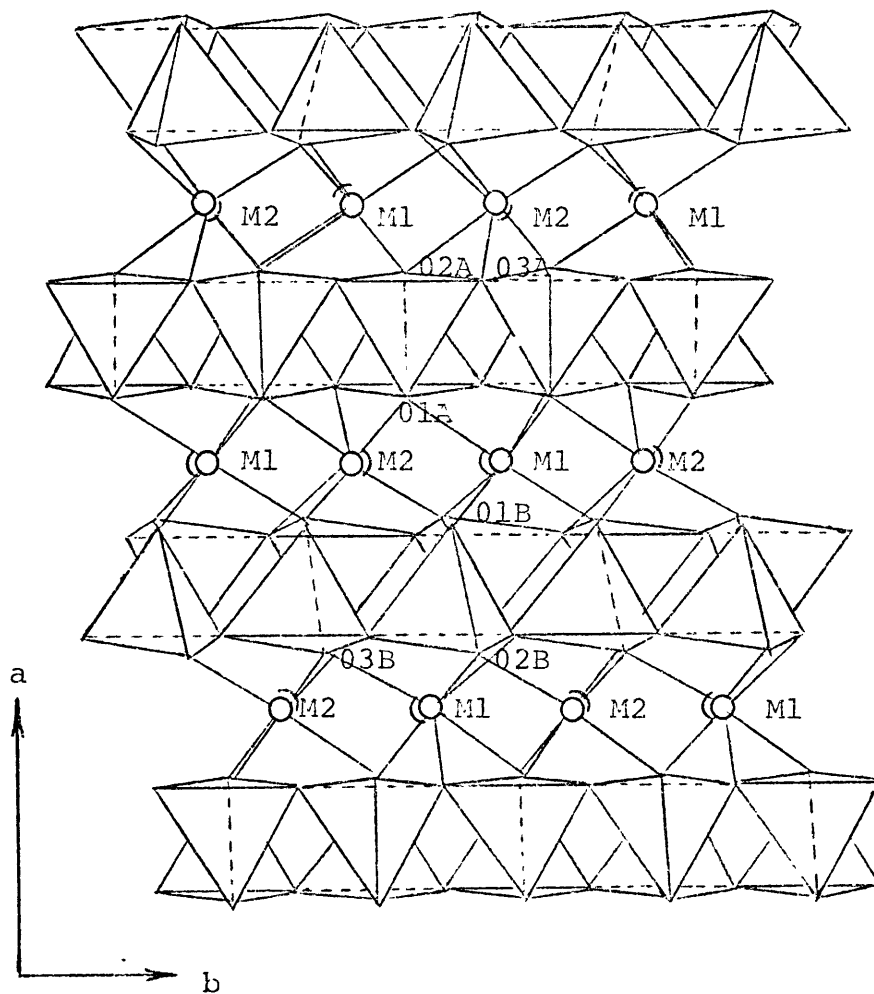


TABLE IV-1

M1 Site		M2 Site	
Atom Pair	Distance (Å)	Atom Pair	Distance (Å)
Fe-01A	2.006	Fe-01A	2.184
Fe-01A'	2.093	Fe-01B	2.127
Fe-01B	2.200	Fe-02A	2.042
Fe-01B'	2.119	Fe-02B	2.013
Fe-02A	2.101	Fe-03A	2.456
Fe-02B	2.152	Fe-03B	2.617
	—————		—————
Mean Fe-0	2.145	Mean Fe-0	2.240

Table IV-1: M1-O and M2-O interatomic distances in orthoferrosilite (Burnham, C.W., 1966).

(02A and 02B); however, Ghose (1965) related the short Fe-O distances to partial covalent character in these bonds.

Burnham also related the long bond distances (Fe-03A and Fe-03B) to surplus positive charge on the two oxygens (03A and 03B). Another significant feature in the structure is the edge sharing of M_2 polyhedron with an SiO_4 tetrahedron; the shared edge is approximately 0.05\AA shorter than unshared edges. The M_1 site shares five of its edges with other M_1 and M_2 sites, and the M_2 polyhedron shares one edge with an SiO_4 tetrahedron and other two edges with two M_1 polyhedra.

The polarized spectra of orthoferrosilite ($Fe_{86}En_{14}$) were reported by Burns (1970). In the present study, the spectra of orthoferrosilite of the same composition were measured at various pressures. At 1 atm., the spectra for the y and z orientations show four main bands in the i.r. region around 5000, 8298, 10526, and 10780 cm^{-1} (Figures IV-4,5). White and Keester (1966) and Runciman et al. (1973) also reported another band at 3100 cm^{-1} . The bands at energies 3100, 5000, and 10780 cm^{-1} were assigned to spin-allowed transitions* in Fe^{2+} contained in M_2 sites, and

* In a regular octahedral site, Fe^{2+} has one spin allowed transition from the ground state $^5T_{2g}$ to the excited state 5E_g ; the energy of this transition is equivalent to $10Dq$ or Δ_0 . However, in a distorted octahedron, the $^5T_{2g}$ and 5E_g levels are split into two or possibly three levels depending on the degree of distortion.

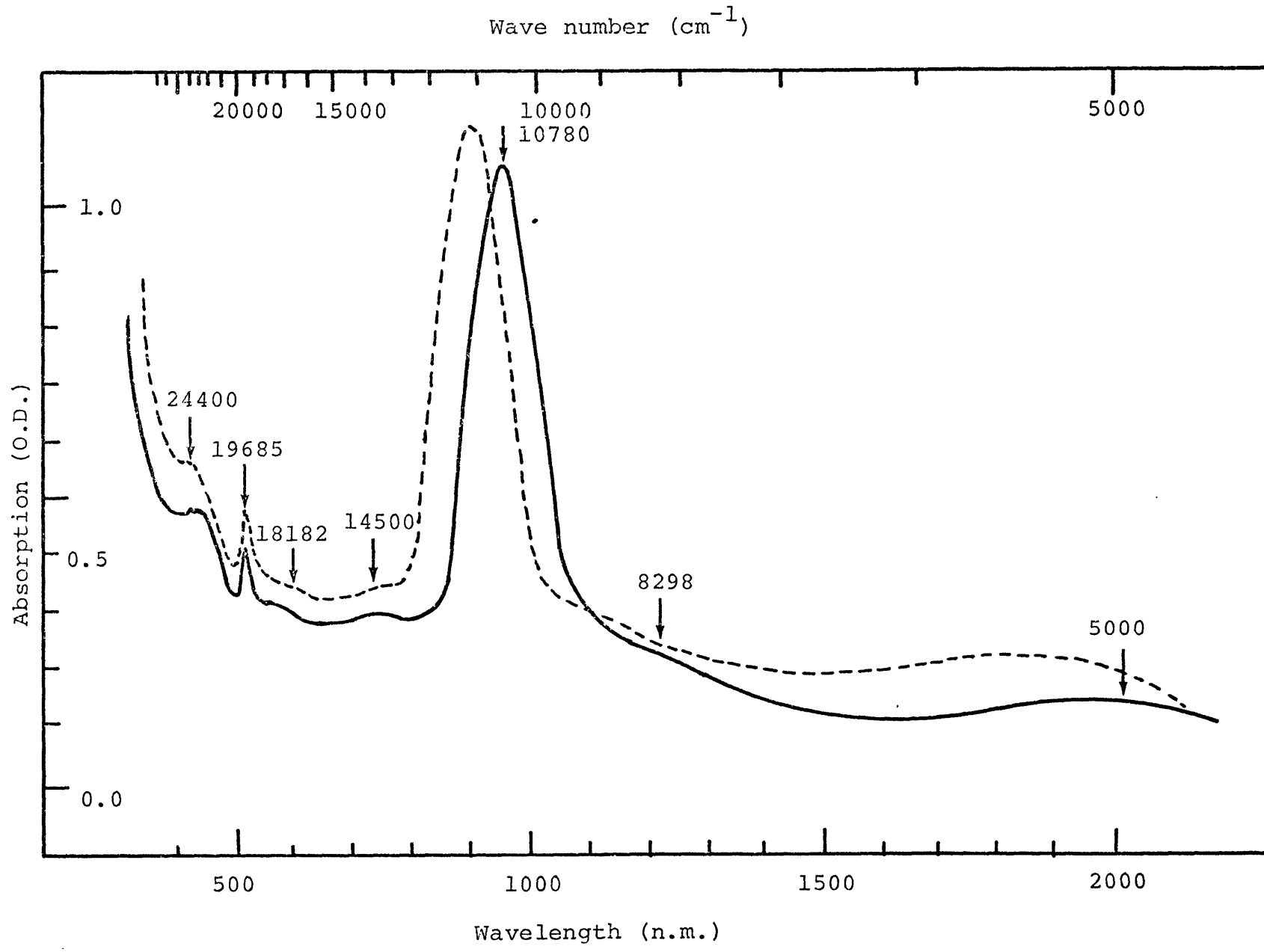
The M_2 polyhedron in orthopyroxenes is distorted from O_h symmetry to approximately C_{2v} ; as a consequence of this, the T_{2g} state is split into three states B_1 , B_2 , and A_2 , and the E_g state splits into A_1 and A_1 states (Runciman et al., 1973).

The ground state is considered to be B_1 and observed spectral bands, assigned to the M_2 site, are related to the following transitions:

FIGURE IV-4

The α^* -spectra of orthoferrosilite at 1 atm. (—) and 20 kb. (-----). Note the shift of C.F. bands in the i.r. region to higher energies at 20 kb.. Whereas the bands in the visible region did not show significant energy shift.

* $\alpha \equiv \gamma$



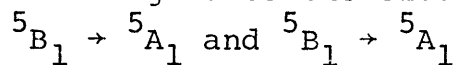
the bands at 8298 and 10526 cm^{-1} to Fe^{2+} in M_1 site (Burns, 1970). Further, there are other weak, but conspicuous, bands in the visible region at 14500, 18182, and 19685 cm^{-1} : the first band is related to electron transfer between Fe^{2+} and Fe^{3+} , and the latter two are due to spin-forbidden transitions in Fe^{2+} .

By considering the site symmetries of the M_1 and M_2 sites shown in Figure IV-2, the metal-oxygen distances given in Table IV-1 the observed transitions in the spectra of orth-ferrosilite shown in Figures IV-4,5, the crystal field energy level diagrams, at 1 atm., for both the M_1 and M_2 sites were constructed (Figure IV-6).

The point group symmetry of the M_2 polyhedron is considered to be close to C_{2v} . The energy separation between the t_{2g} levels in the M_2 site, Δ_1 and Δ_2 , are those reported by Burns (1970a) and ** Shenoy et al. (1969). The energy separation between the t_{2g} levels in the M_1 site are those values reported by Shenoy et al. (1969) and Huggins (1974).

<u>Band Energy (cm^{-1})</u>	<u>Electronic Transition</u>
3100	${}^5B_1 \rightarrow {}^5A_1$
5000	${}^5B_1 \rightarrow {}^5A_1$
10780	${}^5B_1 \rightarrow {}^5A_2$

The M_1 site is also a distorted octahedron, but is more regular than the M_2 site. The two bands at energies 8298 cm^{-1} and 10526 cm^{-1} are assigned to the electronic transition:

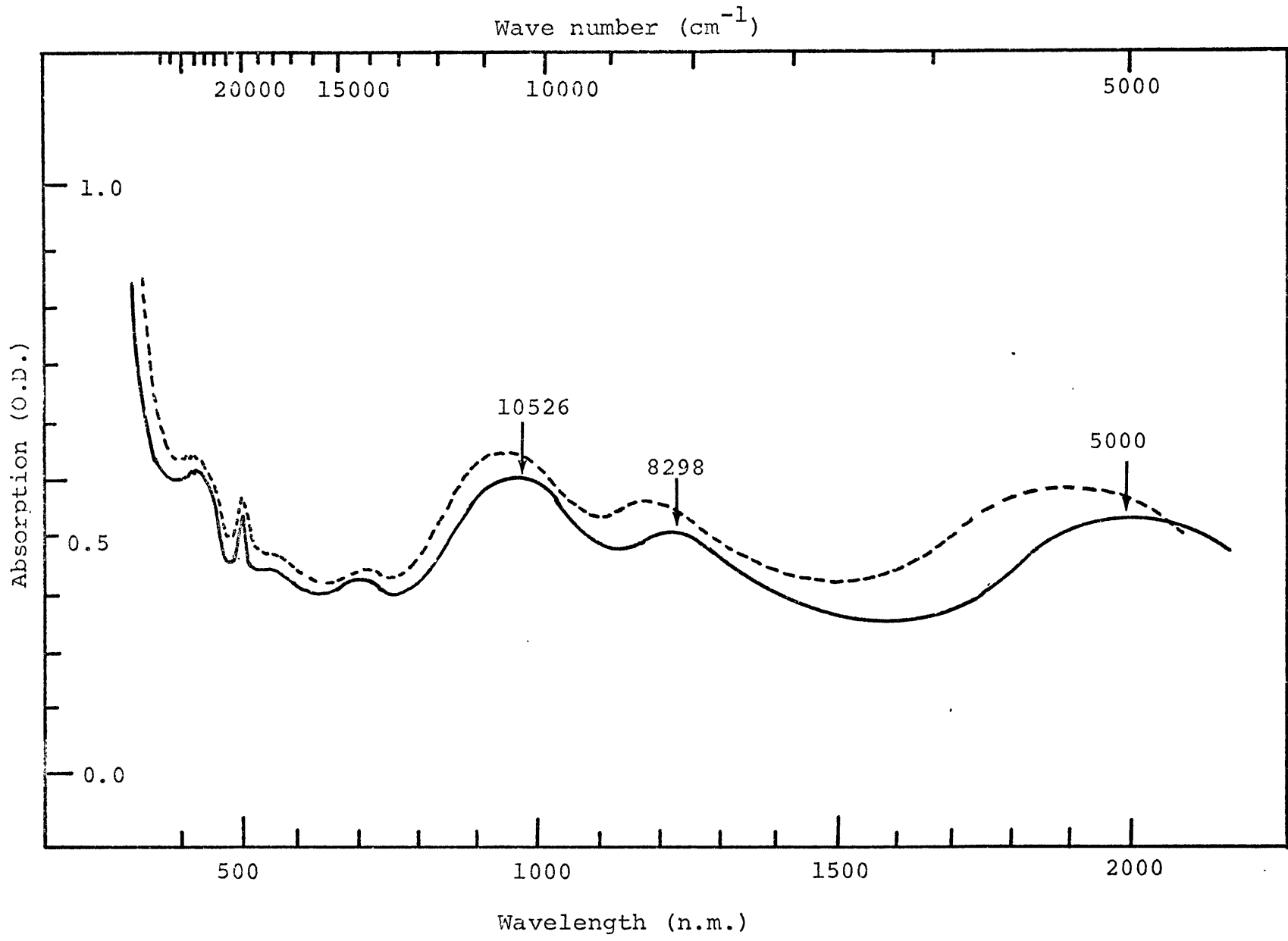


** Shenoy et al. (1969) considered Δ_1 and Δ_2 to have values of at least 1200 cm^{-1} .

FIGURE IV-5

The γ -spectra* of orthoferrosilite at 1 atm. (———)
and 20 kb. (-----).

* $\gamma = z$



Measurements of the polarized spectra of orthoferrosilite ($\text{Fs}_{86}\text{En}_{14}$) at elevated pressures were determined from a single crystal mounted in the diamond cell, orientated in such a way that the y and z axis were contained in a plane parallel to the anvil faces. With increasing pressure, all spectral bands in the i.r. region shift to higher energies (Figures IV-4,5). The rate of energy shift (cm^{-1}/kb) with pressure appears to decrease in the order I>II>III>IV, where the Roman numerals refer to the bands at energies 5000, 8298, 10526, and 10780 cm^{-1} , respectively.

The spectra of orthoferrosilite measured at 19.3 kb enable the energy level diagrams shown in Figure IV-6 to be constructed for Fe^{2+} ions in the M_1 and M_2 sites. Such diagrams are useful for interpreting the symmetries of the M_1 and M_2 polyhedra at high pressures and estimating the energy values of crystal field splitting and crystal field stabilization parameters for each site.

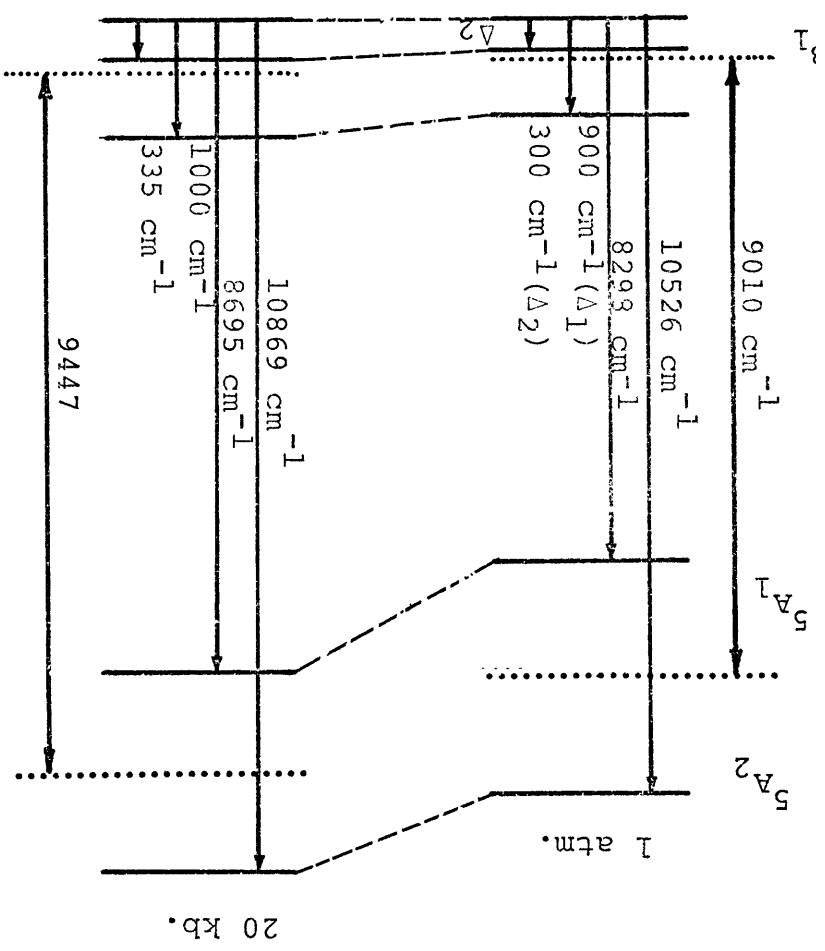
Comparing the energy level diagrams constructed at 1 atm., and 20 kb, it is evident that the d_{z^2} energy level rises in energy much faster than $d_{x^2-y^2}$ as pressure increases. As a consequence of the different rates of energy shift for these two levels, the energy separation between them becomes smaller as pressure increases.

The t_{2g} levels (d_{xy} , d_{xz} , d_{yz}) also became closer to each other due to the rapid rise in energy of the d_{xz} and d_{yz} relative to the d_{xy} orbital.

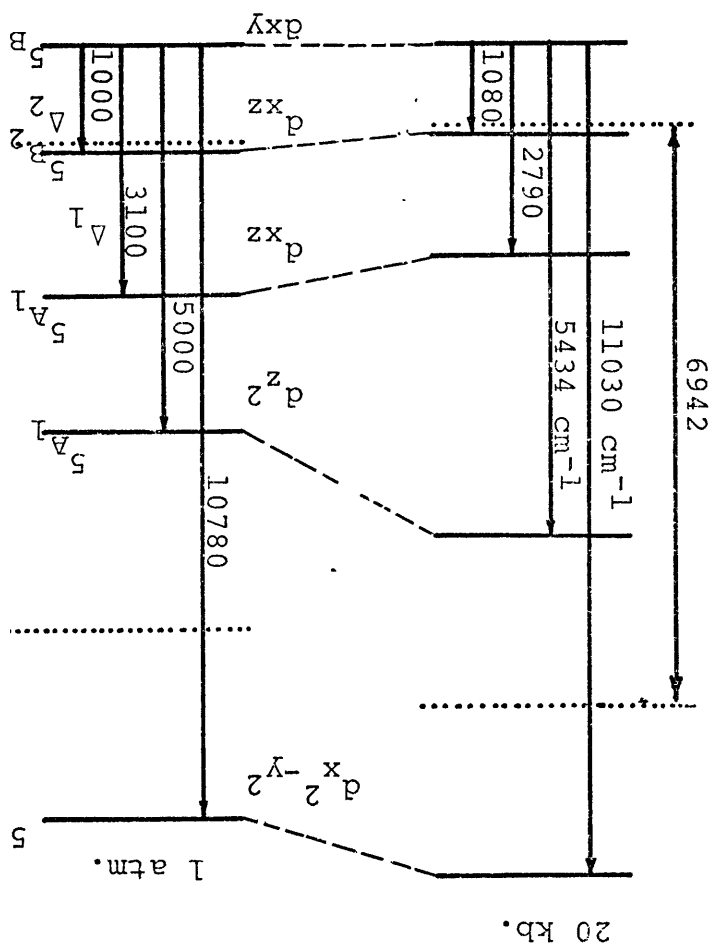
FIGURE IV-6

Energy level diagrams for M1 and M2 sites in
orthoferrosilite constructed at 1 atm. and
20 kb.

M1 Site



M2 Site



To explain the differences in the rates in energy shifts of spectral bands with pressure, three factors should be considered. First, the geometry of the polyhedron which contains the central ion, Fe; second, the metal-oxygen bond distances; and third, the relation given in equation II-7. Considering these factors, it is apparent that the short Fe-O bond distances (Fe-02B and Fe-02A) are directed along the y axes, whereas the long distances (Fe-03A and Fe-03B) are oriented in a direction close to the z axes. At elevated hydrostatic pressures, the longer bonds will be shortened easier than the shorter ones, since the former bonds are weaker than the latter due to their possessing smaller electron density between the oxygen anions and the Fe-cation. As a result of decreasing the Fe-03A and Fe-03B bonds significantly with increasing pressure, the intra-atomic electrostatic repulsion forces increase, causing the d_{z^2} energy level to rise in energy. In fact, all the d levels should increase in energy because of the expected shortening in M-O bond distances. However, electrons localized near the z axis will be repelled more at high pressure due to preferential compression. The net result of pressure on the d-energy levels in the M_2 site, then, will be to decrease the energy separation between the e_g levels (d_{z^2} and $d_{x^2-y^2}$) and to reduce the splitting energy between t_{2g} levels (d_{xy} , d_{xz} , d_{yz}). That is, the M_2 site will become less distorted at elevated pressures.

The influence of higher temperature on metal-oxygen bonds is expected to be similar to that of high pressure. However,

bond expansions rather than shortenings are expected to occur at elevated temperatures.

Smyth (1973) reported the crystal structure of orthopyroxene at temperatures ranging from 25°C to 850°C. Smyth observed that the long Fe-O bonds in the M_2 site expand significantly more than the short bonds. Further, Huggins (1974), from high pressure Mössbauer studies of orthoferrosilite, reported that the M_2 site becomes less distorted with increasing pressure. The results of both Smyth and Huggins are consistent with the predictions discussed earlier, and the results obtained in this study.

It should be mentioned that Mao and Bell (1971) measured the high pressure polarized spectra of synthetic orthoferrosilite (Fe_{100}) at pressures up to 25 kb. They also showed the relative energy shift of crystal field bands with pressure. The results reported by Mao and Bell are in agreement with those obtained in this study. Mao and Bell (1971) constructed energy level diagrams without giving explanation for the differences in the rate of energy shift of spectral bands. In addition, the values of Δ_1 and Δ_2 (the energy separation between t_{2g} levels) shown on their diagrams are inaccurate. This is because Δ_1 was estimated roughly from the energy of a spectral band at 3100 cm^{-1} , which was observed by White and Keester (1966), and Δ_2 was assumed to have energy value of 1000 cm^{-1} without indicating to any reference or giving any reason for this assumption.

The crystal field energy level diagrams shown in Figure IV-6 were constructed from the energies of spectral bands assigned to the M_1 and M_2 sites. The energies of these bands are consis-

tent with those reported by Burns (1970) and by Mao and Bell (1971). However, there is disagreement in the values of the energy separation between the lower d-levels t_{2g}

Burns (1970) and Mao and Bell (1971) estimated Δ_1 and Δ_2 values for the M_2 site about 3100 and 1000 cm^{-1} , and for the M_1 site 100 and 50 cm^{-1} , respectively. These authors assigned these energy values for Δ_1 and Δ_2 on the basis explained above. The values for Δ_1 and Δ_2 , given in this study, are preferable because they were obtained from considering both the high temperature Mössbauer data (Shenoy et al., 1969; Huggins and Abu-Eid, 1974; and Huggins, 1974) and the far infrared studies (White and Keester, 1966; and Runciman et al., 1973) of orthopyroxenes.

The estimated crystal field splitting parameters at 1 atm. for the M_1 and M_2 sites are 9010 and 6460 cm^{-1} , respectively, and the crystal field stabilization energies are 4005 and 4016 cm^{-1} . The energy values of these parameters at 1 atm. indicate that the ferrous ions in the M_1 sites have slightly smaller site preference energies than those in the M_2 sites. However, the difference in CFSE parameter for both sites could be within the error of the experimental measurements; for this reason it may be safe to assume that Fe^{2+} is disordered in orthoferrosilite.

The polarized spectra of orthoferrosilite were measured at various pressures. All bands in the i.r. region shifted to higher energies as pressure increased. Energy level diagrams for the M_1 and M_2 sites were constructed from the energy values of spectral bands measured at about 20 kb. They are shown in Figure IV-6.

Looking at the energy level diagrams constructed at 1 atm. and 20 kb for both the M_1 and M_2 sites, the energy values of the crystal field splitting (CFS) and crystal field stabilization energy (CFSE) parameters can be obtained for both the M_1 and M_2 sites at 1 atm. and at 20 kb. by looking at the energy level diagrams constructed from measurements at these pressures. These values are compared in Table IV-2.

From Table IV-2, the following conclusions can be drawn:

- 1) CFS parameters increase with pressure for both sites, indicating that the volumes of the M_1 and M_2 polyhedra decrease as pressure increases;
- 2) The polyhedral volume decrease with pressure is greater for the M_2 site than for the M_1 site, suggesting that the M_2 site is more compressible. This obtains because Δ_{Δ} ($CFS_{20kb} - CFS_{1 atm}$) for the M_2 site is greater than Δ_{Δ} for the M_1 site;
- 3) The CFSE for the M_2 site, at 1 atm, is slightly larger than that for the M_1 site; however, at high pressures, this parameter becomes greater for the M_1 site. This suggests that Fe^{2+} ions may be more stabilized in the M_1 site than the M_2 site at elevated pressures.

The spectral band in the visible region at about 14500 cm^{-1} shifts slightly to lower energy as pressure increases, suggesting that its assignment as a charge transfer band (Burns, 1970a) could be correct. (The influence of pressure on charge transfer bands will be discussed in detail in the next chapter.) On the other hand, the sharp peaks at 18182 and 19685 cm^{-1} do not show any detectable energy shift with pressure up to 50 kb. The neg-

TABLE IV-2

	CFS		CFSE		
	M1	M2	M1	M2	
1 atm.	9012	6457	4005	4016	cm ⁻¹
	25.77	18.46	11.45	11.48	K.Cal.
20 Kb.	9447	6942	4224	4067	cm ⁻¹
	27.01	19.85	12.08	11.63	K.Cal.
Δ_{Δ}	+ 435	+ 485	+ 219	+ 51	cm ⁻¹
	1.24	1.39	0.626	0.146	K.Cal.

Table IV-2: The energy values of CFS and CFSE parameters for the M1 and M2 sites in orthoferrosilite at 1 atm. and 20 kb.

ligible energy shifts of these bands is another piece of evidence confirming their assignments to spin-forbidden transitions in Fe^{2+} , since such transitions are dependent mostly on Racah parameters B and C which show insignificant changes in their energy values with increasing pressure up to 200 kb (Abu-Eid, 1974).

IV-2.2 Bronzite

The high pressure spectra of another orthopyroxene, bronzite, (composition: $\text{Fs}_{14.5}\text{En}_{85.5}$) from Bamle, Norway were measured at two pressures, 1 atm. and 20 kb. The α -spectrum only was measured at both pressures because of the broadness and low intensities of the bands in the β and γ spectra. The spectra at 1 atm. and 20 kb are shown in Figure IV-7. The two main bands at 5666 and 10953 cm^{-1} in the 1 atm. spectrum were assigned to spin-allowed transitions in Fe^{2+} ions in the M_2 site. At pressures around 20 kb, the first band shifts to 5821 cm^{-1} and the second to 11806 cm^{-1} . The energy values of these crystal field bands at 1 atm. and 20 kb enable the energy level diagrams for Fe^{2+} in the M_2 site to be constructed at both pressures (Figure IV-8).

The values of CFS and CFSE for the M_2 site at 1 atm. and 20 kb were calculated to be:

<u>Pressure</u>	<u>CFS</u>	<u>CFSE</u>
1 atm.	6943	4149 cm^{-1}
20 kb.	7223	4119 cm^{-1}

From the above figures, it is evident that Δ_0 is increased significantly, indicating compression of the M_2 site; however,

FIGURE IV-7

The α -spectrum of bronzite, $\text{Fs}_{14.5}$, measured at
1 atm. (————) and 20 kb. (-----).

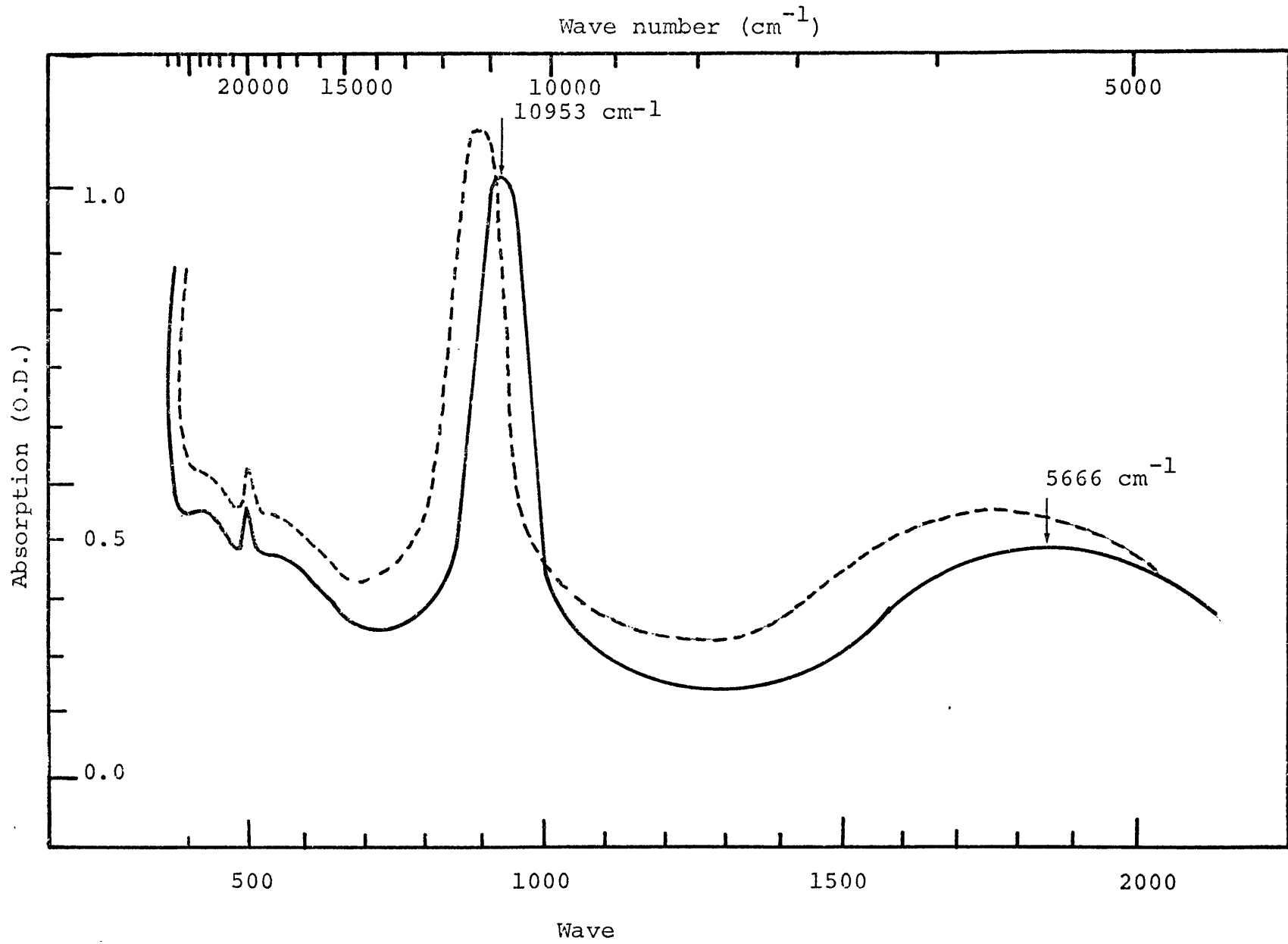
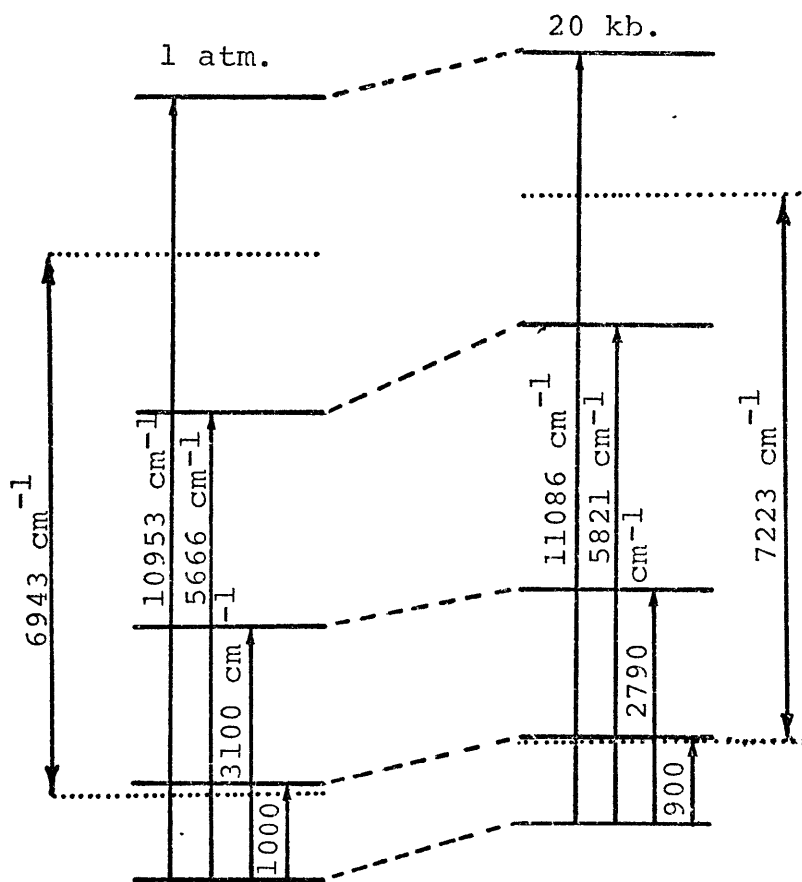


FIGURE IV-8

Energy level diagram of the M2 site in bronzite
constructed at 1 atm. and 20 kb.



M2 Site

the CFSE parameter decreases slightly with pressure, suggesting that Fe^{2+} could possibly be less stable in the M_2 site at high pressures. These results are similar to those obtained for orthoferrosilite ($\text{Fs}_{86}\text{En}_{14}$).

The above results obtained from orthopyroxene minerals are useful for interpreting the distribution of Fe^{2+} between pyroxene mineral phases and predicting possible changes in their structures. The compressibilities of the M_1 and M_2 sites could also be estimated since Δ is proportional to $(-5/3)$ rd power of the volume. These applications will be discussed later in Chapter VII.

IV-2.3 Lunar Ti-augite

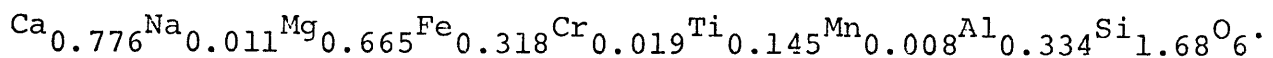
Pyroxenes commonly occur as essential minerals in many of the lunar rocks and soils. Understanding the crystal chemistry of lunar pyroxenes will provide information on the nature and history of magmatic crystallization and mineral fractionations on the moon.

Studies of pyroxene mineral phases, returned from different Apollo missions, revealed their high content of trivalent titanium and divalent iron (Burns et al., 1972b,c,d, 1973; Sung et al., 1974; Mao and Bell, 1973a,b). Since natural minerals on earth containing Ti^{3+} are scarce, lunar Ti-augite is a useful mineral for investigating the influence of pressure on Ti^{3+} crystal field bands. Although the titanium and iron oxidation states have been tentatively identified as Ti^{3+} and Fe^{2+} (Burns et al., 1972b,c,d, 1973; Sung et al., 1974), there are many

controversies and discussions in the literature on the assignments of these spectral bands. The central controversy in the band assignments is whether they arise from crystal field transitions in the cations or from intervalence charge transfer transitions between Fe^{2+} and Ti^{4+} or between Ti^{4+} and Ti^{3+} .

In the present study, the results of high pressure spectral measurements are invoked to resolve the controversies on spectral band assignments. This high pressure technique has been used successfully before by Abu-Eid (1974) and Mao and Bell (1972a,b) to distinguish crystalfield bands from charge transfer bands.

The lunar pyroxene investigated in this project is an augite separated from the Apollo 17 mare basalt sample no. 74275. The major element composition was determined by electron microprobe (Sung et al., 1974) and is summarized in Table IV-3; the chemical formula for this pyroxene (based on 6 oxygens) is:



The crystallography and crystal chemistry of lunar augites and pigeonites from the Apollo 12 and 15 missions were discussed by Burns et al. (1972b), Takeda (1972), Dowty et al. (1972), Hafner et al. (1971), Prewitt et al. (1971), Takeda and Ridely (1972), and Brown and Wechsler (1973). The above authors are in agreement on the site occupancies of iron and titanium. The ferrous ions are disordered between the M_1 and M_2 sites, such that about 45% occupies the M_1 position and 55% the M_2 position. The trend of this site occupancy between M_1 and M_2 varies with

TABLE IV-3

74275,85

<u>Oxides</u>	Av. (14)	Range		Max. Ti	Min. Ti
SiO ₂	45.07	46.76-	43.86	44.29	46.76
TiO ₂	5.25	6.05-	3.54	6.05	3.54
Al ₂ O ₃	6.51	7.09-	4.20	7.05	4.20
Cr ₂ O ₃	0.75	0.94-	0.49	0.64	0.53
MgO	12.51	15.14-	11.75	11.75	15.14
FeO	10.11	12.38-	9.11	10.03	12.38
MnO	0.21	0.25-	0.09	0.20	0.15
CaO	19.10	20.52-	15.32	19.05	15.32
Na ₂ O	0.13	0.20-	0.02	0.16	0.11
Total	99.64			99.22	98.13

Table IV-3: Electron microprobe analyses of Apollo 74275
pyroxene (Sung, C-M., Abu-Eid, R.M., and Burns, R.G., 1974).

the relative enrichment of Ca and Mg, and with the temperature of mineral crystallization from the magma. Ti^{3+} , on the other hand, occupies the M_1 position only.

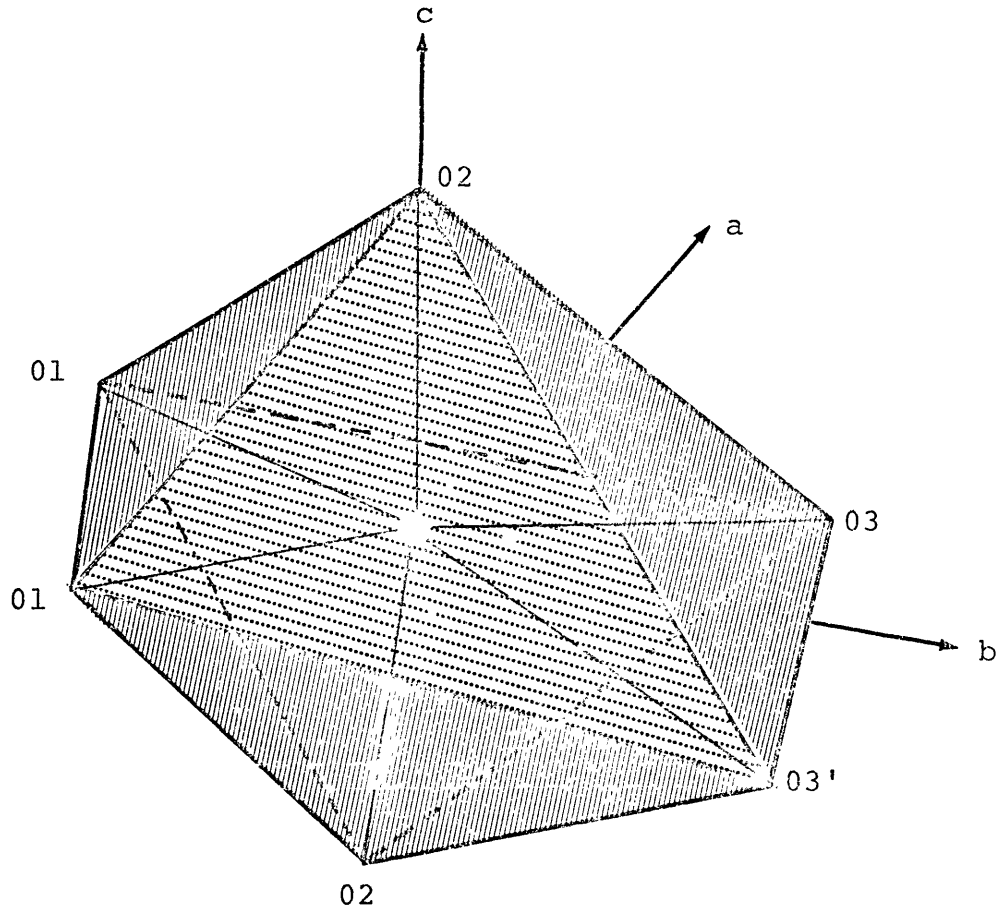
The M_2 polyhedron is a distorted octahedron, whereas M_1 is a fairly regular one. The geometry of both sites relative to the crystallographic axes a, b, and c are shown in Figure IV-9. and the M-O distances are given in Table IV-4. The M_2 polyhedron shares 3 edges with M_1 sites and one edge with an SiO_4 tetrahedron, whereas the M_1 site shares five of its edges with M_1 and M_2 polyhedra.

Figure IV-10 shows the polarized spectra of the 74275 lunar pyroxene for y and z orientations measured at 1 atm. The broad bands in the i.r. region at 4762, 9805, 10101, and 9091 cm^{-1} are due to spin allowed transitions in Fe^{2+} . The first two bands arise from Fe^{2+} contained in the M_2 site, and the latter two bands are related to Fe^{2+} transitions in the M_1 site. In the visible spectral region, there are four bands at energies 19802, 18182, 20920, and 15260 cm^{-1} .

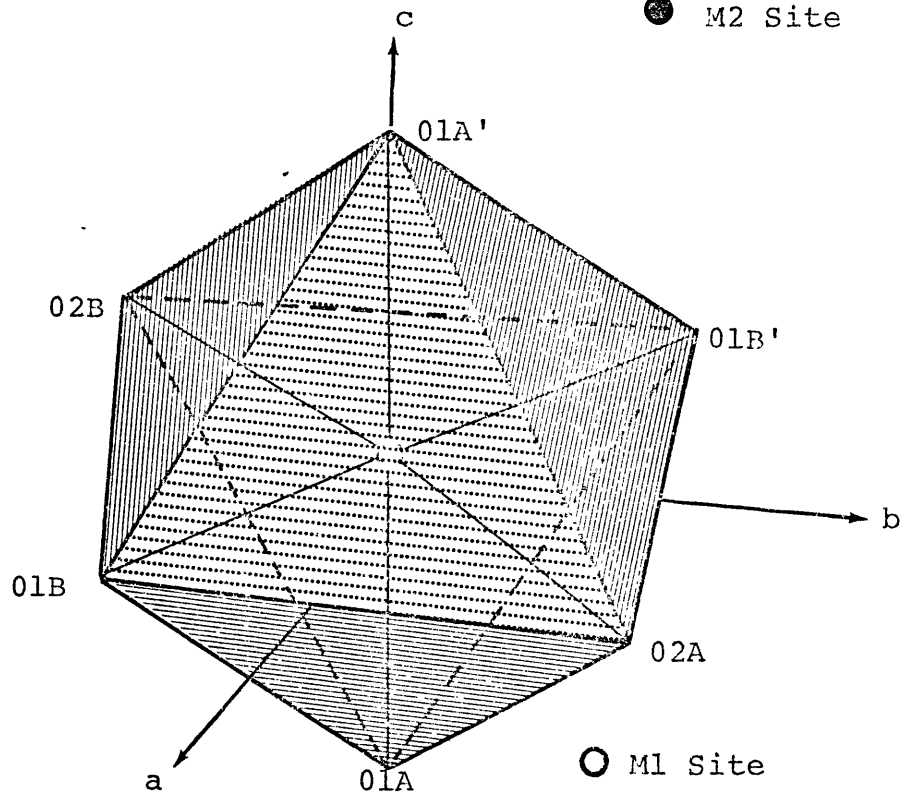
The sharp peak at 19802 cm^{-1} and the broad shoulder at 18182 cm^{-1} are related to spin-forbidden transitions in Fe^{2+} ; however, there is a debate on the assignments of the bands at 20920 and 15260 cm^{-1} . Burns et al. (1972b,c,d, 1973) assigned the two bands to crystal field transitions in Ti^{3+} , whereas Dowty and Clark (1973) and Bell and Mao (1973a,b) assigned them to charge transfer transitions arising from electron transfer between either Fe^{2+} and Ti^{4+} or Fe^{2+} and Fe^{3+} .

FIGURE IV-9

Pictorial views of the M1 and M2 polyhedra in lunar pyroxene. Note the geometrical arrangements of the oxygen atoms relative to a, b, and c-axes.



● M2 Site



○ M1 Site

TABLE IV-4

M1 Site		M2 Site	
M1-01A	2.048 Å	M2-01A	2.166 Å
M1-01A'	2.139	M2-01B	2.133
M1-01B	2.050	M2-02A	2.101
M1-01B'	2.180	M2-02B	2.044
M1-02A	2.024	M2-03A	2.389
M1-02B	2.055	M2-03B	2.627
Mean	2.083	M2-03B'	2.946
		M2-03A'	3.434
		Mean(6)	2.243
		Mean(8)	2.480

Table IV-4: M1-O and M2-O interatomic distances in lunar pyroxene (Takeda, 1972 and Takeda and Ridely, 1972).

Since the spin-allowed transitions of Ti^{3+} (${}^2\text{T}_{2g} \rightarrow {}^2\text{E}_g$) and Fe^{2+} (${}^5\text{T}_{2g} \rightarrow {}^5\text{E}_g$) are only dependent on $10Dq$, their energies should be sensitive to any variation of the metal-ligand bond distances. With increasing pressure (and hence shortening the interatomic bond distances) these bands are expected to shift to higher energies, if they are indeed crystal field transitions. On the other hand, charge transfer bands are expected to show a red shift with pressure.

The energy level diagrams for Fe^{2+} ions in the M_1 and the M_2 sites in lunar augite, which are deduced from the positions of absorption bands in Figure IV-10, are shown in Figure IV-11. The splitting energies of the t_{2g} orbitals in the M_2 site (Δ_1 and Δ_2) are assumed to be 3100 and 2000 cm^{-1} ; these energy values were obtained from Mössbauer parameters at various temperatures using Ingalls model, as will be explained later. The splittings of the t_{2g} orbitals in the M_1 site are very small, and the energy value is estimated to be about 100 cm^{-1} . From the two energy level diagrams (Figure IV-11) the calculated crystal field splittings for the M_1 and M_2 sites are: 9496 and 5583 cm^{-1} , and the crystal field stabilization energies are: 3898 and 3933, respectively. The energy values for these parameters and the energy level diagrams indicate that the M_2 site is a very distorted octahedron and the M_1 site is fairly regular.

The crystal field stabilization energy for the M_2 site is slightly larger than that for the M_1 site, suggesting that ferrous ions prefer the M_2 position. It is of interest to compare

FIGURE IV-10

The polarized absorption spectra of pyroxene
single crystals in rock 74275: γ
spectrum; ----- β spectrum; ————— α
spectrum. ($\alpha=b$; $\beta=a$; $\gamma=c$).

ABSORPTION (O.D)

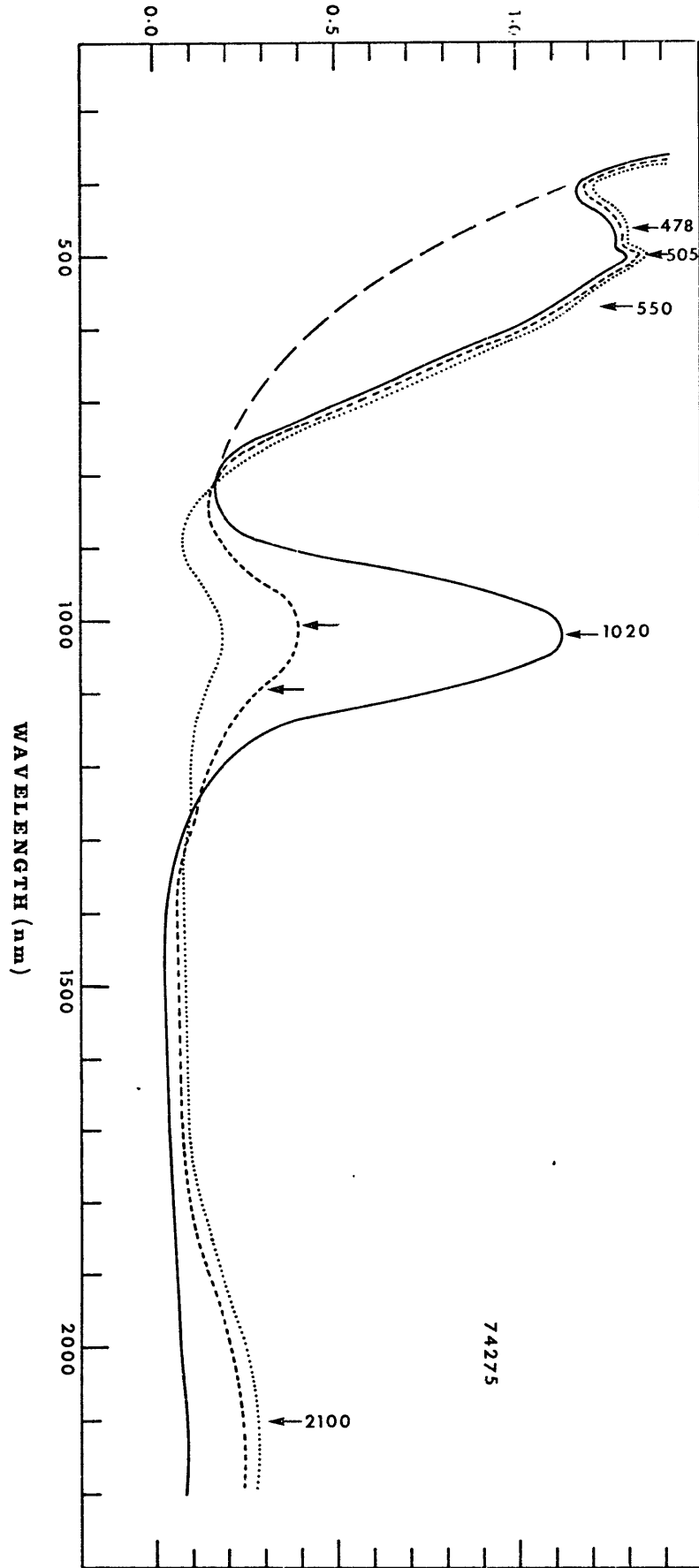
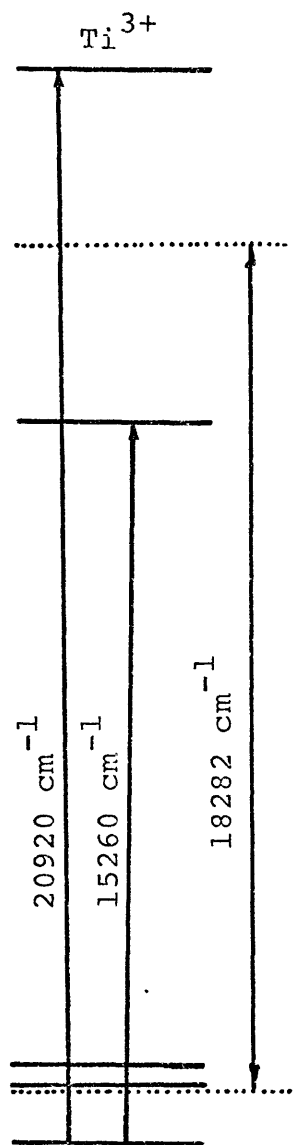
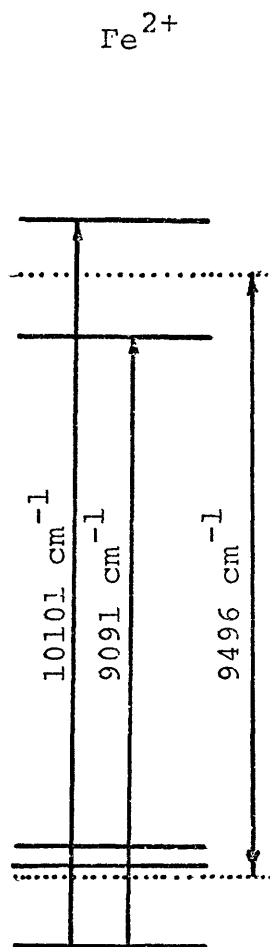


FIGURE IV-11

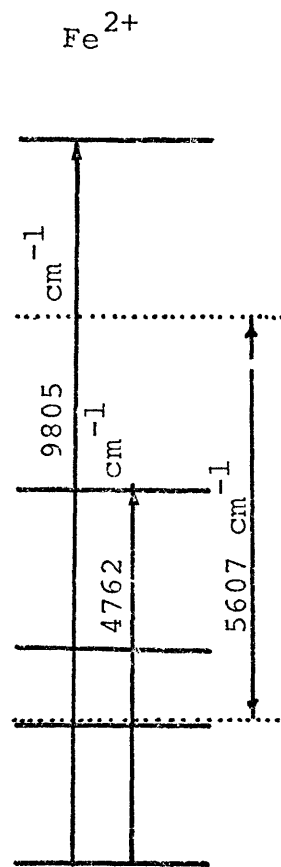
Energy level diagrams of Fe^{2+} cation in the M1 and M2 sites, and Ti^{3+} ion in the M1 site.



M1 Site



M1 Site



M2 Site

the energy level diagrams for both sites with their point group symmetries and crystallographic geometries. From such comparisons, it is evident that orbitals oriented towards the short M-O bonds are at higher energies than those oriented along the long M-O bonds, implying that the electrostatic point charge model applies fairly well to transition metal ions in silicate minerals.

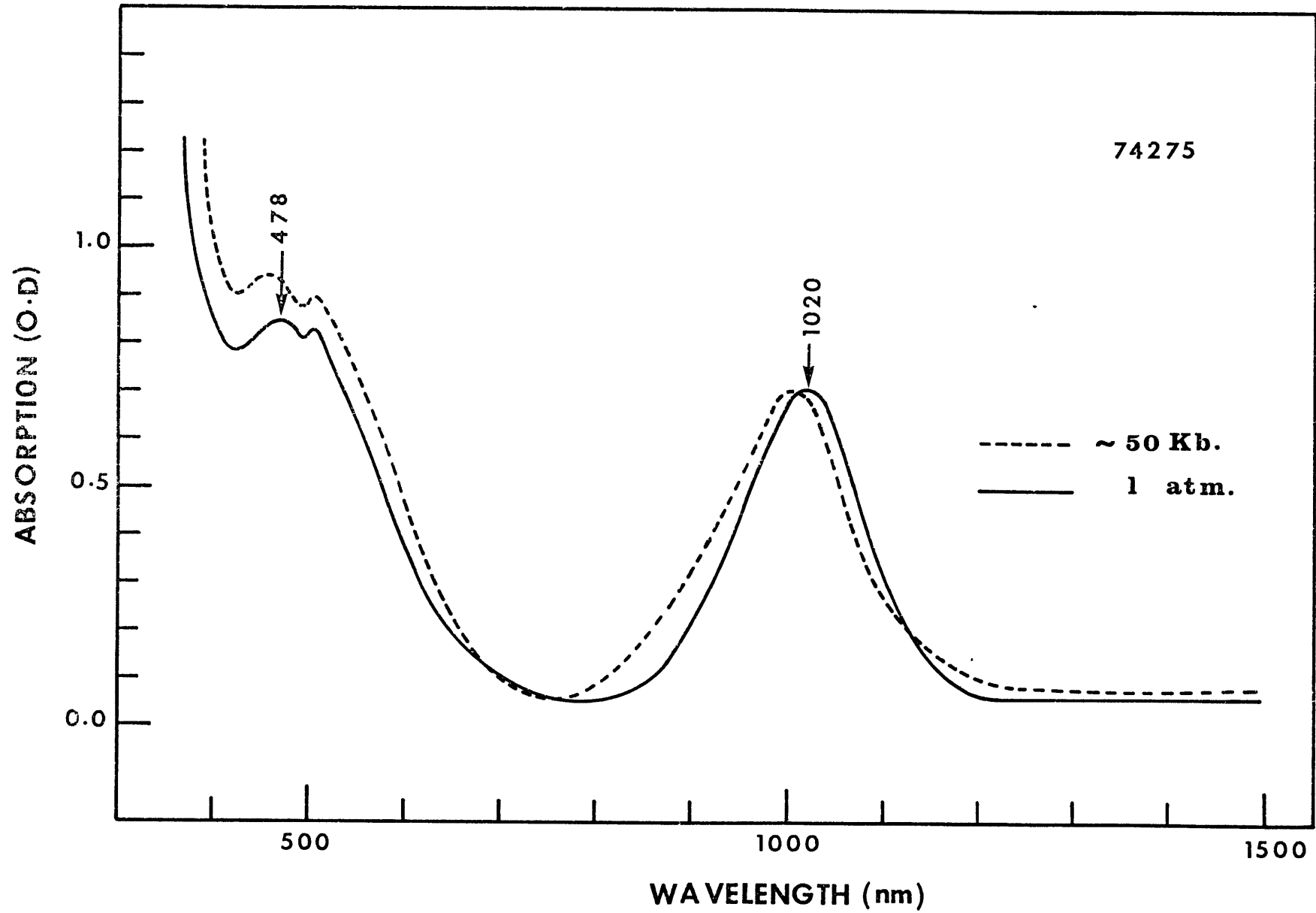
The energy level diagram for Ti^{3+} in the M_1 site was constructed (Figure IV-11) assuming that the assignment by Burns et al. (1972b,c,d) of spectral bands at 20920 and 15226 to Ti^{3+} crystal field transitions is correct. The crystal field splitting energy value for Ti^{3+} in this site, 18032 cm^{-1} , correlates fairly well with other values reported for the Ti^{3+} cation in other compounds (McClure, 1962; Schläfer and Gotz, 1961; Schläfer, 1962). The crystal field stabilization energy parameter, 7273 cm^{-1} , is fairly high relative to the value of the Fe^{2+} in the M_1 site; this indicates that Ti^{3+} has a stronger preference for the M_1 site.

The polarized spectra in the visible and near infrared regions were measured for the lunar pyroxene at pressures up to 50 kb. Figure IV-12 shows the spectra of a single crystal which was mounted in a pressure fluid, using the gasketing method described in Chapter III. The pyroxene crystal in the diamond cell was oriented such that the y and z axes were contained in a plane perpendicular to the pressure axis of the diamond cell.

The absorption bands in the z spectrum were not resolved due to their low intensities and large widths; also the bands at 4762

FIGURE IV-12

The α -spectra of 74275 pyroxene at 1 atm. and
at pressure around 50 kb.



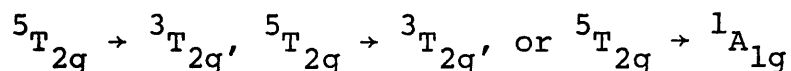
and 15260 cm^{-1} were not resolved in both orientations. Because of this difficulty, energy level diagrams were not constructed at elevated pressures. However, the resolution of spectral bands at 9805, 20920, 19802, and 18182 cm^{-1} was fairly good and the Y spectrum measured at about 50 kb. is shown in Figure IV-12. At high pressures, the absorption bands at 9805 and 20920 cm^{-1} shift to higher energies indicating that they are spin-allowed transitions in Fe^{2+} and Ti^{3+} . This trend of band energy shift is consistent with predictions made earlier in this study and with the previous assignments made by Burns et al. (1972b,c, 1973).

On the other hand, the weak bands at 19802 and 18182 show negligible energy shifts with pressure. This observation may support their assignments to spin-forbidden transitions* in Fe^{2+} . Since spin-forbidden bands depend mostly on Racah parameters, B and C, and to a lesser degree on Dq, and since these parameters, B, C, and Dq, have opposite energy shifts with pressure, such bands may not shift significantly with increasing pressure.

IV-2.4 Blue Omphacite

Omphacites were defined, by Clark and Papike (1968) as pyroxenes whose compositional field lies between the boundary planes $0.2 \leq \text{Na}/(\text{Na} + \text{Ca}) \leq 0.8$ in the system Jd-Ac-Di-He-Tsch**.

* These two transitions may be related to:



The energies of these transitions are given in Table II-1.

** Jd, Ac, Di, He, and Tsch refer to Jadeite ($\text{NaAlSi}_2\text{O}_6$), Acmite ($\text{NaFe}^{3+}\text{Si}_2\text{O}_6$), Diopside ($\text{CaMgSi}_2\text{O}_6$), Hedenbergite ($\text{CaFeSi}_2\text{O}_6$), and Tschermak ($\text{Ca,Al}(\text{SiAl})\text{O}_6$), respectively.

The structure which consists of octahedral and tetrahedral layers, was discussed in detail by Clark and Papike (1968a,b), Clark et al. (1969), and Appleman (1966). The cations in the octahedral layers are distributed among eight positions; four of those positions are occupied by small M_1 cations, e.g. Fe^{2+} , Mg^{2+} , Fe^{3+} , Al^{3+} , Ti^{3+} , and the other four positions are occupied by larger M_2 cations, e.g. Ca^{2+} , K^+ , Na^+ . For the purposes of this study, more emphasis will be placed upon the M_1 polyhedra, since they contain all the pertinent cations, viz. Ti^{3+} , Fe^{2+} , and Fe^{3+} . The M_1 polyhedra are referred to as $Ml(1)$, Ml , $Ml(1)H$, and MlH . The structure of omphacite projected on (100) is shown in Figure IV-13 . The $Ml(1)$ and Ml polyhedra share edges to form another type of octahedral chain (Figure IV-13). The two chain types are linked to each other and with M_2 polyhedra. The M-O distances and site occupancies for the four M_1 sites are summarized in Table IV-5.

From x-ray crystallographic studies and charge balance considerations, Clark and Papike (1968) assumed that Fe^{2+} and Mg^{2+} occupied two M_1 positions, [M_1 and $Ml(1)H$], and Al^{3+} and Fe^{3+} occupied the other two sites [$Ml(1)$ and MlH]. However, Bancroft et al. (1969) showed the Mössbauer spectrum of omphacite fitted to five doublets. One of the Mössbauer doublets was assigned to Fe^{3+} , and the remaining four were assigned to Fe^{2+} in four distinct M_1 positions.

The omphacite used in the current investigation was found by Curtis (1974) in a group of peralkaline intrusions located in central Labrador. The electron microprobe analysis (Curtis,

FIGURE IV-13

The crystal structure of omphacite projected along (100). Note the edge sharing between M1 and M(1) sites and between the M2 and the M1 sites. [Clark and Papike, 1968a,b].

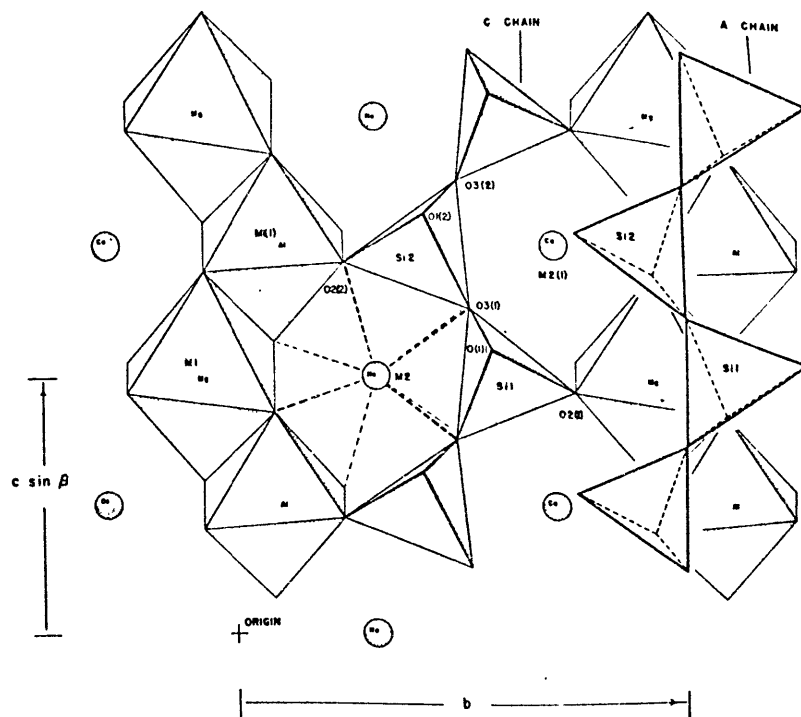


TABLE IV-5

- (a) Site occupancies of M1, M(1), M1H, and M1(1)H sites in omphacite. [Clark and Papike, 1968a, b and Clark et al., 1969].
- (b) M-O interatomic distances in the M1, M1(1)H, M1(1), and M1H sites [Clark and Papike, 1968a,b].

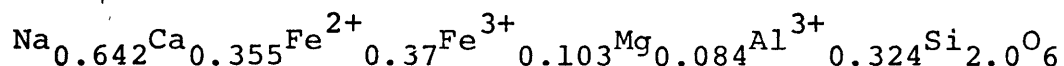
TABLE IV-5(a)

Site	Cation	Occupancy
M1	Mg ²⁺	0.81
	Fe ²⁺	0.19
M1(1)	Al ³⁺	0.95
	Fe ³⁺	0.05
M1H	Al ³⁺	0.82
	Fe ³⁺	0.18
M1(1)H	Mg ²⁺	0.8
	Fe ²⁺	0.2

TABLE IV-5(b)

Site	Oxygen Atom	Distance
M1	01(1)A	2.12 Å
	01(2)A	2.09
	02(1)C	2.01
M1(1)H	01(1)C	2.07
	01(2)C	2.16
	02(2)A	2.06
M1(1)	01(1)A	1.91
	01(2)A	2.03
	02(2)C	1.88
M1H	01(1)C	1.97
	01(2)C	1.99
	02(1)A	1.99

1974) is given in Table IV-6 , and the chemical formula is:



Mössbauer spectra of this omphacite (Burns, unpublished data) showed four doublets; one was assigned to Fe^{3+} , and the other three to Fe^{2+} in three different sites. Mössbauer parameters of the four doublets are:

	<u>Q.S.</u>	<u>I.S.</u>	<u>H.W.</u>	<u>%Area</u>
Fe^{2+}	3.09	1.22	0.37	34.1
	2.45	1.24	0.41	24.5
	2.09	1.21	0.36	19.5
Fe^{3+}	0.335	0.425	0.40	21.9

The absorption spectra of omphacite were measured in the near i.r. and visible regions (Figure IV-14). The two broad bands at energies around 8700 and 10750 cm^{-1} have been assigned to spin-allowed transitions in Fe^{2+} ions contained in the M_1 sites. The large widths of both bands could be attributed to the distribution of ferrous ions among three or four M_1 sites. The above result, from absorption spectra, conform with Mössbauer results obtained by Bancroft et al. (1969) and by Burns (personal communication).

The sharp band at 22727 cm^{-1} is assigned to Fe^{3+} spin-forbidden transition, ${}^6A_{1g} \rightarrow {}^4A_{2g}, {}^4E_g$ (similar to that observed in andradite garnet).

The broad intense band at 15037 cm^{-1} is related to electronic transfer between ferrous and ferric ions, i.e. $\text{Fe}^{2+} \rightarrow \text{Fe}^{3+}$ charge transfer.

To examine the validity of the above assignments, high pres-

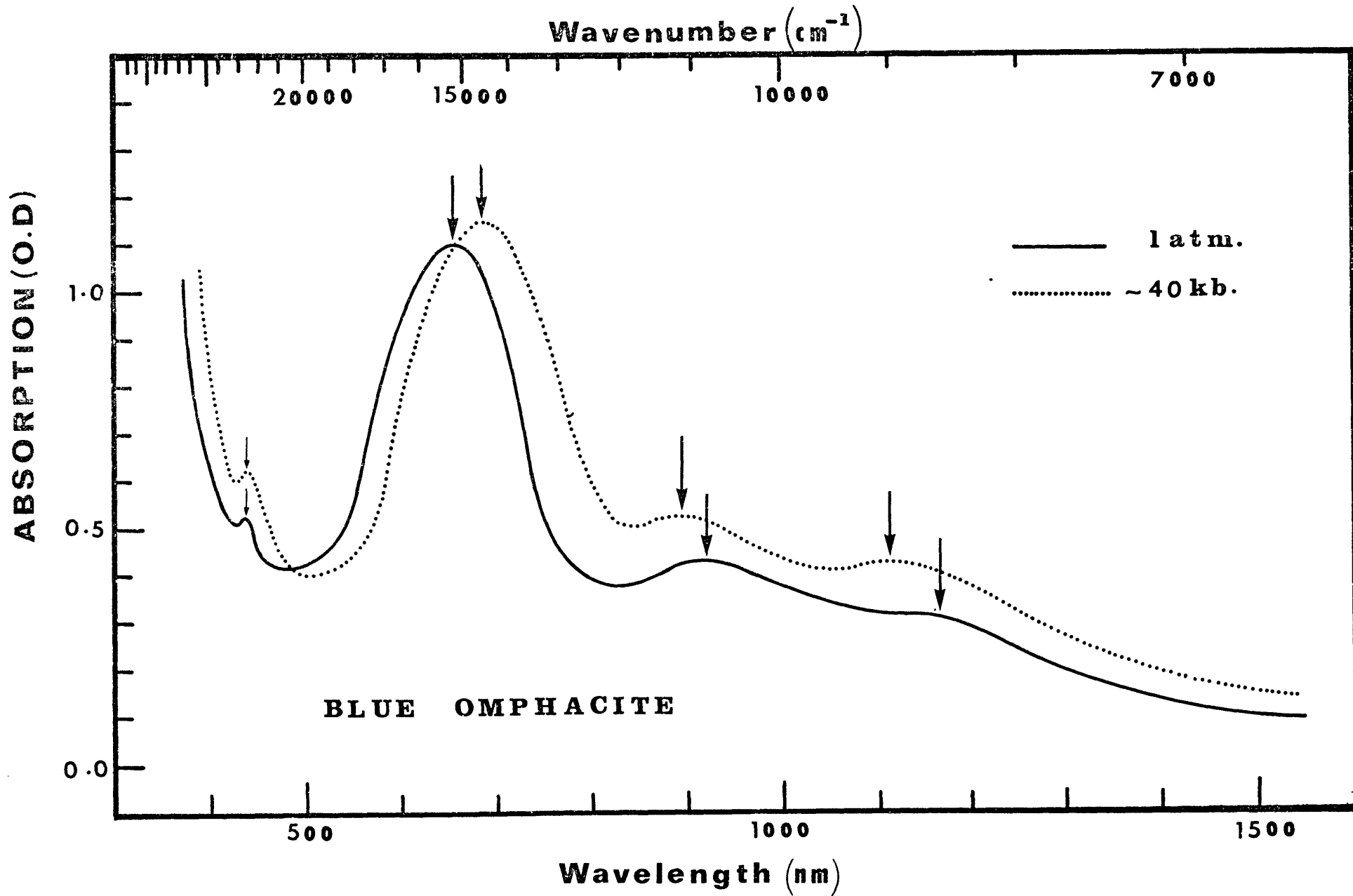
- 138 -
TABLE IV-6

Electron Microprobe Analysis of Blue Omphacite
(L. Curtis, Univ. of Toronto)

SiO ₂	53.1	Si	1.999	
		Al	0.001	2.00
Al ₂ O ₃	7.33	Al	0.324	
TiO ₂	3.48	Ti	0.099	
FeO	10.5	Fe ²⁺	0.330	
Fe ₂ O ₃	4.93	Fe ³⁺	0.140	0.99
MnO	0.53	Mn	0.016	
MgO	1.49	Mg	0.084	
CaO	8.78	Ca	0.355	
Na ₂ O	8.96	Na	0.642	1.00
K ₂ O	0.10	K	0.004	
Cr ₂ O ₃	0.00			
	99.2			

FIGURE IV-14

Absorption spectra of the blue-omphacite single crystal at 1 atm. [—], and at pressure around 40 kb. [.....]. Note the shift of the $\text{Fe}^{2+} \rightarrow \text{Fe}^{3+}$ charge transfer band to lower energy at high pressure.



sure spectral measurements were performed on single crystals of blue omphacite. The spectrum measured at pressure of about 40 kb. is shown in Figure IV-14. The two broad bands in the i.r. region shifted to higher energies. This trend of band shift is in agreement with the above prediction that those bands are crystal field dependent transitions of ferrous ions.

The band at 22727 cm^{-1} did not show any detectable energy shift with increasing pressure up to 40 kb. This trend also confirms its assignment as a spin-forbidden transition in Fe^{3+} .

On the other hand, the broad intense band at 15037 cm^{-1} shifts to lower energy with increasing pressure while its intensity is increasing significantly. The red shift of this band is strong evidence for its assignment as charge transfer transition.

Further, it is of interest to notice in Figure IV-14 that there are no absorption features in the visible region around 20920 cm^{-1} where the Ti^{3+} is expected to absorb. Although this omphacite contains a significant amount of titanium, (see Table IV-6), the absence of absorption peaks around 20920 cm^{-1} could be an indication that most of titanium occurs as Ti^{4+} , since there are no crystal field transitions for this cation. Nevertheless, there may be some contribution of absorption, under the broad band at 15037 cm^{-1} , due to electron transfer between Fe^{2+} and Ti^{4+} ions.

IV-2.5 Rhodonite: $\text{Ca}(\text{Mn,Fe})_4(\text{SiO}_3)_5$

Rhodonite is a pyroxenoid mineral which contains a significant amount of Mn^{2+} . The crystal structure consists of octahed-

ral and tetrahedral layers and the cations in the octahedral layers are contained in five distinct positions designated as M_1 , M_2 . . . M_5 (Peacor and Niizeki, 1963). The calcium ions are ordered preferentially in the M_5 site which is an irregular polyhedron with seven-fold coordination. On the other hand, the Mn^{2+} and Fe^{2+} cations are disordered among the five sites. The M_1 , M_2 , and M_3 sites are close to regular octahedra having average M-O distances of 2.219, 2.215, and 2.228 Å, respectively. However, the M_4 site is extremely irregular, the shortest M-O distance is 1.97 Å, whereas the longest one is 2.87 Å (Peacor and Niizeki, 1963).

Since one of the M-O distances in the M_4 site is exceptionally large, this site could be considered as coordinated only to five oxygen atoms rather than to six.

The absorption spectrum of a rhodonite* crystal fragment was measured at one atm. and at elevated pressures. The high pressure spectra were measured only in the visible region, since the major concern in studying the spectra of rhodonite is to investigate the influence of pressure on Mn^{2+} bands which occur in this region.

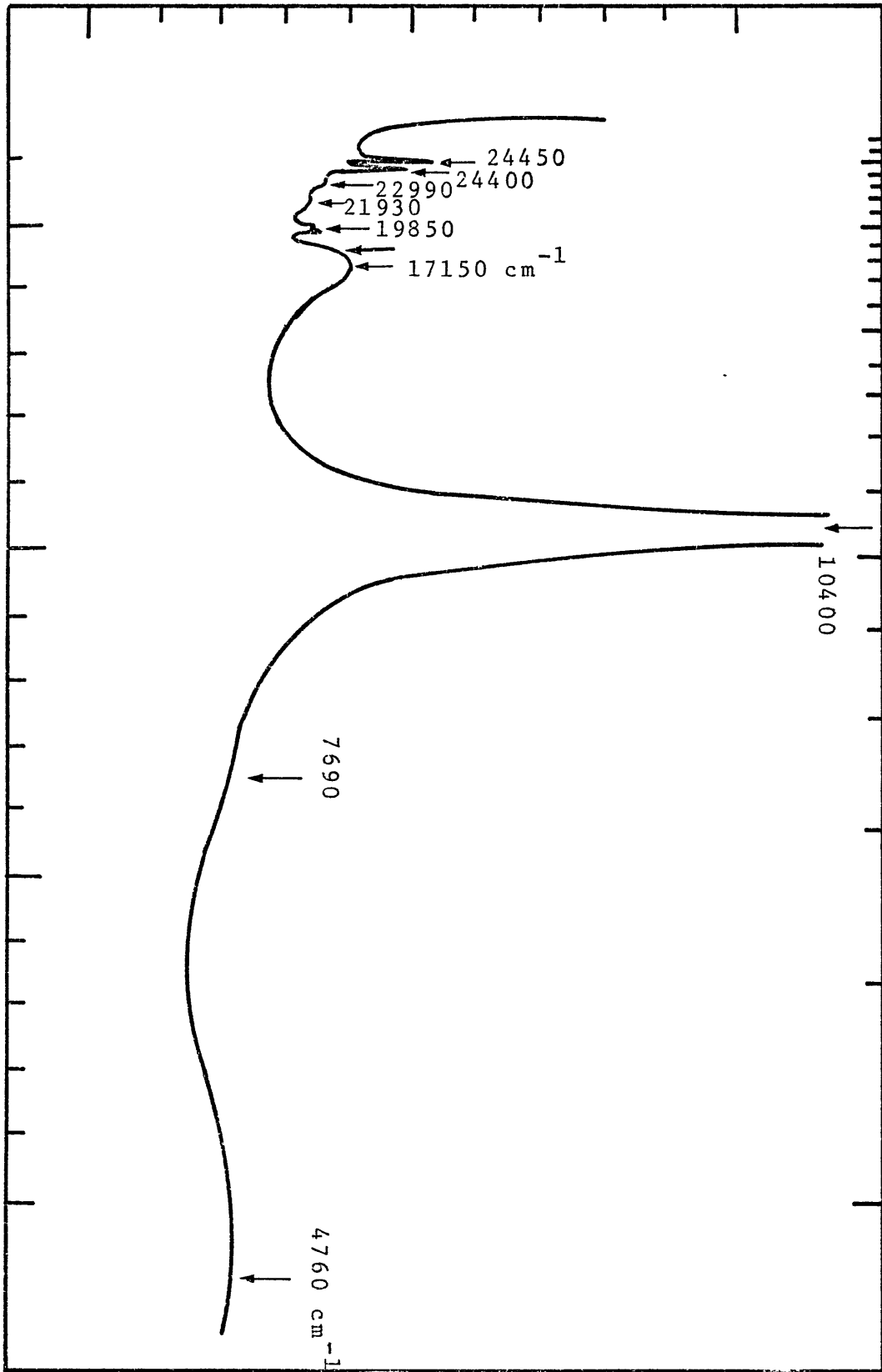
The absorption spectrum of rhodonite in the visible and i.r. regions shown in Figure IV-15 displays the following features:

1. In the i.r. region, there are three broad bands at energies around 4760, 6490, and 7690 cm^{-1} . In addition, there is

* Rhodonite sample from Franklin, New Jersey was provided by Prof. C. Frondel; the chemical formula is unknown, but spectral results indicated high content of Mn^{2+} and Fe^{2+} and a small amount of Mn^{3+} .

FIGURE IV-15

The absorption spectrum of rhodonite measured
in the visible and i.r. regions.



another intense and broad band which covers the energy region 8300-12000 cm^{-1} . This broad band could be resolved into three bands, but the curve fitting was not attempted due to the difficulty in obtaining the absorption maximum which exceeds the limit of the chart recorder.

2. In the visible region, there are many broad and sharp spectral features (Figure IV-15), the most conspicuous of those occur at energies around 17510, 18350, 19850, 21930, 22990, 24000, and 24450 cm^{-1} .

The assignments of the spectral bands in the i.r. and the visible spectral regions are given in Table IV-7. The above assignments yielded energy values of B, C, and 10Dq for Mn^{2+} cation of 664, 3560 and 9250 cm^{-1} , respectively. The electronic transitions and their energies expressed in terms of B, C, and 10Dq for Mn^{2+} are given as:

$$\nu_1 \equiv {}^6A_{1g} \quad {}^4T_{1g} = -10Dq + 10B + 6C - 26B^2/10Dq \quad (1)$$

$$\nu_2 \equiv {}^6A_{1g} \quad {}^4T_{2g} = -10Dq + 10B + 8C - 39B^2/10Dq \quad (2)$$

$$\nu_3 \equiv {}^6A_{1g} \quad {}^4A_{1g} = 10B + 5C \quad (3)$$

$$\nu_4 \equiv {}^6A_{1g} \quad {}^4E_g = 17B + 5C \quad (4)$$

Substituting the above values of B, C, and 10Dq in each equation gives energy values of 17510, 24010, 24440, and 29100 cm^{-1} for the transitions ν_1 , ν_2 , ν_3 , and ν_4 , respectively.

To examine the assignments given in Table IV-7, the high pressure spectral measurements were carried out in the visible region. At elevated pressures, no detectable energy shifts were

observed for most of the absorption bands. However, the bands at 18350 and 21930 cm^{-1} shifted slightly to higher energies suggesting that they could be related to crystal field dependent spin-allowed transitions. Since Fe^{2+} spin-allowed transitions are not expected to occur at those energies, and since Mn^{2+} ion does not have spin-allowed transitions, then the forementioned bands at energies 18350 and 21930 cm^{-1} should correspond to Mn^{3+} spin-allowed transition. Another piece of evidence, supporting these assignments, is the spectrum of Mn^{3+} in piemontite (Figure IV-32) which shows three major bands for Mn^{3+} at 12000, 18250, and 22000 cm^{-1} .

The negligible energy shifts of the remaining bands in the visible region conform with their assignments as spin-forbidden transitions in Mn^{2+} and Fe^{2+} cations (Table IV-7). Let us consider first the spin-forbidden transitions in Mn^{2+} whose energies are expressed in equations 1, 2, 3, and 4. If we assumed that there were energy changes of -2, -8, and +100 cm^{-1} in the parameter B, C, and $10Dq$, respectively, as a result of increasing pressure to about 50 kb., then the energy values of ν_1 , ν_2 , ν_3 , and ν_4 transitions in Mn^{2+} , at this pressure, are expected to be 17400, 23858, 24380, 29014. The differences in positions of the bands measured at 1 atm. and 50 kb. would be about 4, 2.5, 1, and 0.8 nm. These differences are hard to detect on the chart recorder scale and could be within the experimental errors.

Fe^{2+} spin-forbidden transitions were observed often in the spectra of pyroxenes and olivines. The most prominent spectral

TABLE IV-7

Band Energy (cm ⁻¹)	Cation	Transition	Energy in B,C,Dq
4760 6490 7690 8300 10000	Fe ²⁺ Fe ²⁺	$5T_{2g} \rightarrow 5E_g$ in M1, M2, M3, M4, and M5 sites	In reg. Oct. 10Dq
12500 18350 21930	Mn ³⁺ Mn ³⁺ Mn ³⁺	$5E_g \rightarrow 5T_{2g}$ dist. Oct.	In reg. Oct. 10Dq
19850 22990	Fe ²⁺ Fe ²⁺	$5T_{2g} \rightarrow 3T_{1g}$ (H) $5T_{2g} \rightarrow 3T_{2g}$ (H)	$-10Dq+5B+5C-70B^2/10Dq$ $-10Dq+13B+5C-106B^2/10Dq$
17500 24000 24450	Mn ²⁺ Mn ²⁺ Mn ²⁺	$6A_{1g} \rightarrow 4T_{1g}$ $6A_{1g} \rightarrow 4T_{2g}$ $6A_{1g} \rightarrow 4A_{1g}$	$-10Dq+10B+6C-26B^2/10Dq$ $-10Dq+10B+8C-39B^2/10Dq$ 10B+5C

Table IV-7: Assignments of spectral bands in rhodonite.

features are related to these transitions are located at 18200, 19800, and 23250 cm^{-1} . These energy values are in agreement with the band energies observed in the rhodonite spectrum at 18350, 19850, and 22990 cm^{-1} .

It should be mentioned that Gibbons et al. (1974) had studied the spectra of rhodonite samples at different shock pressures; their measurements indicated shift of the Mn^{3+} band at 18500 cm^{-1} to higher energies as pressure increases. At a shock pressure around 496 kb, they reported that Mn^{3+} bands disappeared. They related this phenomenon to a reduction of Mn^{3+} cations in rhodonite. In the present study, no pressure induced reduction has been observed in rhodonite within the pressure range 0-200 kb.

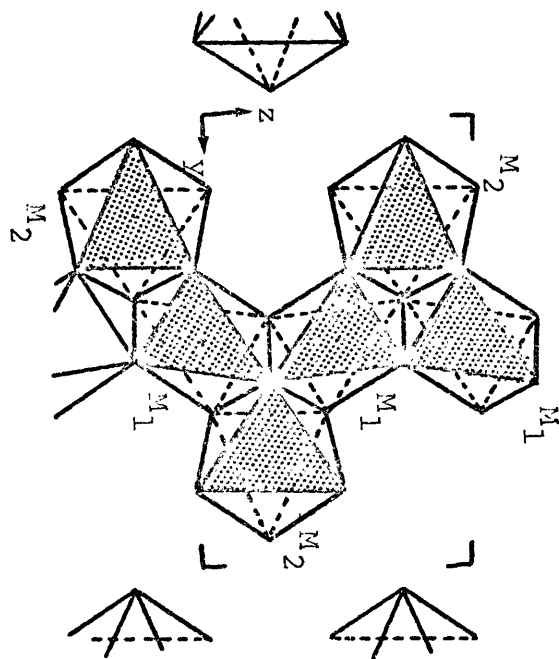
In conclusion, the assignments of spectral bands given in Table IV-7 for rhodonite are consistent and conform with their energy values given in terms of B, C, and 10Dq parameters. The bands related to spin-forbidden transitions were proven to have undetectable energy shifts with pressure, whereas spin-allowed bands showed significant high energy shifts as pressure increases.

IV-3. Olivine .

The structure of olivine has been intensively studied by many crystallographers (Bragg and Brown, 1926; Hanke and Zeeman, 1963; Birle et al., 1968; Finger, 1970, 1971; and Wenk and Raymond, 1971, 1973). It consists of a hexagonal close-packed array of oxygen atoms which form octahedral and tetrahedral cavities partially filled with (Mg,Fe) and Si cations, respectively.

FIGURE IV-16

A portion of an octahedral serrated band in olivine projected on (100). Note the edge sharing between M_1 and M_2 sites. [After Birle, J.D. et al., 1968].



The octahedral sites share edges to form octahedral chains parallel to the Z-axis, and the chains are linked to each other to form the octahedral layer. The chains in two successive layers are linked by means of SiO_4 tetrahedra (Figure IV-16).

The M cations (Mg,Fe) occupy two crystallographically distinct positions designated by M_1 and M_2 . The M_1 and M_2 sites are distorted octahedra which have actual point symmetries C_i and C_s , respectively. However, the local symmetries of both sites, taking into consideration the M-O distances only, have been approximated to higher point group symmetries. Burns (1970b, 1974) considered the M_1 and M_2 local symmetries as D_{4h} and C_{3v} ; however, Runciman et al. (1973) approximated the two site symmetries to C_{2v} .

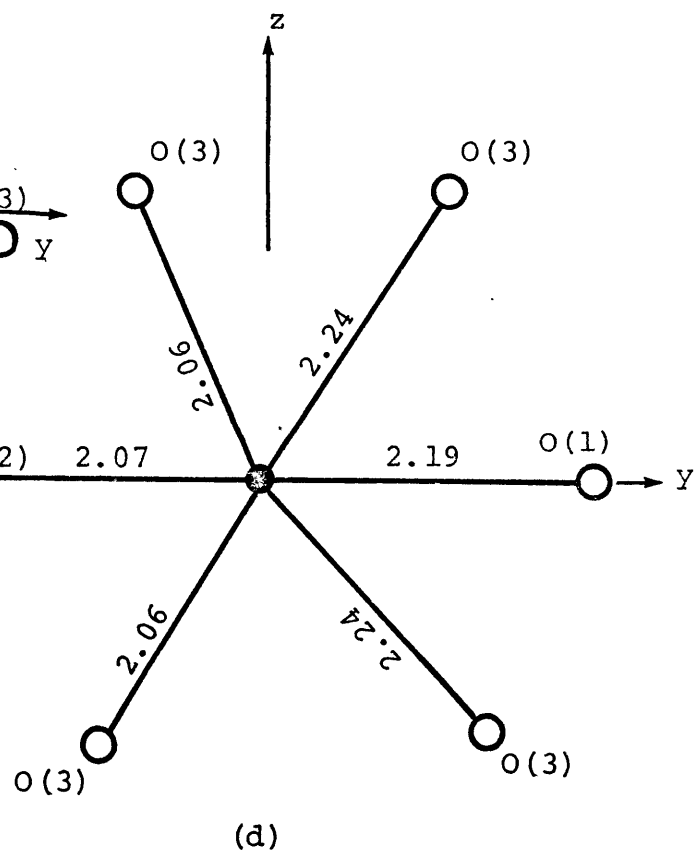
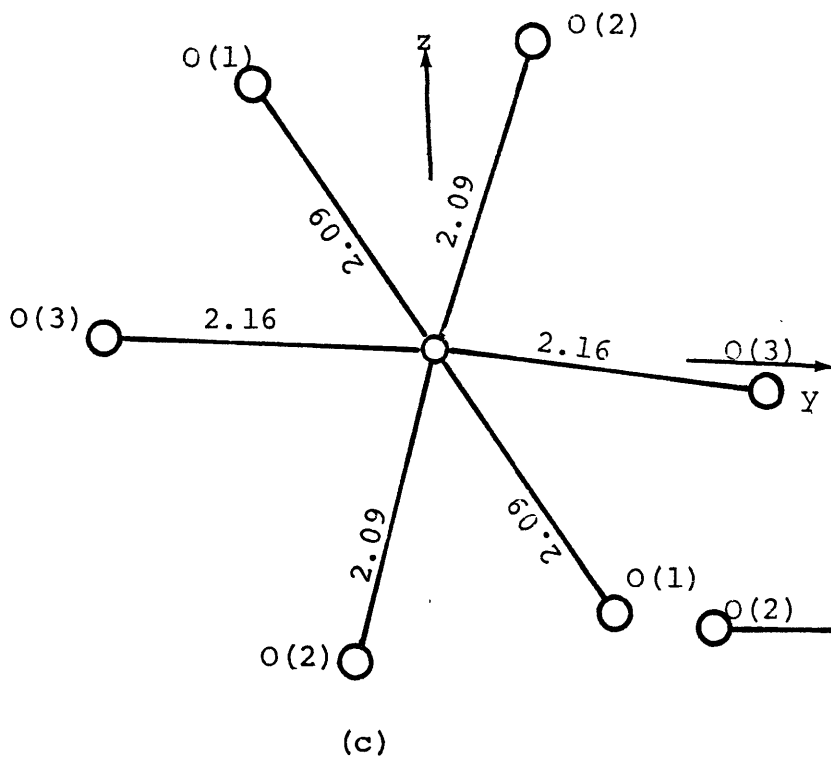
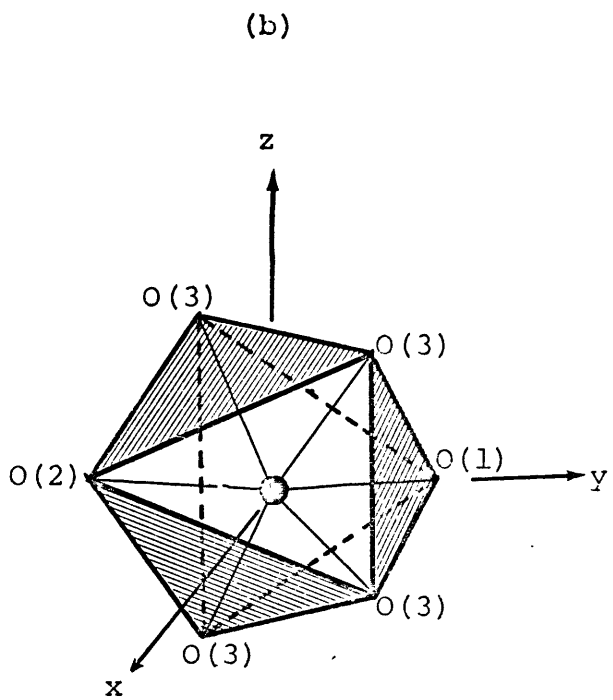
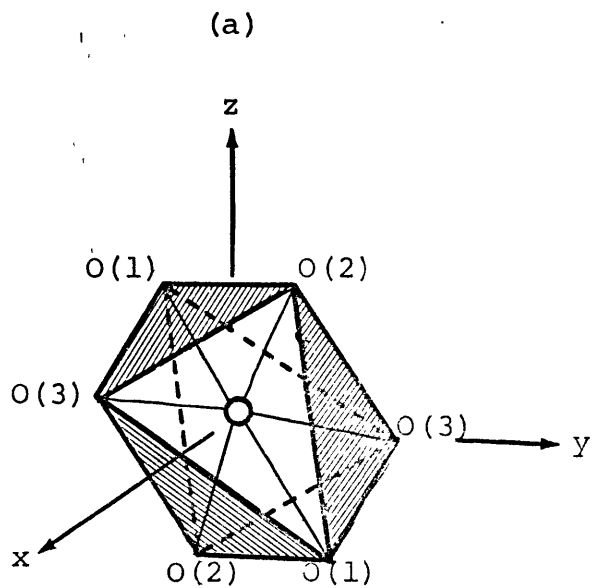
After careful re-examination of the olivine structure reported by Birle et al. (1968), it appeared that the M_1 site should have D_{4h} symmetry. Figures IV-17a,b,c,d illustrate M_1 and M_2 polyhedral symmetries in a pictorial view, and in a view along the x-axis.

The olivine sample, which has been used in this study, is fayalite, Fa_{96} , from Rockport, Massachusetts. The polarized spectra for olivine of the same composition was measured by Burns (1965, 1969a,b, 1970a,b).

Polarized spectral measurements on fayalite (Figure IV-18) are in agreement with those reported by Burns (1970a,b). There are three principle absorption bands in the infrared region; the band maxima of those bands occur at energies around 7350, 9540, and 11100 cm^{-1} . Burns (1970a,b) assigned the first and the third

FIGURE IV-17

The M_1 and M_2 polyhedral symmetries, in olivine, shown in pictorial views (a,b) and in a view along the x-axis (c,d). The interatomic distances are also given in c and d.



band to spin-allowed transitions in Fe^{2+} in the M_1 site, and the second band to spin-allowed transitions in Fe^{2+} ions in the M_2 site. However, Runciman et al. (1973b) related only band II to Fe^{2+} spin-allowed transitions in the M_2 site without giving an explanation of bands I and III. In the present study, assignments of absorption bands in the infrared region conform with that reported by Burns (1970a,b,1974a) and agreed upon by Runciman et al. (1974).

The d-energy level diagrams for both sites M_1 and M_2 (Figure IV-19) were constructed on the following basis:

1. The point group symmetries of the M_1 and M_2 sites are approximated to D_{4h} and C_{2v} symmetries, respectively.
2. The band at 9540 cm^{-1} is assigned to Fe^{2+} in the M_2 site, whereas, the bands at 7350 and 11100 cm^{-1} are assigned to Fe^{2+} in the M_1 site.
3. The energy separations (Δ_1 and Δ_2) between the lower levels t_{2g} , were estimated (Huggins and Abu-Eid, 1974; Huggins, 1974) from Mössbauer spectral data of fayalite obtained at various temperatures (Eibschutz and Ganiel, 1967). These values are:

	Δ_1	Δ_2
M_1 site	1400 ± 200	$620 \pm 20 \text{ cm}^{-1}$
M_2 site	1500 ± 200	$710 \pm 20 \text{ cm}^{-1}$

since the uncertainties in Δ_1 and Δ_2 values are large, the absorption bands observed in the far infrared region (Runciman et al., 1973) were employed to assess the above values more accurately.

FIGURE IV-18

The γ -(——) and α -(-----) spectra of olivine
[Fa₉₆] measured at normal pressure.

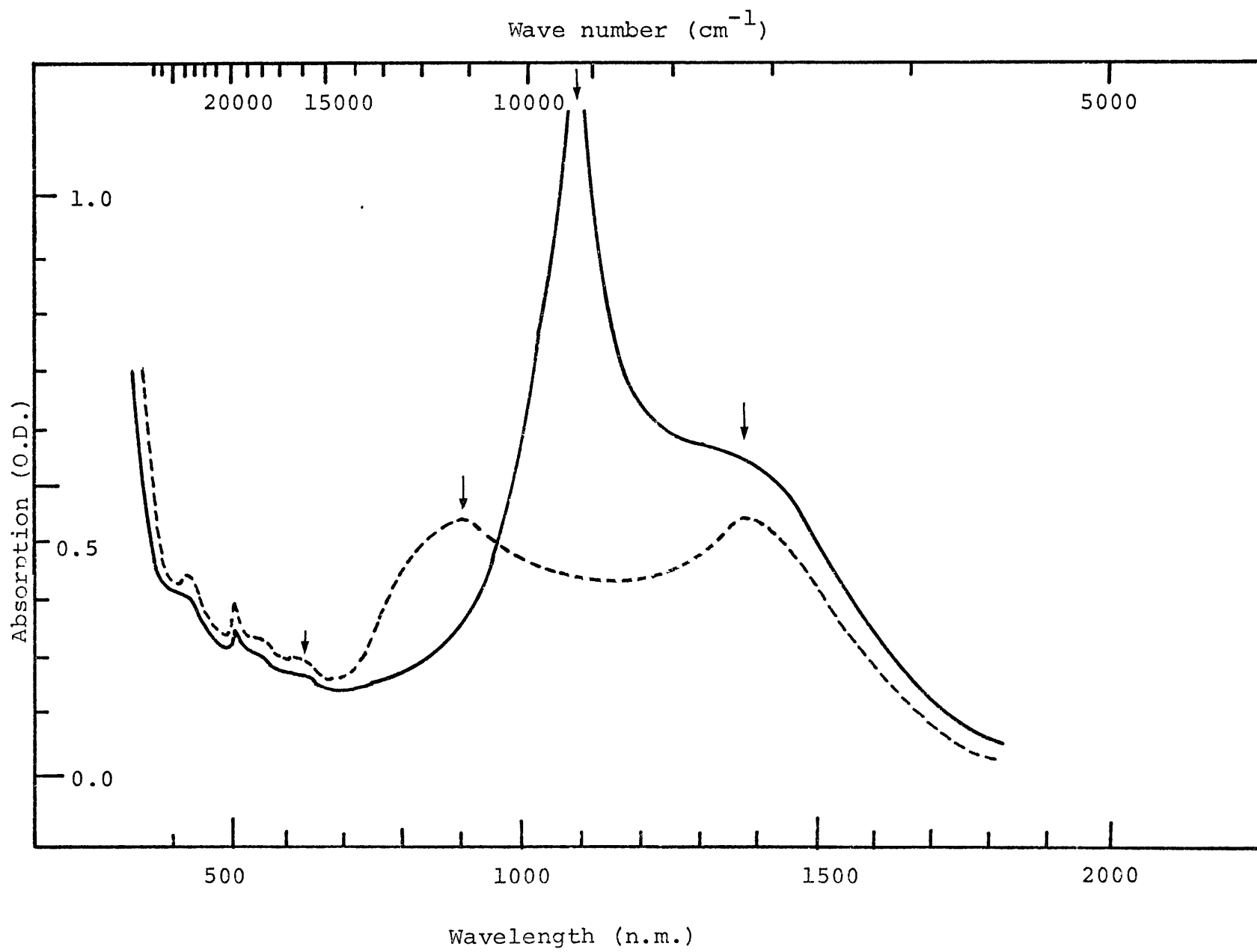
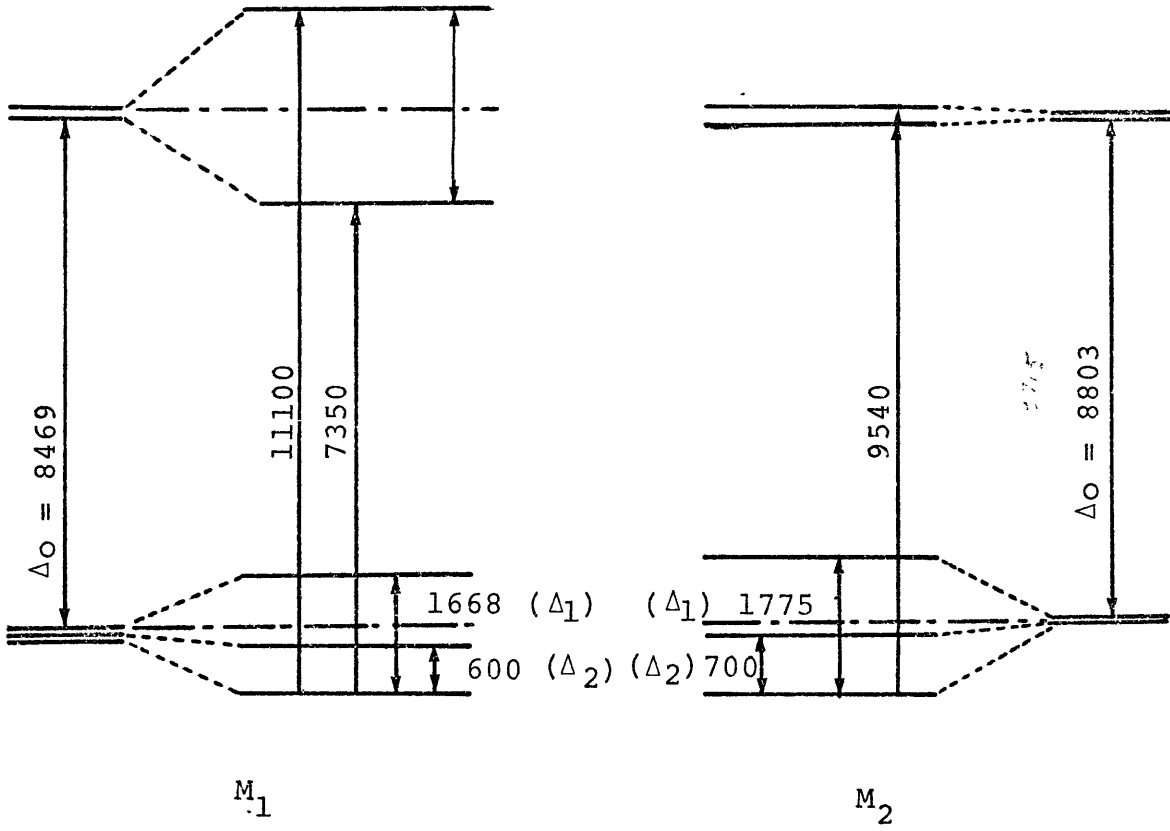


FIGURE IV-19

The d-energy level diagrams for Fe^{2+} in the M_1
and M_2 sites in olivine.

5/15



The energy values of Δ_1 and Δ_2 for the M_1 and M_2 sites, which were estimated from considering both Mössbauer and far infrared spectral data, are given on the energy level diagrams shown in Figure IV-19.

From the energy level diagrams shown in Figure IV-19, the values of the crystal field splitting (CFS) and crystal field stabilization energy (CFSE) parameters were calculated; these values are:

	M_1	M_2
CFS	8469	8715 cm^{-1}
CFSE	4144	4186 cm^{-1}

From the CFSE values for M_1 and M_2 sites, it is apparent that Fe^{2+} ions are very slightly more stabilized in the M_2 site more than in the M_1 site. Burns (1970a,b) obtained similar results; however, the CFSE value for the M_2 site was much higher than the one reported in this study.

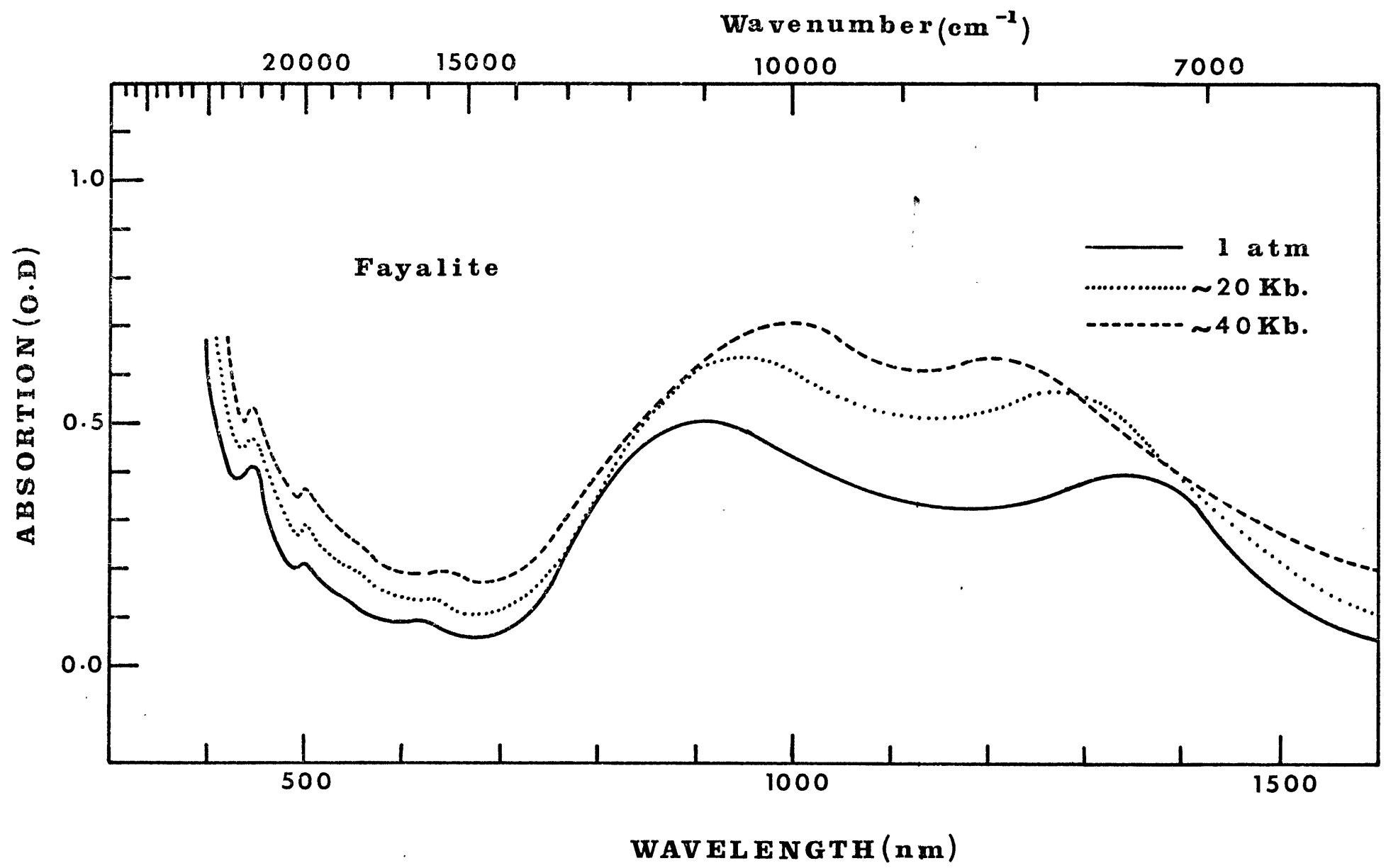
The high pressure absorption spectra for fayalite single crystal were performed on a crystal which was mounted in a pressure fluid after it had been polished and oriented, so that the x and y axes are perpendicular to the pressure axis.

The α -spectra at 1 atm. and at pressures around 20 and 40 kb. are shown in Figure IV-20. The two bands at energies 7350 cm^{-1} and 11100 cm^{-1} are related to Fe^{2+} spin-allowed transitions,

in the M_1 distorted site. With increasing pressure, the band at 7350 cm^{-1} shifted slowly to higher energy, whereas the band at 11100 cm^{-1} shifted slowly to lower energy.

FIGURE IV-20

The α -spectra of a fayalite single crystal at
1 atm., 20 and 40 kb.



The energy level diagrams, shown in Figure IV-21, were constructed from α -spectra measured at 1 atm. and 40 kb.

From these diagrams, it is apparent that there is a small increase in $10Dq$ value at high pressure accompanied by a decrease in the energy separation between the upper levels e_g and between the lower levels t_{2g} . The above results indicate that a more regular octahedral site should be obtained at elevated pressures.

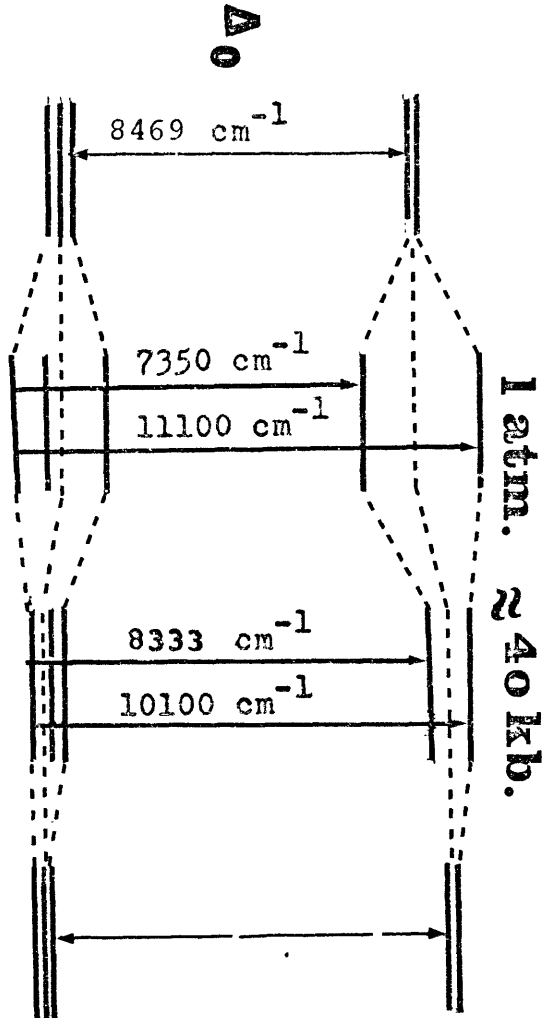
The crystal field splitting parameter (CFS), at 1 atm., was estimated accurately using the high temperature Mössbauer data (Huggins and Abu-Eid, 1974) to estimate the energy separation between the t_{2g} levels (Δ_1 and Δ_2), and the absorption spectral data to determine the splitting energy between e_g levels.

For accurate estimation of CFS and CFSE at high pressures, Mössbauer data at these pressures and at elevated temperatures are warranted. Since such data are unavailable, the estimated values of CFS and CFSE, from absorption spectra only, at elevated pressures are not highly accurate. The estimated energy change in CFS (Δ_o) in 40 kb. for Fe^{2+} ion in the M_1 site is about $+100\text{ cm}^{-1}$. If the same phenomenon takes place for M_2 site, i.e. leading to a more regular octahedral site with increasing pressure, both sites may be undistinguishable, having similar bond lengths; this may be a transition stage in transforming olivine to β or γ spinel. Similar results have been obtained from high pressure absorption spectra (Abu-Eid, 1975), and from high pressure Mössbauer spectra (Huggins, 1974), and more recently from high pressure x-ray studies on olivine single crystals (Hazen, personal communication).

FIGURE IV-21

The energy level diagrams of the M_1 site in fayalite constructed at 1 atm. and 40 kb.

**M₁ Site
FAYALITE**



The sharp peaks in the visible region are assigned to Fe^{2+} spin-forbidden transitions; they showed negligible energy shifts with increasing pressure similar to those of Fe^{2+} spin-forbidden transitions in lunar pyroxenes. However, the band around 16260 cm^{-1} shifted to lower energy, suggesting that it may be a charge transfer band which arises from electron transfer between Fe^{2+} and Fe^{3+} cations (Fe^{3+} exists in trace amounts in olivine). The effect of pressure on charge transfer transitions will be discussed in detail in the next chapter.

IV-4. Garnets

The general chemical formula for the garnet group is $\{\text{X}_3\}[\text{Y}_2](\text{Z}_3)\text{O}_{12}$, where X, Y, and Z refer to the cations occupying polyhedra with dodecahedral, octahedral, and tetrahedral symmetries, respectively.

In the present study, three members of the garnet mineral group were investigated. These are: almandine $\{\text{Fe}_3^{2+}\}[\text{Al}_2^{3+}](\text{Si}_3)\text{O}_{12}$, andradite $\{\text{Ca}_3\}[\text{Fe}_2^{3+}](\text{Si}_3)\text{O}_{12}$, and uvarovite $\{\text{Ca}_3\}[\text{Cr}_2^{3+}](\text{Si}_3)\text{O}_{12}$.

The structure of garnet minerals (Fig. IV-22) was discussed by many authors, e.g. Gibbs and Smith (1965), Geller (1967), and Novak and Gibbs (1971). It consists of SiO_4 tetrahedra alternating with YO_6 octahedra, which share corners to form a continuous three-dimensional framework. The oxygen atoms coordinated to Y and Z cations also define a triangular dodecahedral cavity consisting of 8 oxygens which are filled by x cations.

The garnet structure is characterized by having a high per-

FIGURE IV-22

The garnet crystal structure projected along the z-axis showing the framework of alternating tetrahedra and octahedra and the 8-fold dodecahedra which contain the {X} cations. [Novak and Gibbs, 1971.]

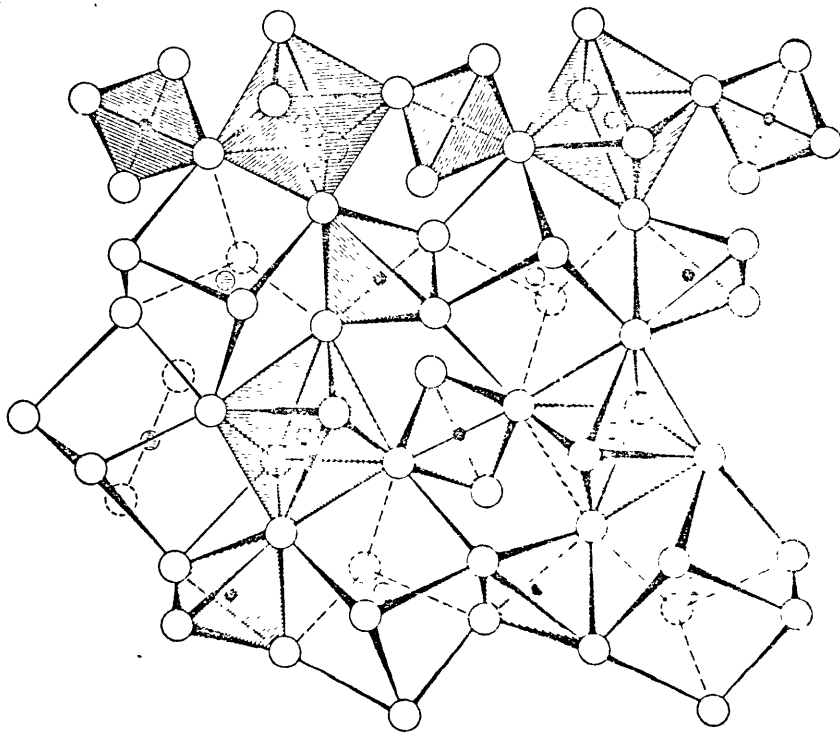


Fig. IV-22

centage of edge-shared coordination polyhedra (Fig. IV-23a). This is due mostly to the fact that each oxygen atom is coordinated to two x-cations, one y-cation, and one z-cation. As a consequence of this, each tetrahedron shares two of its edges with two dodecahedra, and each octahedra shares six edges with six dodecahedra. Furthermore, the dodecahedral site shares ten of its edges with other polyhedra; it shares two of them with tetrahedra, four with octahedra, and four more edges with other dodecahedra. As a result of having a large number of shared edges in the structure, the 8-fold and 6-fold coordinated sites are distorted from the regular cubic and octahedral symmetries.

Since Fe^{2+} ions in almandine occupy the dodecahedral sites, and since Fe^{3+} and Cr^{3+} ions in andradite and uvarovite occupy the 6-fold coordination sites, our attention, in the crystal chemical studies of garnets, will be centered around the site symmetries and metal-oxygen distances of the 8-fold 6-fold coordination sites.

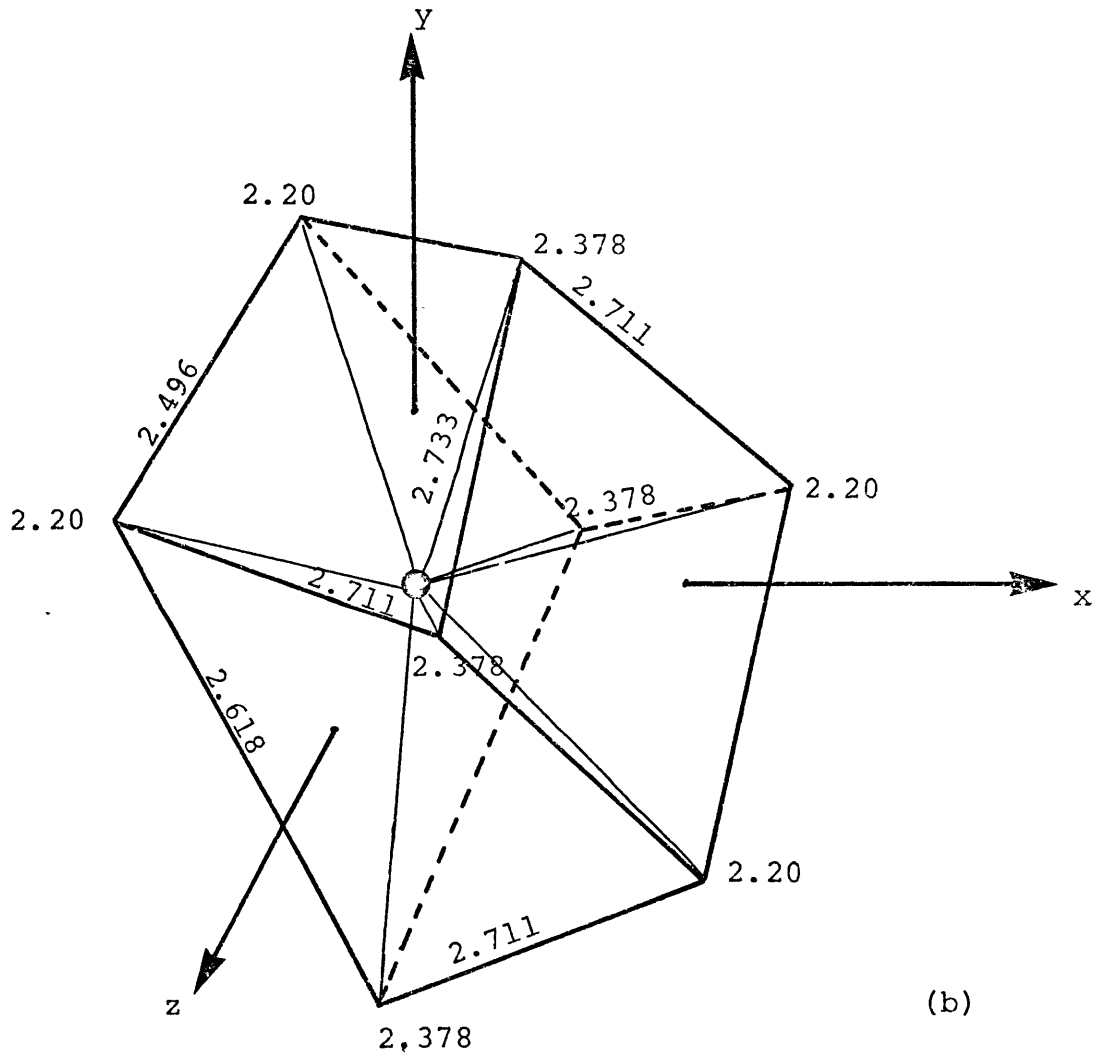
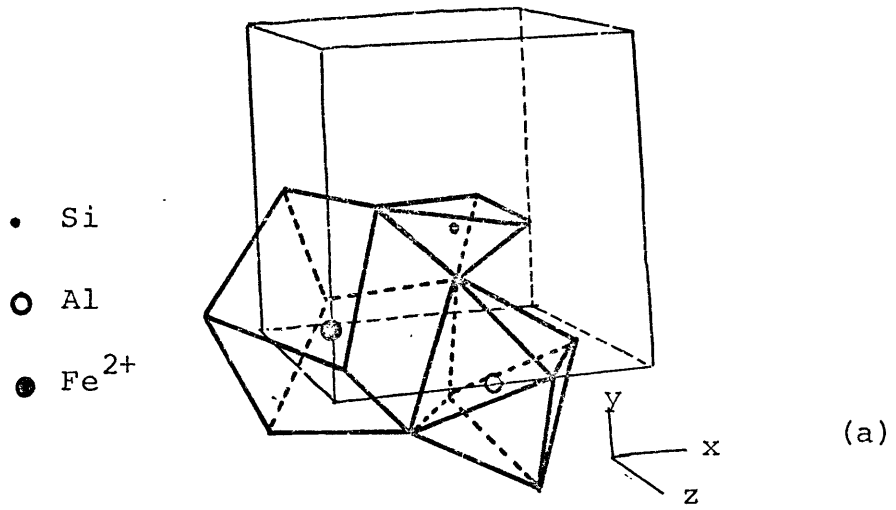
IV-4.1 Almandine

The almandine sample* used in this study was analyzed by Whipple (1973) using electron microprobe and wet chemical analyses. Mössbauer studies of Fe in almandine showed only absorption peaks related to Fe^{2+} in 8-fold coordination site, and no Mössbauer absorption related to Fe^{3+} was detected.

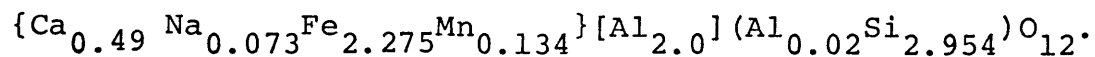
* Locality, Washington Camp, contact metamorphic copper deposits, Arizona. MIT research collection specimen 4623(2593).

FIGURE IV-23

- (a) Shows the coordination polyhedra of oxygen atoms about Si, Al, and Fe^{2+} atoms in almandine. It shows, also, the shared edges between the polyhedra.
- (b) Shows the interatomic distances (X-O and O-O) of the XO_8 triangular dodecahedron.



The crystal chemical formula derived from the analysis data reported by Whipple (1973) is:



The interatomic distances (X-O and O-O) of the XO_8 triangular dodecahedron are shown in Figure IV-23b. From this figure it is apparent that Fe^{2+} cation is contained in a distorted cube which has a D_2 site symmetry. The splitting of d-energy levels in octahedral, cubic, and dodecahedral (D_2) symmetries are illustrated in Figure IV-24. In octahedral symmetry, the d-levels split into a doubly degenerate state, 5E_g , and a triply degenerate state, ${}^5T_{2g}$. In this symmetry, the ${}^5T_{2g}$ state is the ground, low energy state, and 5E_g is the excited, high energy state. The energy separation between ${}^5T_{2g}$ and 5E_g levels is denoted by Δ_o . Conversely, in a cubic symmetry, the ground state is 5E_g and the higher energy excited state is ${}^5T_{2g}$; the cubic crystal field splitting parameter, designated by Δ_c , is equivalent to $8/9 \Delta_o$ (if distances are the same in both symmetries).

When the cubic symmetry is distorted, e.g. becomes D_2 symmetry as in the case of Fe^{2+} site symmetry in almandine, the two levels, 5E_g and ${}^5T_{2g}$, split further into two and three energy levels, respectively. The d-levels in a D_2 symmetry are designated according to point group theory by: 5A_1 , 5B_1 , 5A_2 , 5B_2 , and 5B_3 (Figure IV-24c).

The absorption spectra of almandine at 1 atm. were measured by Burns (1970), White and Moore (1972), and more recently by Runciman and Sengupta (1974). The absorption spectra of alman-

FIGURE IV-24

Energy level diagrams illustrating the splitting of d-energy levels in octahedral, cubic, and dodecahedral symmetries (a,b, and c). Figure (d) shows the energy level diagram of Fe^{2+} in almandine at pressure around 200 kb..

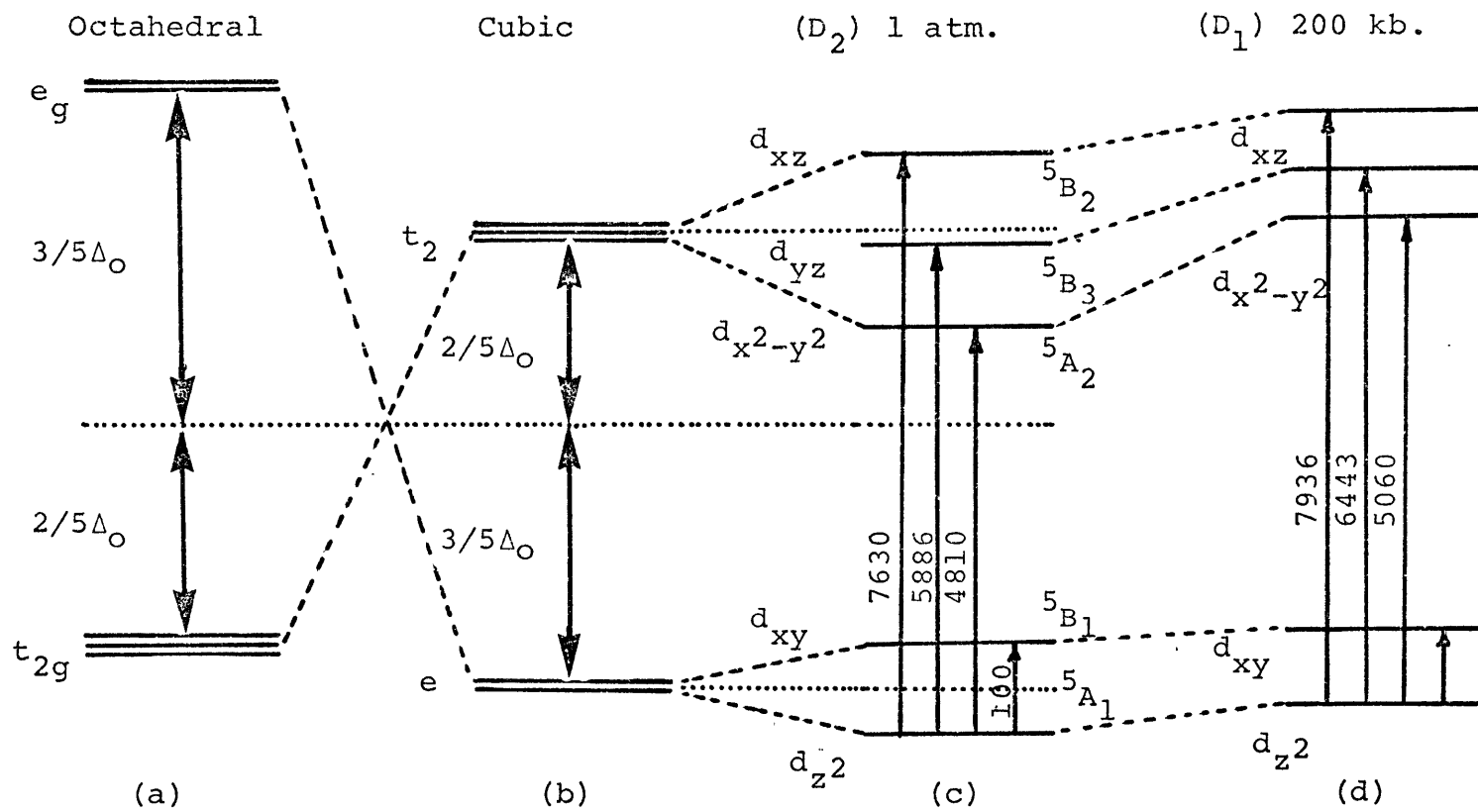
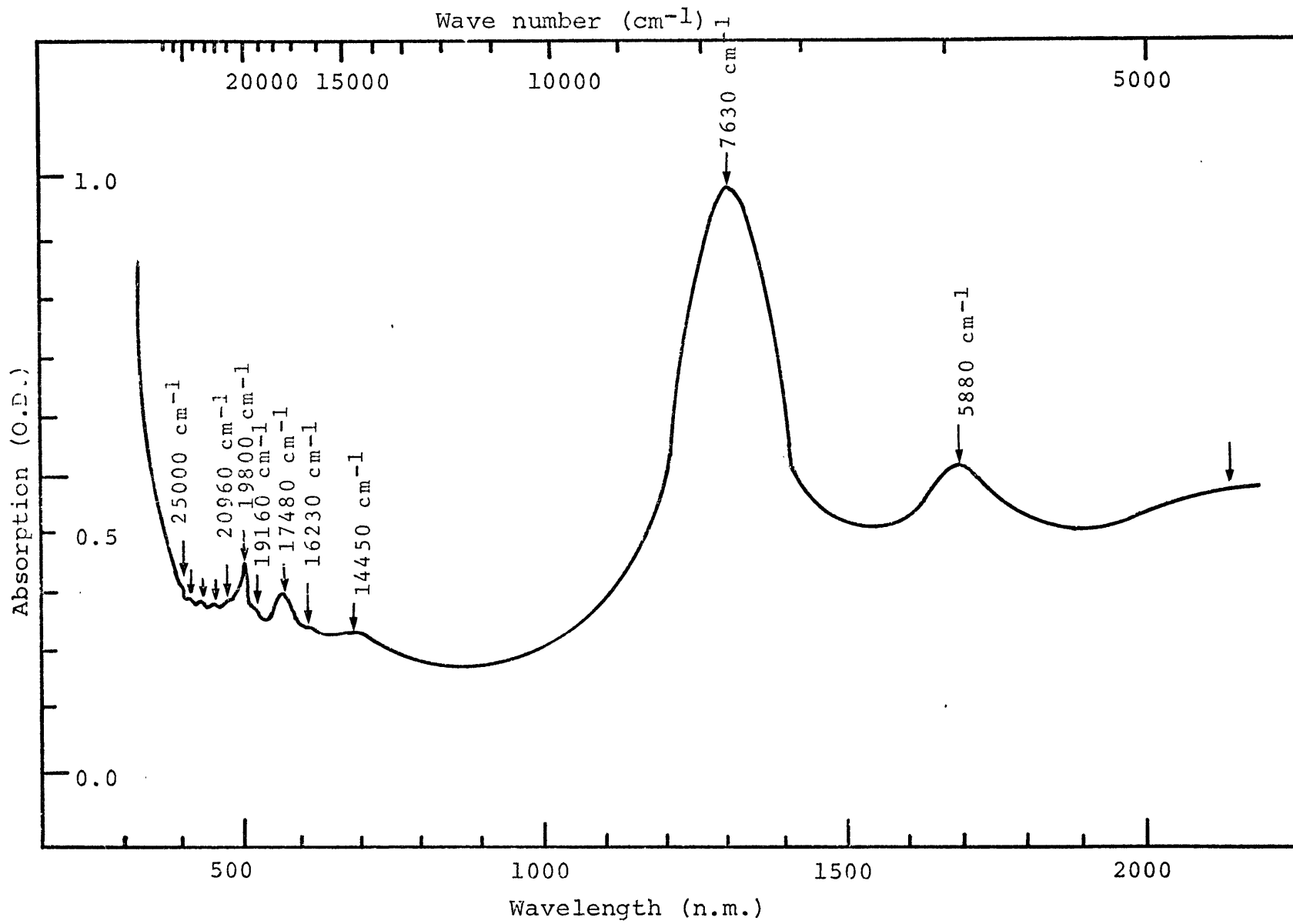


FIGURE IV-25

The absorption spectrum of almandine garnet
measured at normal pressure.



dine measured at 1 atm. is shown in Figure IV-25. Two bands were observed at energies 5880 and 7630 cm^{-1} . In addition, a shoulder of another band which has maximum absorption at 4310 cm^{-1} was also observed in the spectrum. The three bands are related to spin-allowed transitions in Fe^{2+} ions contained in D_2 symmetry; this assignment conforms with those suggested by Burns (1970a) and White and Moore (1972). The energy separation between the two energy levels, 5A_1 and 5B_1 (between the lowest two energy levels), was determined by Lyubutin and Dodokin (1971b), Huggins and Abu-Eid (1974), and Huggins (1974). This energy separation is $1100 \pm 50 \text{ cm}^{-1}$. Using this value and the above mentioned energies of crystal field bands, the energy level diagram for Fe^{2+} in almandine was constructed (Figure IV-24c). The crystal field splitting, Δ_c , and the crystal field stabilization energy parameters, estimated from the energy level diagram, are: 5390 and 3784 cm^{-1} , respectively. In the visible region, many weak and sharp peaks were observed at energies 14450, 16230, 17480, 19160, 19800, 20960, 21640, 23700, 24450, and 25000 cm^{-1} . These bands are assigned in general to spin-forbidden transitions in Fe^{2+} and Mn^{2+} ions.

In a cubic electrostatic field, Fe^{2+} has three main spin-forbidden transitions; these are: $^5T_2 \rightarrow ^3T_1$, $^5T_2 \rightarrow ^3E$, and $^5T_2 \rightarrow ^1A_1$. However, in a D_2 symmetry, the first excited state, 3T_1 , will split into three different states or levels designated by 3B_1 , 3B_2 , and 3B_3 ; the second excited state, 3E , will split also into two states denoted by 3A and 3B_1 ; however, the third state, 1A_1 , will stay the same.

The spin-forbidden transitions for Mn^{2+} in a cubic electrostatic field are: ${}^6A_1 \rightarrow {}^4T_1$, ${}^6A_1 \rightarrow {}^4T_2$, and ${}^6A_1 \rightarrow {}^4A_1$. In a D_2 symmetry, each of the triply degenerate states, 4T_1 and 4T_2 , will split into three levels, and the 4A_1 state will stay the same. Since Mn^{2+} concentration in the almandine sample is very low, only its sharp and intense spin-forbidden peaks could be observed.

On the basis of the above argument, the bands in the visible region were assigned to spin-forbidden transitions in Fe^{2+} and Mn^{2+} cations. These assignments are given in Table IV-8

The high pressure electronic spectra of almandine were measured on a powdered specimen at pressures up to about 200 kb. The spectra measured at pressures around 1 atm., 50, 100, and 200 kb., are shown in Figure IV-26. With increasing pressure, the three bands in the infrared region shifted to higher energies; however, the bands in the visible region did not show any detectable energy shift except for the band at 17480 cm^{-1} which shifted very slightly to lower energy, indicating that it may be related to the spin-forbidden transition, ${}^5T_2 \rightarrow {}^3T_1$, or ${}^5T_2 \rightarrow {}^1A_1$, since both of them are dependent to a small degree on $-10Dq$ (see Table I, Chapter II). The other spin-forbidden transitions did not show significant energy shifts, possibly because they are crystal field independent.

The magnitude of energy shift for the i.r. band at 4300 cm^{-1} could not be measured since the maximum absorption of the band occurs at energy lower than the minimum energy limit of the

TABLE IV-8

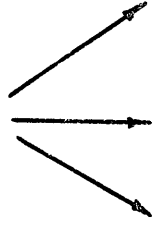
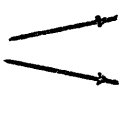
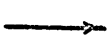
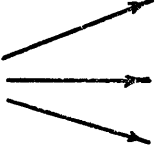

Electronic Transition in Cubic Symmetry	Transition in D ₂ Symmetry	Energy (cm ⁻¹)	Cation
$5T_2 \rightarrow 3T_1$ 	$3B_1$	14450	Fe ²⁺
	$3B_2$	16230	
	$3B_3$	17480	
$5T_2 \rightarrow 3E$ 	$3A$	19160	Fe ²⁺
	$3B_1$	19800	
$5T_2 \rightarrow 3A_1$ 	$3A_1$	25000	
$6A_1 \rightarrow 4T_2$ 	$4B_1$	20960	Mn ²⁺
	$4B_2$	21640	
	$4B_3$	23700	
$6A_1 \rightarrow 4A_1$ 	$4A_1$	24450	Mn ²⁺

Table IV-8: Electronic transitions of Fe²⁺ in almandine garnet.

spectrophotometer used in this project. The magnitude of the energy shifts of the remaining two bands in the i.r. region are given below:

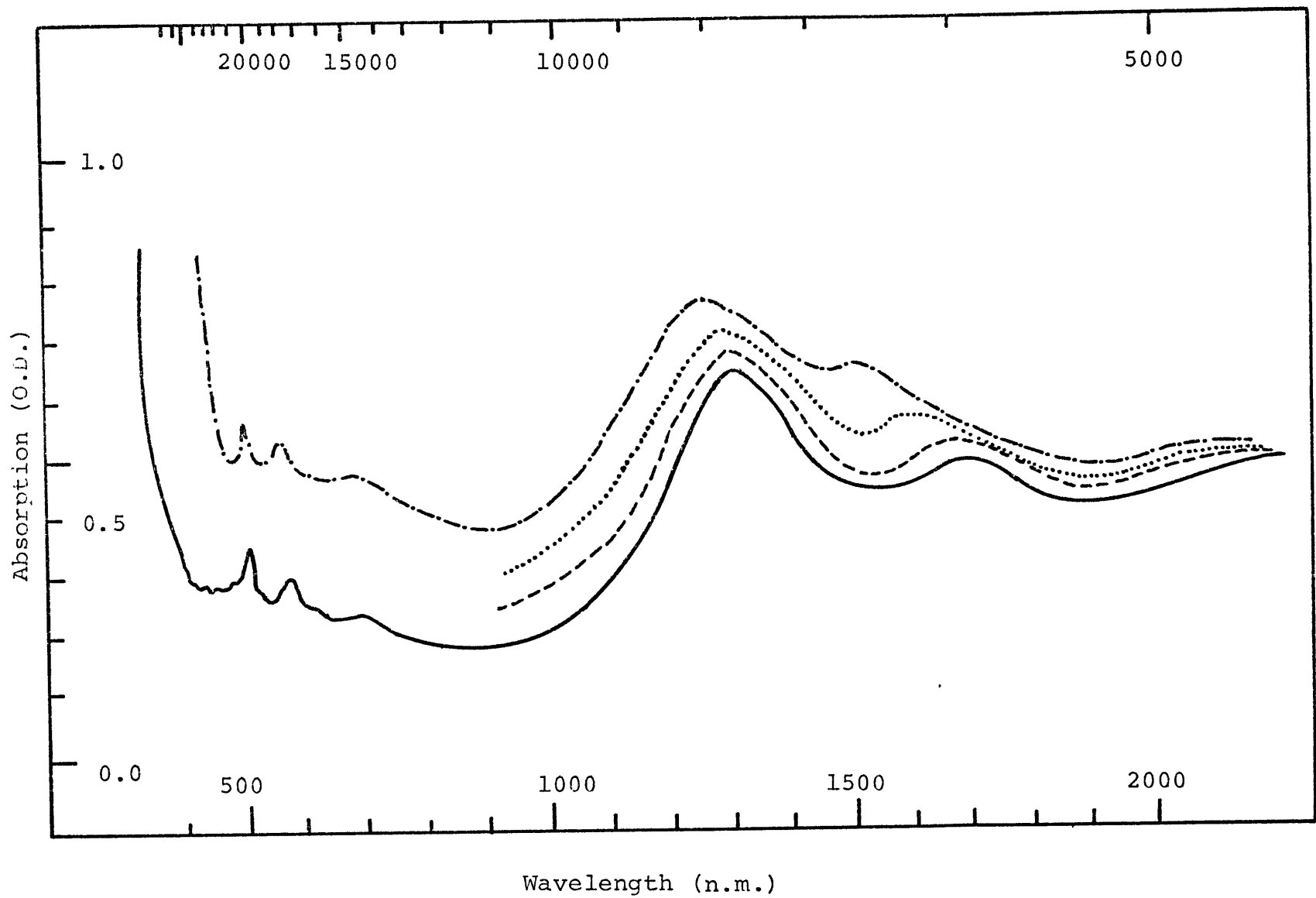
P	1 atm.	50 kb.	100 kb.	200 kb.
Energy (Band II)	5882	6006	6154	6443
Energy (Band III)	7663	7722	7732	7936

The energies of the band maxima for the two bands at four different pressures indicate consistent high energy shifts of both bands. However, it is obvious that the rate of energy shift of band II, which occurs at 5882 cm^{-1} at 1 atm., is about twice the rate of energy shift for band III. Since the energy location of band I, which occurs at 4330 cm^{-1} , could not be obtained, it was not possible to determine accurately the energy values of CFS and CFSE for Fe^{2+} at these pressures. Nonetheless, the energy level diagram shown in Figure IV-24d, was constructed to show qualitatively the energy positions of d-levels at pressures around 200 kb. This diagram shows that the energy separation between the upper d-levels becomes smaller at elevated pressures, indicating an increase in the regularity of the 8-coordination site.

The high pressure spectral results on the almandine garnet also indicated that the longer metal-oxygen bonds are shortened more than the shorter ones as pressure increases. This conclusion was drawn from the rate of energy shift of bands II and III with pressure. Band II corresponds to transition from d_{z^2} orbital to d_{xz} , whereas band III is due to electronic transition

FIGURE IV-26

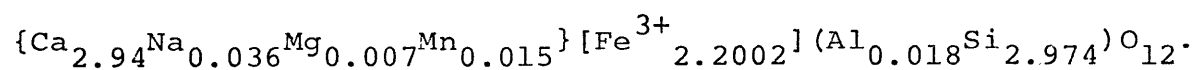
The absorption spectra of almandine garnet measured at pressures: 1 atm. (—); 50 kb. (----); 100 kb. (.....); and 200 kb. (-.-.-.-). [The spectral measurements were made on a powdered sample.]



from d_{z^2} to d_{yz} orbital. Since the loops of the d_{yz} orbital are orientated towards oxygen atoms at a distance of 2.343 Å from Fe^{2+} cations, whereas the loops of the d_{xz} orbital are orientated towards the oxygen atoms at a shorter distance, 2.198 Å, from Fe^{2+} cation, and since the electrostatic repulsion forces along d_{yz} orbital are increasing significantly more than those along d_{xz} as pressure increases, then the oxygens at a distance of 2.343 Å should be approaching the Fe^{2+} cation faster than those oxygens at a distance of 2.198 Å (i.e. the rate of shortening of M-O distances for oxygens located at long distances from the central ion is more than that for oxygens at shorter distances). These results are significant for understanding the mechanism of phase transitions from garnet structure to other possible, more dense structures; this will be discussed in Chapter VII.

IV-4.2 Andradite

The chemical composition of the andradite sample* used in this study can be described by the formula:



and the Fe^{2+}/Fe^{3+} ratio, as determined from Mössbauer spectra, is 0.004 - 0.002 (Whipple, 1973).

Mössbauer and absorption spectral studies (Whipple, 1973; Abu-Eid, 1974) of the andradite used in the current investiga-

* From Graham County, Arizona; near Crystal Peak. Harvard collection No. 98087.

tion proved that the ferric ions are ordered in the 6-fold coordination site.

The optical spectra of garnet minerals having chemical composition close to the ideal chemical formula of andradite have been measured by many authors (Manning, 1967b, 1972; Moore and White, 1972). The spectra of andradite used in this investigation (Figure IV-27) is similar to the spectra reported by Manning (1967) and Moore and White (1972). However, the spectrum shown in Figure IV-27 , has fewer absorption features than the spectra reported by Manning and Moore and White; this is due to the fact that the garnet used in this study does not contain a significant amount of other transition metal ions (e. g. Mn^{2+} , Fe^{2+} , and Ti^{3+}) as the other garnets investigated by the above authors. These cations contribute additional spectral features in the visible region which add more complexity to the spectrum.

Since the andradite involved in this study contains only Fe^{3+} cations, the spectral features observed in the visible region (Figure IV-27) should belong to the spin-forbidden transitions in Fe^{3+} cations contained in the 6-fold coordination site. These transitions are:

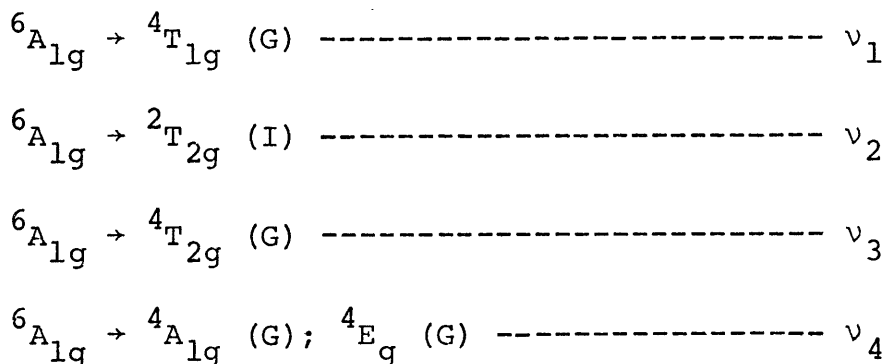
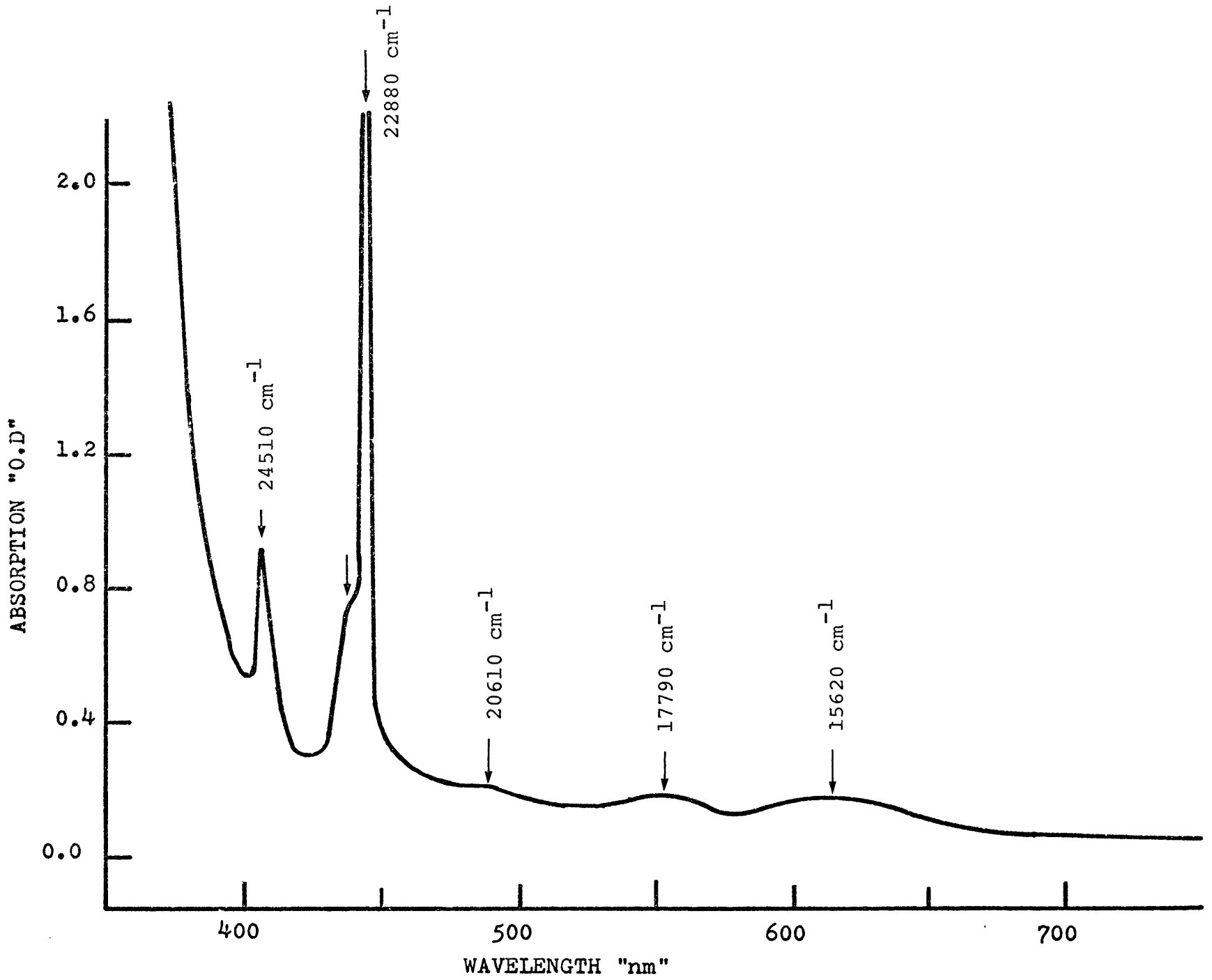
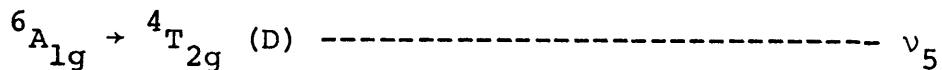


FIGURE IV-27

The absorption spectra of Fe^{3+} in andradite
garnet.





The energies of these transitions could be expressed in terms of B, C, and 10Dq; these energy values are given in many references, e.g. Figgis (1966); Tanabe and Sugano^o (1954a,b); and Lever (1968).

$$\nu_1 = -10Dq + 10B + 6C - 26B^2/10Dq \quad (5)$$

$$\nu_2 = -20Dq + 15B + 10C - 140B^2/10Dq \quad (6)$$

$$\nu_3 = -10Dq + 18B + 6C - 38B^2/10Dq \quad (7)$$

$$\nu_4 = 10B + 5C \quad (8)$$

$$\nu_5 = 13B + 5C \quad (9)$$

The spectrum shown in Figure IV-27 shows several bands at energies 15620, 17790, 20610, 22880, and 24510 cm^{-1} . The bands in the energy region 15620 - 20610 cm^{-1} are broad and weak, whereas the other bands at higher energies are sharp and relatively intense. The narrow widths and the relatively large intensities of the latter bands may be related to transitions that depend only on B and C parameters, and are independent of the crystal field parameter 10Dq; these are ν_4 and ν_5 transitions. On the other hand, the broad bands occurring at lower energies should be related to the remaining transitions ν_1 , ν_2 , and ν_3 .

The electronic transition ν_4 is related to two excited states, ${}^4A_{1g}(G)$ and ${}^4E_g(G)$; the energy values of these two states are the same when the octahedral site is regular. However, due to Jahn-Teller distortion, the two energy levels corresponding to the above states will have different energies; the

energy separation between the two levels is usually small, on the order of 200 cm^{-1} .

On the basis of the above discussion, the two sharp peaks at energies 22670 and 24510 cm^{-1} were assigned to ν_4 and ν_5 transitions, respectively. Considering the energies of these transitions (in terms of B, C, and $10Dq$) given in equations (8) and (9), B and C parameters were evaluated; these are 613 and 3308 cm^{-1} , respectively.

The absorption bands at energies 15620 , 17790 , and 20610 cm^{-1} are assigned to the transitions ν_1 , ν_2 , and ν_3 ; the energies of these transitions are given in equations (5), (6), and (7). Substituting for the values of ν_1 , ν_2 , and ν_3 , B and C in equations (5), (6), and (7), the energy value of $10Dq$ parameter, 9500 cm^{-1} , was estimated.

Moore and White (1972) obtained B, C, and $10Dq$ energy values for grossular garnet as 614 , 3332 , and 12600 cm^{-1} , respectively. The B and C values are consistent with those obtained above; however, the $10Dq$ parameter for grossular is significantly larger than andradite.

The inconsistency in $10Dq$ energy values for the two garnets is expected since the average M-O distances in the YO_6 octahedra are 2.024 and 1.924 \AA in andradite and grossularite, respectively (Novak and Gibbs, 1971), and $10Dq$ is proportional to r^{-5} , where r is the average M-O distance. Considering this relation, and using the $10Dq$ value of Moore and White (1972), the estimate of $10Dq$ in andradite can be given by:

$$12600 \times (1.924/2.024)^5 = 9780 \text{ cm}^{-1}.$$

This value for $10Dq$ is fairly consistent with the value obtained in this study.

Measurements of the high pressure spectra of andradite were attempted on crystal fragments (thicknesses $\sim 20\mu$) mounted in the diamond cell as was described early in Chapter III. High pressure spectral measurements on powdered specimens were also attempted. Unfortunately, there were many difficulties encountered in carrying out such measurements: these are:

1. The weak and broad bands assigned to transitions ν_1 , ν_2 , and ν_3 could not be observed due to the small thicknesses of the samples used in the high pressure cell.

2. The diamond absorption bands occurring at energies 24100, 24810, and 25380 overlap on the andradite bands occurring at energies 22880 and 24510 cm^{-1} .

3. With increasing pressure, the absorption edge of andradite shifts to lower energy, which then partially obscures the sharp bands.

The diamond absorption background was reduced by placing another diamond cell in the reference beam. Using this method, the band at 22880 cm^{-1} was distinguished. However, the first and the third difficulties could not be solved, and the remaining bands were unable to be identified.

As a result of these difficulties, only the sharp band at energy 22670 cm^{-1} was distinguished in the high pressure spectra of garnet.

With increasing pressure on the andradite single crystal up to about 50 kb., no significant energy shift was detected. Using a powdered specimen and increasing the pressure up to about 100 kb. a small low energy shift was observed for the sharp band at 22670 cm^{-1} ; the magnitude of this shift could not be evaluated due to the experimental difficulties mentioned earlier. Since this transition is independent of $10Dq$ and depends only on B and C, then the negligible energy shift of this band should limit the changes in B and C with pressure to being very small; alternatively, it may also be related to the incompressible nature of the andradite garnet. With increasing pressure up to 200 kb., the absorption edge of andradite shifted to lower energy and obscured the sharp bands.

In summary, the conclusions which can be drawn from the high pressure spectra of andradite is that the Racah parameters, B and C, do not change significantly with increasing pressure up to 200 kb. Above 150 kb., the absorption edge starts to shift significantly to lower energy and masks the spin-forbidden transitions in Fe^{3+} .

IV-4.3 Uvarovite

The end member of the garnet series, uvarovite $\{\text{Ca}_3\}[\text{Cr}_2^{3+}](\text{Si}_3)\text{O}_{12}$, was synthesized by Huggins (1974) from a mixture of CaO , SiO_2 (silicate glass) and $(\text{NH}_4)_2\text{Cr}_2\text{O}_7$ held for 5 days at 1 kb. and 675°C .

The spectra of the powdered specimen mixed with NaCl (as internal standard for pressure calibration) were measured at 1

atm. 95 and 177 kb., and are shown in Figure IV-28.

The two bands in the 1 atm. spectrum at energies 15667 cm^{-1} (ν_1) and 22727 cm^{-1} (ν_2) are assigned to electronic transitions from the ground state, ${}^4A_{2g}(F)$, to the higher energy states, ${}^4T_{2g}(F)$ and ${}^4T_{1g}(F)$, respectively. The energies of ν_1 and ν_2 are given as:

$$\begin{aligned}\nu_1 &= 10Dq \\ \nu_2 &= 15Dq + 7.5B - 6B(1+\mu)^{1/2}\end{aligned}$$

where $\mu = [(10Dq-9B)/12B]^2$

The above equations were derived from Tanabe and Sugano (1954a) secular determinants, and were used by Parson and Drickamer (1958), Reiner (1969), and Poole (1964) to calculate the values of B and 10Dq for Cr^{3+} complexes.

From the first transition, ν_1 , 10Dq can be obtained directly from the energy of the band maximum, and B can be determined from the two transitions, ν_1 and ν_2 , by means of the relationship:

$$B = 1/3[(2\nu_1 - \nu_2)(\nu_2 - \nu_1)/9\nu_1 - 5\nu_2] \quad (10)$$

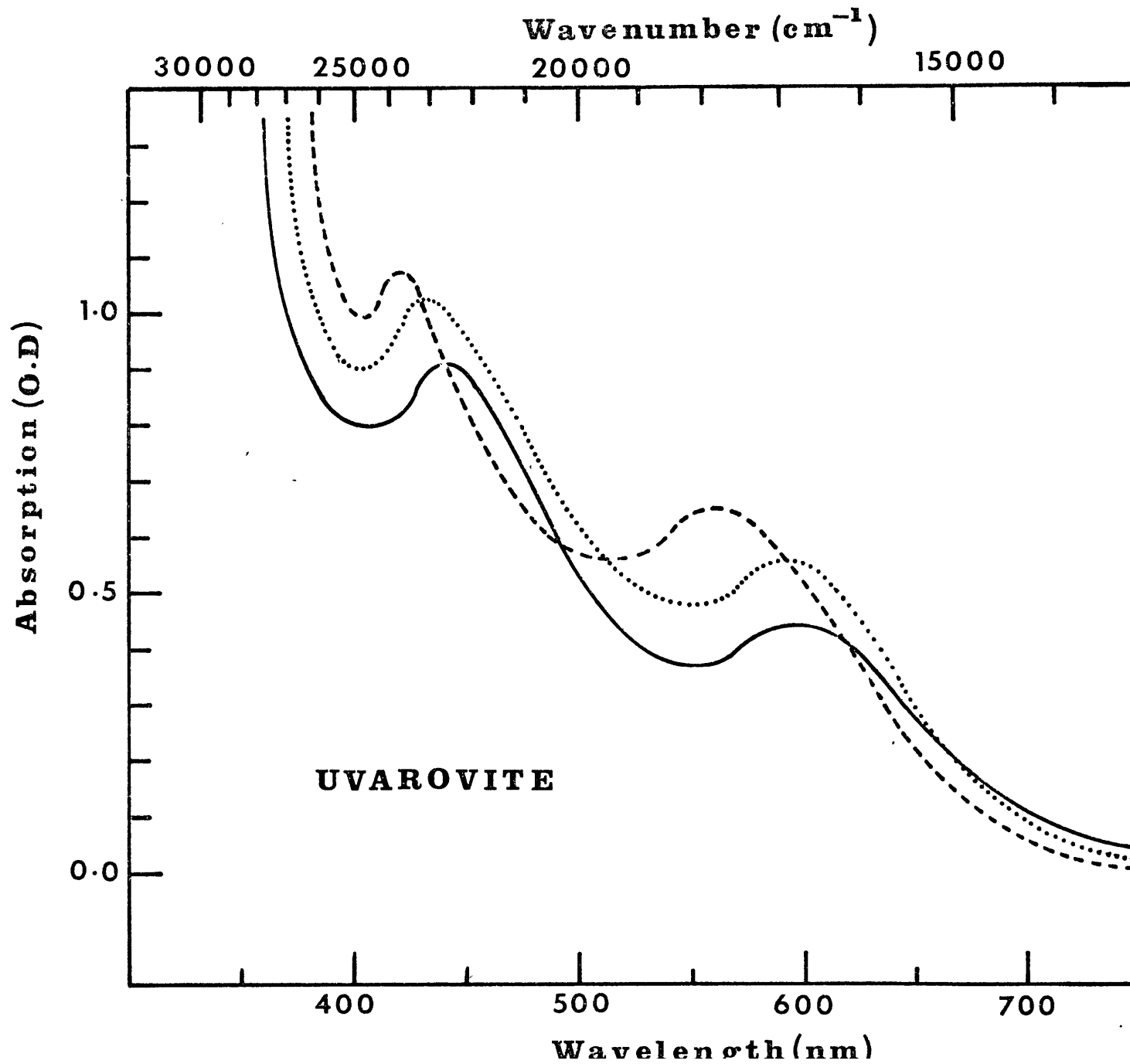
The following values of B have been calculated at three different pressures for Cr^{3+} in uvarovite:

<u>Pressure</u>	<u>B (cm⁻¹)</u>	<u>ν_1 (cm⁻¹)</u>	<u>ν_2 (cm⁻¹)</u>
1 atm.	589	16,667	22,727
95 kb.	582	17,007	23,041
177 kb.	577	17,668	23,697

It is evident, from the above results, that there is a consistent decrease in the value of B with increasing pressure

FIGURE IV-28

The absorption spectra of synthetic uvarovite measured at 1 atm. (—); 95 kb. (.....); and 177 kb. (-----).



(about $0.067 \text{ cm}^{-1}/\text{kb.}$). Further, considering the negligible shift of Fe^{2+} spin-forbidden transitions, which are dependent mostly on B, and the undetectable change with pressure in the energies of Fe^{3+} transitions in andradite, which are dependent on B and C, these results may lead us to believe that up to 200 kb. the ionic model in silicate minerals still holds, and only a very slight increase in the degree of covalency of the metal-ligand bond is expected. For uvarovite and other mineral phases containing Fe^{2+} , there is also a consistent increase in $10Dq$, which is related to shortening of the metal-ligand distances and hence decreasing the volume of the polyhedron.

IV-5. Epidotes

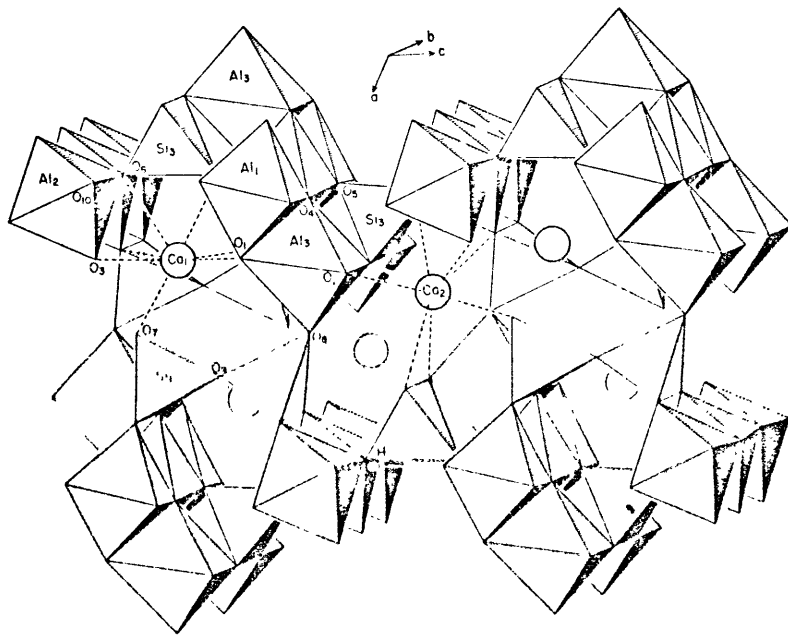
The basic chemical formula of the epidote group is given as $\text{Ca}_2\text{M}_3\text{Si}_3\text{O}_{12}\text{OH}$, where M refers to the trivalent octahedral cations such as Mn^{3+} , Al^{3+} , and Fe^{3+} .

The structure of epidote was described by Ito et al. (1954) and Dollase (1968, 1969). It consists of octahedral chains extending along the b-axis and joined to one another by means of single (SiO_4) and double (Si_2O_7) tetrahedral groups (Figure IV-29). There are three crystallographically distinct octahedral positions which are designated here by M(1), M(2), and M(3); these sites are frequently filled by trivalent or divalent cations such as Al^{3+} , Fe^{3+} , Mn^{3+} , and Fe^{2+} . The M(1) and M(2) sites are fairly regular octahedra, whereas the M(3) site is very distorted.

The site occupancies and ordering of the transition metal

FIGURE IV-29

The structure of epidote viewed along the
b-axis (Dollase, W.A., 1968).



ions in the epidote structure have been discussed in the mineralogical literature (Burns and Strens, 1967; Bancroft et al., 1967, 1974; Dollase, 1969). Although there are minor controversies on the site occupancies of Fe^{3+} and Mn^{3+} in the M(1) and M(2) sites, it is generally accepted that Fe^{3+} and Mn^{3+} cations occupy preferentially the distorted M(3) site.

In the present study, two members of the epidote group used by Burns and Strens (1967) were investigated: first, an epidote which contains 0.864 Fe^{3+} per formula unit, called here Fe^{3+} -epidote, and second, an epidote which contains 0.625 Mn^{3+} , and referred to as Mn^{3+} -epidote or piemontite. The spectra and the crystal chemistry of the two epidotes used in this study are discussed in some detail in the following discussion.

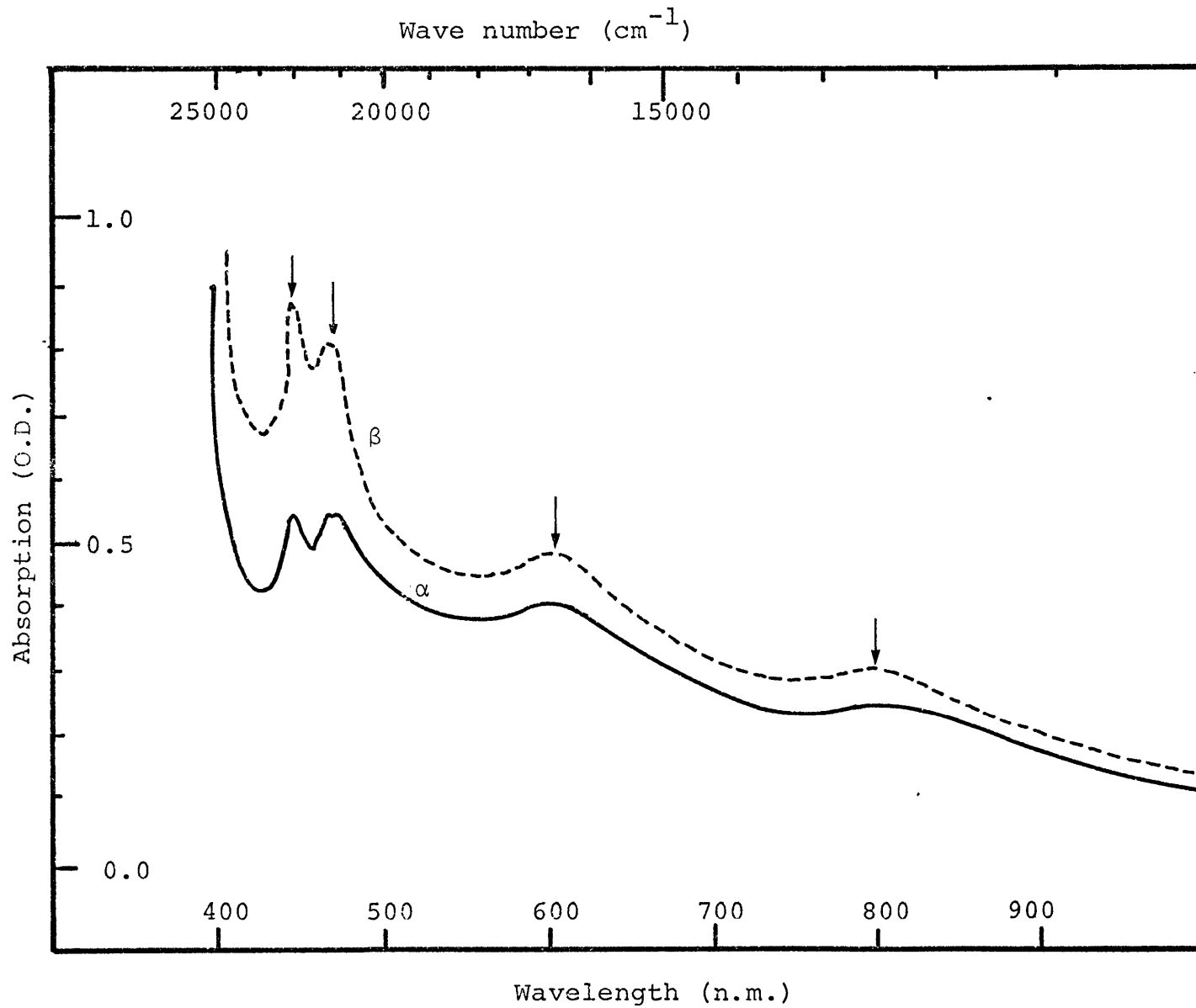
IV-5.1 Fe^{3+} -Epidotes

The polarized absorption spectra of Fe^{3+} -epidote were measured at two different pressures, 1 atm. and 20 kb.. Measurements of the spectra were made on a single crystal which was oriented in the liquid-pressure cell, such that the b and c axes are contained in a plane perpendicular to the pressure axis.

Figure IV-30 shows the α and β spectra of epidote measured at 1 atm.. In the infrared region there is one broad band at 12500 cm^{-1} , which is assigned to the spin-forbidden transition (${}^6\text{A}_{1g} \rightarrow {}^4\text{T}_{1g}$) in octahedrally coordinated Fe^{3+} . The large width of the band could be related to the distortion of the M(3) site. In the visible region, there are two broad bands at 16530 and

FIGURE IV-30

The α -(——) and β -(-----) spectra of Fe^{3+} -
epidote measured at 1 atm.



18350 cm^{-1} , and two sharp, and relatively intense, bands at 21190 and 21980 cm^{-1} .

Earlier in this chapter, it was pointed out that Fe^{3+} cations in a regular octahedral site produce three main spin-forbidden transitions between the ground state, ${}^6\text{A}_{1g}$, and the higher energy excited states, ${}^4\text{T}_{1g}$, ${}^4\text{T}_{2g}$, and (${}^4\text{A}_{1g}$, ${}^4\text{E}_g$). In a distorted octahedral site, the energy levels which correspond to each excited state may become non-degenerate and split into more than one level. As a consequence of this, two or more spectral bands observed in the spectra may be related to each spin-forbidden transition in a regular site.

In the spectra of epidote, the two bands at energies 16530 and 18350 cm^{-1} are assigned to the spin-forbidden transition, ${}^6\text{A}_{1g} \rightarrow {}^4\text{T}_{2g}$, and the two sharp peaks at 21190 and 21980 cm^{-1} are related to the transition, ${}^6\text{A}_{1g} \rightarrow {}^4\text{A}_{1g}$ and ${}^6\text{A}_{1g} \rightarrow {}^4\text{E}_g$, respectively. On the basis of Orgel's (1955) energy level diagram for the Fe^{3+} ion in octahedral coordination, Burns and Strens (1967) made similar assignments of epidote spectral bands. In addition, Burns and Strens (1967) calculated the crystal field splitting parameter, $10Dq$, of Fe^{3+} in epidote to be equivalent to $12750 \pm 100 \text{ cm}^{-1}$.

The above assignments of the epidote spectra and the energy value of $10Dq$ were examined in this study using the energy values of Fe^{3+} spin-forbidden transitions given in equations (5), (7), and (8), and the high pressure spectral technique.

In regular octahedron, the energy of the transition, ${}^6\text{A}_{1g} \rightarrow$

${}^4A_{1g}$, 4E_g is equivalent to $10B + 5C$. Since the two sharp peaks at energies 21190 and 21980 cm^{-1} were assigned to the transitions, ${}^4A_{1g}$ and 4E_g , their average energy, 21585 cm^{-1} , is considered here as equivalent to $10B + 5C$.

Assuming a B value of 612* cm^{-1} for Fe^{3+} in the octahedral site, and using equation (8), the energy value of C is estimated to be 3093 cm^{-1} . Taking the energy value 17440 (the average energy of the two bands at 16530 and 18350 cm^{-1}) as equivalent to the energy of the spin-forbidden transition, ${}^6A_{1g} \rightarrow {}^4T_{2g}$, in a regular octahedron, and using equation (8), the estimated $10Dq$ value is found to be $11200 \pm 100 \text{ cm}^{-1}$. Using this energy of $10Dq$, $11200 \pm 100 \text{ cm}^{-1}$, and the energy values of B and C as determined above, the energy of spin-forbidden transition, ${}^6A_{1g} \rightarrow {}^4T_{1g}$, was estimated to be 12610 cm^{-1} . This value conforms with the assignment of the broad band at energy 12500 cm^{-1} to the spin-forbidden transition, ${}^6A_{1g} \rightarrow {}^4T_{1g}$.

On the other hand, using the energy value 12750 cm^{-1} as equivalent to $10Dq$, and changing the values of B and C in a way that equation (8) holds always, and the employing of equations (5) and (7), to obtain the energies of the spin-forbidden transitions ${}^4T_{1g}$ and ${}^4T_{2g}$, it was not possible to obtain energy values for the transitions which are consistent with the observed energies of the epidote spectral bands. On the basis of the above argument, the $10Dq$ value, $11200 \pm 100 \text{ cm}^{-1}$, is preferable

* Similar to the value obtained for Fe^{3+} in garnets.

to the value estimated by Burns and Strens (1967).

The high pressure optical spectral method was employed to examine further the above assignments and to study the influence of pressure on Fe^{3+} absorption bands in epidote. With increasing pressure up to about 20 kb., no significant change has been observed in the spectra except for a small low energy shift of the sharp energy bands at 21190 and 21980 cm^{-1} .

The other broad bands may have been shifted to lower energies, but the magnitude of the energy shift is very small and hard to determine due to the large widths of the two bands. Nevertheless, although the shifts of the sharp peaks was also very small, they were estimated to be about -100 and -60 cm^{-1} for the two bands at 21190 and 21980 cm^{-1} , respectively.

Considering the average value of this shift, -80 cm^{-1} , and using equation (8), with the assumption that $C \approx 5B$, the energy change in B was estimated to be -2 cm^{-1} in 20 kb.. The absorption edge was also observed to shift to lower energy as the pressure increased to 20 kb.. These results are similar to those obtained for andradite garnet.

IV-5.2 Mn^{3+} -epidote (Piemontite)

Piemontite is a manganiferrous epidote which contains significant amounts of Mn^{3+} cations in the very distorted octahedral M(3) site. The site symmetry of Mn^{3+} and the M-O distances are shown in Figure IV-31a . Due to the site distortion, the spin-allowed transition, ${}^5E_g \rightarrow {}^5T_{2g}$, in Mn^{3+} is split into three

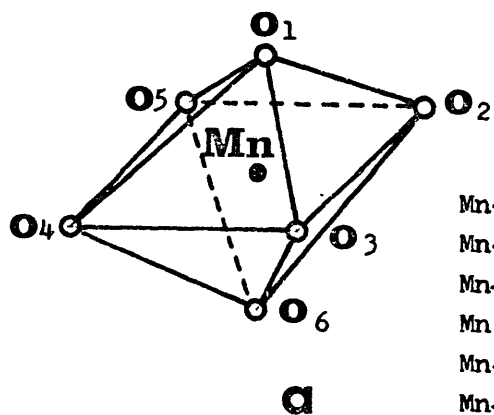
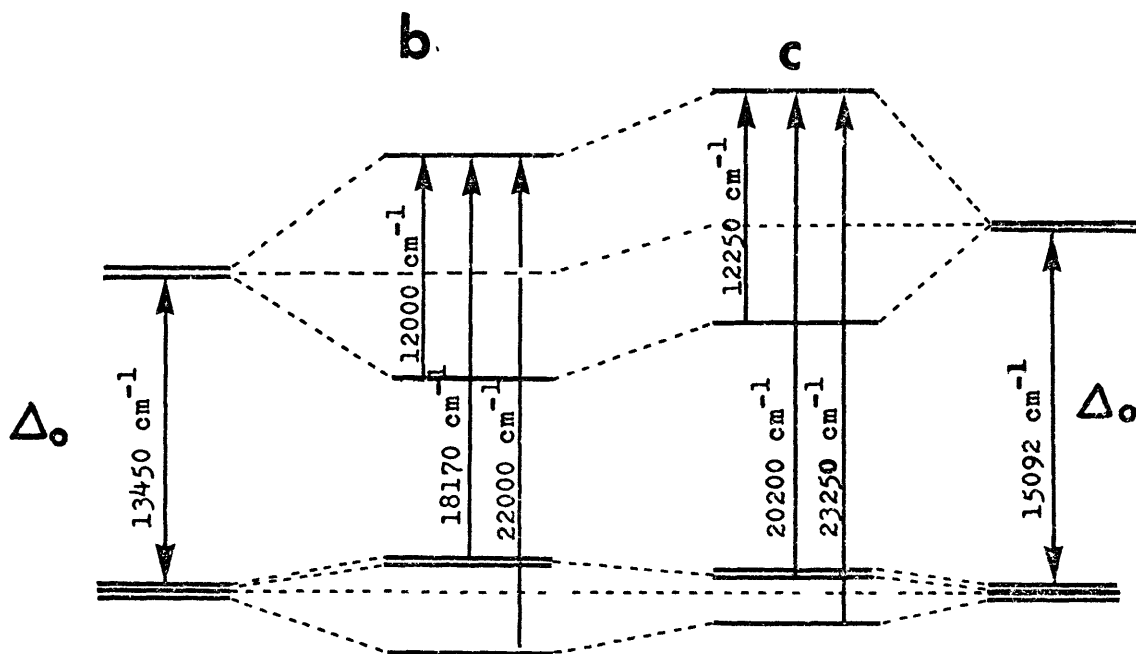
FIGURE IV-31

- (a) The very distorted octahedral site of Mn^{3+} in piemontite and the M-O distances.
- (b) The energy level diagram of Mn^{3+} ion constructed at 1 atm.
- (c) Energy level diagram of Mn^{3+} constructed from the spectra measured at 200 kb.

PIEMONTITE

1 atm.

197 kb.



**Mn³⁺ in distorted
octahedral site**

- Mn-O₁ = 1.89
- Mn-O₂ = 2.02
- Mn-O₃ = 2.02
- Mn-O₄ = 2.18
- Mn-O₅ = 2.18
- Mn-O₆ = 2.03

transitions as a consequence of removing the degeneracies of the lower t_{2g} levels and the higher energy e_g levels (Figure IV-31b).

The polarized 1 atm. spectra of piemontite, containing 0.625 Mn^{3+} , were reported by Burns and Strens (1967) and Burns (1970). The optical absorption bands for piemontite were assigned to electronic transitions in Mn^{3+} d-levels, as illustrated in the energy level diagrams (Figure IV-31b).

The spectra of piemontite contain one broad band at 12000 cm^{-1} and other intense and sharp bands at energies 18170 and 22000 cm^{-1} . The assignments of those bands are illustrated in the energy level diagram shown in Figure IV-31b.

from this diagram the crystal field splitting parameter, $10Dq$, is estimated to be 13450 cm^{-1} .

With increasing pressure, the band at 18170 cm^{-1} shifted to higher energy and there was an increase in its width and intensity. The band at 22000 cm^{-1} also shifted to higher energy but at a slower rate, while the band at 12000 cm^{-1} showed a very slow blue shift (Figure IV-32). The magnitudes of energy shifts of the two bands at energies 18170 and 22000 cm^{-1} are shown in Figure

IV-33. The energy values of each band were obtained at different pressures; from these values, energy level diagrams of Mn^{3+} d-orbitals were constructed, from which the crystal field parameters CFS and CFSE were evaluated at each pressure.

From the energy level diagrams shown in Figure IV-34, it is obvious that the crystal field splitting parameter in-

FIGURE IV- 32

The absorption spectra of Mn^{3+} in a powdered Mn^{3+} sample of piemontite at 1 atm. (.....) and 197 kb. (———).

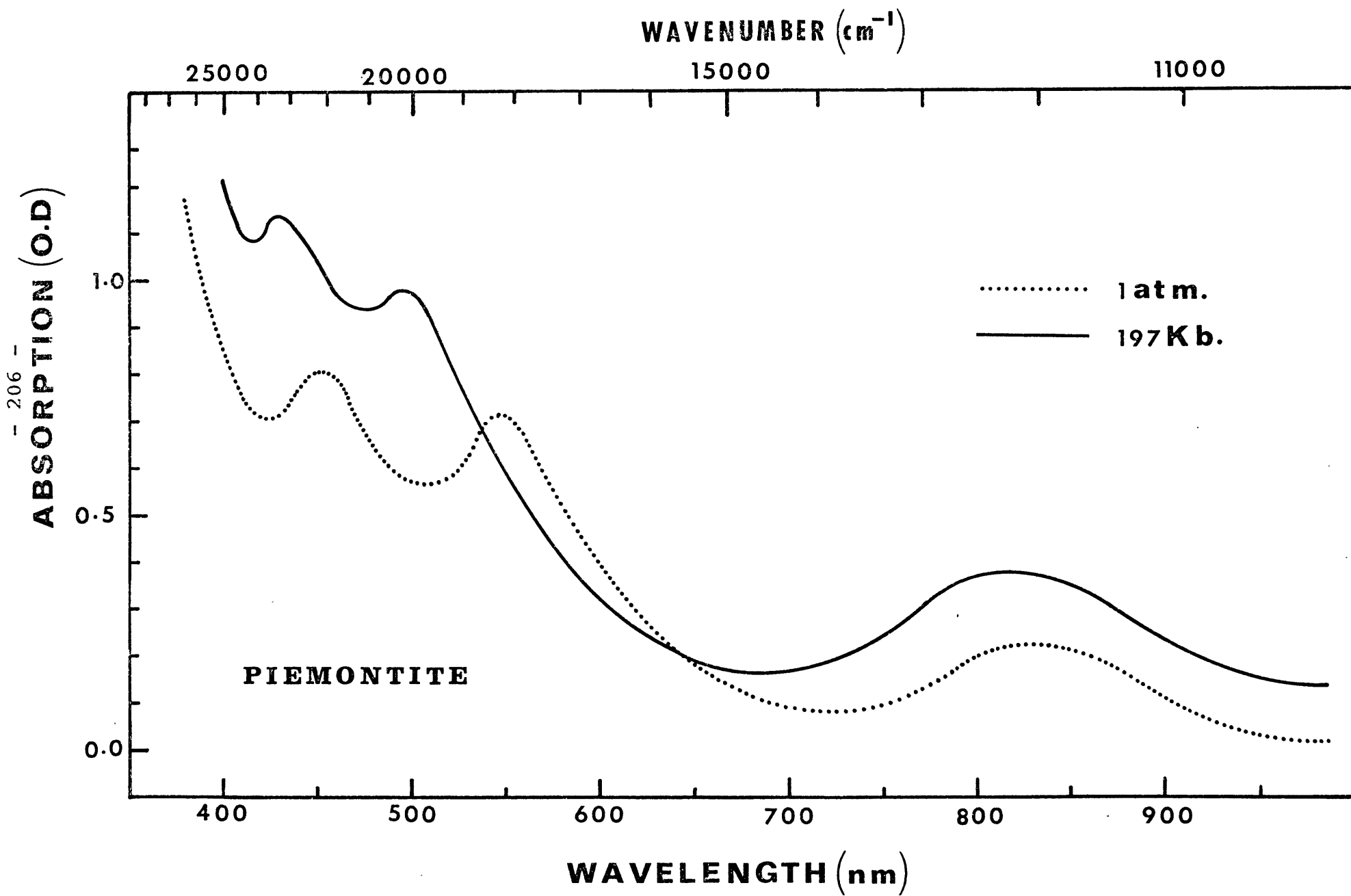


FIGURE IV-33

The pressure-induced energy shift of Mn^{3+}
absorption bands in piemontite:

———— energy shift of the band at
18170 cm^{-1}

----- energy shift of the band at
22000 cm^{-1} .

$\Delta\nu$ is the difference in band energy at
pressure P and at 1 atm..

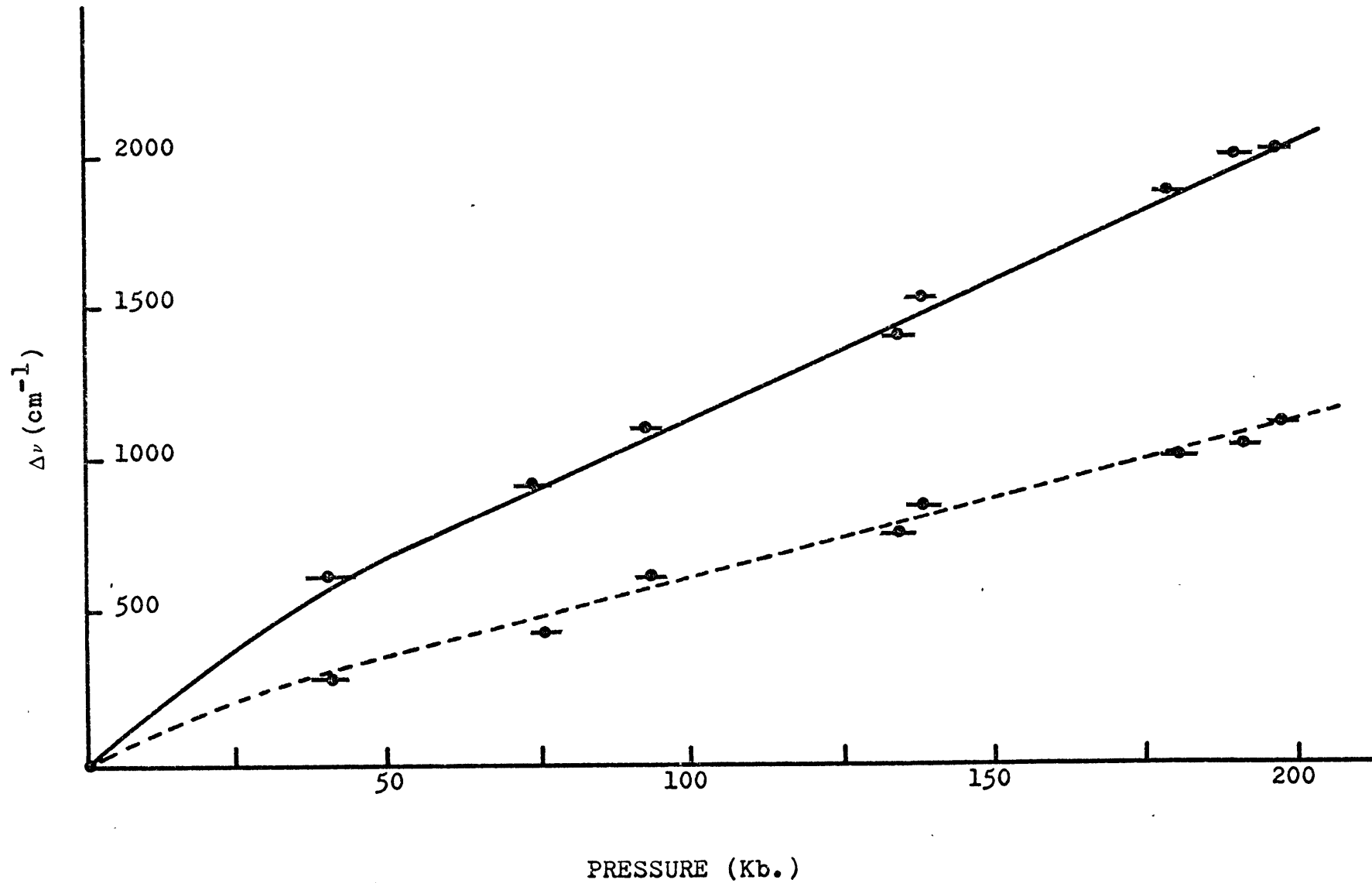
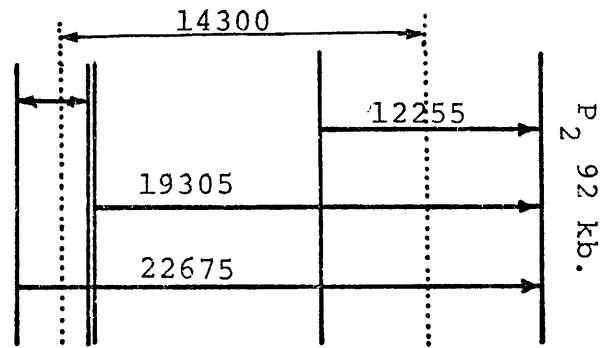
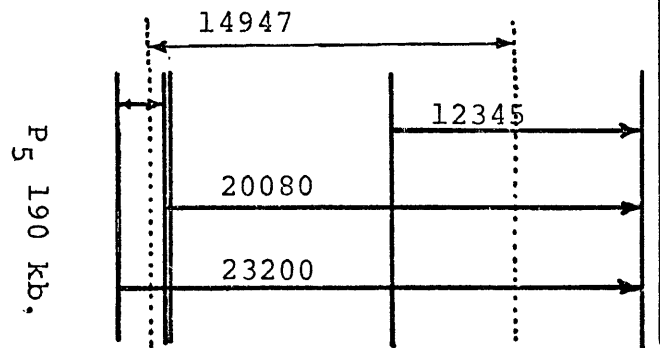
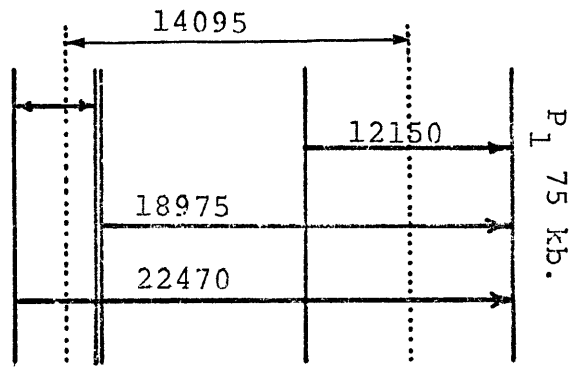
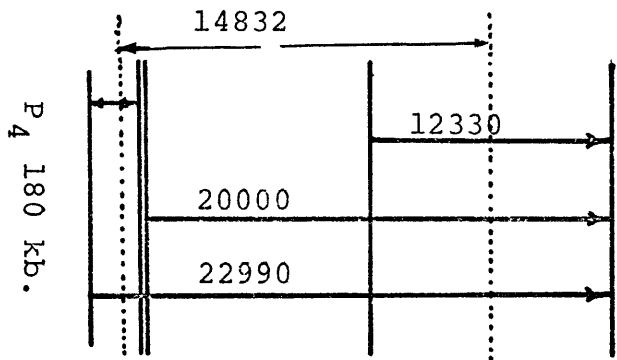
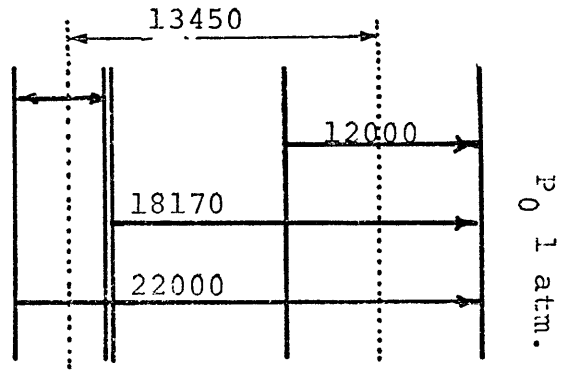
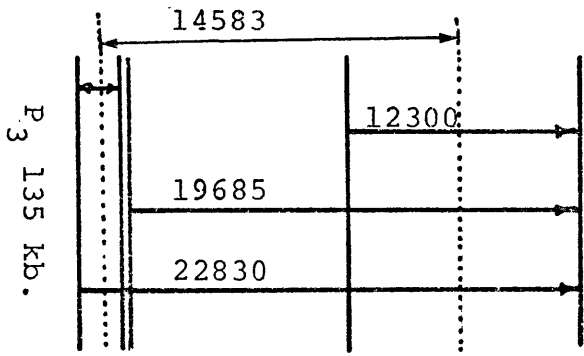


FIGURE IV-34

Energy level diagrams of Mn^{3+} d-orbitals constructed at 1 atm., 75 kb., 92 kb., 135 kb., 180 kb., and 190 kb.. From these diagrams the CFS and CFSE energy values were obtained at each pressure.



creases consistently with pressure; the estimated maximum change obtained for Δ_o is about 1642 cm^{-1} in 197 kb.. The rate of energy change in Δ_o or 10Dq parameter with pressure (Fig.IV-35) conforms with its dependence on the interatomic (ligand-metal) distances and the compressible nature of piemontite. The energy values of 10Dq were estimated at various pressures and then related to the volume of the polyhedron containing Mn^{3+} . Thus, the compressibility of the Mn^{3+} site was estimated at three different pressures and then correlated with the compressibility of the bulk mineral. The bulk moduli and compressibilities of transition metal ion sites is discussed further in Chapter VII.

One notable feature of Figure IV-35 is at low pressures there is a rapid increase in 10Dq indicating significant shortening in M-O distances and then appreciable changes in the volumes of the polyhedra containing Mn^{3+} cations. However, at moderate pressure, the rate of 10Dq energy change decreases and then at high pressure the change became very small.

It should be mentioned that the Mn^{3+} bands at 22000 and 18170 cm^{-1} are intense and sharp even for powdered and NaCl-diluted specimens. Furthermore, the pressure-induced energy shifts of the band at 18170 cm^{-1} is large and may be used to calibrate the pressure in the diamond cell.

The increase in the energy value of CFSE with pressure (Fig.IV-35) is also an indication of the stability of Mn^{3+} ions in piemontite. In fact, the large CFSE value is related to the large energy separation (δ) between the upper levels e_g . Although the en-

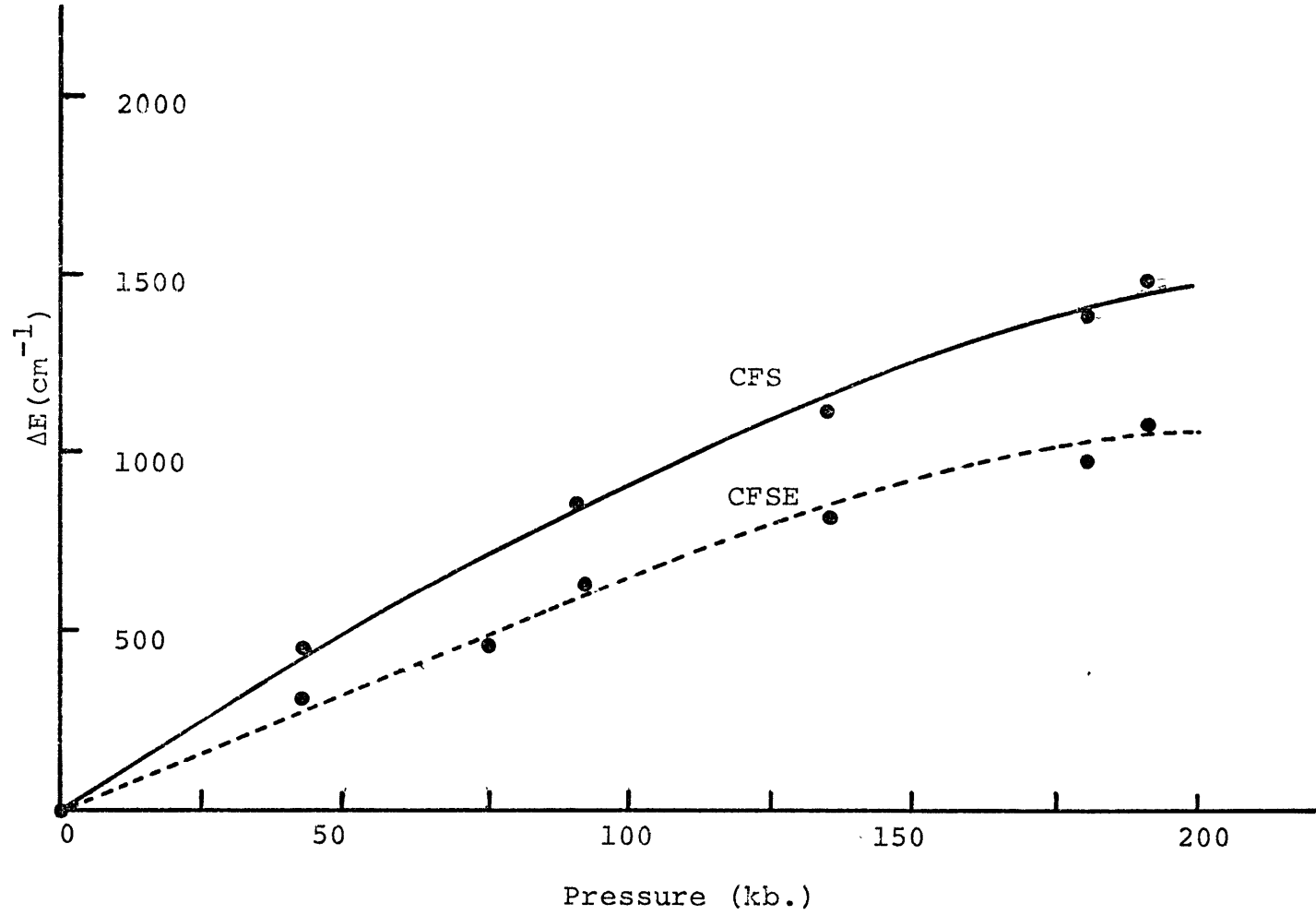
FIGURE IV-35

The rates of pressure-induced energy changes in
CFS and CFSE parameters:

————— CFS

----- CFSE

$$\Delta E(\text{cm}^{-1}) = [\text{CFS}_P - \text{CFS}_{P_0}] \text{ or } [\text{CFSE}_P - \text{CFSE}_{P_0}]$$



ergy separation between the lower levels t_{2g} (Δ_1) decreases significantly with pressure, δ , however, increases slightly.

Thus, it appears that the splitting energy between the upper levels, $d_{x^2-y^2}$ and d_{z^2} , is necessary to stabilize Mn^{3+} .

IV-6. Miscellaneous Minerals

In the previous sections, the high pressure spectral data have been presented for silicate minerals containing transition metal ions in octahedral and cubic symmetries. Since it is the purpose of this study to investigate the high pressure spectra of minerals containing transition metal ions of different d-electronic configuration and of various polyhedral symmetries, a suite of minerals were selected which contained Fe^{2+} , Fe^{3+} , Co^{2+} , and Cu^{2+} ions in tetrahedral square-planar and octahedral site symmetries. These minerals are listed below:

<u>Mineral Name</u>	<u>T.M. Ions</u>	<u>Site Symmetries</u>
Staurolite	Fe^{2+}	Tetrahedral
Lusakite	Co^{2+}	Tetrahedral
Melilite	Fe^{2+}	Tetrahedral
Dioptase	Cu^{2+}	V. dist. Oct. or Sq. plane
Gillespite	Fe^{2+}	Square planar
Glaucophane	Fe^{2+} , Fe^{3+}	Octahedral

IV-6.1 Staurolite

The crystal structure of staurolite was described by Hanisch (1966) and Smith (1968). The ideal chemical formula may

FIGURE IV-36

Pictorial view of the Fe^{2+} tetrahedral site in staurolite (Table IV-10 is also on the next page).

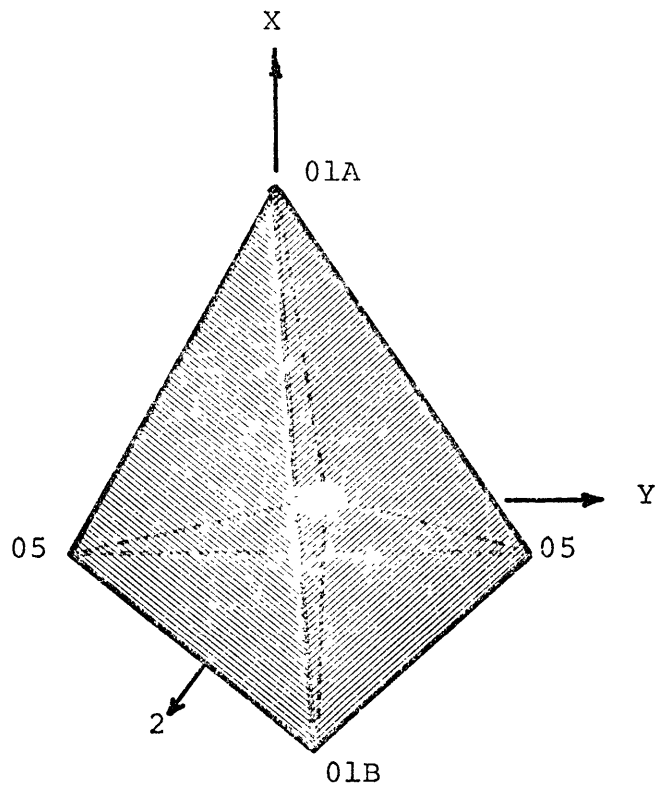


FIGURE IV-36

TABLE IV-10

Atom Pair	Distance (Å)
Fe-O (1A)	2.046
Fe-O (1B)	2.043
Fe-O (5)	1.972
Mean	2.02
O(1A) - O(1B)	3.230
2O(1B) - O(5)	3.268
2O(1B) - O(5)	3.325
O(5) - O(5)	3.325
Mean	3.257

M-O and O-O interatomic distances in staurolite (From Smith, 1968).

be given by: $[Al]_{\sim 18}(Fe)_{\leq 4}(Si)_8O_{48}H_{\sim 4}$. In the structure, there are seven octahedral sites principally occupied by Al and two tetrahedral sites; one is occupied mostly by Fe and the other by Si. The major concern in studying staurolite structure is the site symmetry of Fe^{2+} ion.

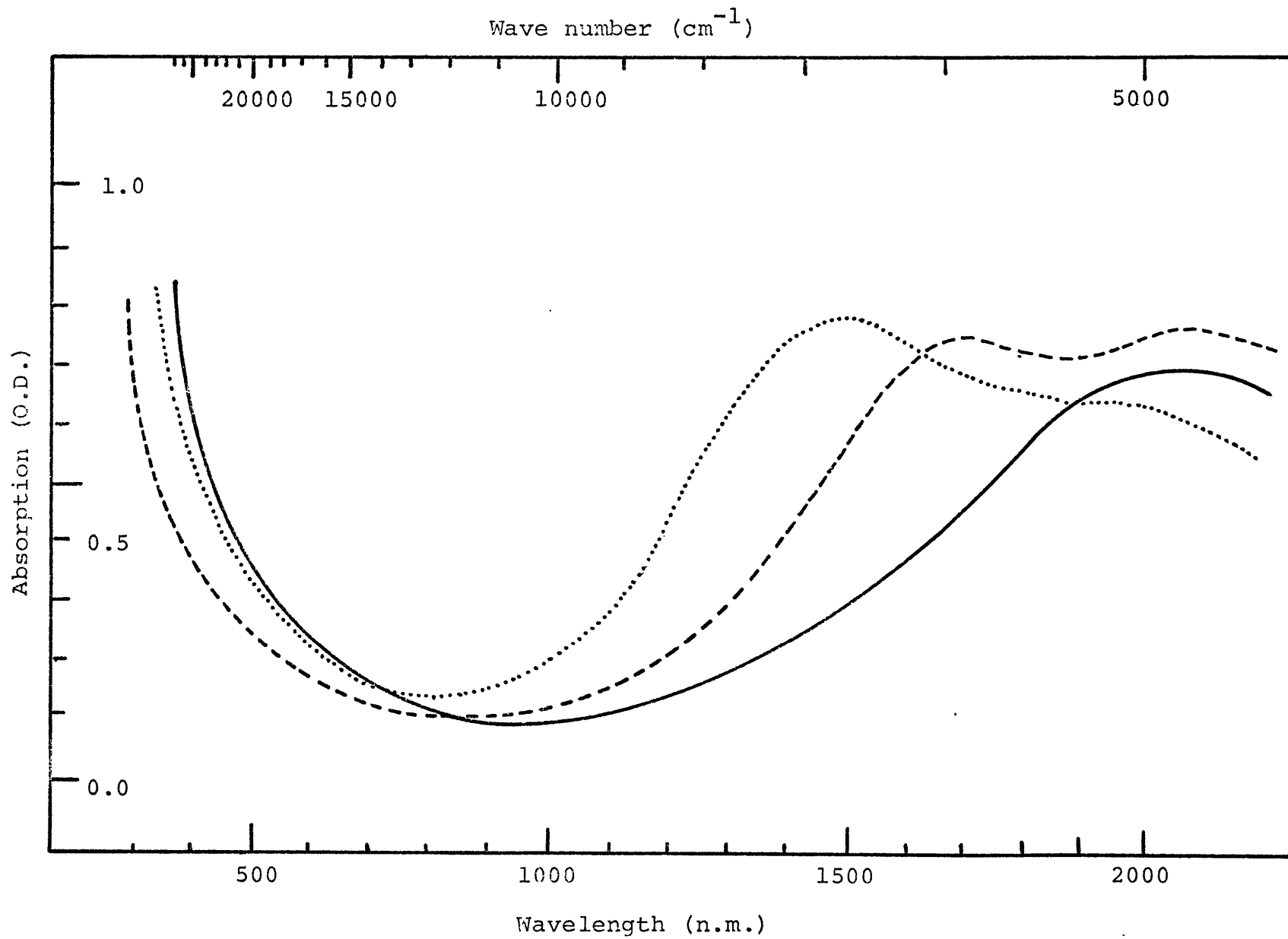
Ferrous ions occur in a 4-fold coordination polyhedron which is slightly distorted; the geometry of the tetrahedral site and the M-O and O-O distances are shown in Figure IV-36.

The staurolite sample used in this study contains 1.42 Fe^{2+} ions per formula units. The polarized spectra of staurolite (Figure IV-37), which consists of a broad absorption band spanning the energy region $7000-4550\text{ cm}^{-1}$ was measured by Burns (1970a). The site symmetry of staurolite could be approximated to D_2 symmetry. Hence, two or three absorption bands are expected to be observed in the spectra of Fe^{2+} in this symmetry. In fact, the broad absorption in the i.r. region can be fitted to two or three bands.

Using a powdered staurolite sample, the spectra were measured at different pressures. Due to the large width of the absorption band in the infrared region, it was not possible to locate the position of maximum absorption and then to go further for quantitative studies of band energy shift versus pressure. However, the broad band was observed to shift slowly to higher energy with increasing pressure and the absorption edge shifted to lower energy. These results indicate that the broad absorption is related indeed to crystal field transitions in Fe^{2+}

FIGURE IV-37

The polarized absorption spectra of staurolite measured at 1 atm. [----- α spectrum; β spectrum; ——— γ spectrum].



contained in the tetrahedral site.

IV-6.2 Lusakite

Lusakite is a cobaltian staurolite which contains a significant amount of Co^{2+} in the tetrahedral site. The sample used in this study was provided by Professor Roger Burns (locality: Lusaka, Zambia); it contains 1.82 Co^{2+} ions per formula unit in addition to trace amounts of Fe^{2+} .

The spectra of lusakite, at 1 atm., was reported by Burns (1970 a). It contains three main absorption features in the infra-red region located at energies 6170, 7120, and 8000 cm^{-1} ; in the visible region there are also three sharp peaks at energies 15500, 17090, and 18440 cm^{-1} .

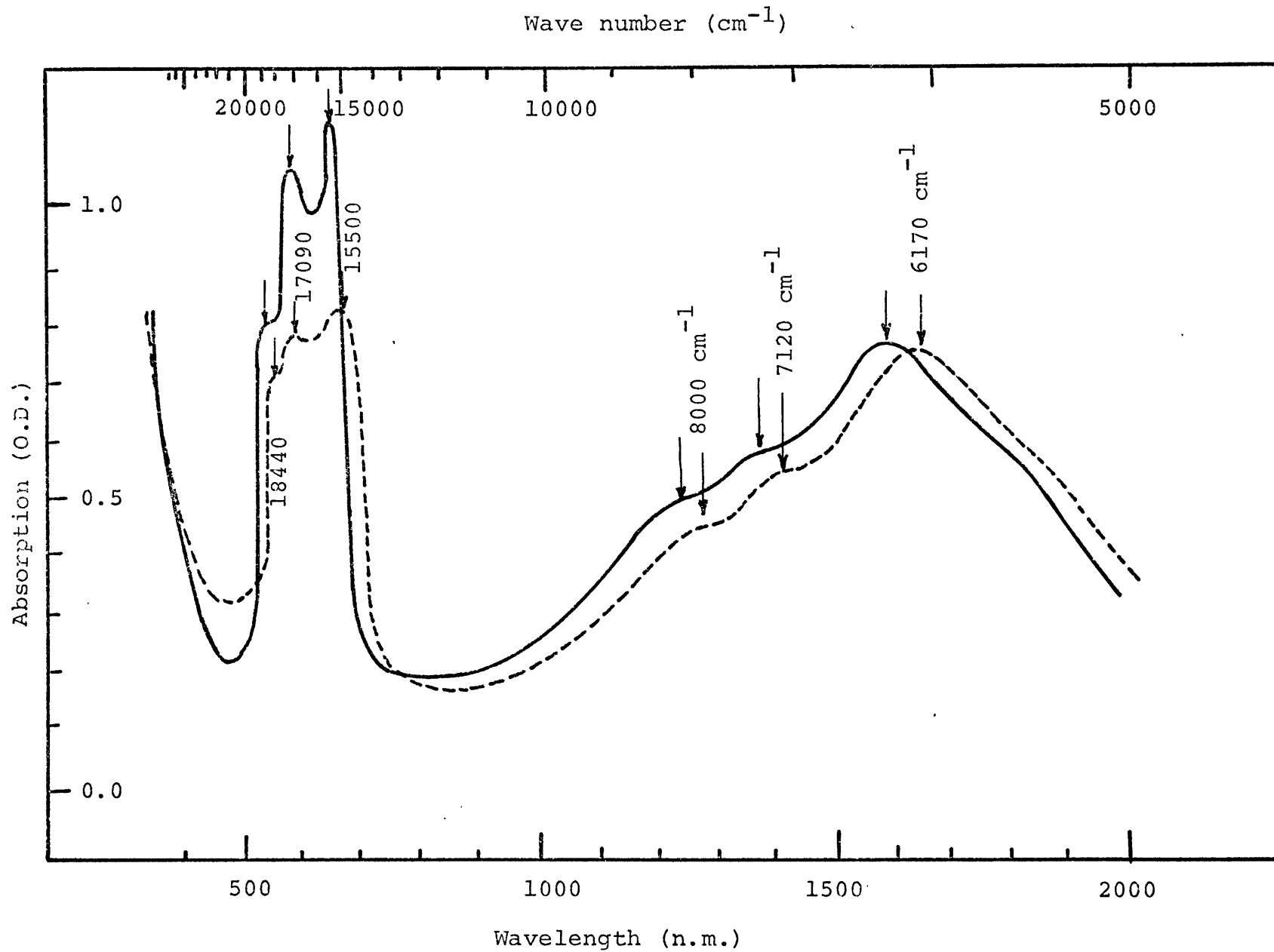
The Co^{2+} tetrahedral site symmetry and M-O distances are expected to be similar to that of Fe^{2+} in staurolite. However, the M-O distances for Co^{2+} are expected to be shorter than those of Fe^{2+} , due to the slightly smaller ionic radius of the former. In addition, the energies of Co^{2+} electronic transitions are different from Fe^{2+} . For these reasons, the absorption bands for Co^{2+} occur at different energies from those of Fe^{2+} .

Co^{2+} ions in a regular tetrahedral site have three spin-allowed transitions which take place from the ground state, ${}^4\text{A}_2$ (F), to the excited states, ${}^4\text{T}_2$ (F), ${}^4\text{T}_1$ (F), and ${}^4\text{T}_1$ (P). The energies of the above transitions were calculated by Tanabe and Sugano (1954a,b) and were used by many authors, e.g. Zahner and Drickamer (1961); Stephens and Drickamer (1961); and Lever (1968). These energies are given below in terms of the param-

FIGURE IV-38

The spectra of lusakite single crystal measured
at 1 atm. and 30 kb.

- - - (1 atm.); ————— (30 kb.)



eters B, C, and Dq:

$$\nu_1 \equiv {}^4A_2(F) \rightarrow {}^4T_2(F) = 10Dq \quad (10)$$

$$\nu_2 \equiv {}^4A_2(F) \rightarrow {}^4T_1(F) = 15Dq + 7.5B - \frac{1}{2}(225B^2 + 100Dq^2 - 180Dq R)^{1/2} \quad (11)$$

$$\nu_3 \equiv {}^4A_2(F) \rightarrow {}^4T_1(P) = 15Dq + 7.5B + \frac{1}{2}(225B^2 + 100Dq^2 - 180Dq R)^{1/2} \quad (12)$$

The excited states mentioned above are triply degenerate when Co^{2+} occupies a regular tetrahedral site. However, in a distorted tetrahedron, each state will split into three, giving rise to three absorption features.

The spectrum of lusakite in Figure IV-38 shows two triple-peaked absorption bands designated here as ν_2 and ν_3 ; these are assigned to the spin-allowed transitions in Co^{2+} in the distorted tetrahedral site. Another triple-peak at lower energy was expected, which should be related to the ν_1 transition. Indeed, a broad absorption is observed in the energy region $<5000 \text{ cm}^{-1}$, but the location of the band maxima were unable to be determined. On this basis, transition ν_1 should occur at energy $<5000 \text{ cm}^{-1}$. The energy of this transition, ν_1 , as given in equation (10), is equivalent to $10Dq$. $10Dq$ value for Fe^{2+} in staurolite could not be estimated accurately due to the large widths of absorption bands; however, it would be safe to assume that its energy value is $\sim 4500 \text{ cm}^{-1}$.

The B energy value of tetrahedrally coordinated Co^{2+} ions in $ZnAl_2O_4:Co^{2+}$ was estimated by König (1971) to be about 750 cm^{-1} . Taking these energy values of B and $10Dq$, and substitut-

ing in equation (10), (11), and (12), yielded energy values of 4500, 7737, and 17013 cm^{-1} for ν_1 , ν_2 , and ν_3 transitions, respectively. Comparison of these energies with the average energies of the triple-peak bands observed in the spectra provides good evidence that the above assignments of absorption bands are correct.

The high pressure polarized spectra of lusakite single crystals mounted in the diamond cell were measured at 1 atm., 5 kb., 20 kb., and 30 kb. (Figure IV-38). The spectral bands were observed to shift to higher energies with increasing pressure. The energy values of the spectral bands at four different pressures are given in Table IV-9. At elevated pressures, the three bands in the i.r. region shifted to higher energies; however, the band at 6170 cm^{-1} shifted more rapidly than the other two bands at 7120 and 8000 cm^{-1} . The energy values of the spectral bands at four different pressures are given in Table IV-9.

The energy level diagram shown in Figure IV-39 were constructed to explain the mechanism of electronic transitions at different pressures. From these diagrams, it is apparent that the splitting energies between the high energy, t_2 , orbital set decreases with increasing pressure. This is an indication of a decrease in the degree of distortion of the tetrahedral site.

The other set of spectral bands in the visible region show-

TABLE IV-9
Co²⁺ crystal field band energies at 1 atm,
5 kb., 20 kb., and 30 kb.

FIGURE IV-39
Energy level diagrams of Co²⁺ in lusakite at
1 atm, 20 kb., and 120 kb.

TABLE IV-9

	1 atm.	5 kb.	20 kb.	30 kb.
v_2	6173	6192	6289	6329
	7120	7142	7236	7266
	7975	8000	8100	8130
v_3	15463	15500	15575	15625
	17064	17094	17137	17167
	18518	18536	18580	18610

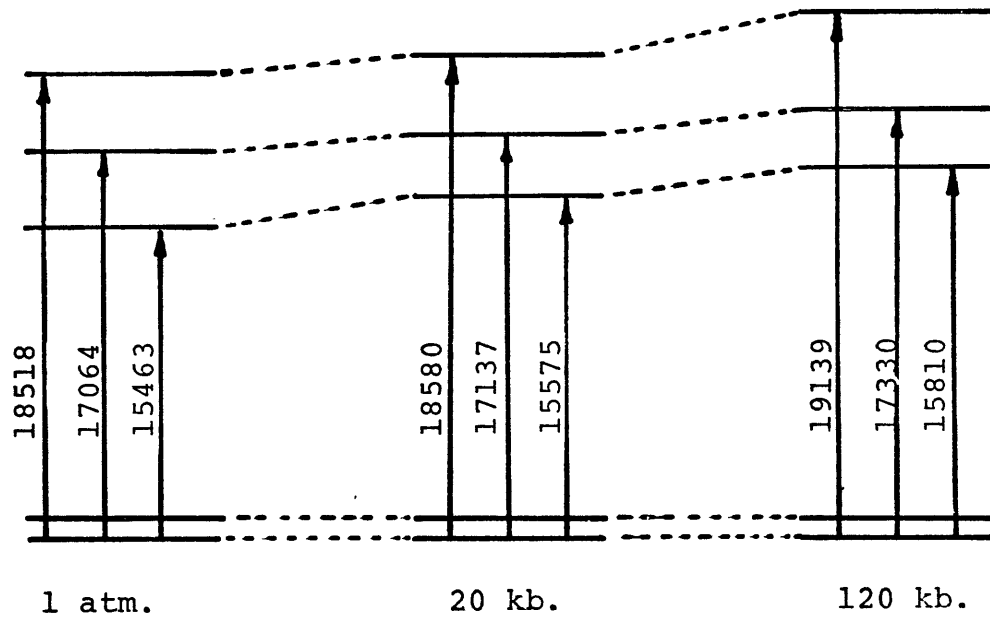


FIGURE IV- 39

ed a similar trend of energy shift with pressure as those bands in the infrared region. However, the two bands at energies 17090 and 18440 cm^{-1} shifted at a slower rate than the band at 15500 cm^{-1} . The trend of band energy shift with pressure in the visible region is also an indication of increasing the regularity of the tetrahedral site.

The high pressure visible spectra for powdered lusakite sample were also measured at about 50 and 120 kb.. The spectral peaks in the visible region showed appreciable blue shift with increasing pressure up to 120 kb.; the visible spectra at 1 atm. and 120 kb. are shown in Figure IV-40.

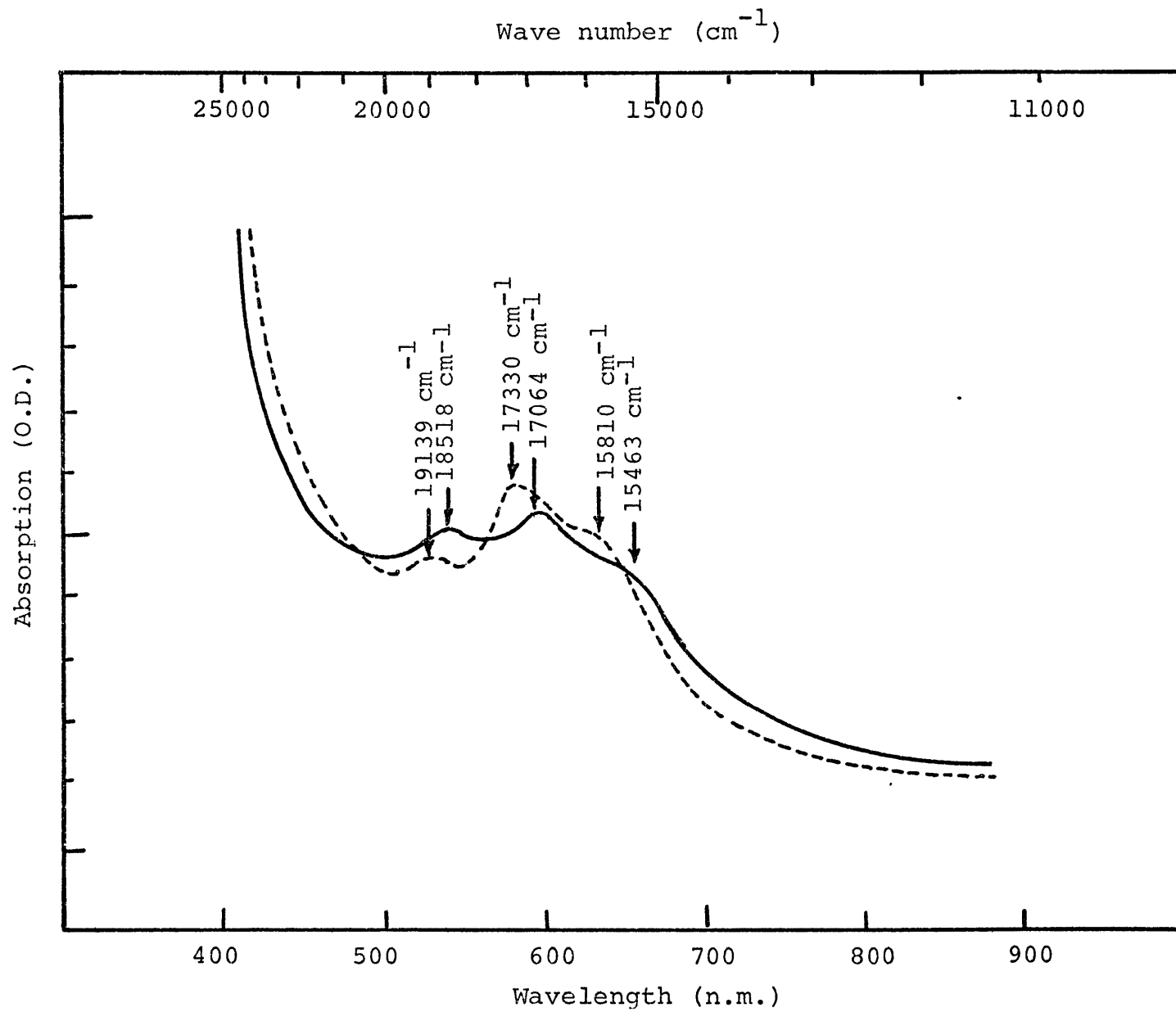
It should be mentioned that 10Dq energy value cannot be estimated from ν_2 and ν_3 transitions, since their energy values are dependent on Racah parameter B, in addition to 10Dq. As a consequence of this, 10Dq values were not estimated at different pressures. Nevertheless, the high energy shift of ν_2 and ν_3 with pressure is evidence for a positive energy change in 10Dq value at elevated pressure. Furthermore, if the B energy value was assumed to decrease very slightly with pressure ($\Delta B \approx 5 \text{ cm}^{-1}$ in 100 kb.), as it was shown in the previously investigated minerals, then the estimated energy change in 10Dq should be about 100 cm^{-1} in 30 kb..

This energy change in 10Dq value is much less than that observed for Fe^{2+} , Cr^{3+} , and Mn^{3+} cations contained in octahedral sites. These results demonstrate that the tetrahedral site is rather incompressible and tends to become more regular as pres-

FIGURE IV- 40

The spectra of lusakite powder measured at 1 atm.
and 120 kb..

————— (1 atm.); - - - - - (120 kb.)



sure increases.

IV-6.3 Melilite {Ca,Na,K}(Mg,Fe,Al,Si)₃O₇

The melilite structure consists essentially of tetrahedra which are arranged in a sheet-like pattern in the x-y plane. The sheets are repeated along the z-axis and held together by Ca-O linkages (Smith, 1953).

The Ca, K, and Na cations occupy the 8-fold coordination site, while the remaining cations, Si, Mg, Fe, and Al, occupy the 4-fold coordination sites.

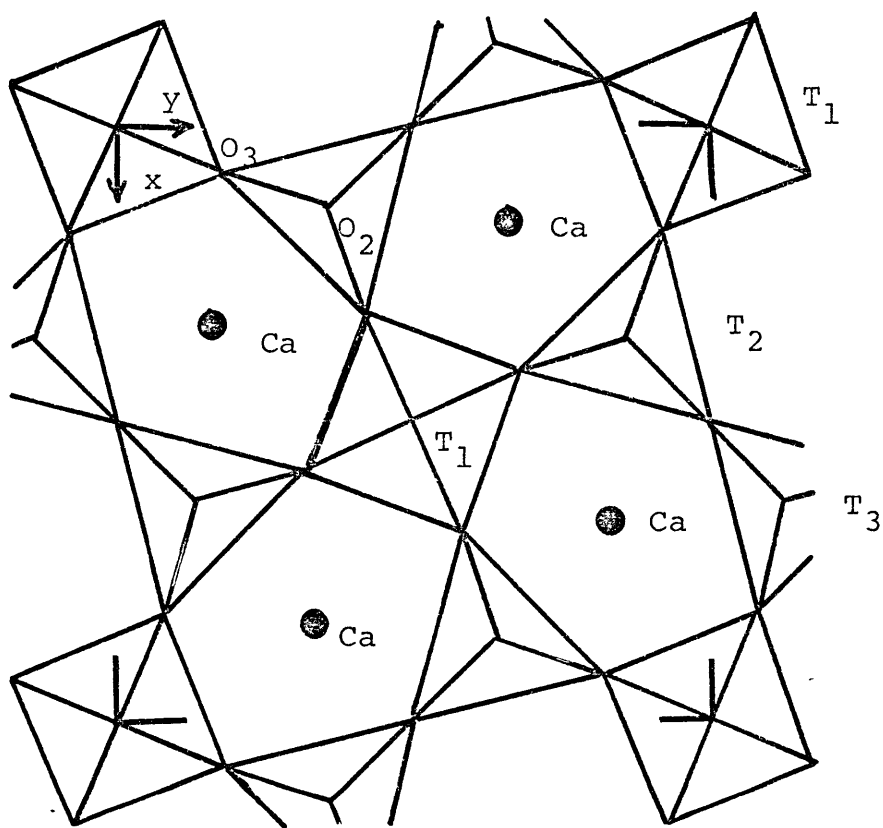
There are three tetrahedral sites in the structure denoted by T₁, T₂, and T₃ (Figure IV-41). The silicon atoms occupy the T₂ and T₃ sites only, and Al³⁺ can occupy any of the three sites; Mg and Fe ions, however, occupy only the T₁ site.

Smith (1953) determined the M-O distances in the tetrahedral sites and obtained an average Mg-O distance of 1.87 Å. In the present study, the average Fe-O distance is assumed to be 1.92 Å since the ionic radius of Fe²⁺ is 0.05 Å larger than that of Mg²⁺ (Shannon and Prewitt, 1969). Further, the site symmetries and crystal chemistry of Fe²⁺ and Fe³⁺ ions were investigated intensively using the optical absorption, Mössbauer, and electron microprobe techniques.

Three samples of melilite of different chemical compositions and of different localities were studied; these are referred to

FIGURE IV-41

The crystal structure of melilite projected on
(001). [Smith, 1953.]



as melilite(I), (II), and (III). The typical electron microprobe analyses for the three melilites are given in Table IV-11.

The Mössbauer spectrum of melilite(I), measured at room temperature, is shown in Figure IV-42 . It consists of one doublet with the values of isomer shift (I.S.) and quadruple splitting (Q.S.) of 0.95 and 2.37 mm/sec., respectively. These values are comparable with those reported by Bancroft et al. (1967) for the tetrahedrally coordinated Fe^{2+} in staurolite. In addition, the isomer shift value also falls within the range of those values corresponding to Fe^{2+} ions in tetrahedral sites (Table IV-12). A four-peak computer fit was attempted; however, the process has failed to converge. It is evident then from Mössbauer spectrum of melilite(I) that there is no detectable absorption related to Fe^{3+} and all of Fe^{2+} ions occur in one tetrahedral site.

To obtain additional information on the site regularity or distortion, the Mössbauer spectra of the same specimen was measured at liquid nitrogen temperature (77°K). The spectrum obtained at 77°K is essentially the same as that measured at room temperature. However, the Mössbauer peaks are narrower in the low temperature spectrum, and the Q.S. value has increased significantly. This is an indication that the tetrahedral Fe^{2+} site is slightly distorted rather than being an extremely distorted one. From the difference in Q.S. values at room temperature and 77°K, and using Ingall's model (1964) and Huggins' method (1974), the energy separation between the lower levels, e, was estimated

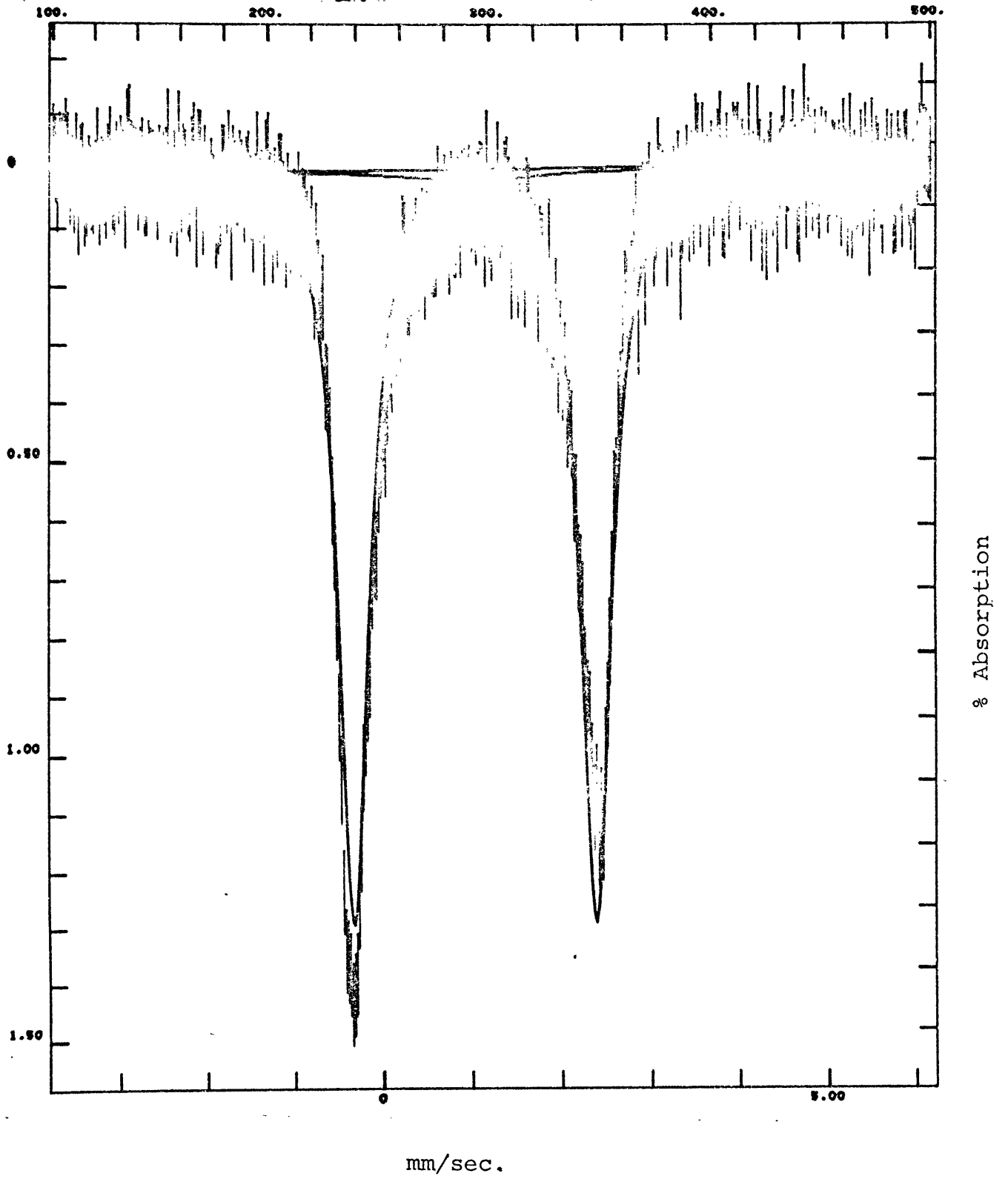
TABLE IV-11

Oxide	Melilite I (wt.%)	Melilite II (wt.%)	Melilite III (wt.%)
SiO ₂	43.41	42.05	41.73
TiO ₂	0.00	0.04	0.03
Al ₂ O ₃	5.84	6.77	6.80
Cr ₂ O ₃	.00	0.00	0.00
FeO	2.37	5.16	6.89
MgO	9.13	7.04	5.87
MnO	0.13	0.16	0.19
CaO	35.34	34.17	33.23
K ₂ O	0.07	0.26	0.25
Na ₂ O	3.24	3.00	3.26
Total	99.53	98.65	98.23

Electron microprobe analyses of melilite I,
II, and III.

FIGURE IV-42

Mössbauer spectrum of melilite I at room temperature.



to be $550 \pm 50 \text{ cm}^{-1}$.

Mössbauer spectral measurements were also made on melilite (II) and (III) at room temperature. The spectrum of the first consists of one doublet with the values of I.S. and Q.S. are 0.293 and 1.082, respectively; these values correspond to Fe^{3+} in tetrahedral site. A four-peak fit was tried but the process of fitting has failed to converge, indicating that more than 95% of the total iron is in the trivalent state. Mössbauer spectrum of melilite(III), on the other hand, was fitted into two doublets, one corresponding to tetrahedral Fe^{2+} and the other to Fe^{3+} in the tetrahedral site.

The optical absorption spectra of melilite(I), (II), and (III) were measured at 1 atm. (Figure IV-43). The melilite(I) shows a broad and intense absorption band spanning the energy region $5000\text{-}7500 \text{ cm}^{-1}$, and no significant absorption was observed in the visible region.

On the other hand, melilite(II) did not show any absorption features in the i.r. region. However, an intense absorption edge which starts at about 16500 cm^{-1} sweeps into the visible and u.v. regions. Due to this intense absorption, spectral features expected to be observed for Fe^{3+} , at about 24000 cm^{-1} , were obscured. Melilite(III) showed spectral features intermediate to those obtained for melilite(I) and melilite(II). Since the optical spectra of melilite(I) are more obvious than those of melilite(II) and (III), they have been investigated further for curve-fitting and high pressure studies.

TABLE IV-12

Mineral Name	Q.S. mm/sec	I.S. mm/sec	wt.% Fe ²⁺ or Fe ³⁺	Site	Band Width mm/sec
Melilite I (Rm. Temp.) [This work]	2.369	0.944	Fe ²⁺ (2.25)	Tet.	0.415
Melilite I (Liq.N ₂ Temp.) [This work]	2.7031	1.0379	Fe ²⁺ (2.25)	Tet.	0.407
Melilite II (Rm. Temp.) [This work]	1.0821	0.2926	Fe ³⁺ (5.56)	Tet.	0.6439
Hematite [1]	0.37	0.39	Fe ³⁺ (100)	Tet.	-
Iron Microcline [2]	0.60	0.21	Fe ³⁺ (5.2)	Tet.	0.45
Blue-Sapphirine [3]	0.87 2.57	0.30 1.15	Fe ³⁺ (1.00) Fe ²⁺ (1.69)	Tet. Oct.	0.65 0.40
Yellow-Sapphirine [3]	0.78 1.37	0.30 0.27	Fe ³⁺ (3.74)	Tet. Tet.	0.52 0.59
Staurolite	2.29	0.95	Fe ²⁺ (11.52)	Tet.	-
Gillespite (1 atm.) [4]	0.51	0.851	Fe ²⁺	Sq. plane	-
Gillespite (above 26 kb.) [4]	2.02	1.13	Fe ²⁺	V.dist. tet.	-

[1] Vaughan, R.W. and Drickamer, H.G. (1967).

[2] Huggins, F.E. (1974).

[3] Bancroft, G.M., Burns, R.G., and Stone, A.J. (1968).

[4] Abu-Eid, R.M., Burns, R.G., and Mao, H.K. (1973).

Table IV-12: Mössbauer parameters of various minerals containing Fe²⁺ and Fe³⁺ cations in octahedral (oct.), tetrahedral (tet.), and square planar sites.

FIGURE IV- 43

Absorption spectra of melilite I, (a), melilite II,
(b), and melilite III, (c).

-- 240 --

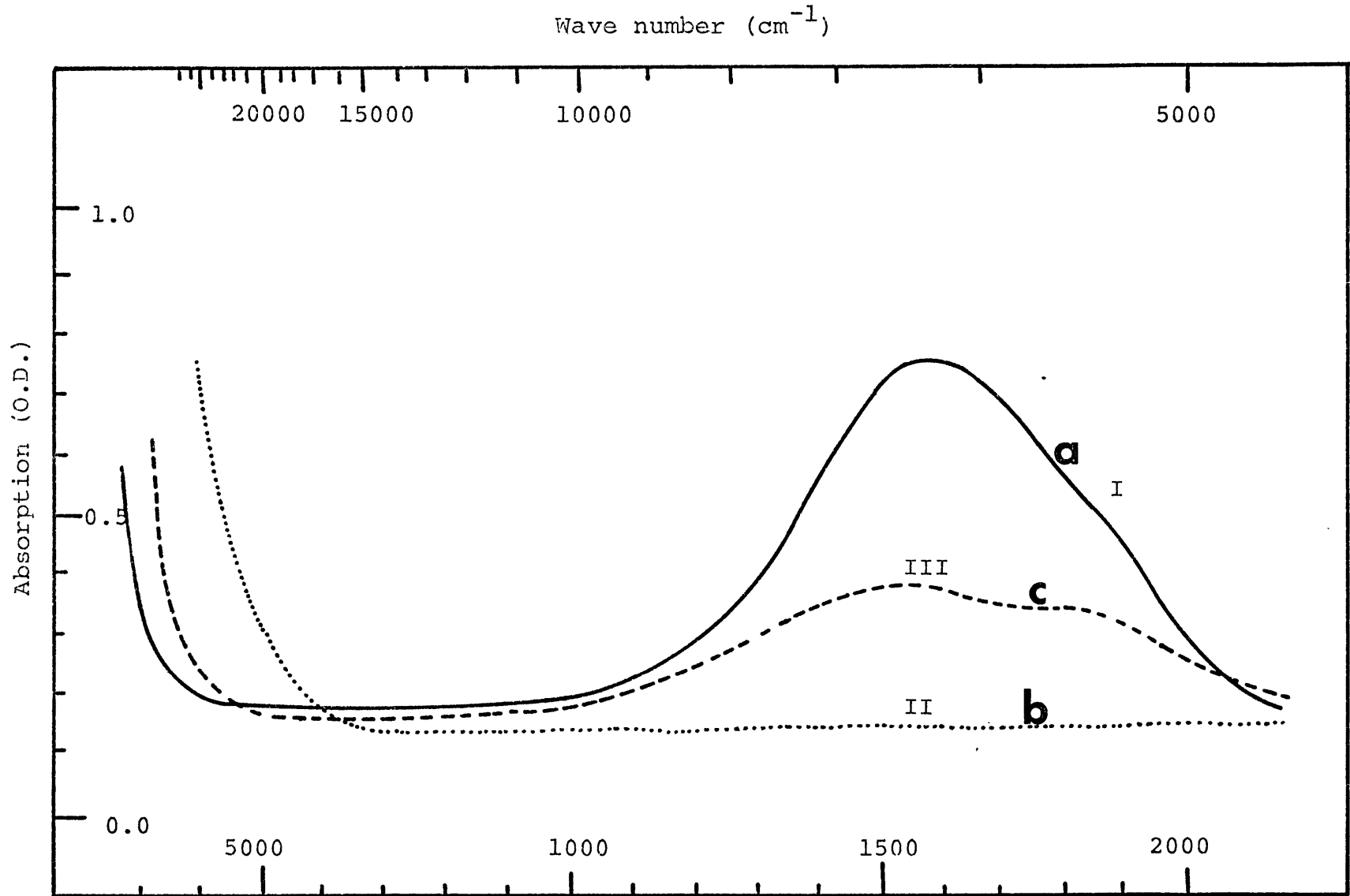
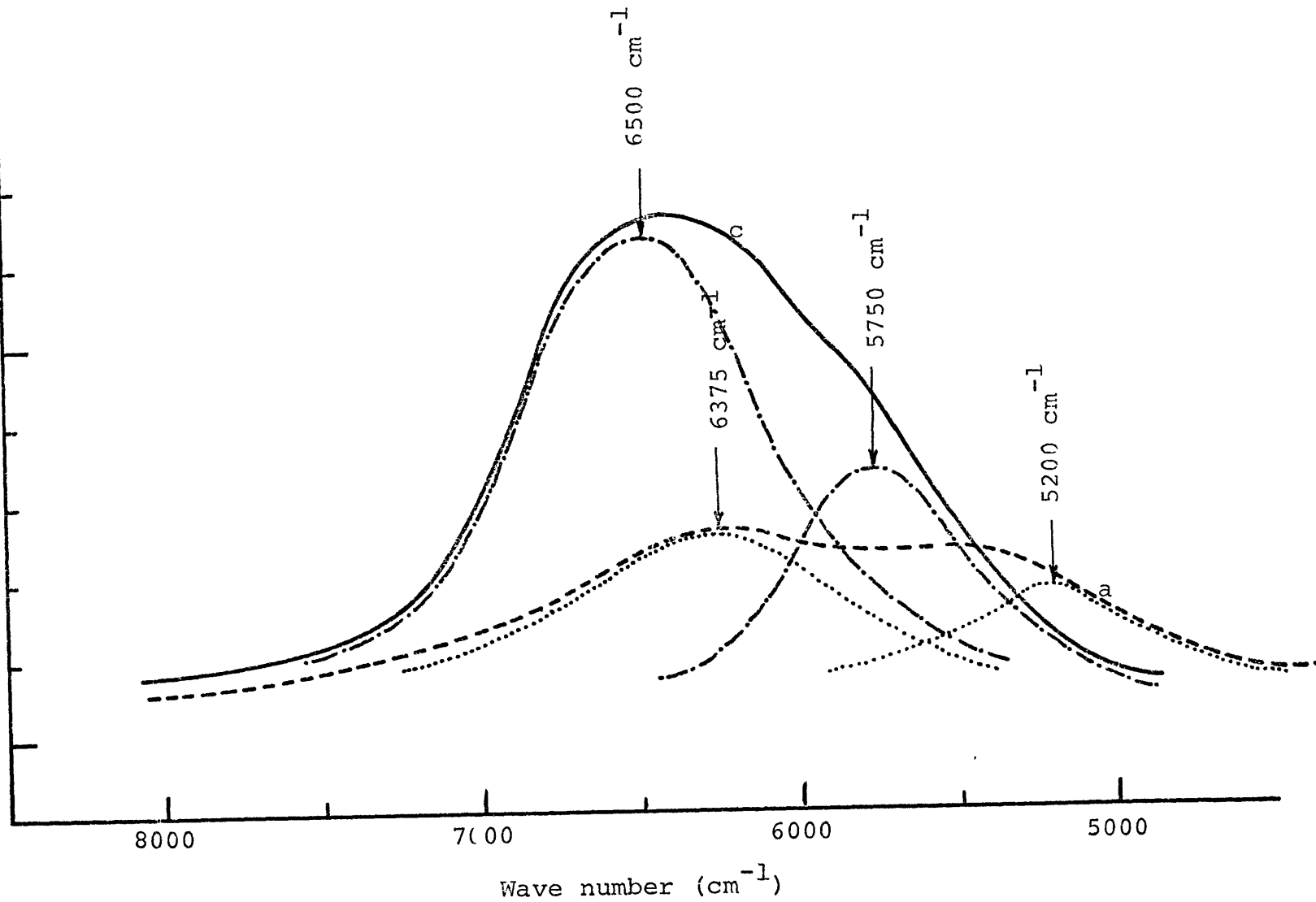


FIGURE IV-44

The i.r. polarized spectra of melilite "I" measured at 1 atm., ——— c-spectrum; ----- a-spectrum.

- 242 -

Absorption (O.D.)



The polarized spectra of melilite(I) (Figure IV-44) were obtained for two orientations, "a" and "c". The "c" spectrum consists of an intense and broad absorption under which two bands were fitted at energies 5750 and 6500 cm^{-1} . The "a" spectrum, however, showed a broad and weak absorption; two broad and weak bands were fitted under this spectral profile at energies 5200 and 6375 cm^{-1} .

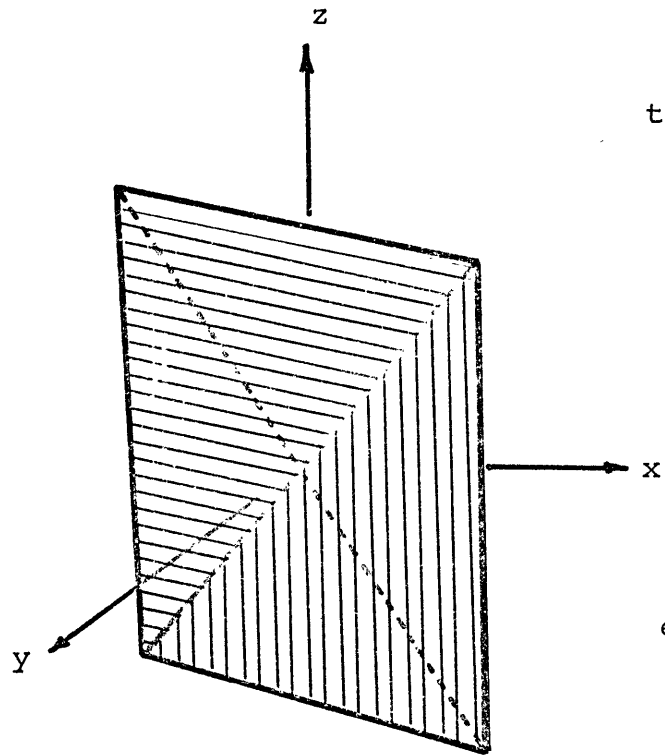
In constructing the energy level diagram for Fe^{2+} in tetrahedral site, the energies of spectral bands observed in the c-spectrum only were taken into consideration since they were very well defined and their energies were accurately determined. Using spectral band energies and the energy separation between e-levels, which was estimated to be 550 cm^{-1} , as explained above, the energy level diagram shown in Figure IV-45a was constructed. From this diagram, the following information has been gained:

1. The T_1 tetrahedral site which contains Fe^{2+} cation is slightly distorted (Figure IV-45b). This is due to the observed non-degeneracy of " t_2 " and "e" orbital sets.
2. The energy levels are assigned to 5B_1 , 5A_2 , 5B_2 , and 5E states which correspond to D_{2d} symmetry, i.e. the site is preferably considered to have the point group symmetry D_{2d} rather than T_d .
3. Since the energy separation between (d_{xz} , d_{yz}) orbital set and d_{xy} orbital is about 750 cm^{-1} , it is predicted that the Fe^{2+} tetrahedron is compressed along the z-axis.

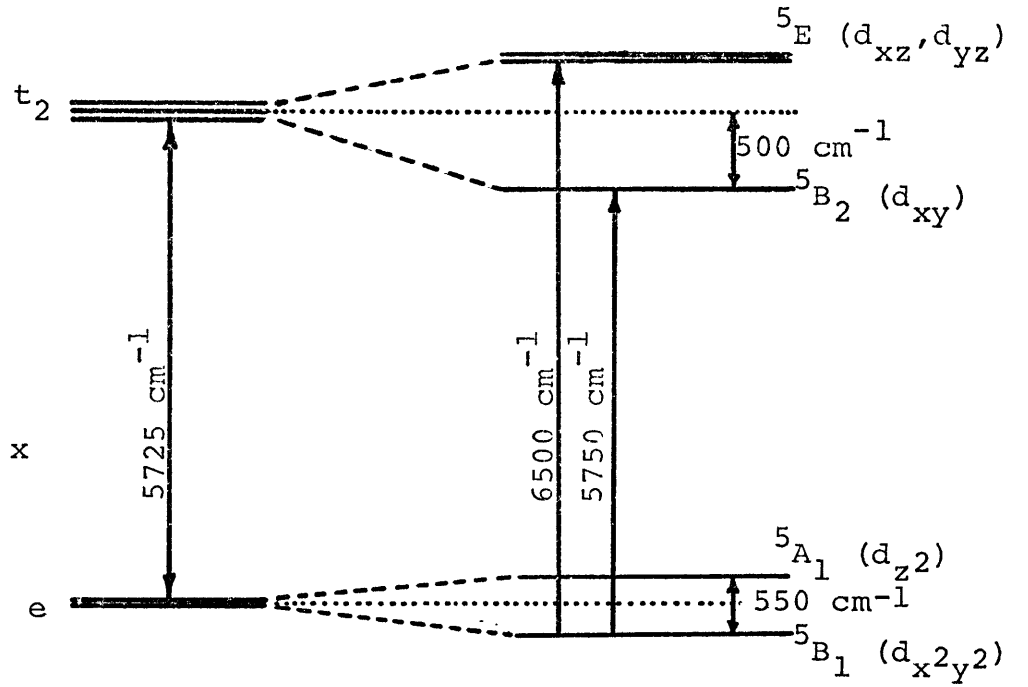
see figure

FIGURE IV-45

- (a) The energy level diagram of Fe^{2+} in melilite I constructed from the curve-fitted c-spectrum shown in Figure (IV-45).
- (b) A pictorial view of the tetrahedral site of Fe^{2+} in melilite I. Note the elongation along the z-axis which is predicted for the measured spectra.



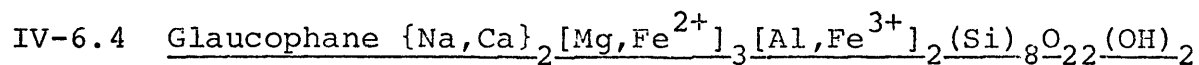
(b)



(a)

4. The CFS and CFSE parameters were estimated to be 5725 and 3710 cm^{-1} . These values are much less than the values obtained for Fe^{2+} in octahedral site, indicating that Fe^{2+} is more stable in the 6-coordination site.

The high pressure spectra of melilite(I) were obtained at different elevated pressures. With increasing pressure, the Fe^{2+} bands were observed to shift to higher energies. However, the magnitudes of band energy shifts were unable to be obtained accurately due to the large widths of the absorption band. The magnitude of band energy shift, in 30 kb., was estimated to be roughly $<100 \text{ cm}^{-1}$. This energy change is comparable to that obtained for Fe^{2+} ions in staurolite.

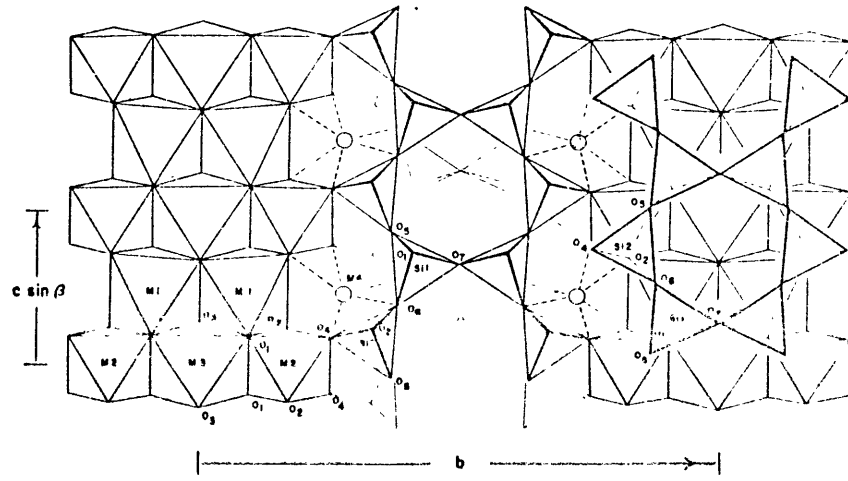


The structure of glaucophane is shown in the two views illustrated in Figures IV-46a,b. Viewing the unit cell in glaucophane along the a-axis, the structure may be described as consisting of octahedral bands repeated along the c-axis and cross-linked by double SiO_4 tetrahedral chains (Figure IV-46a) The view along the c-axis, on the other hand, shows alternating octahedral and tetrahedral layers stacked along the a-axis (Papike and Clark, 1968).

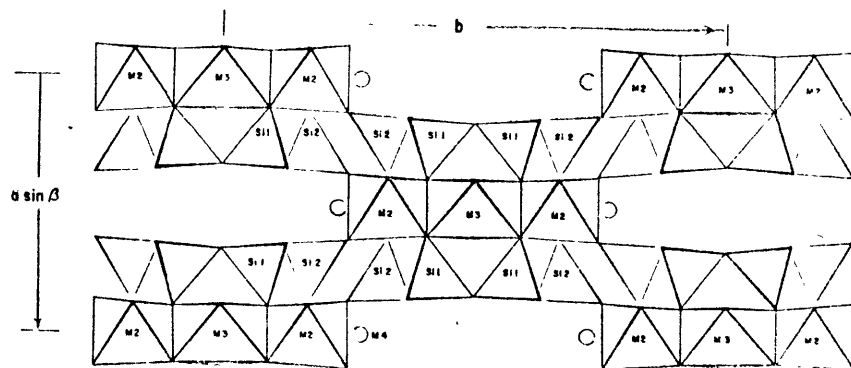
The structure contains two tetrahedral sites occupied by silicon atoms and designated by Si_1 and Si_2 . In addition, there are four 6-fold coordination sites denoted by M_1 , M_2 , M_3 , and

FIGURE IV- 46

- (a) A view of the glaucophane structure along "a" showing the octahedral bands stacked along the c-axis. [From Papike and Clark, 1968.]
- (b) A view of the glaucophane structure along the c-axis showing the alternating octahedral and tetrahedral layers along the a-axis. [From Papike and Clark, 1968.]



(a)



(b)

M_4^* . The M_1 and M_3 sites are fairly regular and are occupied by Fe^{2+} and Mg^{2+} cations. The M_2 site is distorted and is usually occupied by Fe^{3+} and Al^{3+} ions. The M_4 position, however, is fairly large and mostly occupied by large cations such as Na and Ca^{2+} (Whittaker, 1949; and Papike and Clark, 1968).

Burns and Prentice (1968) studied further the site occupancies of Fe^{2+} and Fe^{3+} ions (using an infrared method) and confirmed the above assignments. However, they reported that a small fraction of Fe^{2+} ions may occur in the M_1 and M_3 positions and Fe^{2+} ions are relatively enriched in the M_1 site.

The M_1 site shares six of its edges with other polyhedra; it shares two of them with $2M_2$ polyhedra and another two with $2M_3$ and two more edges are shared with M_1 and M_4 positions.

The M_3 polyhedron also shares six of its edges, four of them with $4M_1$ sites and the remaining two are shared with $2M_2$ polyhedra. On the other hand, the M_2 site shares five edges only; it shares two edges with $2M_4$ positions, two with $2M_1$, and another edge with the M_3 polyhedron.

The cations in the two M_1 and the one M_3 sites, per half unit cell, are each coordinated to two $(OH)^-$ ions and four oxygen atoms, and the cation in each of the two M_2 positions is surrounded by six oxygens. The M-O distances and site symmetries of M_1 , M_2 , and M_3 positions are illustrated in Table IV-13 and Figure IV-47.

* The M_4 site may be considered as 6- or 8-fold coordination.

FIGURE IV-47

The M1, M2, and M3 polyhedra in glaucophane.

TABLE IV-13

M1-O, M2-O, and M3-O interatomic distances in glaucophane. [From Papike and Clark, 1968b].

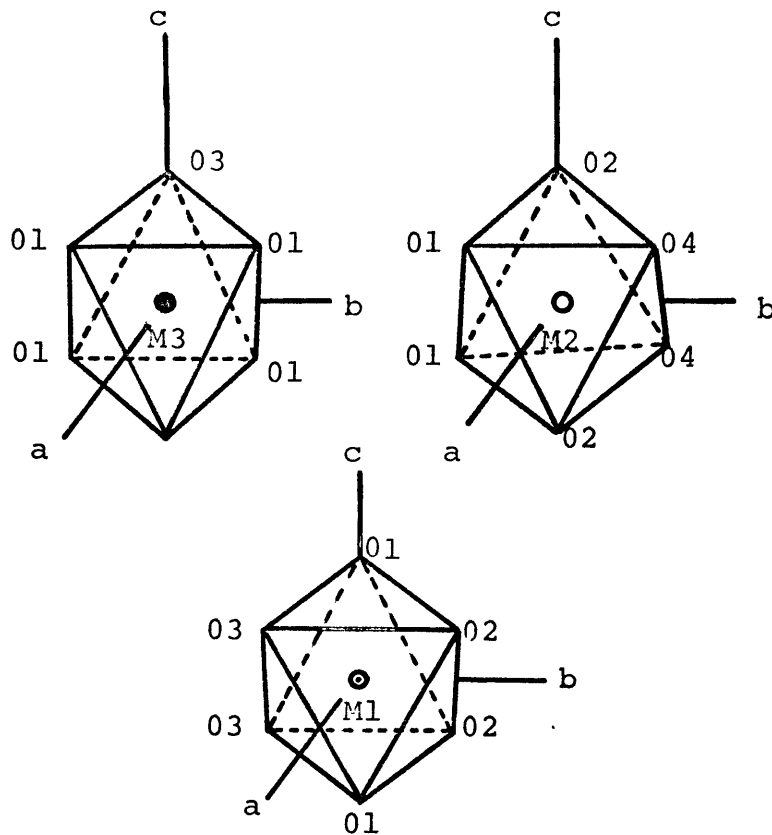


FIGURE IV-48

Atom Pair	Distance (Å)
(2)M(1) - 0(1)	2.078
(2)M(1) - 0(2)	2.082
(2)M(2) - 0(3)	2.100
Average	2.087
(2)M(2) - 0(1)	2.038
(2)M(2) - 0(2)	1.943
(2)M(2) - 0(4)	1.849
Average	1.943
(4)M(3) - 0(1)	2.103
(2)M(3) - 0(3)	2.077
Average	2.094

TABLE IV-13: M-O Distances in Glaucophane.

The polarized absorption spectra of glaucophane were reported by Bancroft and Burns (1969) and Burns (1970). Figure IV-48 shows the α -spectrum which contains four sharp peaks at energies 7067, 7102, 7133, and 7163 cm^{-1} ; these bands represent the first overtone of the O-H stretching frequency (Burns and Prentice, 1968). The α -spectrum also shows two broad absorption bands at 9708 and 11905 cm^{-1} . These are assigned to the spin-allowed transitions in Fe^{2+} ions contained in the M_1 and M_3 positions.

In the β and γ spectra, no sharp peaks were observed in the energy region 7000-7200 cm^{-1} , but only two broad bands at 9900 and 11900 cm^{-1} were identified in the i.r. region (Figure IV-48).

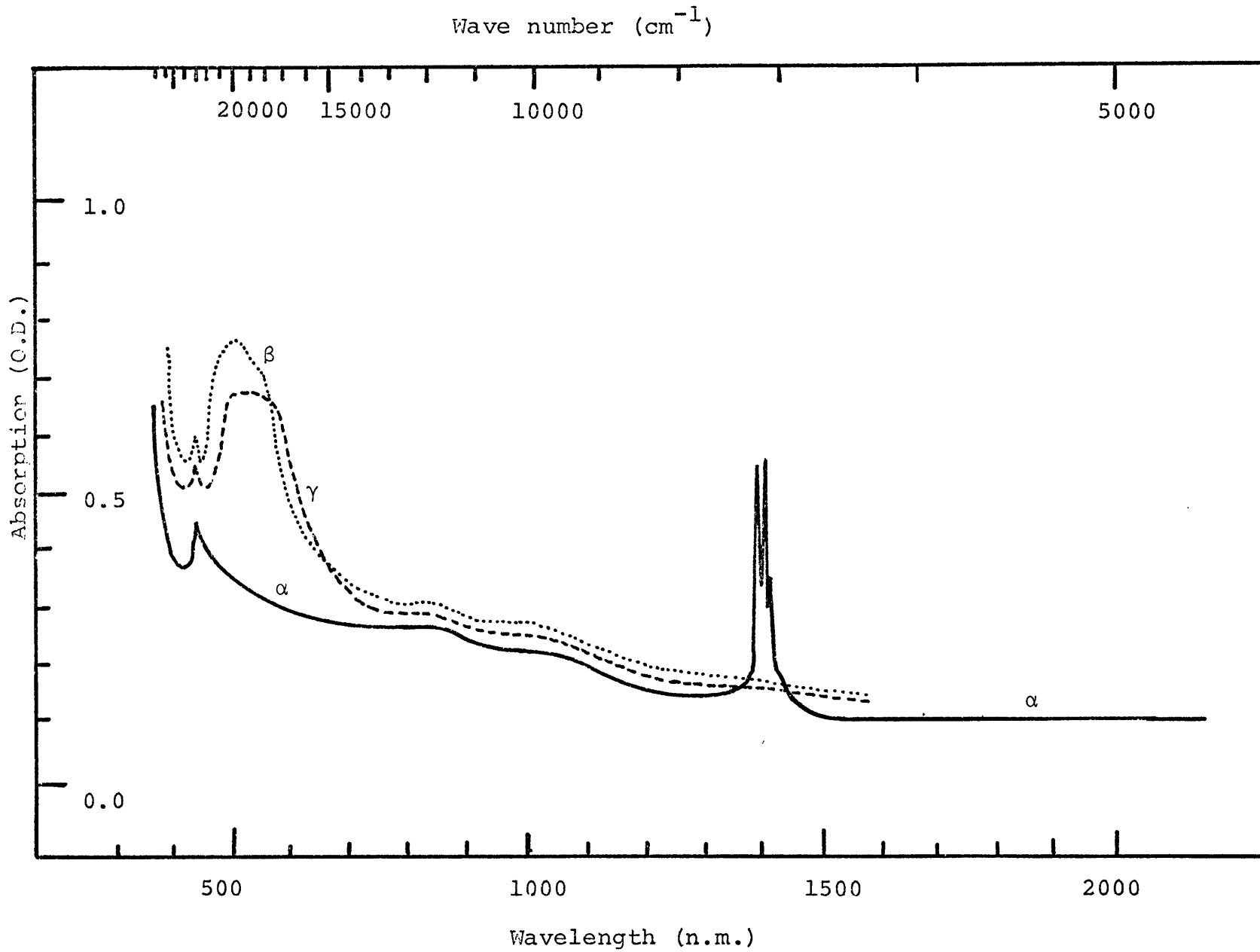
In the visible spectral region, the α -spectrum did not show any significant absorption; meanwhile, the β and the γ spectra did show broad absorption features in the energy region 14000-20000 cm^{-1} , in addition to a sharp and conspicuous peak at 22830 cm^{-1} . The broad absorption in the visible region is related to electron transfer between Fe^{2+} ions in the M_1 and M_3 sites and the neighboring Fe^{3+} ion in the M_2 site. The sharp peak at 22830 cm^{-1} is assigned to the spin-forbidden transition, ${}^6A_{1g} \rightarrow {}^4E_g; {}^4A_{1g}$, in Fe^{3+} .

The high pressure polarized spectra of a glaucophane crystals, mounted in the diamond cell, were measured for the different orientations α , β , and γ . At elevated pressures, the four peaks related to the overtone stretching frequency of the OH^- ions become broad and then disappeared at pressures around 50 kb., indicating that the pressure influence is to inhibit the

FIGURE IV-48

The polarized spectra of glaucophane measured at normal pressure:

————— α -spectrum
..... β -spectrum
----- γ -spectrum



O-H stretching vibration. The broad bands around 10000 and 12000 cm^{-1} , attributed to CF transitions in Fe^{2+} , shifted to higher energies as expected. In the visible region, the broad absorption band increased significantly in intensity and shifted slightly to lower energy as pressure increased.

The effect of pressure on charge transfer bands will be discussed in some detail in the next chapter. The sharp absorption peak at 22830 cm^{-1} showed a red shift ($\sim 100 \text{ cm}^{-1}$) as pressure increased to 50 kb.; this low energy shift conforming with its assignment as a spin-forbidden transition in Fe^{3+} .

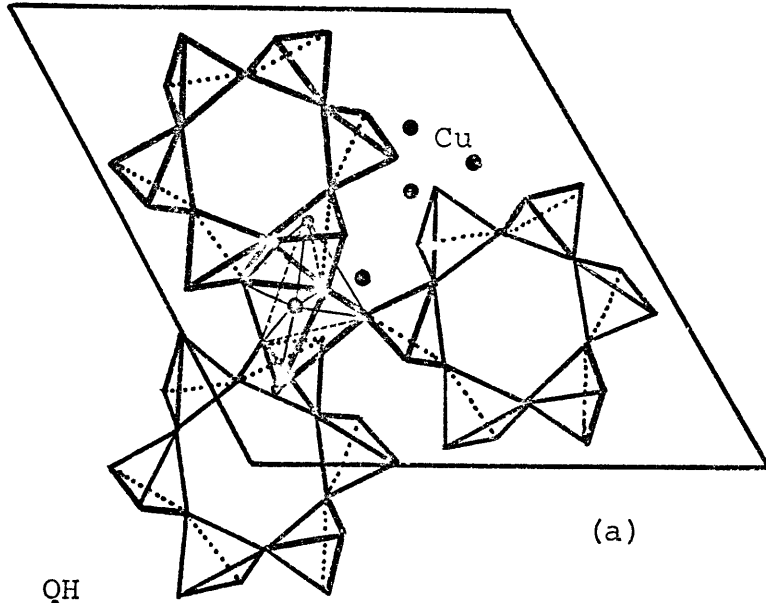
IV-6.5 Diopside [$\text{CuSiO}_3 \cdot \text{H}_2\text{O}$]

Diopside is a ring silicate mineral which contains Cu^{2+} ions in a very distorted octahedral site. The crystal structure was refined by Heide and Boll-Dorberger (1955), and the magnetic and diffuse reflectance spectral properties were discussed by Newnham and Santoro (1967).

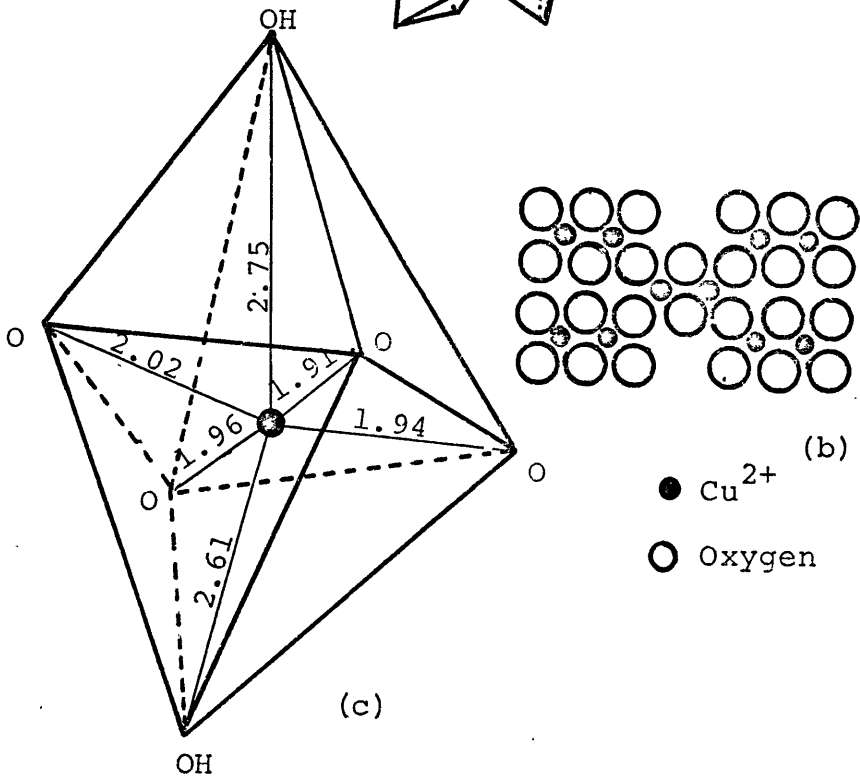
The structure consists of hexagonal, Si_6O_{18} , rings interconnected by Cu^{2+} ions which are surrounded by four oxygens and two OH^- ions (Figure IV-49a). Each Cu^{2+} polyhedron shares one edge with another neighboring Cu^{2+} site and two corners with other Cu^{2+} polyhedra; it shares also four of its corners with four SiO_4 tetrahedra. The geometry of the Cu^{2+} site and the Cu-O and Cu-OH distances are illustrated in Figure IV-49c. From Figure IV-49b,c it appears that the Cu^{2+} site has a C_s symmetry; however, considering the four Cu-O distances to be the same, the point group symmetry may be approximated to C_{4v} .

FIGURE IV-49

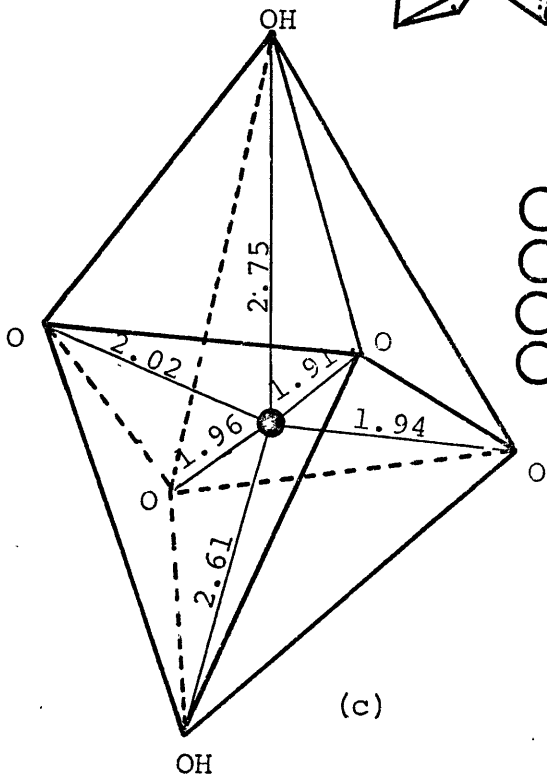
- (a) The structure of diopase viewed along the c-axis. It shows the distorted octahedral site of Cu^{2+} ion and the hexagonal Si_6O_{18} rings interconnected by Cu^{2+} polyhedra.
[From Heide and Boll-Dornberger, 1955.]
- (b) A schematic diagram showing the edge and corner sharings between two Cu^{2+} polyhedra.
[Newnham and Santoro, 1967.]
- (c) The Cu^{2+} distorted octahedron and the Cu-O and Cu-OH distances.



(a)



(b)
● Cu^{2+}
○ Oxygen



(c)

Newnham and Santoro (1967) measured the diffuse reflectance spectrum of powder diopside and reported only one absorption peak at 13300 cm^{-1} , which they related to the ${}^2E_g \rightarrow {}^2T_{2g}$ transition of the $\text{Cu}^{2+} 3d^9$ electron configuration.

In the present study, the absorption spectra of diopside single crystals were measured at 1 atm. and high pressures. The spectrum at 1 atm. (Figure IV-50) showed a broad absorption profile covering the energy region $8500\text{-}18000 \text{ cm}^{-1}$. Three absorption bands were identified in this region; they were located at energies around 10000 , 11765 , and 13800 cm^{-1} . Using a thick crystal of diopside, another three weak absorption bands were observed at energies 4878 , 4950 , and 5076 cm^{-1} ; however, in a thin specimen, those bands could not be identified.

In a regular octahedral symmetry, Cu^{2+} ions are expected to have one spin-allowed transition from the ground state, 2E_g , to the higher energy excited state, 2T_g ; the mechanism of this transition is illustrated in Figure IV-51a. In tetragonal fields, however, the ground state, 2E_g , will split into two levels (2B_1 and 2A_1) and ${}^2T_{2g}$ will split into 2B_2 and 2E levels (Figure IV-51b). Thus, in C_{4v} point group symmetry, Cu^{2+} ions are expected to show three electronic transitions; these are: ${}^2B_1 \rightarrow {}^2B_2$, ${}^2B_1 \rightarrow {}^2A_1$, and ${}^2B_1 \rightarrow {}^2E$.

The three spectral bands observed at energies 10000 , 11765 , and 13800 cm^{-1} are assigned to the above transitions in Cu^{2+} ; the mechanisms of these transitions are explained in the energy level diagram shown in Figure IV-51b. The three weak bands in the long wave i.r. at energies 4878 , 4950 , and 5076 cm^{-1} are related to O-H stretching frequency; these peaks are similar

FIGURE IV- 50

The absorption spectra of diopase measured at
1 atm. (————) and 50 kb. (-----).

- 260 -

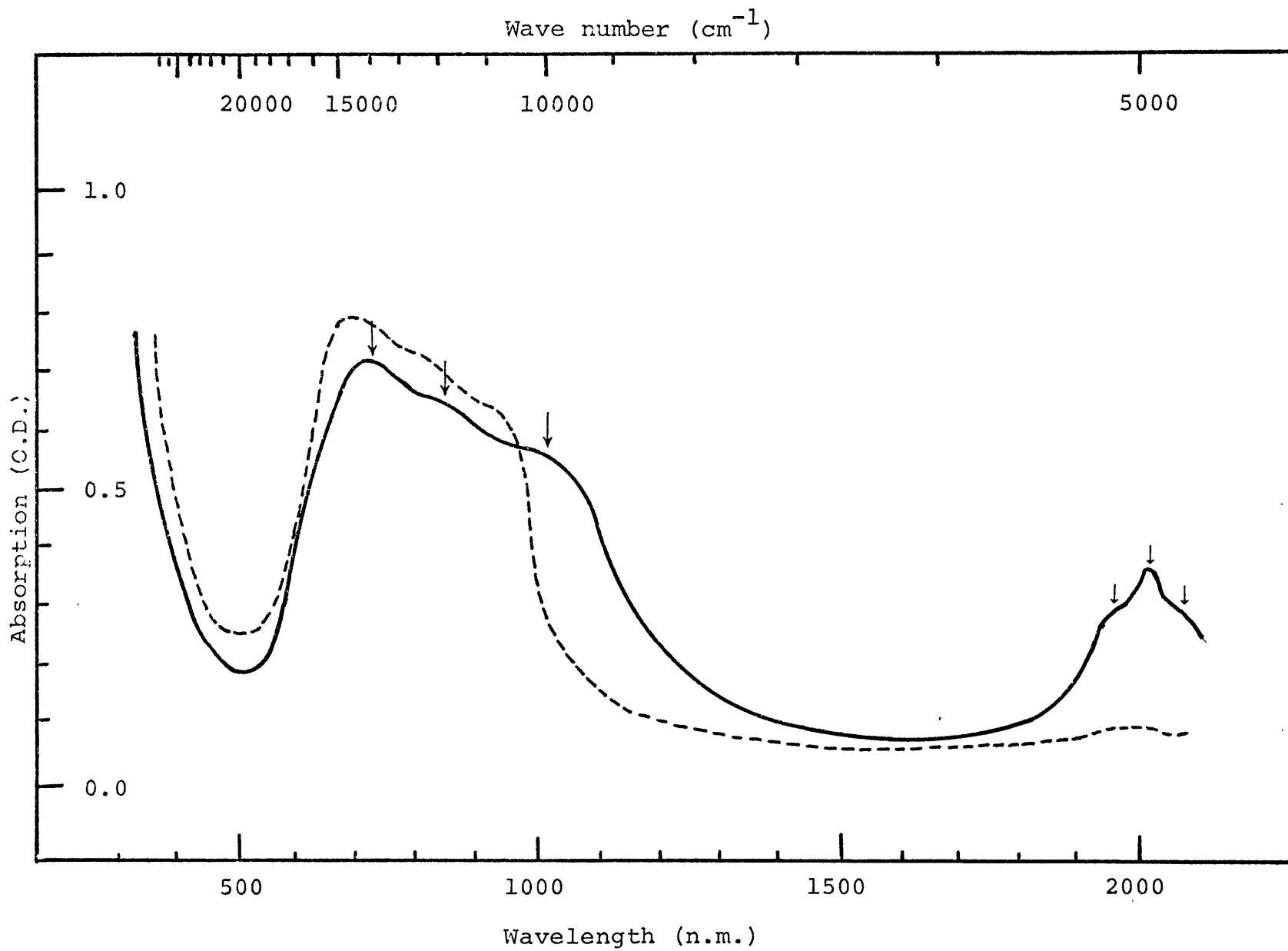
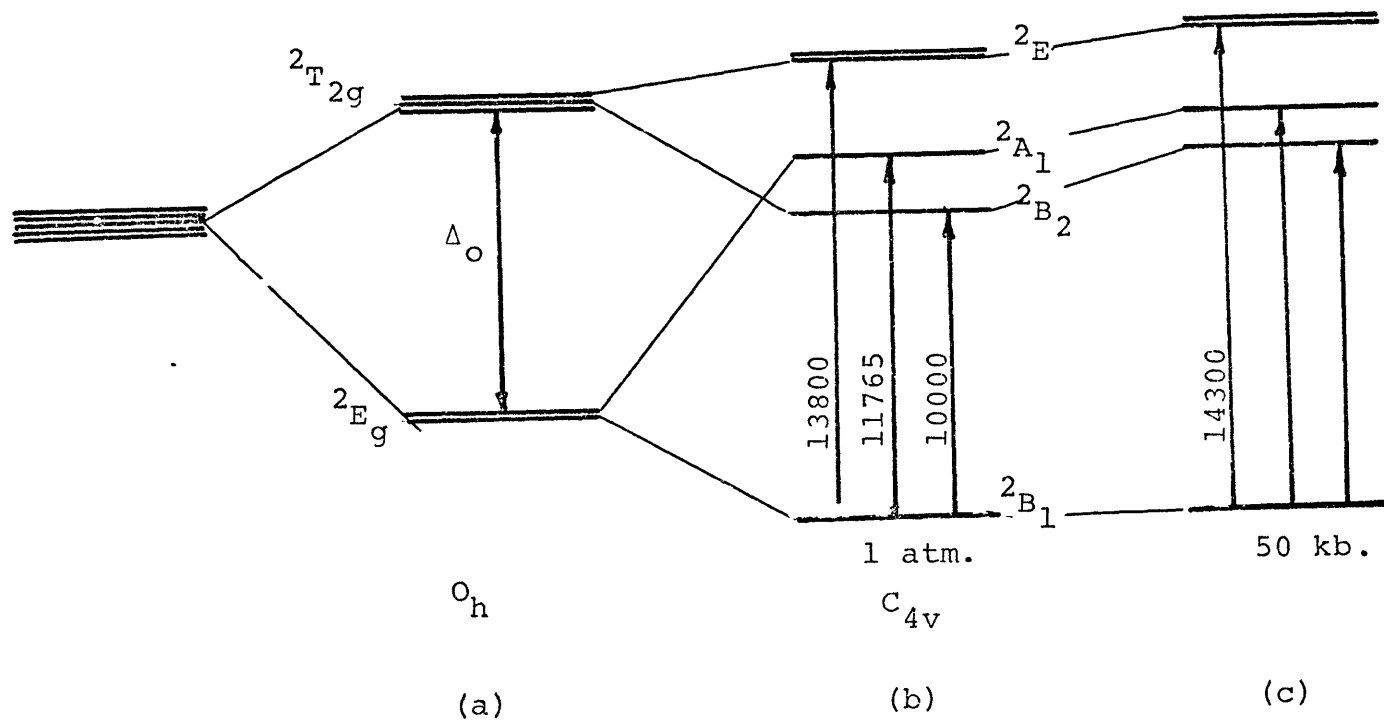


FIGURE IV-51

Cu^{2+} energy level diagrams in O_h and C_{4v} symmetries
(a,b). Figure (c) shows the d-energy levels at
50 kb..



to those observed in glaucophane, but they are broader and less intense and occur at longer wave lengths.

Measurements of the high pressure spectra of diopside were attempted. At elevated pressures, the spectral profile of Cu^{2+} ions showed an obvious blue shift; however, the positions of spectral bands in the infrared region could not be obtained due to their large widths. Nonetheless, the absorption maximum of the band at 13800 cm^{-1} was identified and observed to shift to 14300 cm^{-1} with increasing pressure up to about 50 kb.. Other significant features, which were observed in the high pressure spectra, are the narrowing of the absorption profile and the decreasing absorption in the long wavelength i.r. region (Fig.IV-50).

These phenomena may be an indication of increasing CFS parameter and decreasing the energy separation between the high energy levels, i.e. decreasing the degree of distortion of the octahedral site.

IV-6.6 Gillespite [$\text{BaFeSi}_4\text{O}_{10}$]

Gillespite is a rare mineral which contains Fe^{2+} cations in a square planar site. The effect of pressure on the spectra of ferrous ions in this site have been intensively studied. Some dramatic changes were observed in the spectra at pressure around 26 kb.. The detailed results of the high pressure spectral studies on gillespite are given in detail in Chapter VI.

CHAPTER V

EFFECT OF PRESSURE ON CHARGE TRANSFER BANDS

V-1. Introduction

It was mentioned earlier, in chapter II, that charge transfer spectral bands are related to two types of electronic transitions; first, a metal to metal ($M \rightarrow M$) charge transfer and second, a ligand to metal ($L \rightarrow M$) or metal to ligand ($M \rightarrow L$) electron transfer.

The first type of electronic transfer in transition metals occurs from a d-orbital of one metal ion of lower oxidation state to another d-orbital of a neighboring cation with higher valence state; this transfer is referred to as "Intervalence" transfer (Hush, 1967, 1968). When the two cations involved in the electron transfer process have identical nuclei e.g. Fe^{2+} and Fe^{3+} , the charge transfer process is known as homonuclear intervalence transfer. However, if the two nuclei are dissimilar e.g. Fe^{2+} and Ti^{4+} , it is referred to as heteronuclear intervalence transfer. The second type of charge transfer transition arises from excitation of an electron in an orbital of primarily ligand character to another orbital of principally metal character or vice versa.

There are two major spectral parameters that define charge transfer bands; these are their energies at the absorption maxima and their intensities. To explain the effect of pressure on charge transfer bands, it is mandatory to understand the nature of the physical parameters that control their energies and intensities. The second section of this chapter is allocated to

discuss such parameters and to predict the influence of pressure on them. In the final two, the high pressure charge transfer data (M-M, L-M, M-L), are presented and correlated with the theoretical predictions made in section V-2.

V-2. Band Energies, Intensities, and Influence of Pressure

Charge transfer bands have been treated in a non-uniform method by many authors using different models; the most commonly used of these are: molecular orbital, valence bond, and free electron approach models. Since it is not the objective of this thesis to discuss the theoretical details of these models, emphasis will be placed only on the parameters that involve the band energies and intensities, wherever it applies in any of these models.

Drickamer and Frank (1973) tackled the electron transfer problem using both the valence bond resonance approach and molecular orbital theory. In this approach, the total energy associated with an electron transfer ($h\nu_{CT}$) from a donor (D) to an acceptor (A), is related to the ionization potential of the donor (I_D), and the electron affinity to the acceptor (E_A), the energy separation between the energy levels of the donor and the acceptor (G_0), and the coulombic attractive energy between the two ions A and D (G_1). Drickamer and Frank (1973) derived a formula which relates $h\nu_{CT}$ with the above energy terms involved in the charge transfer process; this is expressed as:

$$h\nu_{CT} = I_D - (E_A + G_1 - G_0) + \frac{\beta_0^2 + \beta_1^2}{I_D - (E_A + G_1 - G_0)} \quad (1)$$

where β_0 and β_1 are terms proportional to the negative value of S_{01} , the overlap integral between the donor and the acceptor orbitals.

At elevated pressures, the interatomic distances D-A are expected to decrease, which then would cause an increase in the degree of orbital overlap, i.e. increase in the parameter S_{01} . Using equation (1), it is evident then that the increase in S_{01} value should lead to a decrease in $h\nu_{CT}$.

The influence of pressure on the other parameters, G_1 , G_0 , I_D , and E_A are not well understood yet. However, it is generally accepted, based on band theory, that the energy separation between the A and D levels should decrease with decreasing interatomic distance, i.e. G_0 should decrease with pressure. The ionization potential of the donor may decrease slightly and the electron affinity of the acceptor may increase as the donor-acceptor interatomic distances decrease.

Robin and Day (1967) used a similar approach to the one used by Drickamer and Frank; however, it was used to explain the energies of M-M charge transfer transitions only. The expression they gave for the energy of such transitions is:

$$h\nu_{CT} = E_A - E_I - E_{mad} \quad (2)$$

where E_A and E_I are the electron affinity and the ionization potential of the donor and acceptor, respectively, and E_{mad} is the madelung energy expended in moving an optical electron from D to A in the electrostatic field of all other charges. E_{mad} may

be related to the second and third terms given in equation (1).

Hush (1967, 1968) and Drickamer et al. (1972) used another model to predict M-M charge transfer band energies. In this model, they related the frequency and band width of an optical transfer absorption to the rate of homogeneous thermal electron exchange. The energy of the charge transfer transition in this model was given in equation II-8, and the influence of pressure was also predicted to shift charge transfer bands to lower energies.

Recently, Johnson (1973) used a more sophisticated approach in which he calculated the energies of molecular orbital levels for different inorganic compounds. Johnson's model was extended further to calculate the energy values of M-L charge transfer transitions in minerals (Tossell et al., 1973, 1974; Loeffler et al., 1974); this model is known as the "SCF- X_{α} Scattered Wave Method". The parameters related to M-O distances in this method are complex; however, it is essentially based on solving the one electron Schrödinger equation in three regions describing the electron density of an atomic cluster, e.g. ML_6 or ML_4 cluster. The total potential energy, $V(r)$, in this system is:

$$V(r) = V_c(r) + V_{x\alpha}(r) \quad (3)$$

where $V_c(r)$ refers to the coulombic interaction and repulsion forces, and $V_{x\alpha}(r)$ is a function related to the local electronic charge density, $\rho(r)$ as:

$$V_{x\alpha}(r) = 6\alpha [(3/8 \pi) \rho(r)]^{1/3} \quad (4)$$

With increasing pressure, the electronic charge density is expected to increase so that $V_{x\alpha}$ will increase. The coulombic

interaction and repulsion forces may increase or decrease slightly with decreasing interatomic distances, depending on the nature of M-L or M-M systems. The net result then will be a decrease in the potential energy of each cluster region, and hence a decrease in the energy value of charge transfer spectral bands.

The general expression for the intensity of a charge transfer band is:

$$f = K v_{\max}^2 \mu_{EN}^2 \quad (5)$$

where f is the oscillator strength, K is a constant, v_{\max} is the frequency at the band maximum, and μ_{EN} is the transition dipole. With increasing pressure, the resonance interaction should increase so that the value of the μ_{EN} should increase (Drickamer and Frank, 1973). Since the pressure tends to decrease v_{\max} , as it was explained above, then the change in intensity of the charge transfer band with pressure may be used as a balance to indicate the net influence of both effects on charge transfer band intensities or the dominance of one over the other. Thus, it is well known that increasing pressure tends to increase intensities of both types of charge transfer bands (M-M and M-L) (Drickamer and Frank, 1973; Abu-Eid, 1974a,b,c,; Mao, 1974). Due to this fact, the transition dipole is considered to be the dominant factor which causes significant increases in band intensities.

V-3. Effect of Pressure on M-M Charge Transfer Bands

M-M charge transfer bands appear commonly in the spectra of

natural minerals containing transition elements in different oxidation states, e.g. Fe^{2+} , Fe^{3+} , and Ti^{3+} , Ti^{4+} . They generally occur in the energy region $13000\text{-}18000\text{ cm}^{-1}$ and are characterized by their polarization dependence, i.e. their energies and intensities are sensitive to direction of the light electric vector, \vec{E} , relative to the donor-acceptor vector in the crystal lattice. The intensities and energies of M-M C.T. bands depend also on the other factors, such as the nature of the donor and acceptor ions and the intervening ligands, the M-M interatomic distances, and the mole fractions of both cations involved in the electron transfer process.

Spectral bands related to $\text{Fe}^{2+} \rightarrow \text{Fe}^{3+}$, $\text{Ti}^{3+} \rightarrow \text{Ti}^{4+}$, and $\text{Fe}^{2+} \rightarrow \text{Ti}^{4+}$ were reported for many natural minerals by many authors (Hush, 1967; Faye, 1968, 1971; Faye et al., 1968; Burns, 1970; Dowty and Clark, 1973; Manning, 1968, 1969; Prewitt et al., 1972; Bancroft and Burns, 1969; Robbins and Strens, 1972, 1968). However, there still are controversies concerning their assignments and the magnitude of their energy values. In the present section, the structural aspect of M-M charge transfer bands will be discussed and then the high pressure charge transfer spectral data will be presented for three minerals, viz. glaucophane, a blue omphacite, and vivianite.

• V-3.1 Glaucophane

The charge transfer absorption in glaucophane arises from the excitation of an electron in the t_{2g} level of an Fe^{2+} ion to the t_{2g} level of a neighboring Fe^{3+} cation. The β and the γ

visible spectra of glaucophane were measured at 1 atm. and at pressures around 50 kb. (Figures V-1a,b,c, and d). In each, β and γ , spectrum two absorption bands were fitted under the absorption envelope which covers the energy region 14000-20000 cm^{-1} ; the two bands are located at energies 16130 and 18350 cm^{-1} . The β spectrum is generally more intense than γ , and no charge transfer absorption features were detected in the third orientation, α . It was also noticed that the two C.T. bands had equal intensities in the γ spectrum, whereas in the β spectrum the band at 18350 cm^{-1} is significantly more intense than the one at lower energy.

In explaining the above spectral features and the mechanism of their polarization dependence, the following factors were taken into consideration:

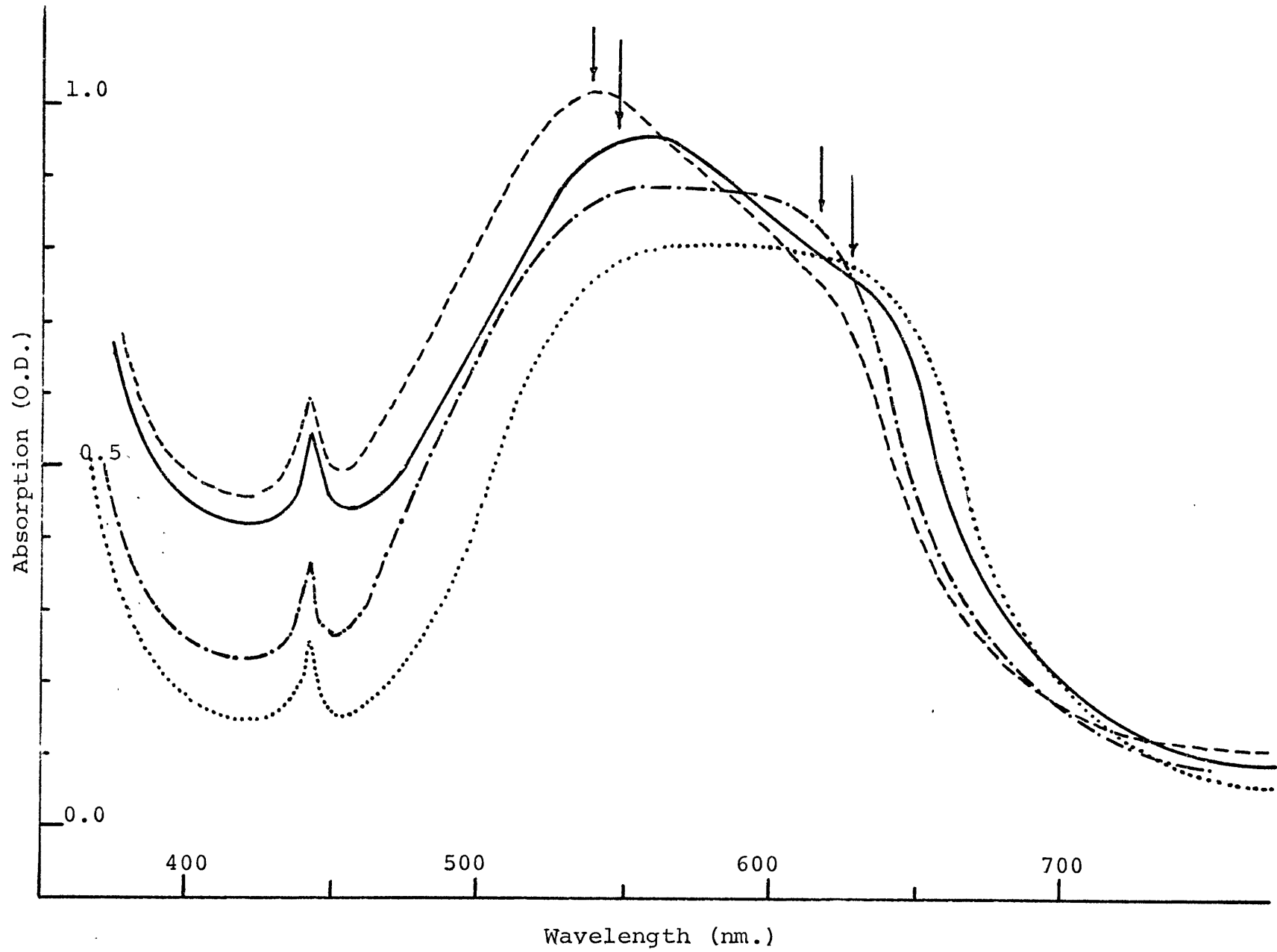
1. The intensity of a C.T. band is proportional to the mole fraction ratio $(\text{Fe}^{2+} + \text{Fe}^{3+})/(\text{Fe}^{2+} - \text{Fe}^{3+})$.
2. The probability of M-M electron transfer is significantly enhanced by edge sharing between the donor and the acceptor polyhedra.
3. The intensity of the C.T. band is proportional to the magnitude of the electric vector component in the direction of the donor-acceptor axis in the crystal structure.
4. The probability of electron transfer increases with decreasing M-M distances, and the energy of the C.T. transition decreases with shortening M-M or M-L distances.

To take the above principles into account, the positional

FIGURE V-1

β and γ spectra of glaucophane measured at 1 atm.
and 50 kb.

a) — β -spectrum, 1 atm.; b) ----- β -spectrum,
50 kb.; c) γ -spectrum, 1 atm.; d) -.-.-.-. γ -spectrum, 50 kb..



parameters of the M_1 , M_2 , and M_3 sites and their interatomic M-M distances and bond angles (MMM) are summarized in Table

V - 1 . From the positional parameters, it is evident that Fe cations in M_1 , M_2 , and M_3 sites occur in a plane perpendicular to the a-axis. Therefore, the electric vector, \vec{E}_{11x} , component along each M-M direction is zero. Consequently, no charge transfer absorption should be observed for the light polarized along the α -indicatrix axis; this prediction conforms with the results obtained above. On the other hand, the components of the electric vector, \vec{E}_{11y} , along the directions M_2-M_3 , M_1-M_3 , and M_1-M_2 are: E, 0.519E, and 0.515E, respectively; and that of \vec{E}_{11z} components along M_2-M_3 , M_1-M_3 , and M_1-M_2 are: 0, 0.857E. Since the intensity of a given charge transfer band is proportional to the projection of the \vec{E} vector along the M-M distance, then the intensity of absorption of light polarized along the β indicatrix for all three possible transitions is expected to be more than that along the γ . This prediction is also consistent with the polarized spectra shown in Figure IV-48.

The occurrence of two charge transfer bands at different energies may be related to the two electron transfer processes $Fe_{M_3}^{2+} \rightarrow Fe_{M_2}^{3+}$ and $Fe_{M_1}^{2+} \rightarrow Fe_{M_2}^{3+}$; in addition, there may be some contribution of absorption arising from $Fe_{M_1}^{2+} \rightarrow Fe_{M_3}^{3+}$ electron transfer or vice versa.

The large widths of absorption charge transfer bands may also be related to the distortion of the M_2 site which contains Fe^{3+} ions. In this site, then, the t_{2g} orbital set of an Fe^{3+}

TABLE V-1

(a) The positional parameters of the M_1 , M_2 , and M_3 sites.

<u>Site</u>	<u>x</u>	<u>y</u>	<u>z</u>
M_1	0	0.0908	0.5
M_2	0	0.1807	0
M_3	0	0	0

(b) The M-M interatomic distances.

<u>M-M</u>	<u>distance (Å)</u>
$M_1 - M_2$	3.09
$M_2 - M_3$	3.206
$M_3 - M_1$	3.099

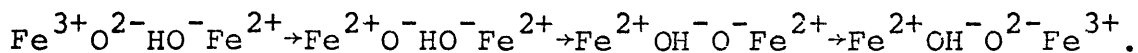
(c) Bond angles \widehat{MMM} .

<u>\widehat{MMM}</u>	<u>angle</u>
$M_3M_2M_1$	59°
$M_3M_1M_3$	62°15'
$M_1M_3M_2$	58°45'

ion may split into two or three levels, and the transferred electron may occupy any of the t_{2g} levels (d_{xy} , d_{xz} , or d_{yz}) depending on the electron transfer excitation energy.

With increasing pressure up to about 50 kb., the charge transfer absorption profile shifted to lower energy and the absorption increased significantly. The magnitudes of the pressure induced energy shifts of the C.T. bands at 16130 and 18350 cm^{-1} is estimated roughly to be 400 and 600 cm^{-1} , respectively, with increasing pressure up to 50 kb.. The rapid shift of the second band to low energy may be due to an appreciable shortening of M_3-M_2 distances relative to M_1-M_2 ; in fact, this could be true since the M_3-M_2 distance is significantly longer than M_1-M_2 . The increase in charge transfer absorption intensity is expected since with decreasing M-M distances, the probability of an electron transfer transition will increase which causes an increase in the transition dipole, μ_{EN} .

It should be mentioned here that the occurrence of water molecules or OH^- groups in the structure coordinated to the transition metal ions facilitate the charge transfer process and may enhance the intensity. This phenomenon was observed by Littler and Williams (1965) who suggested that a possible mechanism of electron transfer ($\text{Fe}^{2+} \rightarrow \text{Fe}^{3+}$) in crocidolite mineral is:



The evidence they gave in support of such a mechanism is the similarity between the activation energy of conduction (16 Kcal.

mole⁻¹) to that of oxidation of crocidolite (21 Kcal. mole⁻¹).

The presence of water in mineral structures was also recognized to be a significant factor in enhancing other electronic processes such as pressure-induced reduction (Gibbons et al., 1974). Such a process will be discussed in Chapter VII.

V-3.2 The Blue-Omphacite

It was mentioned in Chapter IV that x-ray studies of the site occupancies of Fe ions in omphacite (Clark and Papike, 1968) indicated that Fe²⁺ ions are predominant in two sites, M₁ and Ml(1)H, and Fe³⁺ ions occupy mostly the MlH position. In addition, Mössbauer and optical absorption studies (Burns, unpubl. data; Abu-Eid, 1974) on the blue omphacite proved the occurrence of Fe²⁺ ions mostly in two positions with a small fraction in another third site, and Fe³⁺ was found to occupy only one position.

On the basis of the above studies, it is assumed here that Fe²⁺ ions occupy preferentially the Ml and Ml(1)H sites, and a small fraction of Fe²⁺ ions may occur in the Ml(1) position; on the other hand, Fe³⁺ is considered to occupy only the MlH site. From the atomic parameters of the Fe ions in the four octahedral sites (Table V-2a), the M-M distances were calculated and given in Table V-2b . From these distances, it is evident that except for the Ml(1)H-MlH distance (which is 3.112 Å), the remaining M-M distances are significantly large; as a consequence of this, Fe²⁺ → Fe³⁺ electron transfer is unlikely to occur between cations occupying polyhedra other than MlH and Ml(1)H.

TABLE V-2

(a) The atomic parameters of the Fe ions in the four octahedral sites in omphacite.

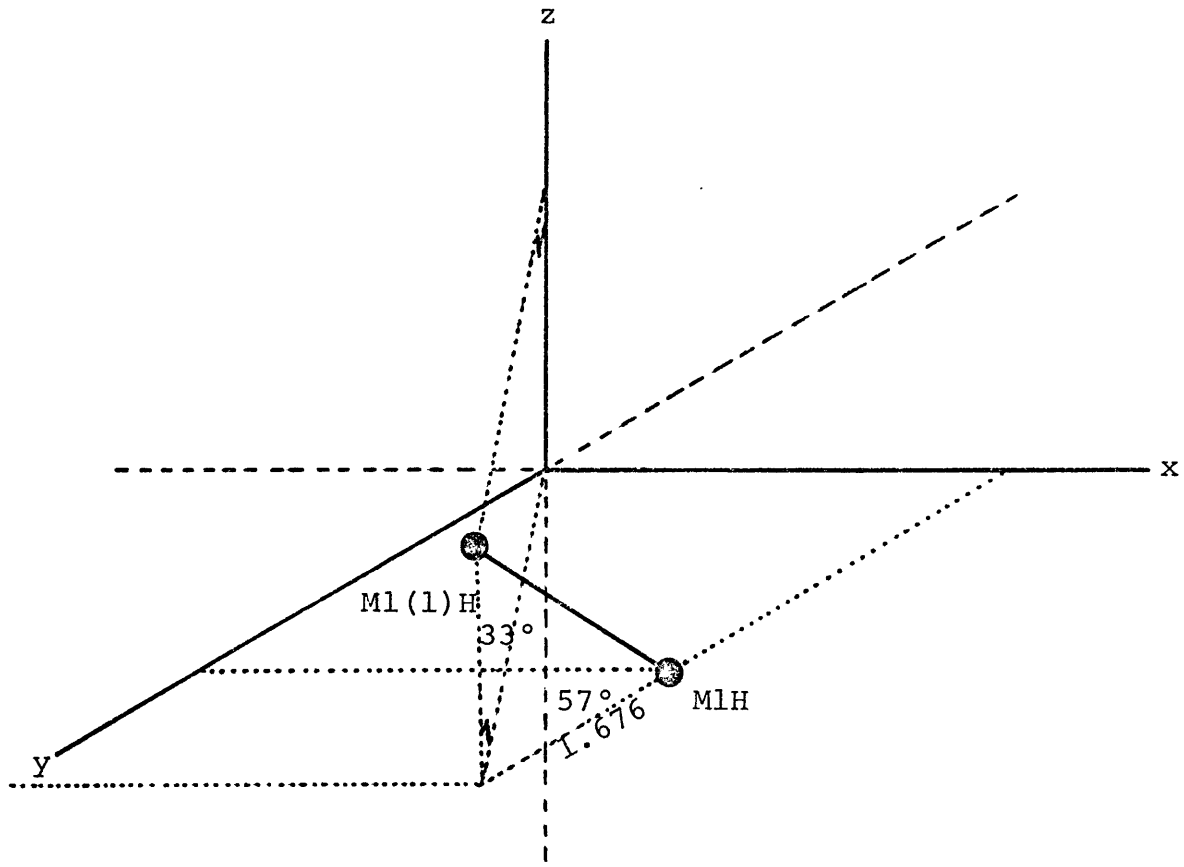
Site	x	y	z
M1	0	7.99	0
M1(1)	0	0.878	2.62
M1H	4.779	3.544	0
M1(1)H	4.779	5.22	2.622

(b) M-M distances in omphacite

M-M	Distance (Å)
M1(1) - M1H	4.756
M1H - M1(1)H	3.112
M1(1)H - M1(1)	6.457
M1 - M1H	6.527
M1 - M1(1)H	5.523

FIGURE V-2

The M1H-M1(1)H direction relative to the x, y, and z-axes.



The absorption band observed in the 1 atm. spectrum (Figure IV-14) at 15037 cm^{-1} is related to the electron transfer between a Fe^{2+} ion in M1(1)H position and a Fe^{3+} cation in the M1H site; the process of charge transfer is also facilitated through the shared edge between two sites.

To predict the relative intensity of the charge transfer band in the three orientations x, y, and z, the M1H-M1(1)H direction was located relative to the three axes x, y, and z, and are shown in Figure V-2 . Since none of the electric vectors along the three major axes (\vec{E}_{11x} , \vec{E}_{11y} , and \vec{E}_{11z}) are perpendicular to the M1-M1(1)H direction, charge transfer absorption is expected to be observed for each crystallographic orientation. Moreover, the most intense absorption is predicted to be the z-spectrum, since the magnitude of the electric vector component, \vec{E}_{11z} , along Fe^{2+} - Fe^{3+} direction is more than the other two components, \vec{E}_{11y} and \vec{E}_{11x} . The polarized charge transfer spectra of the blue omphacite measured at 1 atm. conforms with the above predictions. However, the variation in intensity of absorption is also related to the concentrations of the total iron and titanium; this may suggest a possible contribution of $\text{Fe}^{2+} \rightarrow \text{Ti}^{4+}$ electron transfer absorption to the charge transfer band at 15037 cm^{-1} . Further, for correlation of color and pleochroism in the blue omphacite with the absorption spectra, another factor should be considered. This is the contribution of M-L or L-M absorption near the vis-u.v. regions boundary; this absorption is mostly due to Fe-O and Ti-O electron transfers. Absorption in vis-u.v. region could decrease the width of the

transmission window and then may lead to changes in color.

The charge transfer spectra of the blue omphacite single crystal was measured at pressure around 40 kb. (Figure IV-14). At this pressure, the charge transfer band increased in intensity and shifted to lower energy. The energy shift is approximately 650 cm^{-1} . The pressure-induced red shift of the blue omphacite charge transfer band correlates fairly well with the low energy shift of the glaucophane charge transfer band, and conforms with the predictions made early in this chapter.

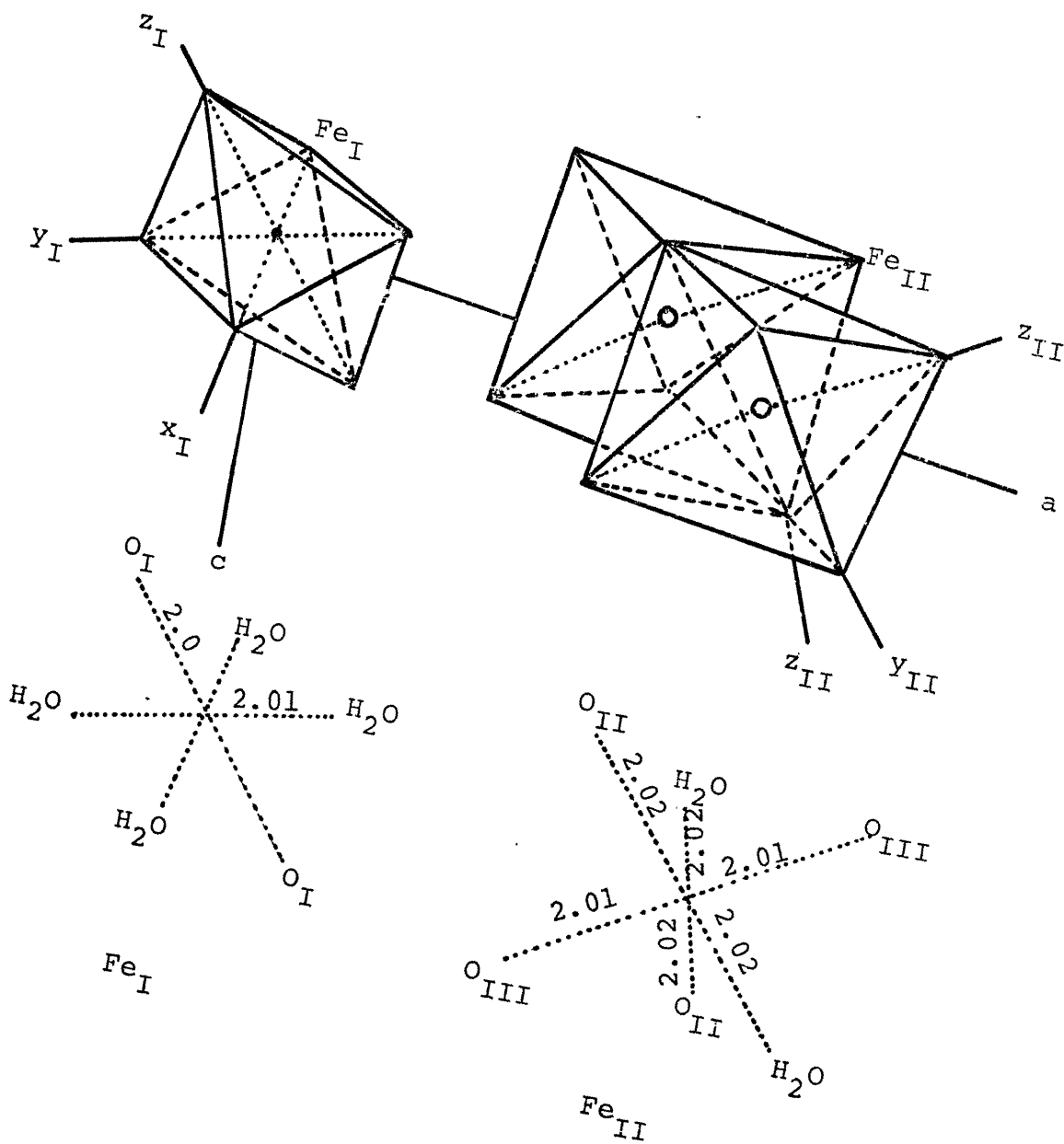
V-3.3 Vivianite: $\text{Fe}_3(\text{PO}_4)_2 \cdot 8\text{H}_2\text{O}$

Vivianite is a rare mineral which has been intensively studied by many crystallographers, mineralogists, and chemists because of its interesting mineralogical and optical properties. Vivianite is usually colorless. However, when it is cleaved and exposed to air, it rapidly turns blue (Hush, 1967; Faye et al., 1968). The color change of vivianite has been related to the oxidation of ferrous ions contained in its structure.

Mori and Ito (1950) determined the crystal structure of vivianite; they found that Fe ions are contained in two octahedral positions denoted by Fe_I and Fe_{II} . The Fe_I site is coordinated to four H_2O molecules and two oxygen atoms, and the Fe_{II} position is linked to two H_2O ligands and four oxygens; the site symmetries and Fe-O distances for both positions are shown in Figure V - 3 . Other significant features in the structure of vivianite are the common O-O edge-sharing of

FIGURE V-3

Fe_I and Fe_{II} site symmetries and M-L distances in
vivianite.



Fe_{II} octahedra and the linkage of Fe_I and Fe_{II} octahedra by means of H₂O-H₂O bonds. Further, the Fe-Fe distances were calculated from the atomic coordinates given by Mori and Ito; these are:

$$\text{Fe}_I - \text{Fe}_{II} = 5.237 \text{ \AA}$$

$$\text{Fe}_I - \text{Fe}_I = 8.396 \text{ \AA}$$

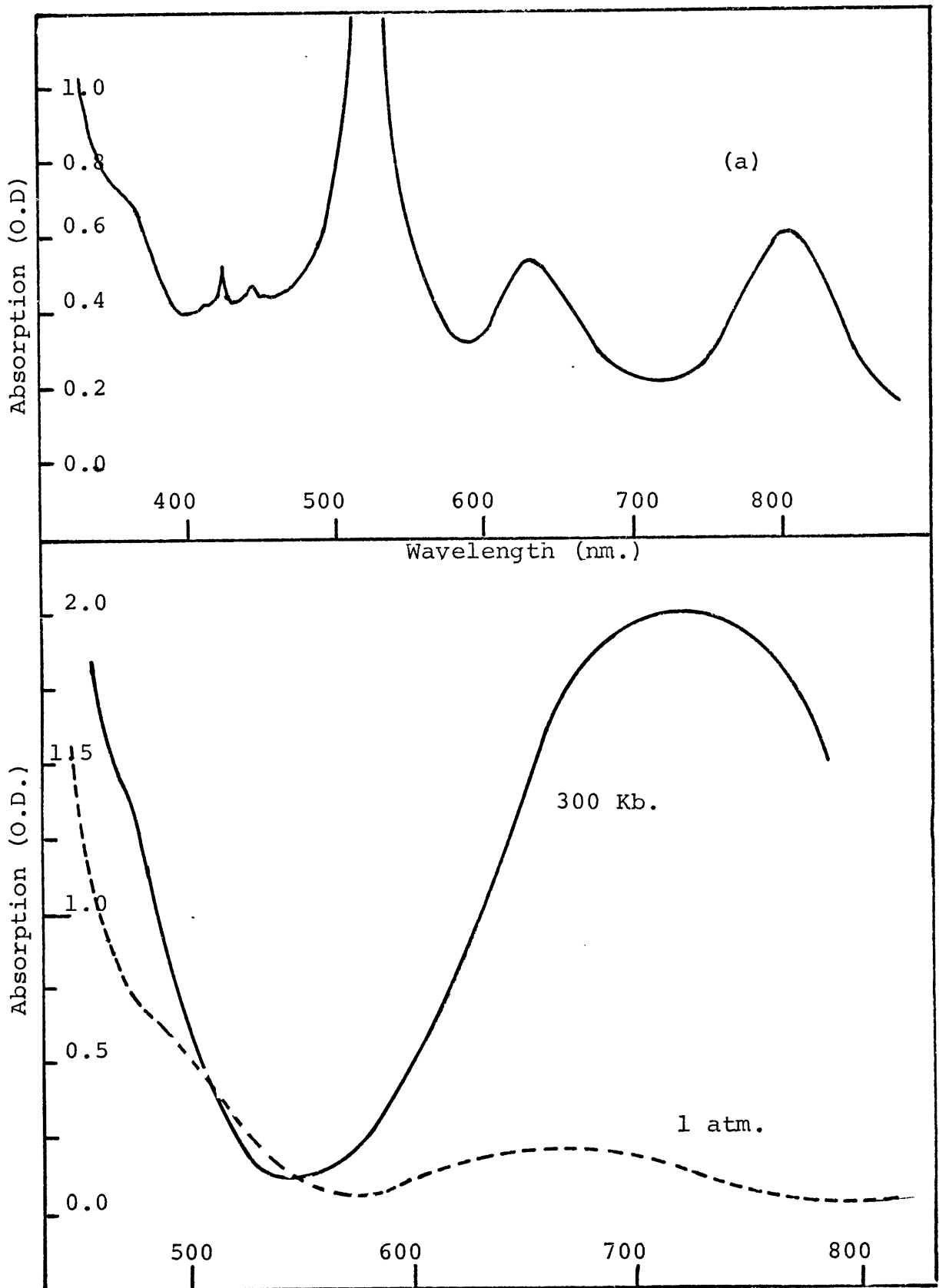
$$\text{Fe}_{II} - \text{Fe}_{II} = 2.921 \text{ \AA}$$

When the ferrous ion is oxidized, Fe³⁺ may occur in the Fe_{II} site. The electron transfer between Fe ions contained in Fe_I and Fe_{II} or Fe_I and Fe_I are unlikely to occur, due to the large interatomic distances. However, it is most likely that electron transfer takes place between ferric and ferrous ions occupying Fe_{II} positions, since the Fe_{II}-Fe_{II} distance is very short.

The absorption spectra of vivianite at 1 atm. was reported by many authors, e.g. Faye et al. (1968); Townsend and Faye (1970); Hush (1967); Robbins and Strens (1972); Mao (1974). The spectrum (Figure V-4) shows two bands in the i.r. region at energies 8200 and 11600 cm⁻¹, and a third broad and intense band at 15400 cm⁻¹. In addition, there are many sharp and weak absorption features in the visible region. Faye et al. (1968) assigned the intense band at 15400 cm⁻¹ to Fe²⁺ → Fe³⁺ charge transfer, and the two bands at 8200 and 11600 cm⁻¹ were assigned to the spin-allowed transitions in Fe²⁺. Furthermore, they related the appearance of these two bands to the dynamic Jahn-Teller mechanism acting in a nearly regular octahedral crystal field.

FIGURE V-4

- (a) Absorption spectra of vivianite at 1 atm.
(from Faye et al., 1968).
- (b) M-M charge transfer spectra of vivianite at
1 atm. and at 300 kb. (Mao, H.K., 1974).



In the present study, the band at 8200 cm^{-1} is assigned to the spin-allowed transition, ${}^5T_{2g} \rightarrow {}^5E_g$, in Fe^{2+} contained in the Fe_{II} position, and the band at 11600 cm^{-1} to Fe^{2+} in the Fe_{I} site. This assignment is supported by the fact that the two sites, Fe_{I} and Fe_{II} , have different average M-O distances; in addition, the M-O distances given by Mori and Ito (1950) for both sites, indicated fairly regular octahedral sites. The sharp and weak peaks in the visible region are assigned to the spin-forbidden transitions in Fe^{2+} and Fe^{3+} in both sites. The assignment of the broad and intense band at 15400 cm^{-1} to $\text{Fe}^{2+} \rightarrow \text{Fe}^{3+}$ electron transfer (Faye, 1968; Hush, 1967) appears to be correct; this is due to its polarization dependence. This band is predicted to have intense absorption along the b-axis and weak or no absorption along a and c axes. This prediction was made by relating $\text{Fe}_{\text{II}}-\text{Fe}_{\text{II}}$ direction to the electric vector components along a, b, and c-axes. Due to the fact that $\text{Fe}_{\text{II}}-\text{Fe}_{\text{II}}$ direction is parallel to "b" and then \vec{E}_{11b} has a one unit component along the $\text{Fe}^{2+} \rightarrow \text{Fe}^{3+}$ direction, whereas, \vec{E}_{11a} and \vec{E}_{11c} have zero components along that direction. This prediction conforms with the polarized spectra of vivianite reported by Faye *et al.* (1968) and Townsend and Faye (1970).

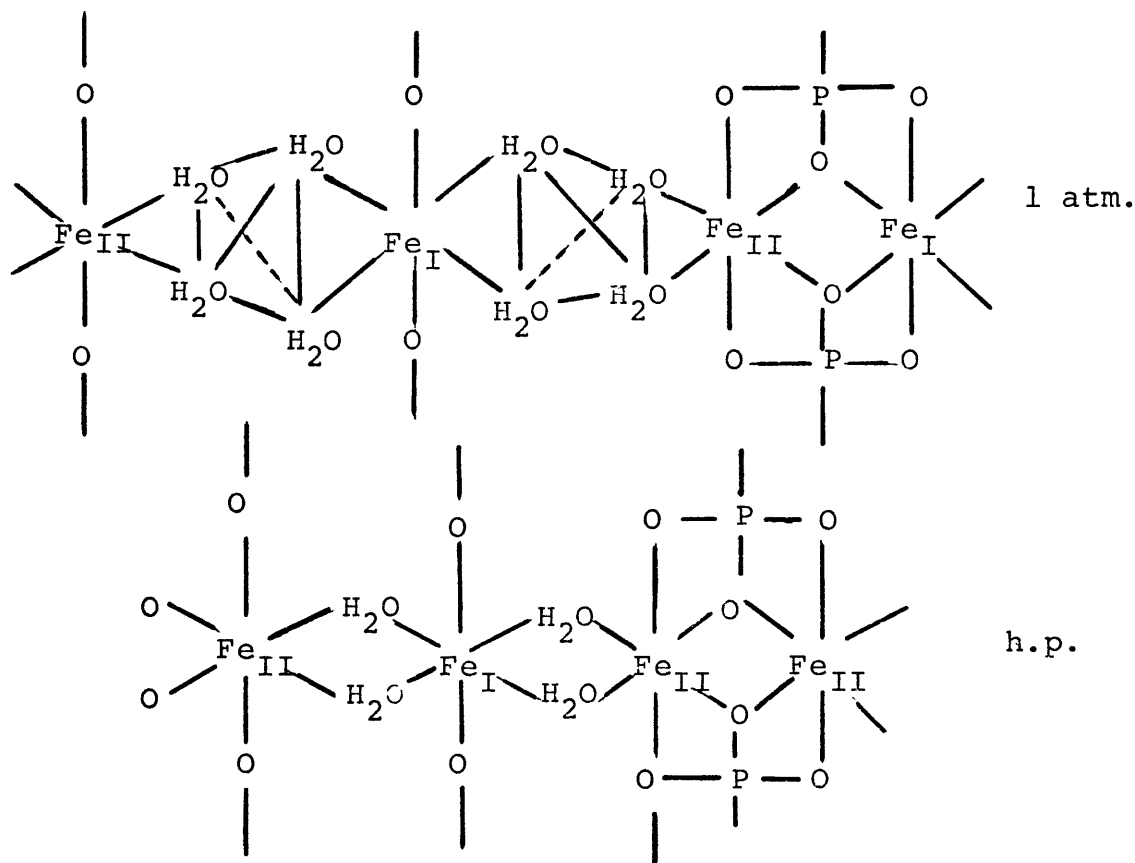
Mao (1975) measured the high pressure optical spectra of vivianite and reported a low energy shift of the C.T. band of about 1100 cm^{-1} in 300 kb.. Mao also indicated that the intensity of the band at this pressure increased 50 times above its intensity at 1 atm., and the color of vivianite changed from a very light blue to a deep green color. Mao, however, did not

give a specific explanation for the tremendous increase in C.T. band intensity, but related the increase to a phenomenon similar to that observed in the high pressure visible spectra of olivine which involves O→M electron transfer.

It was shown in the h.p. spectra of glaucophane and the blue-omphacite that C.T. band intensities increased by about 20 to 50% over 40-50 kb.. Assuming that the same effect takes place in vivianite, it is expected that a five-fold increase in the C.T. band intensity over 300 kb. would be observed compared to its intensity at 1 atm.. This prediction contradicts Mao's observation. Consequently, there may be other factors influencing the C.T. band intensity at very high pressures (300 kb.); they are:

1. A possible change in vivianite structure at 300 kb.. It was mentioned above that the octahedral bands in the structure are linked together by means of H₂O-H₂O hydrogen bond. Since this bond is very weak (Pauling, 1960; Day and Selbin, 1962), it is unlikely to be stable at this elevated pressure. With increasing pressure, the molecular distances, H₂O-H₂O are expected to decrease significantly. As a result, the two water molecules between two adjacent octahedral bands may be expelled from the structure.

The chemical formula may then be written as Fe₃(PO₄)₂·2H₂O, and the structures at 1 atm. and high pressure may be represented as shown below:



The proposed high pressure structural change may lead to a significant decrease in the unit cell parameter "b"; however, the charge balance will not be affected. Assuming that the high pressure structural formula, given above, is correct, then the Fe_I and Fe_{II} interatomic distance will be close to 2.6 \AA , and the Fe cations in Fe_I and Fe_{II} sites will share a common H_2O-H_2O edge. These new structural features could enhance

and facilitate electronic transfer between Fe ions occupied in these two positions, and then lead to an appreciable increase in C.T. band intensity.

2. A possible overlap of crystal field bands over charge transfer bands. The two crystal field bands at 8200 and 11600 cm^{-1} are expected to shift to higher energies with increasing pressure, whereas the charge transfer band shifts to lower energy. At 300 kb., the three spectral bands may be located close to each other so that they may overlap and cause an increase in intensity of the absorption profile.

3. A possible pressure-induced reduction of ferric ions. Pressure-induced reduction processes were reported by Drickamer and Frank (1973); Gibbons et al. (1974); and Burns et al. (1972). Gibbons suggested that the occurrence of OH^- ions enhance appreciably the process of Mn^{3+} reduction. Since vivianite contains substantial amounts of OH^- ions, it is tempting to assume that most of the Fe ions occur in the divalent oxidation state at 300 kb.. If this is the case, most of the absorption may be related to the spin-allowed transition in Fe^{2+} ions.

At this stage, none of the above possibilities could be confirmed or rejected, but it will be advantageous to take the above views into consideration, especially in the theoretical studies of high pressure charge transfer spectra.

V-3.4 Fayalite and Orthoferrosilite

The divalent Fe^{2+} cation is predominant in olivine and pyroxene minerals, and a small fraction of the iron(III) oxida-

tion state may occur in these minerals. Consequently, $\text{Fe}^{2+} \rightarrow \text{Fe}^{3+}$ charge transfer bands may appear occasionally as broad and weak spectral features. As a result of this, it was difficult to study the nature of these bands at elevated pressures. Nonetheless, in the spectra of orthoferrosilite, a broad band was observed at 14500 cm^{-1} , which was assigned to $\text{Fe}^{2+} \rightarrow \text{Fe}^{3+}$ electron transfer (Burns, 1970). The electron transfer in ferrosilite may occur between Fe ions occupying M_1 and M_2 sites through the shared O-O edges; the M_1-M_1 and M_1-M_2 distances are short enough (3.15 and 3.08 \AA , respectively) which makes the process of electron transfer amenable.

In the fayalite spectrum (Figure IV-18), the broad weak absorption at 16260 cm^{-1} was related to $\text{Fe}^{2+} \rightarrow \text{Fe}^{3+}$ charge transfer (Abu-Eid, unpubl. data, 1971; Mao and Bell, 1972a). The ferrous ions occur predominately in M_1 and M_2 sites, whereas the ferric cation may occur in trace amounts in both sites. Charge transfer may occur between Fe ions in olivine, since the Fe-Fe interatomic distances in both sites are relatively short ($M_1-M_1=3.05\text{\AA}$ and $M_1-M_2=3.18\text{\AA}$) and each position shares edges with the neighboring polyhedra. The C.T. band at 16260 cm^{-1} shifted about 400 cm^{-1} to lower energy as pressure increased to 40 kb.. The trend of low energy shift and increase in intensity with pressure of C.T. bands appears to be common in most silicate minerals.

IV-4. Effect of Pressure on M-L and L-M Charge Transfer Absorption

This type of electronic absorption occurs in every mineral

and appears as an absorption edge near the end of the short wave blue region. The absorption maxima of M-L and L-M C.T. bands are rarely obtained since the magnitudes of their integrated intensities are extremely large. The best model which explains their energy values is that of Johnson in which he uses the SCF- X_{α} method (Johnson, 1973) to determine the molecular orbital energy levels of ML_x polyhedra. Johnson's model was used recently by Loeffler et al. (1974) to calculate the energies of M-L and L-M charge transfer absorptions in lunar materials. Moreover, it was also used by Tossell et al. (1973, 1974) to calculate the electronic structure of certain minerals such as rutile and hematite.

In the present study, charge transfer bands will be treated qualitatively using molecular orbital theory and their pressure-induced low energy shift will be explained using M.O. and band gap models. The basis of M.O. theory was discussed in Chapter II and will not be repeated here.

The M-L and L-M charge transfer absorption in all silicate minerals showed a slight red-shift, with increasing pressure. However, some other minerals showed significant low-energy shifts at medium pressures (around 50-60 kb.) and showed also changes in their color. These minerals include crocoite, vanadinite, and hematite. For the purpose of this study, the inorganic compound $KMnO_4$ was also investigated at elevated pressures.

In the following sections, the results of high pressure C.T. spectral studies on these minerals will be presented and interpreted qualitatively by molecular orbital theory.

V-4.1 Crocoite

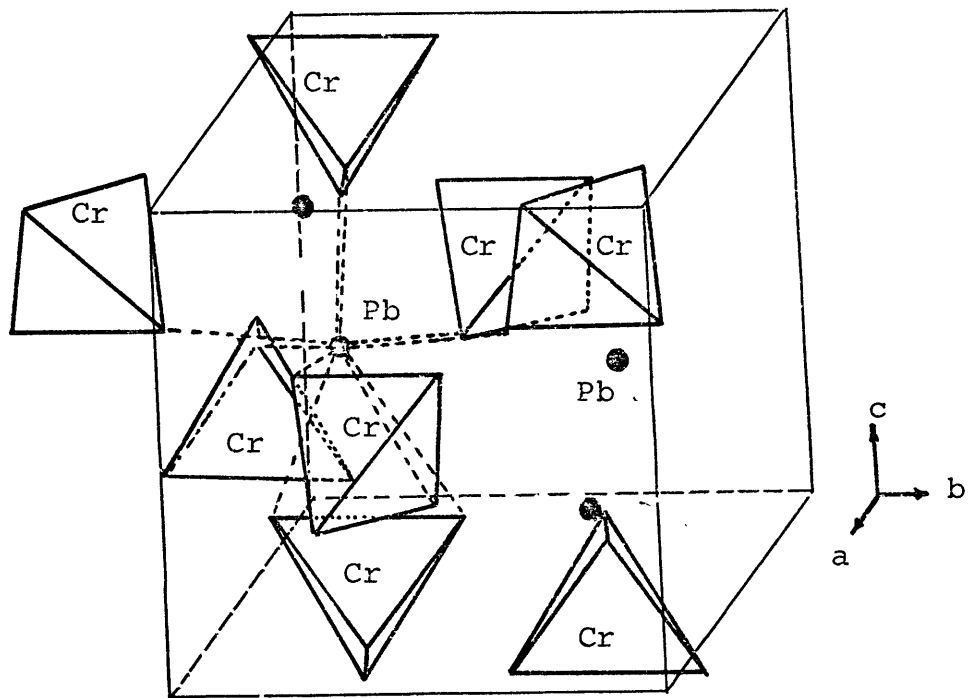
Crocoite [PbCrO_4] contains Cr^{6+} in a distorted tetrahedral site (C_1 symmetry). The structure was determined and refined by Quarenì and De Pieri (1964; 1965), respectively. The chromium atom is surrounded by a tetrahedron of oxygen atoms and the lead atom is surrounded by seven CrO_4 tetrahedra as shown in Figure V-5 . The Cr-O interatomic distances are: Cr-O₁=1.61 Å, Cr-O₂=1.67 Å, Cr-O₃=1.66 Å, and Cr-O₄=1.67 Å. The lead atom is surrounded by ten oxygen atoms with Pb-O distances ranging from 2.53-3.44 Å.

The crocoite sample used in this study (from Dundas, Tasmania, Harvard collection no. 101794) was provided kindly by Professor C. Frondel of Harvard University. The sample has a chemical formula close to the ideal formula given above. However, x-ray studies, using the powder method, indicated that this crocoite sample may contain two isomorphous species, which belong to two different space groups.

Quarenì and De Pieri (1965) studied the crystal structure of crocoite from the same locality (Dundas, Tasmania) as the sample under the current investigation. They reported that it belongs to the monoclinic system, space group $P2_1/A'$, with the unit cell parameters at: $a=7.12\text{Å}$, $b=7.44\text{Å}$, and $c=6.80\text{Å}$. On the other hand, Collotti et al. (1959) reported an orthorhombic modification of synthetic lead chromate PbCrO_4 , which belongs to the space group P_{nma} , and which has cell dimensions $a=8.67\text{Å}$, $b=5.59\text{Å}$, and $c=7.13\text{Å}$. The intensities and d-values of x-ray diffraction

FIGURE V-5

A clinographic projection of the crocoite structure; not the CrO_4^{--} tetrahedral arrangement (from Quarenì and De Pieri (1965)).



(a) Monoclinic			PbCrO ₄	(b)		
d (Å)	I/I ₀	hkl	d (Å)	I/I ₀	hkl	
5.43	10	01 $\bar{1}$	4.40	40	011	
4.96	25	011	4.33	45	200	
4.38	25	11 $\bar{1}$	3.92	30	111	
3.76	12	111	3.70	30	201	
3.48	55	200	3.56	50	002	
3.28	100	10 $\bar{2}$, 120	3.42	70	210	
3.15	12	210	3.29	70	102	
3.03	65	012	3.09	60	211	
3.00	30	11 $\bar{2}$	2.841	45	112	
2.71	16	20 $\bar{2}$	2.798	100	020	
2.60	14	112	2.675	35	301	
2.55	18	21 $\bar{2}$	2.468	25	212	
2.32	14	031, 300	2.347	40	220	
2.25	25	13 $\bar{1}$, 10 $\bar{3}$	2.288	20	103	
2.09	25	212	2.247	35	302	
1.978	20	13 $\bar{2}$	2.231	40	221	
1.847	25	32 $\bar{2}$, 132	2.199	30	022	
			2.166	15	400	
			2.128	60	122	
			2.117	55	113	
			2.020	40	410	
			1.966	20	222	
			1.841	70	402, 303	
			1.771	35	123	
			1.710	55	230	

(c)		(d)	
1 atm.		high pressure (after quenching)	
$d(\text{Å})$	I/I_0	$d(\text{Å})$	I/I_0
5.364	5	4.835	5
4.923	15	4.512	7
4.332	25	4.00	5
3.68	10	3.618	30
3.44	30	3.470	25
3.243	60	3.414	25
3.129	7	3.22	60
3.001	50	2.907	40
2.797	100	2.792	>100
2.692	7	2.305	35
2.588	10	2.225	10
2.525	15	2.114	65
2.311	40	2.071	30
2.235	40	1.948	65
2.147	60	1.815	30
2.08	30	1.806	60
1.955	70	1.748	70
1.838	55	1.512	30
1.788	60	1.447	15
1.746	50	1.430	12
1.685	40	1.398	7
		1.366	20
		1.35	10

lines for the two modifications of crocoite are correlated with those obtained for the crocoite sample used in this study (Tables V-3a,b,c and d). From these tables, it is evident that the most intense x-ray lines of the crocoite sample under the current investigation belong to the orthorhombic modification; however, there are other less intense lines which may belong to the monoclinic form. It should be mentioned that the orthorhombic form of natural crocoite was not reported before. There is a possibility that grinding may be the cause of having the orthorhombic form, if indeed the natural crocoite sample should belong to the monoclinic system.

Since the major concern of this study is to investigate the high pressure spectra of crocoite, rather than its crystal structure, further detailed x-ray studies were not continued.

The absorption spectra of crocoite was measured at 1 atm. for both powder and single crystal specimens. The spectrum showed, in general, very intense absorption in the energy region between 19000-27000 cm^{-1} (Figure V-6a). Because of the huge optical density of this band, the absorption maximum was unable to be monitored until a very thin crystal fragment (about 25 μ in diameter) was used in the sample beam. The low energy absorption edge measured at 1 atm. (Figure V-6a) starts at a wavelength 550 nm (18180 cm^{-1}), and there appears to be three absorption bands under the broad, intense absorption profile which extends from 19000 to 27000 cm^{-1} . The three bands were located at energies 19600, 21280, and 23530 cm^{-1} . These bands are assigned to ligand to metal electronic transfer transitions.

FIGURE V-6

- (a) The visible spectrum of crocoite crystal fragment measured at 1 atm. (the crystal exhibits orange color).
- (b) Absorption spectrum of crocoite powder subjected to pressure around 20-30 kb. (the color changes around this pressure from orange to red; note the shift of the absorption edge).
- (c) The absorption spectrum of crocoite measured at pressure around 60 kb. (the color changes from red to black; note the tremendous shift of the absorption edge).

CROCOITE PbCrO_4

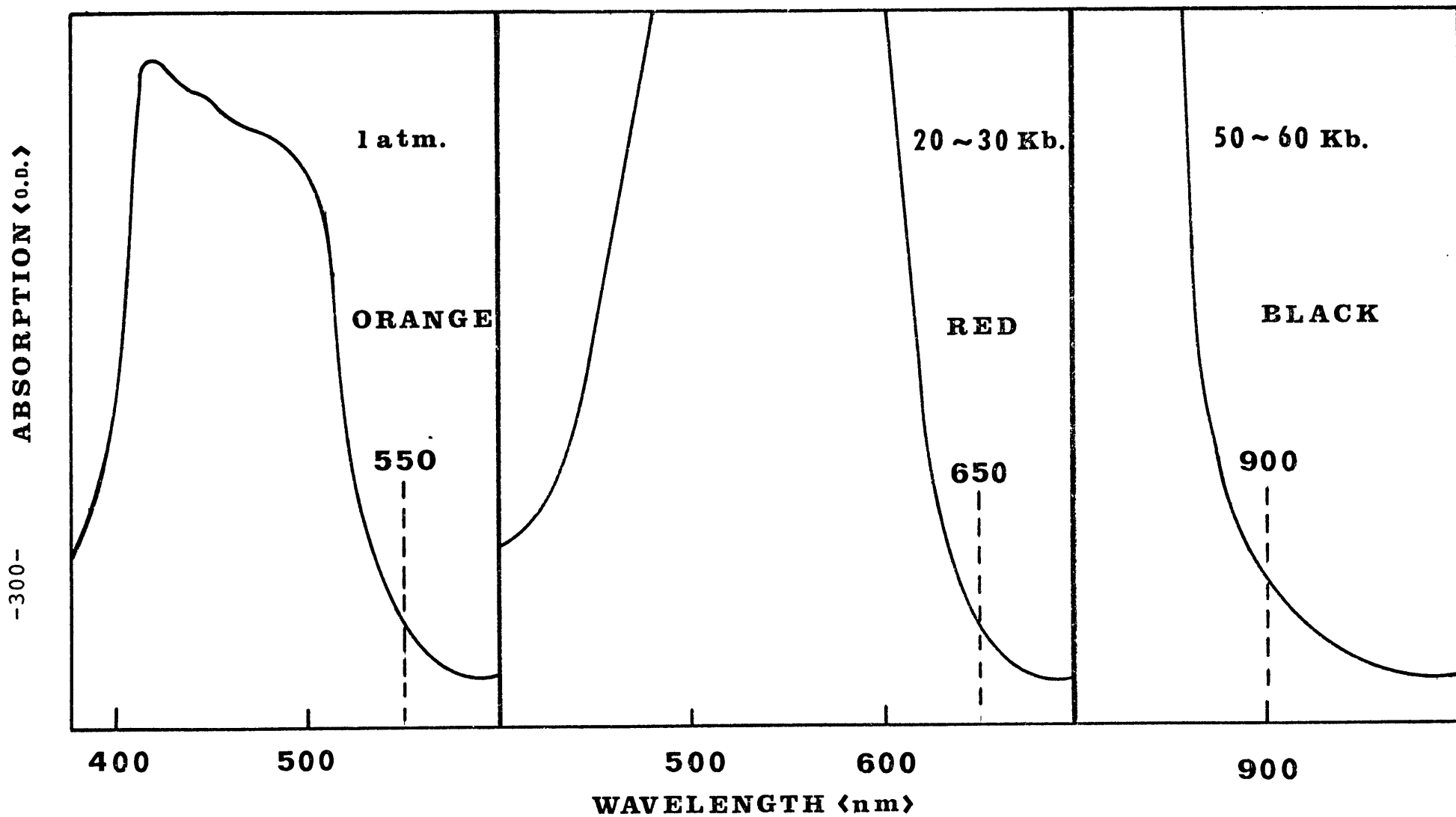
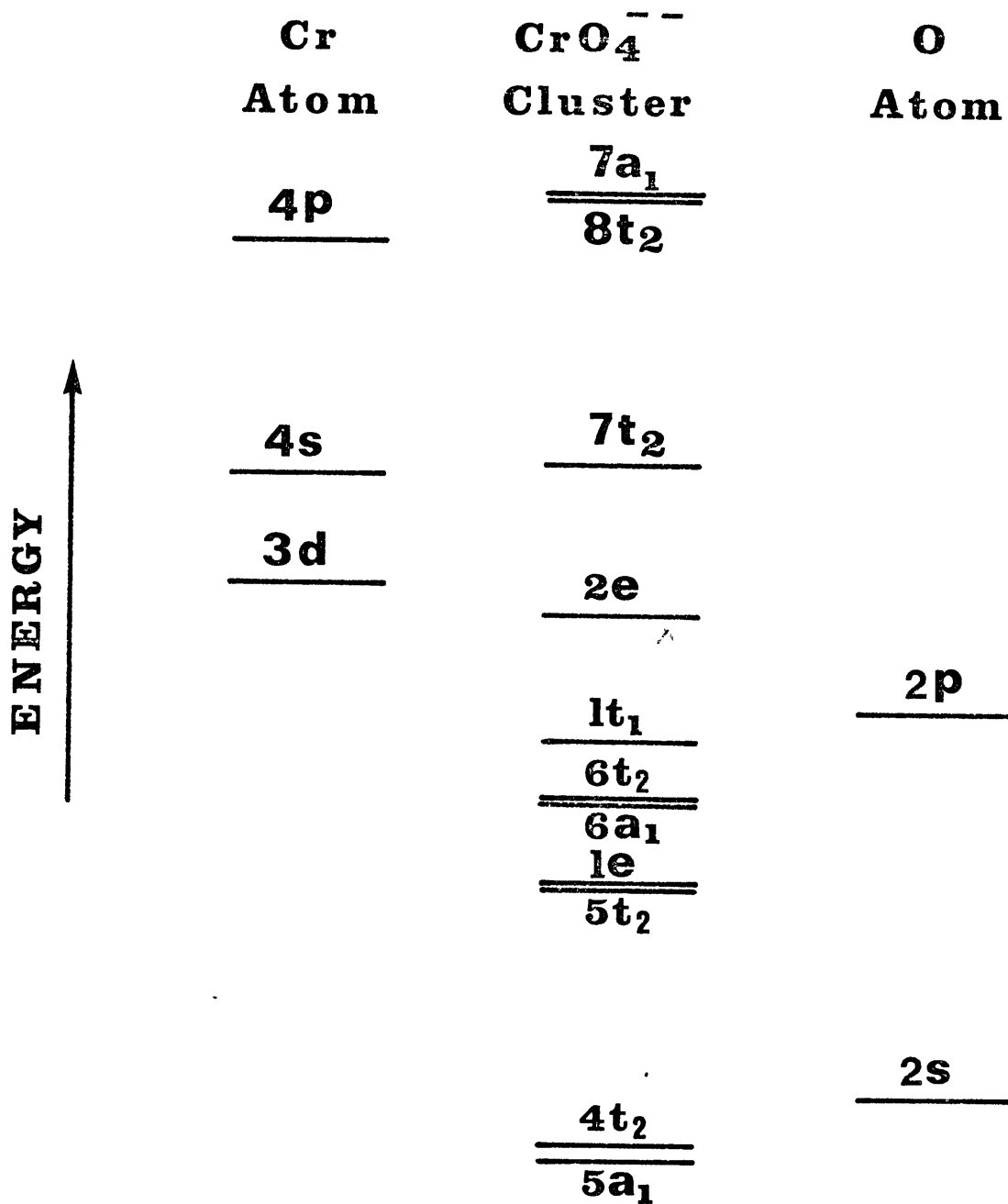


FIGURE V-7

The molecular orbital energy level diagram of the tetrahedral chromate ion (modified from the energy levels of CrO_4^{--} (Wolfsberg and Helmholz, 1952) and MnO_4^- levels (Johnson, 1973)).



CrO₄²⁻ MO Electronic Energy Levels

It is believed that the splitting of the major absorption features into their bands is caused from the distortions of the CrO_4 tetrahedron (there are three different Cr-O distances).

As it was mentioned earlier, the mechanism of charge transfer transitions cannot be explained using crystal field models; molecular orbital theory provides satisfactory explanations for such kinds of transitions.

For this purpose, the molecular orbital energy level diagram for the tetrahedral chromate ion (Figure V-7) was constructed schematically, based on data of Wolfsberg and Helmholtz (1952) and Johnson (1973) who reported energy levels for the complex ion, MnO_4^- . In this figure, the levels below $2e$ are filled with electrons, and the levels above $1t_1$ are empty (no d electrons for Cr^{6+} ions); the broad band in the visible spectra of crocoite is due to electron transfer from $1t_1$ to the $2e$ level.

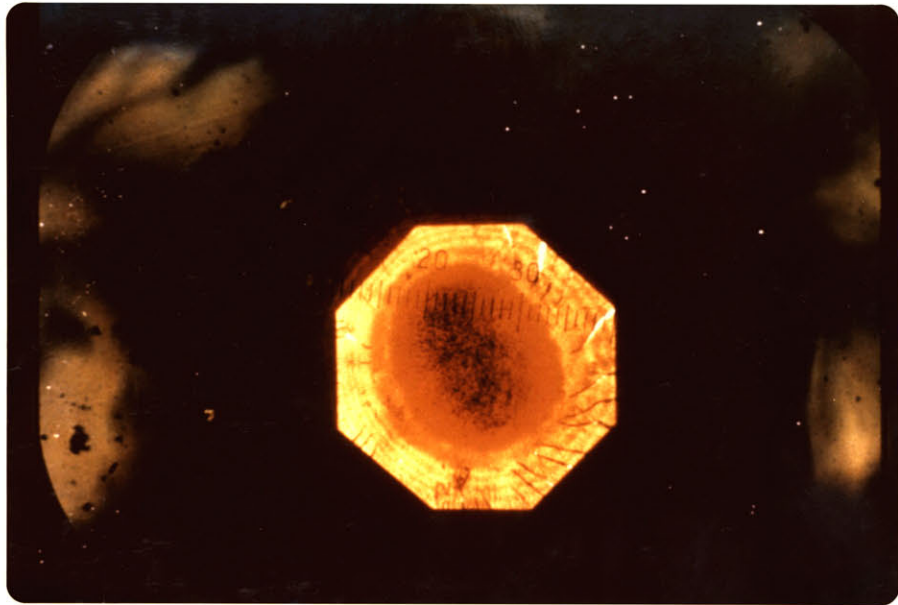
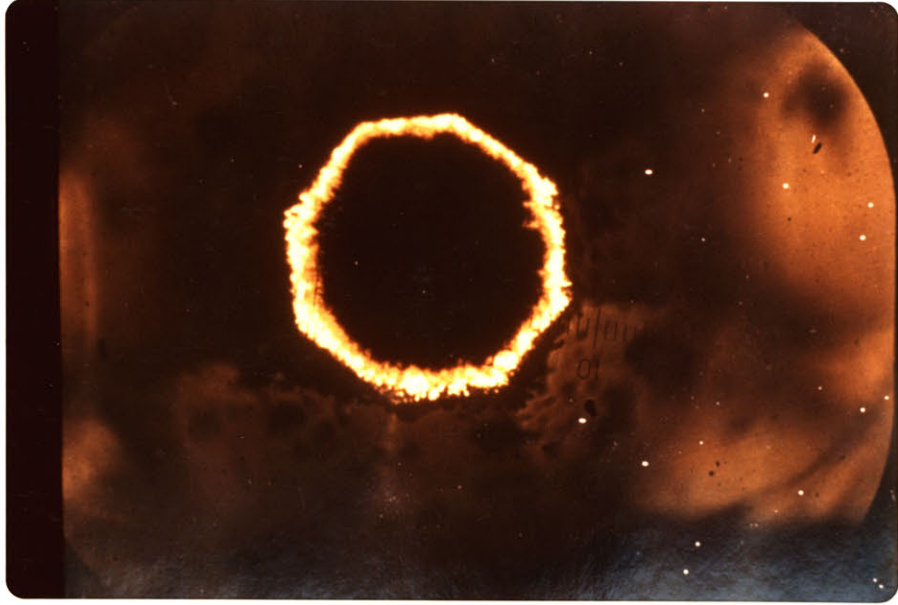
With increasing pressure, the energy separation between the two levels, $7t_2$ and $2e$, will increase and then the energy gap between $1t_1$ and $2e$ levels will decrease. So, it is expected that a red shift of the charge transfer band will be observed as pressure increases.

At pressures around 20-30 kb., the band increased in width and intensity, and the absorption edge shifted to about 650 nm (15380 cm^{-1}) (Figure V-6b). This shift is remarkably rapid (about 3000 cm^{-1} in 25 kb.) and is accompanied by a color change from orange to red (Figures V-8a,b).

Increasing the pressure further to about 50-60 kb. causes

FIGURE V-8

- (a) A photograph of crocoite sample subjected to 100 kb. in the diamond cell.
- (b) This photograph was taken when the pressure was lowered to 60 kb. (note the black, red, and orange regions).



the absorption edge to shift further towards the infrared region to about 900 nm (11100 cm^{-1}) (Figure V-6c), i.e. there is a negative energy shift of about 7500 cm^{-1} in 55 kb.. A color change, red to black (Figure V-8a,b) was also observed at this pressure; the high energy limit of this band could not be reached due to the huge increase in the band width and intensity. It should be mentioned that after releasing the pressure, the color changed back from black to red, and the absorption edge shifted to higher energy. At normal pressure, the recovered sample showed an orange-red color, which appeared to be darker than the color of the sample before it had been subjected to pressure. The spectrum of the recovered sample showed an intense absorption in the visible region and the absorption edge was located at 16500 cm^{-1} , i.e. it occurred at lower energy than where it was before applying pressure.

The x-ray diffraction pattern of the recovered sample was measured (Table V-3d) and compared with that obtained at 1 atm. before applying pressure. From the data in Tables V-3c and V-3d , it is apparent that most of the d-values have decreased, indicating that there is some remaining locked-in strain on the sample. It is also apparent from the two tables that there are no significant irreversible changes in the structure.

The rapid shift of the absorption edge is well explained in the molecular orbital energy level diagram shown in Figure V- 7 . Nevertheless, some changes in the electronic and/or physical properties may occur as a result of decreasing the

energy separation between $1t_1$ and $2e$ levels. When these two levels become close to each other, one or more electrons may become stable in the $2e$ level, since this level primarily belongs to the chromium ion. The Cr(V), Cr(IV), or Cr(III) oxidation states may be stabilized as long as the pressure is applied. Assuming that Cr(VI) has been reduced, then crystal field transitions should be observed for chromium ions of lower oxidation states. Unfortunately, these transitions occur at energies where the L-M charge transfer transition occurs, and they may be obscured by the absorption edge. Decreasing the energy separation between the highest energy levels in the valence band and lowest energy level in the conduction band should increase the electrical conductivity of the mineral. Where these levels become close enough to each other, the mineral may exhibit metallic character.

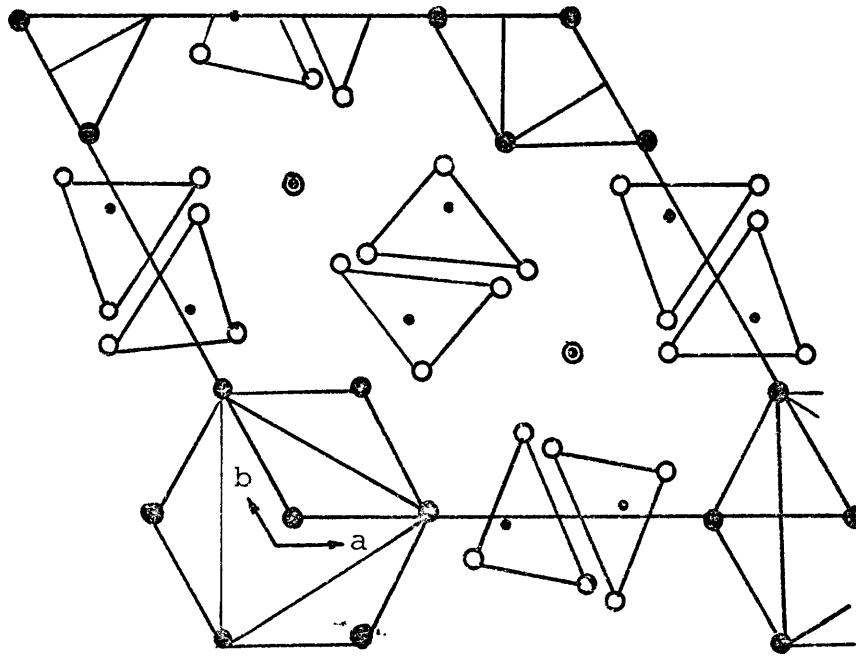
The rapid red shift of the absorption edge and the associated color change is not fully understood yet, but it may be related to: (a) pressure-induced reduction of Cr^{6+} to lower oxidation states, or (b) to changes in the structure, or (c) to closing the energy gap between conduction and valence bands. However, all these phenomena may actually take place at elevated pressure, since they are inter-related.

V-4.2 Vanadinite $[\text{Pb}_5(\text{VO}_4)_3\text{Cl}]$

Vanadinite is a rare mineral which contains vanadium in the penta-valent oxidation state. The structure, determined by Trotter and Barnes (1958), belongs to the space group $P6_3/m$

FIGURE V-9

A projection of vanadinite structure on the
c-axis (from Trotter and Barnes, 1958).



- vanadium
- ⊙ 2 lead
- chlorine
- lead

and has the unit cell dimensions: $a=10.331\text{\AA}$ and $c=7.343\text{\AA}$. The projection of vanadinite structure on the c-axis (Figure V-9)

shows the vanadium atoms each of which is coordinated to four oxygens forming a VO_4 tetrahedron; the Cl^- anion is shown surrounded by six Pb^{2+} cations at the corners of a regular octahedron. The VO_4 tetrahedron is fairly distorted; the V-O distances are $1.76\text{\AA}(2)$ and $1.72\text{\AA}(2)$, and the O-O distances vary from 2.56\AA to 3.01\AA .

At normal pressure vanadinite is translucent and has an orange-red color. The spectrum at 1 atm. was measured in the visible region; no spectral features were observed in this region, except for an absorption edge which starts at about 18900 cm^{-1} and extends into the u.v. region. However, when a very thin crystal fragment was used, the absorption maxima of two bands were identified at energies 22750 and 25650 cm^{-1} (Figure V-10a). These two bands are related to electron transfer from energy levels of principally ligand character (belonging to the oxygen ligands) to the empty lower energy d-levels, "e", of a V^{5+} cation. The occurrence of two bands in the spectrum may be due to the two different V-O interatomic distances. The occurrence of those bands at energies higher than those observed in the spectra of crocoite may be due to the longer ligand-cation distances in vanadinite.

With increasing pressure, the C.T. absorption increased in width and intensity, and the absorption edge shifted rapidly to lower energy (Figures V-10b,c). The low energy shift of

FIGURE V-10

- (a) Absorption spectra of a vanadinite crystal fragment measured at 1 atm. (the crystal exhibits orange-red color).
- (b) The spectra of a powdered crocoite sample subjected to pressure around 30-40 kb. (the color is deep red at this pressure; note also the low-energy shift of the absorption edge).
- (c) The spectrum of crocoite sample at pressure around 80 kb. (the color changed to black and the absorption edge shifted far into the i.r. region).

VANADINITE

-312-

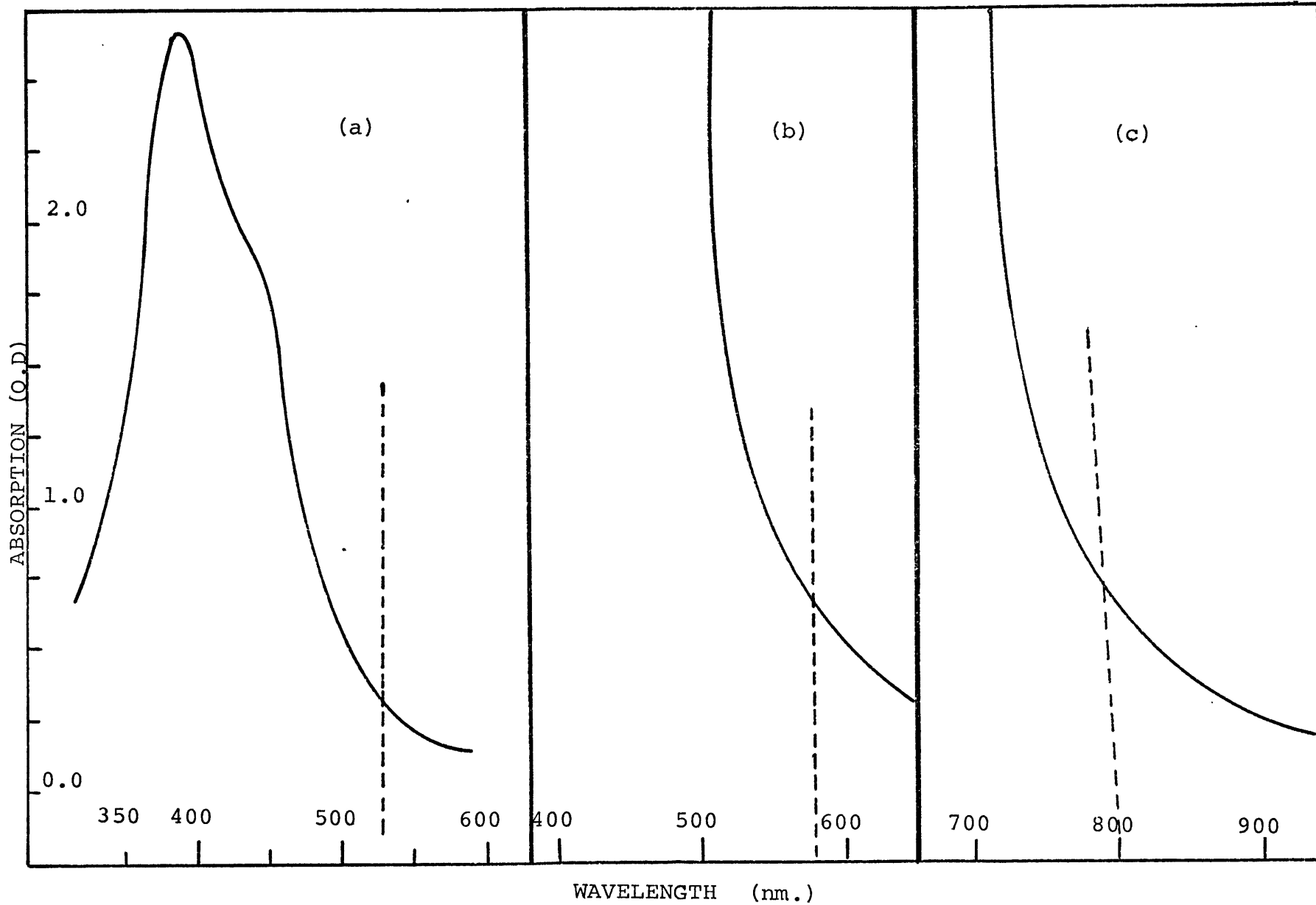
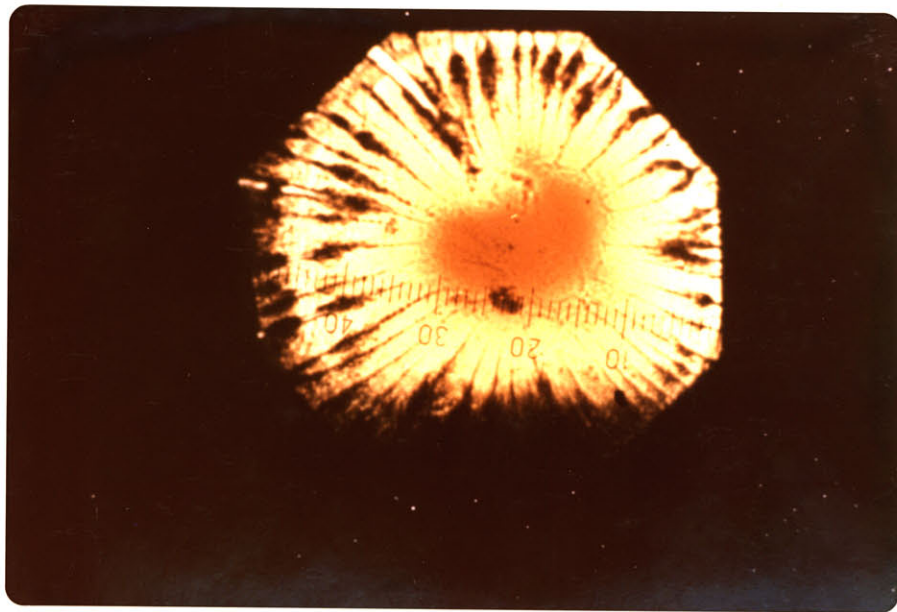
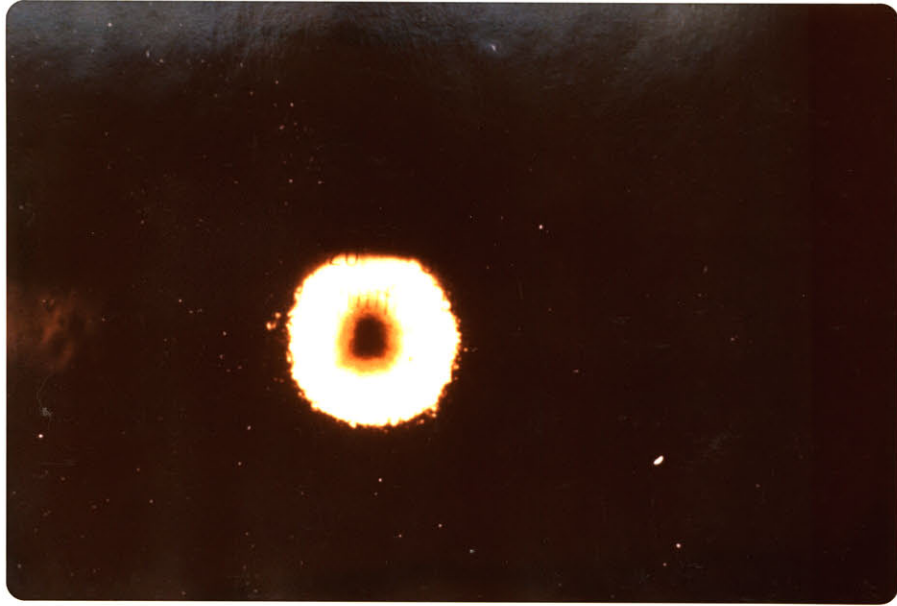


FIGURE V-11

- (a) A vanadinite sample subjected to about 80 kb. at the central region of the diamond anvil. Note the three colored zones: black, red, and orange.
- (b) A photograph showing a crocoite sample subjected to high pressure and quenched rapidly in the diamond cell.



the absorption edge produced a change in color from orange to deep red color, and then to black, (Figures V-11 a, b). The color change in this case occurred at higher pressures than crocoite, and the phase boundaries were more distinct.

The phenomenon of pressure-induced color change and the rapid low energy shift in vanadinite appears to be exactly the same as the one observed in crocoite. Thus, the explanations given for this phenomenon in crocoite may be applied to vanadinite as well.

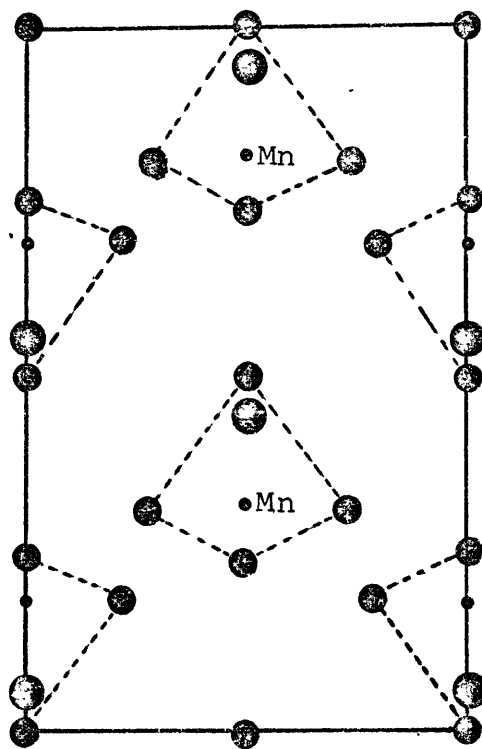
V-4.3 Potassium Permanganate: KMnO_4

KMnO_4 was used in this study to examine further the influence of pressure on charge transfer spectra of d^0 transition metal ions. It was also used because it is a strongly oxidizing agent, because it contains Mn(VII) which could be reduced easily to the lower oxidation states. The crystal structure of KMnO_4 has four distinct MnO_4^- anions and four K^+ ions; the Mn-O distances and the site symmetry of the MnO_4^- tetrahedra are shown in Figure V-12 .

The optical spectrum (vis.-u.v.) of KMnO_4 was measured by Holt and Ballhausen (1967). It consists of four absorption bands at energies 18550, 28250, 32360, and 44450 cm^{-1} . Johnson (1973) investigated the electronic structure of KMnO_4 , using the SCF- X_α Scattered Wave Method, and assigned those bands to the transitions: $1t_1 \rightarrow 2e$; $6t_2 \rightarrow 2e$; and $5t_2 \rightarrow 2e$, respectively. It should be mentioned that the M-O energy level diagrams of MnO_4^- ions is similar to that of CrO_4^{--} shown in Figure V-7.

FIGURE V-12

Crystal structure of KMnO_4 projected on (001)
(from Mooney, 1931).



- Mn
- O
- K

Consequently, the reader is referred to that figure to understand the electronic transitions involved in the MnO_4^- ion.

In the present study, the spectrum of KMnO_4 powder was measured in the i.r. and visible regions at various pressures. At normal pressure, an extremely intense absorption band was observed at 18870 cm^{-1} . In addition, the low energy limb of another band was identified as an absorption edge which starts off at 24000 cm^{-1} . The absorption maxima of this band could not be located due to the energy limit of the spectrophotometer, which is 27500 cm^{-1} . This absorption edge could be related to the low-energy limb of the absorption band at 28250 cm^{-1} (reported by Holt and Ballhausen (1967)).

The color of KMnO_4 at normal pressure is deep purple; this color is related to the observed transmission window in the energy region $22000\text{-}24000 \text{ cm}^{-1}$. With increasing pressure, the absorption band at 18870 cm^{-1} and the absorption edge at 24000 cm^{-1} shifted substantially to lower energies. When the powdered KMnO_4 specimen was subjected to about 60 kb. between the two diamond anvils and observed under the microscope, three color regions across the anvil face were identified (Figure V-13). The central region, where the pressure maximum is about 60 kb., has a higher refractive index than the other regions, and has a very deep red-black color. The intermediate zone has a red-pinkish color, and the outside zone has a violet or purple color. The absorption spectrum for each color zone was measured in the i.r. and visible regions (Figure V-14 a,b). The spectrum of

FIGURE V-13

A photograph of KMnO_4 subjected to about 60 kb..

Note the three colored zones.

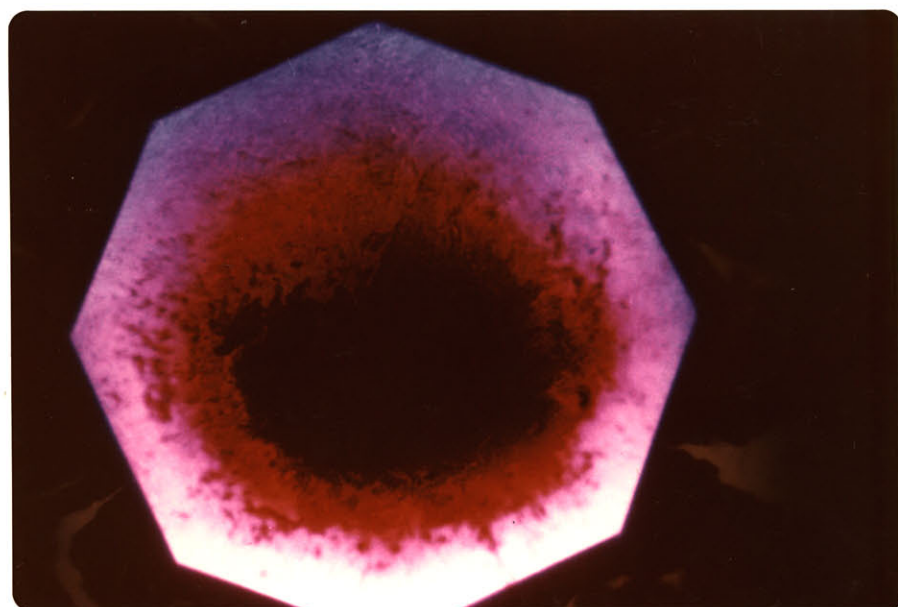
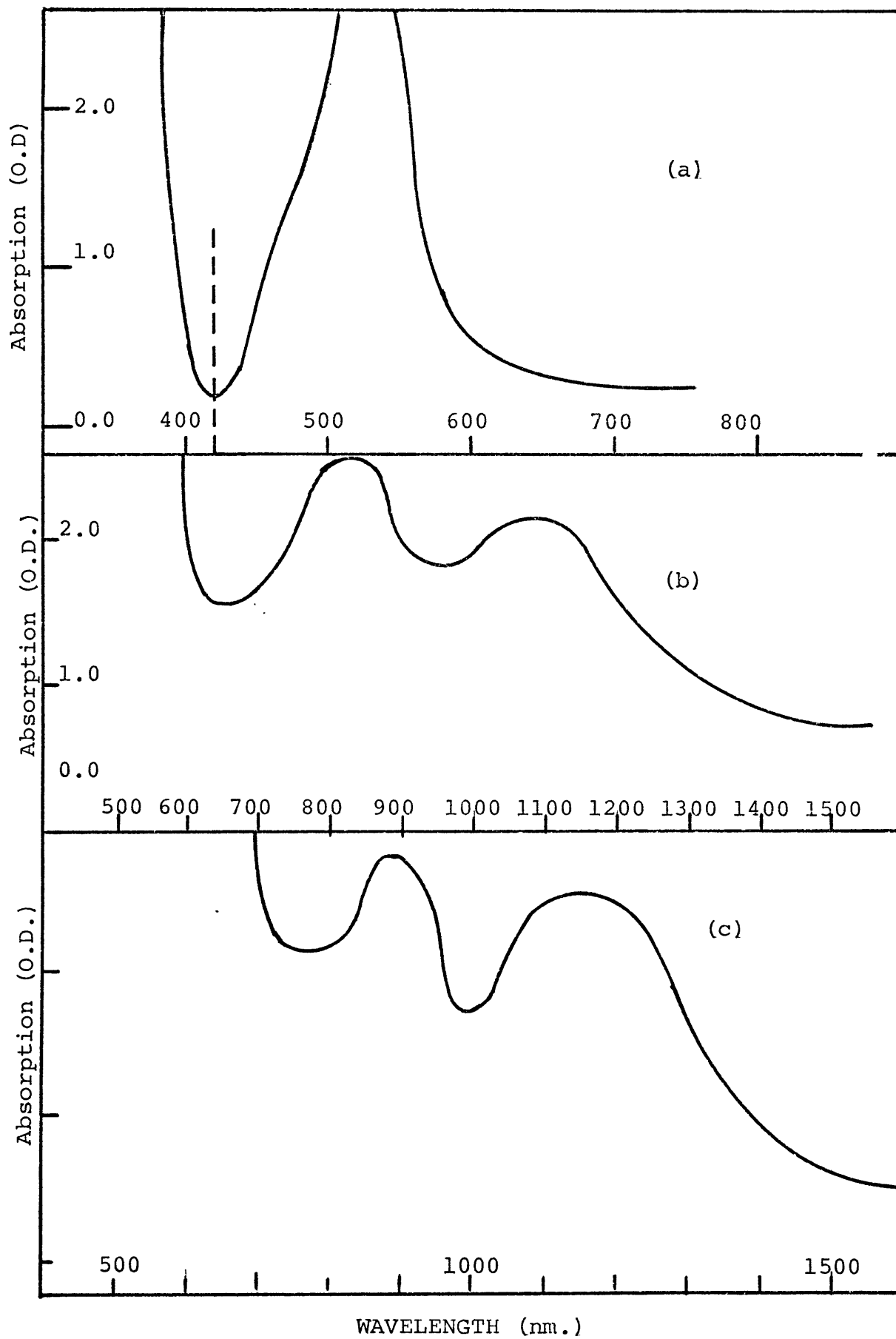


FIGURE V-14

The absorption spectra of KMnO_4 sample subjected to elevated pressures in the diamond anvil press.

- (a) ————— the spectrum measured at low pressure (pink color)
- (b) ----- the spectrum of the red zone (medium pressure).
- (c) the spectrum of the dark-central zone.



the red-black zone (Figure V-14b,c) consists of a very broad and intense absorption band which extends from 7000 cm^{-1} to 10150 cm^{-1} . The maximum of this band was located at 8700 cm^{-1} ; another band of smaller width and intensity was also observed at 11110 cm^{-1} . There is a narrow transmission window in the energy region $12000\text{-}15000 \text{ cm}^{-1}$, which may be the cause of the observed deep red color. The spectrum then showed an absorption edge which started at 15150 cm^{-1} and swept the remaining part of the visible region. The absorption bands at 8700 and 11110 cm^{-1} in the high pressure spectrum are assigned to the two transitions $1t_1 \rightarrow 2e$ and $6t_2 \rightarrow 2e$. The broad absorption in the visible region could be related to the third transition $1t_1 \rightarrow 7t_2$.

From the above results, it is evident that the energy separations between the molecular orbital energy levels have decreased significantly which may cause the stabilization of one or more electrons in the d-level $2e$. In fact, there may be some contribution of absorption which may be related to the crystal field transition, $2e \rightarrow 7t_2$.

The spectrum of the violet zone near the anvil periphery is similar to the spectrum obtained at 1 atm., while the spectrum of the intermediate zone showed spectral features similar to the central zone, but the absorption bands were located at higher energies. It appears that pressure-induced reduction of Mn^{7+} may have occurred; however, crystal field bands arising from lower oxidation states may have been masked by the charge transfer absorptions. It is also quite possible that the KMnO_4 was changed, since there is an apparent evidence of changes in the

optical properties and the refractive index.

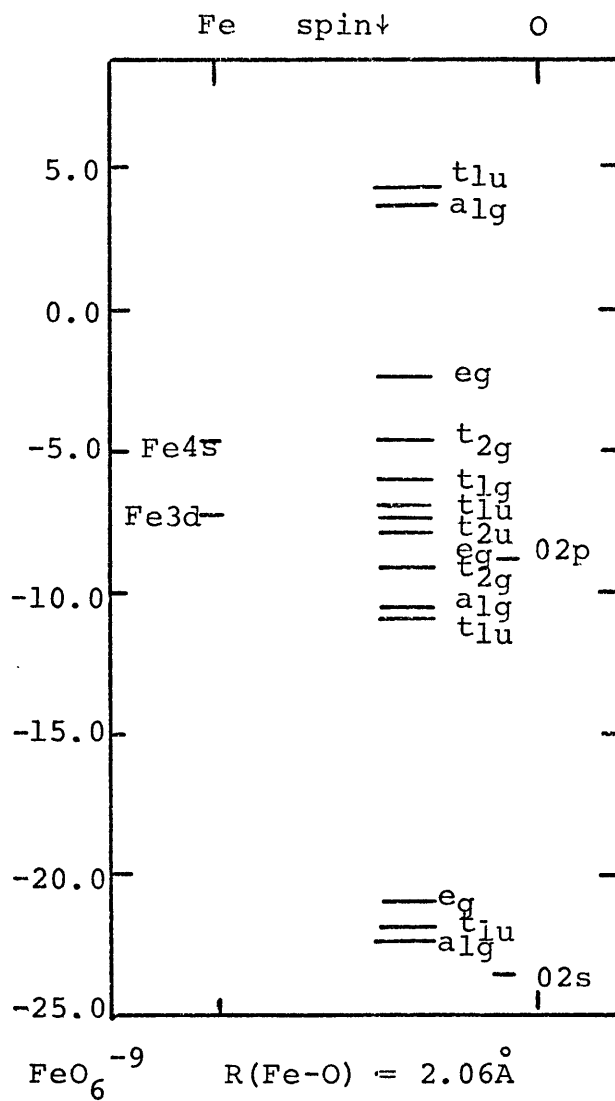
V-4.4 Hematite: Fe₂O₃

The crystal structure of hematite is similar to that of corundum (α -Al₂O₃), which was determined by Bragg and Bragg (1916) and re-examined by Willis and Rooksby (1952) and Newnham and de Haan (1962). It consists of oxygen atoms arranged in hexagonally close packed layers. Successive oxygen layers enclose Fe³⁺ cations between them in fairly regular octahedral positions with the longest Fe-O distance being 2.09Å and the shorter one 1.96Å. Further, each Fe-octahedron shares one of its edges and one face with two different octahedra. The diffuse reflectance spectrum of Fe₂O₃ was reported by Vratny and Kokalas (1962) and Tandon and Gupta (1970). The former authors observed three spectral features at 17750, 15330, and 9680 cm⁻¹, and related them to electronic transitions from the valence band to the conduction band in Fe₂O₃. On the other hand, the latter authors reported five spectral features at energies 11630, 21500, 28570, 34480, and 43900 cm⁻¹. They related the first two bands to crystal field transitions in Fe³⁺, and the remaining three bands to electron transfer transitions. Tossell et al. (1974) studied the electronic structure of hematite using molecular orbital theory and constructed M.O. energy level diagrams for the FeO₆⁹⁻ ionic cluster (Figure V-15). They calculated the lowest L-M charge transfer transitions in ferric ions to occur at 25300 cm⁻¹ (1t_{2u}→2t_{2g}) and at 29400 cm⁻¹ (1t_{2u}→2t_{2g}).

In the present study, the spectrum of hematite at normal

FIGURE V-15

M.O. energy level diagram for FeO_6^{9-} ionic cluster
(from Tossell et al., 1974).

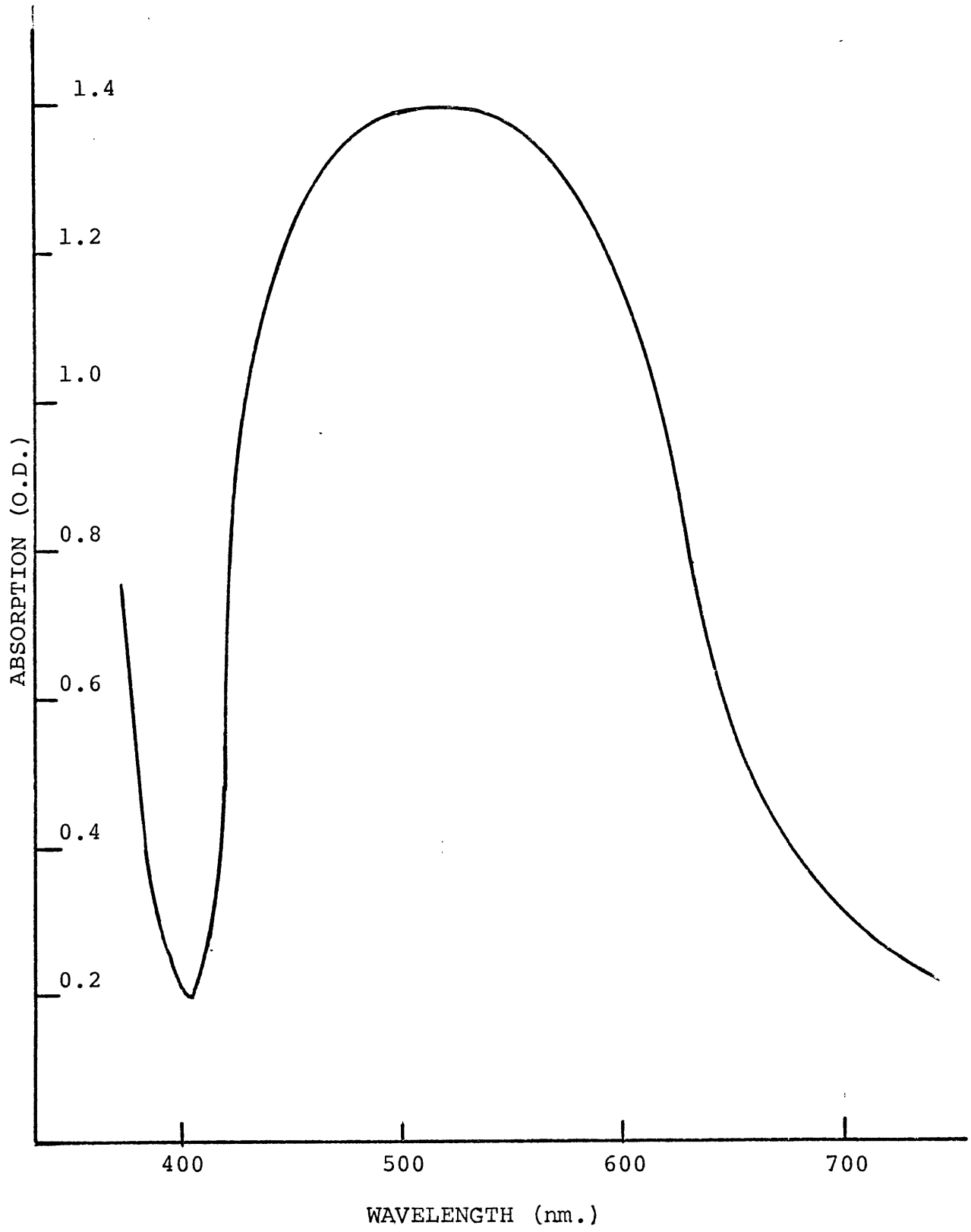


pressure could not be obtained due to the immense optical density which causes the hematite mineral to be almost opaque. To enable the absorption spectral measurement to be made, a hematite powdered sample was placed between the diamond anvils and subjected to high pressures. The sample was observed to become partly transparent at pressure around 100 kb. and showed a deep red color; increasing the pressure to about 200 kb., the hematite sample turned a black color. After releasing the pressure and recovering the sample, the spectrum was measured at normal pressure (Figure V-16). It consists of an extremely intense and broad absorption band which extends from 14300 cm^{-1} to 26300 cm^{-1} ; the maximum of the band was located at about 19400 cm^{-1} . The spectra of hematite were also measured while the sample, between the diamond anvils, was at pressures around 100 kb. and 200 kb.. The spectrum at 100 kb. showed a similar broad and intense absorption band with maximum at about 17800 cm^{-1} , whereas the spectrum measured at 200 kb. showed that the band had shifted significantly into the i.r. region where its maximum could not be located.

The broad absorption band at 19400 cm^{-1} observed in the hematite appears to be the same band reported by Tandon and Gupta (1970) occurring at 21500 cm^{-1} . However, this band may have shifted to lower energies as a consequence of subjecting it to elevated pressure. Tandon and Gupta assigned this band to the crystal field spin-forbidden transitions ${}^6A_{1g} \rightarrow {}^4E_g$, ${}^4A_{1g}$ in Fe^{3+} ions; this assignment could be an error since the

FIGURE V-16

The optical absorption spectra of a hematite powdered sample subjected to 100 kb. (the spectrum was measured after quenching).



intensity of this band is huge and cannot correspond to the spin-forbidden transitions in Fe^{3+} .

Correlating the intensity and energy of this band in hematite with the other bands observed in the spectra of KMnO_4 , crocoite, and vanadinite could lead to the conclusion that it is due to a charge transfer transition. This transition may occur from the non-bonding ligand orbital, $6t_{1u}$, to the Fe^{3+} d-level, $1t_{1g}$. The other spectral features observed by Tandon and Gupta (1970) could be related to other electronic transfer transitions from the non-bonding ligand orbitals to t_{2g} and e_g levels, or from e_g levels to the higher energy antibonding levels. The spin-forbidden transitions, however, could be masked by the intense charge transfer absorption.

V-4.5 Silicates

In all silicate minerals so far studied, the tail of the ligand to metal (or metal-ligand) charge transfer transition is always observed in their spectra; this tail is frequently referred to as the "absorption edge". For every case, there is a small shift of this tail to lower energy as pressure increases. Since it was not possible in this study to locate the maximum of the charge transfer absorption, the magnitude of the pressure-induced energy shift could not be determined accurately.

Runciman et al. (1973) measured the polarized u.v. spectrum of olivine and observed two intense and broad absorption bands at energies around 34000 and 39000 cm^{-1} ; these two bands may be

related to L-M and M-L charge transfer transitions*.

Mao and Bell (1972) reported a rapid low energy shift of the absorption edge in olivine which takes place prominently at pressures around 100 kb.. They reported also a significant increase in the electrical conductivity above this pressure. Further, Mao (1974) reported that above 200 kb. the fayalite olivine becomes opaque as a consequence of the absorption edge shifting far into the i.r. region.

The pressure induced low-energy shift of the charge transfer absorption in olivine is related to a decrease in the energy separation between the non-bonding ligand orbitals and the transition metal d-orbitals and between the d-orbitals and the higher energy non-bonding levels. The decreases in the splitting energies between these levels are also closely related to narrowing the energy gap between valence band and conduction bands, as it is apparent from the significant increase in the electrical conductivity.

With increasing pressure, the higher energy M-L C.T. band at 39000 cm^{-1} may shift more rapidly than the L-M band, which is at 34000 cm^{-1} . At pressure around 100 kb. the two bands may overlap so that the intensity of charge transfer absorption will increase substantially and continue to shift to lower energy as pressure increases.

The rapid shift of the absorption edge to lower energy was

* According to Tossell *et al.* (1974), the two transitions may be assigned to $6t_{1u} \downarrow \rightarrow 2t_{2g} \downarrow$ and $3e_g \downarrow \rightarrow 7a_{1g} \downarrow$.

also observed in the spectra of orthoferrosilite when the sample was heated to about 500°C and subjected to 100 kb.. The pressure-induced C.T. absorption shift phenomenon may occur in most silicate minerals and could be a significant factor which controls the processes of heat transfer in the earth's interior.

Nevertheless, some attention should be paid on the possibility of other changes taking place during the shift of the absorption edge. Those changes may occur in the electronic structure such as the pressure-induced reduction or spin-pairing, or in the crystal structure itself. Furthermore, when the applied pressures and temperatures are extremely high (250 kb., 1000°C), disproportionation of the mineral phase to its oxide components may also take place. These phenomena will be discussed in Chapters VI and VII.

Chapter VI

PRESSURE-INDUCED PHASE TRANSFORMATIONS IN GILLESPIE, EGYPTIAN-BLUE AND AZURITE

VI-1. Introduction

Phase transformations in solids may be classified into three major categories; first, structural phase transitions, which involve changes in the atomic coordination or the positional parameters of atoms in the crystal structure. Second, electronic phase transitions, which arise due to changes in the electronic structure, i.e. in the arrangement or distribution of electrons in the atomic or molecular energy levels. A third type of phase transition is possible corresponding to both types of changes, i.e. structural and electronic as well.

The first category of phase transition was intensively studied by many workers of different disciplines in science (Smoluchowski, 1957) and has been widely recognized as a common phenomenon which occurs in natural minerals when they are subjected to elevated pressures and/or temperatures (Schairer, 1957; Buerger, 1957, 1971; Bridgman, 1963; Kennedy, 1957; Ringwood and Searbrook, 1963).

Ringwood (1970) reviewed phase transformations in mantle minerals and related the rapid increase of the seismic velocity at 350-450 Km. to the transformation of olivine into a spinel-like structure. Numerous other examples of pressure and/or temperature-induced structural changes in minerals were reported by many authors, e.g. (Ringwood and Major, 1970; Ringwood and Reid, 1968; Ito et al., 1971; Ringwood et al., 1967; Akimoto and Sato,

1968; Ahrens and Grahams, 1972; Abu-Eid and Hazen, 1974; Ming and Bassett, 1975).

On the other hand, electronic phase transitions, although demonstrated experimentally to occur in inorganic or organic complexes (Drickamer and Frank, 1973), are not well understood yet, and no concrete evidence has been given so far to confirm the occurrence of this phenomenon in silicate minerals.

In pressure-induced electronic phase transformations, there are two types of electronic processes involved; they are the pressure-induced reduction, e.g. Fe(III) \rightarrow Fe(II) and the high-spin (h.s.) \rightarrow low-spin (l.s.) transition. The pressure-induced reduction of Fe(III) and Mn(III) were reported to occur in magnesioriebeckite (Burns et al., 1972a) and rhodonite (Gibbons et al., 1974, respectively. The process of $Fe_{h.s.}^{2+} \rightarrow Fe_{l.s.}^{2+}$ transitions was reported by Strens (1966, 1969a) to occur in gillespite at pressure around 25 kb.. However, Abu-Eid et al. (1973) and Abu-Eid and Hazen (1975) predicted theoretically and demonstrated experimentally that the spin-transition process alone does not occur in gillespite at this pressure. Thus, a displacive structural phase transition was tentatively identified using optical absorption, Mössbauer, and x-ray techniques.

In this chapter, the pressure-induced phase transition will be presented for three minerals, viz., gillespite ($BaFeSi_4O_{10}$), Egyptian-blue ($BaCuSi_4O_{10}$), and azurite, $Cu_3[CO_3]_2(OH)_2$. The high pressure transition in gillespite has been studied intensively using different techniques, whereas Egyptian-blue and

azurite were studied using only the high pressure spectral technique and by observation under the microscope.

VI-2. Gillespite

2.1 Introduction

Gillespite is a micaceous mineral which has an intense red color and basal cleavage perpendicular to the c-axis. The crystal structure of gillespite belongs to the space group P4/ncc and the unit cell, with the parameters $a=7.495\text{\AA}$ and $c=16.05\text{\AA}$, contains four $\text{BaFeSi}_4\text{O}_{10}$ formula units (Pabst, 1943).

One of the most interesting features of the structure is the square planar coordination of the ferrous ion. The crystal field splitting parameter (CFS) in this square planar site has its greatest value compared to other ferrous sites in silicate minerals. Since the CFS increases rapidly with decreasing cation-ligand distances, it was predicted that transition of the ferrous ion from the high-spin to the low-spin state may take place when the crystal field splitting parameter exceeds the pairing energy required to couple the electrons in the low energy levels (Strens, 1966, 1969). Strens reported a high-spin to low-spin transition in Fe^{2+} in gillespite, around 24 kb.. Strens' evidence for the phase change is the change in color, red to colorless, and the featureless spectra of gillespite above the transition pressure.

In this study, evidence for a structural change rather than spin-pairing in gillespite at pressure around 26 kb. will be presented. This type of phase transition is interpreted from the

abrupt low-energy shift of crystal field bands and the color change (from red to blue) around the transition pressure.

Further evidence for the change in the structure has been obtained (Abu-Eid and Hazen, 1975; Hazen and Abu-Eid, 1974) from the high pressure x-ray crystallographic studies on gillespite. High pressure Mössbauer studies (Tossell and Vaughan, unpubl. data) have also shown significant changes in the Mössbauer parameters of iron in gillespite around this pressure, which was interpreted by Abu-Eid et al. (1973) to be due to structural changes in gillespite.

VI-2.2 Experimental Methods

The diamond-anvil cell was employed for optical and spectral studies of gillespite single crystals subjected to pressures up to 100 kb.. The gasketing technique discussed in Chapter III was employed to achieve a true hydrostatic pressure condition on an oriented single crystal.

The crystal, after polishing and being oriented using the spindle stage, was dropped in a methanol-ethanol liquid mixture (4:1 by volume) with the required axis (in this case, the c-axis) perpendicular to the pressure axis. The pressure was generated by driving the two anvils against the metal gasket, thereby transferring the pressure to the liquid and then to the sample.

The pressure was calibrated using $KCl(I) \rightarrow KCl(II)$ transi-

Further, pressure calibration was also achieved using the pres-

sure shift of the sharp R-line fluorescence spectrum of ruby (Forman et al., 1972).

The polarized spectra of a gillespite single crystal below and above the transition pressure were measured using the Cary 17 spectrophotometer with a newly constructed optical attachment (see Chapter III). The measured spectra of one single crystal in the visible region were fitted into three peaks having Gaussian shape using DuPont 310 Curve resolver.

Spectral measurements above the transition pressure (26 kb.) were made on two single crystals of gillespite; one oriented in the diamond cell with the c-axis perpendicular to the pressure axis and another having the c-axis perpendicular to the anvil faces. Using two differently oriented gillespite crystals, the spectra for all possible orientations of the high pressure phase were obtained.

The high pressure single crystal x-ray technique will not be discussed here and the reader is referred to Merrill (1973), Merrill and Bassett (1974), Weir et al. (1965, 1969), and Hazen and Burnham (1974) for a general description of this technique.

VI-2.3 Results

Gillespite absorbs polarized light very strongly when the c-axis is parallel to the electric vector, \vec{E} . In this orientation, the crystal exhibits a very intense red color (Figure VI-3a). On the other hand, when the c-axis is perpendicular to \vec{E} , the crystal shows a pale pink color (Figure VI-2a).

The polarized absorption spectra of a gillespite single crystal

FIGURE VI-1(a)

The polarized absorption spectra of a gillespite single crystal mounted in the diamond cell, without increasing pressure, [..... E-spectrum; —— O-spectrum] and at pressure around 26 kb., [_._._._._. E-spectrum; - - - - - O-spectrum]. (Spectral measurements were made on a crystal oriented in the diamond cell such that the c-axis is perpendicular to the pressure axis).

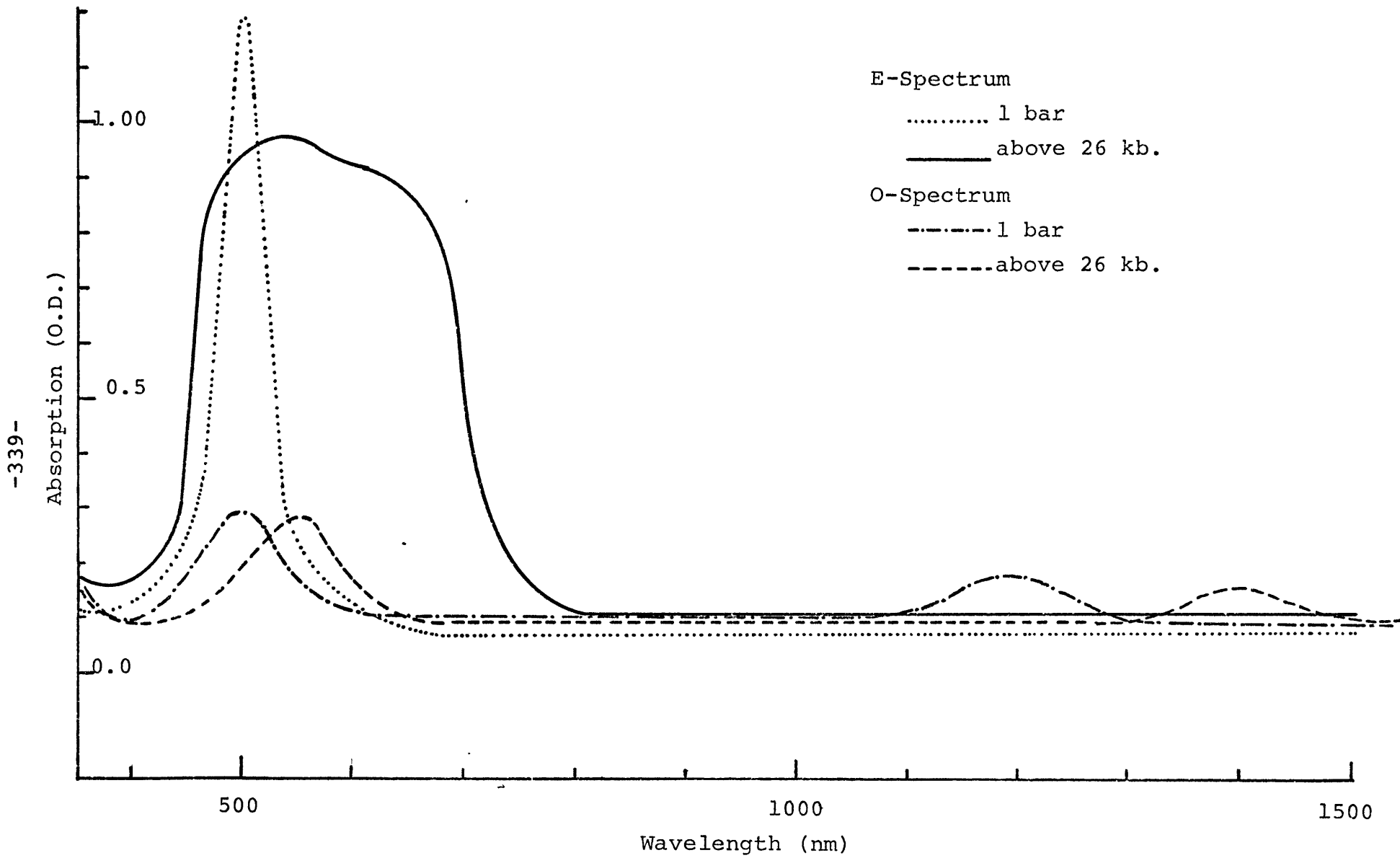
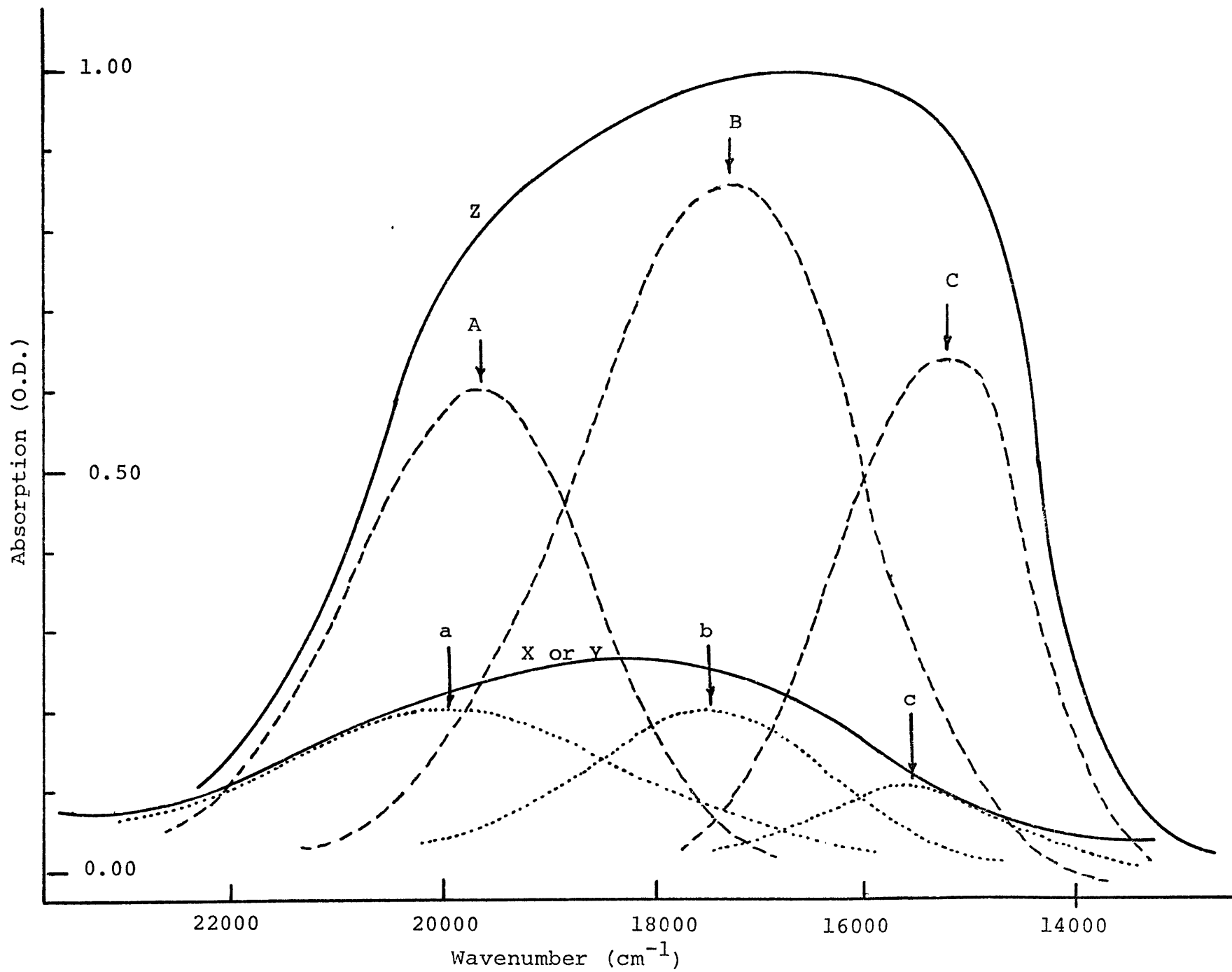


FIGURE VI-1(b)

The visible absorption spectra of gillespite single crystal measured above the transition pressure. The horizontal scale was converted from wavelength (n.m.) to wave number (cm^{-1}). The spectral envelope for both orientations, c (—) and a or b (----) were fitted into three peaks having Gaussian shape using DuPont 310 Curve Resolver.

The data obtained from Figure IV-1(b) are summarized in the following table:

Orientation	Band	Band Max.	% Absorption
z.	A	19540	27
	B	17200	47
	C	15120	25
x or y	a	19950	48
	b	17550	33
	c	15500	16



mounted in the diamond cell, without increasing pressure, is shown for the two orientations in Figure VI-1a.

The intensities of spectral bands in the polarized spectra of gillespite correlate very well with the observed colors.

The absorption spectra of gillespite at 1 atm. was measured by Burns et al. (1966) and the ground state of Fe^{2+} was established as $^5A_{1g}$. In addition, the observed spectral bands were assigned to the following transitions:

<u>Energy of the Band</u> (cm^{-1})	<u>Orientation of</u> <u>Electric Vector</u>	<u>Electronic Transition</u>
20160	$\vec{E} \perp c$	$^5A_{1g} \rightarrow ^5B_{1g}$
8305	$\vec{E} \perp c$	$^5A_{1g} \rightarrow ^5B_{2g}$
19650	$\vec{E} \parallel c$	$^5A_{1g} \rightarrow ^5B_{1g}$

These assignments are consistent with the square planar site symmetry of ferrous iron.

With increasing pressure on the gillespite crystal in the liquid cell, and measuring the spectra at various pressures, crystal field bands shifted slowly to higher energies. However, at pressure around 26 ± 2 kb., the crystal changes color dramatically from red to blue. Figure VI-3b shows the blue color of the crystal in the polarized light when c is parallel to \vec{E} . Rotating the crystal 90° (i.e. $E \perp c$), the color changes to pale blue (Figure VI-2b). Figures VI-1a,b show the polarized spectra of a gillespite crystal above the transition pressure for two orientations designated here as a and c.

Repeating the previous measurements on another crystal in the pressure cell oriented with the c -axis perpendicular to the

FIGURE VI-2

- (a) This colored photograph shows a gillespite single crystal in polarized light, the electric vector being horizontal or E-W on this photograph and the next three photos. Here, then, the electric vector is perpendicular to the c-axis. This crystal has been cut parallel to the c-axis and subjected to pressure just below the transition pressure, 26 kb.. Notice the pale pink color.
- (b) The same crystal, just above the transition pressure. Notice that the color has changed from pale pink to pale blue.

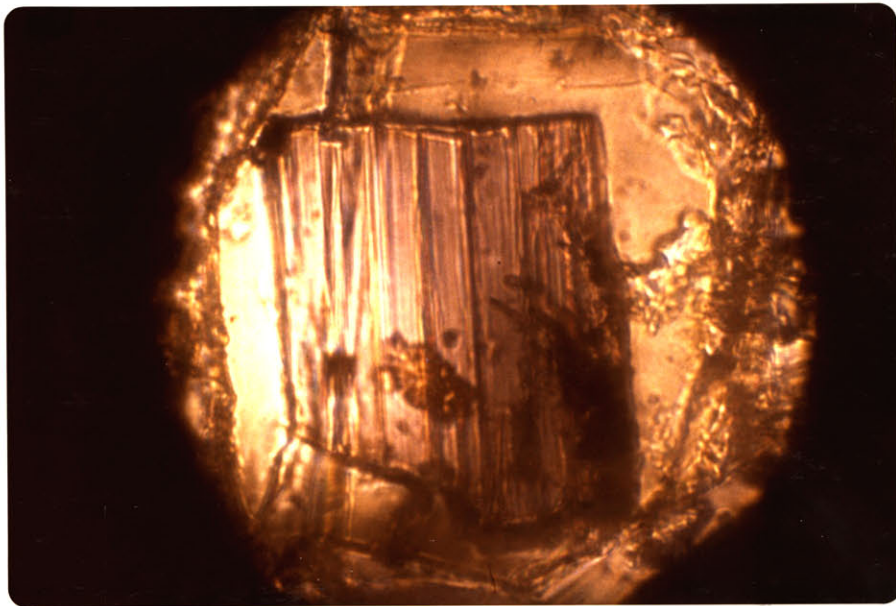
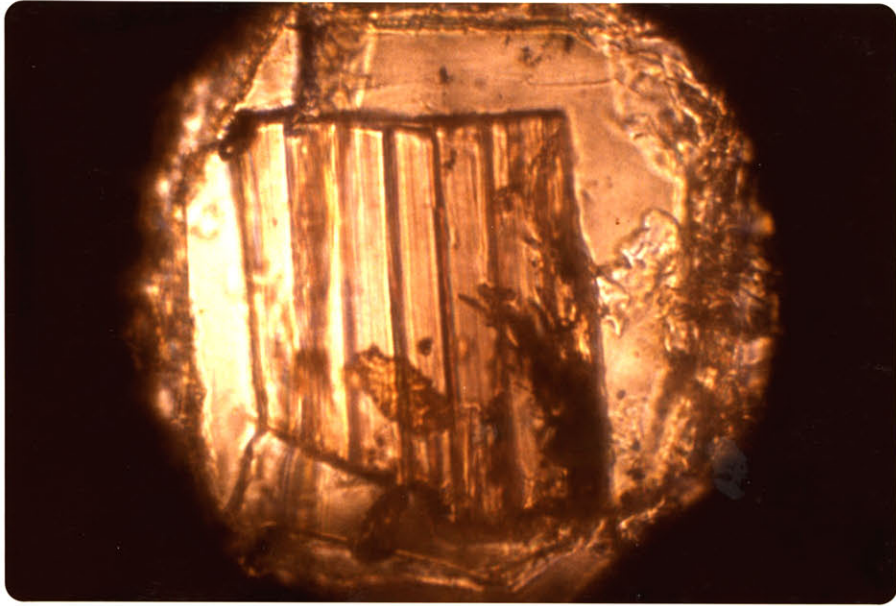
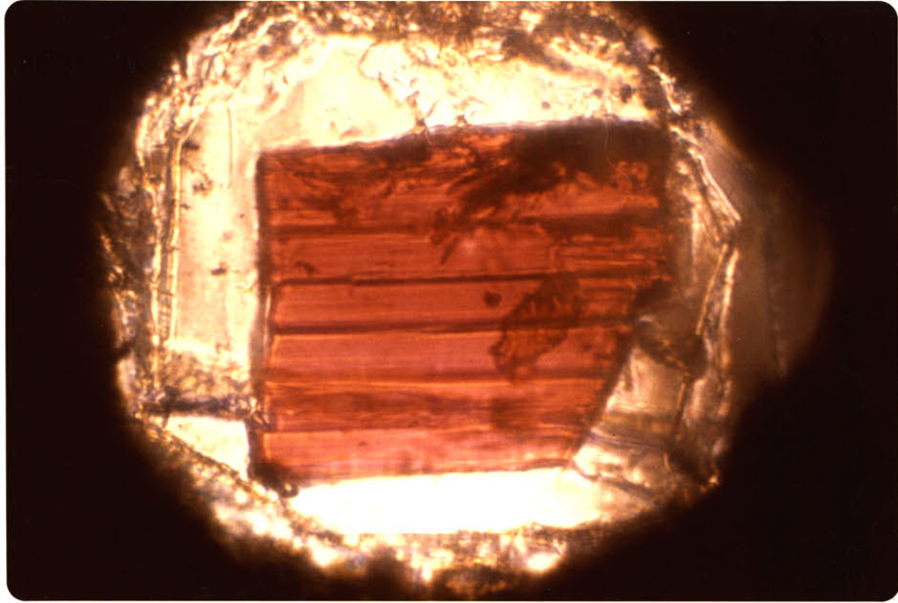


FIGURE VI-3

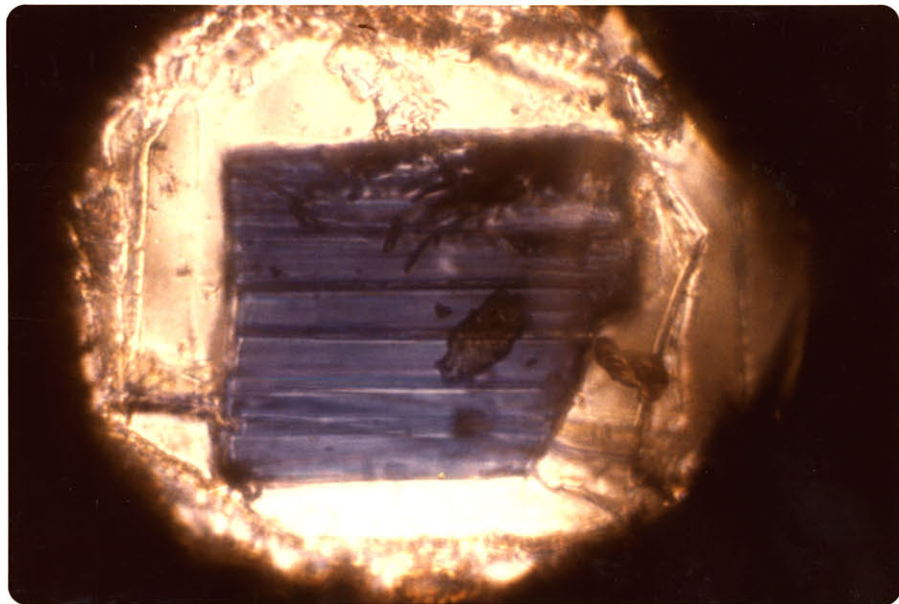
(a) This photograph shows the same crystal rotated 90° so that the electric vector is parallel to the c-axis; that is perpendicular to the square plane. The crystal exhibits this intense red color when the pressure is just below 26 kb..

FIGURE VI-3

(b) A photograph of the same crystal subjected to pressure just above 26 kb.. Notice that the color has changed from red to intense blue. Notice also the uniform color suggesting that the pressure in the cell is almost hydrostatic.



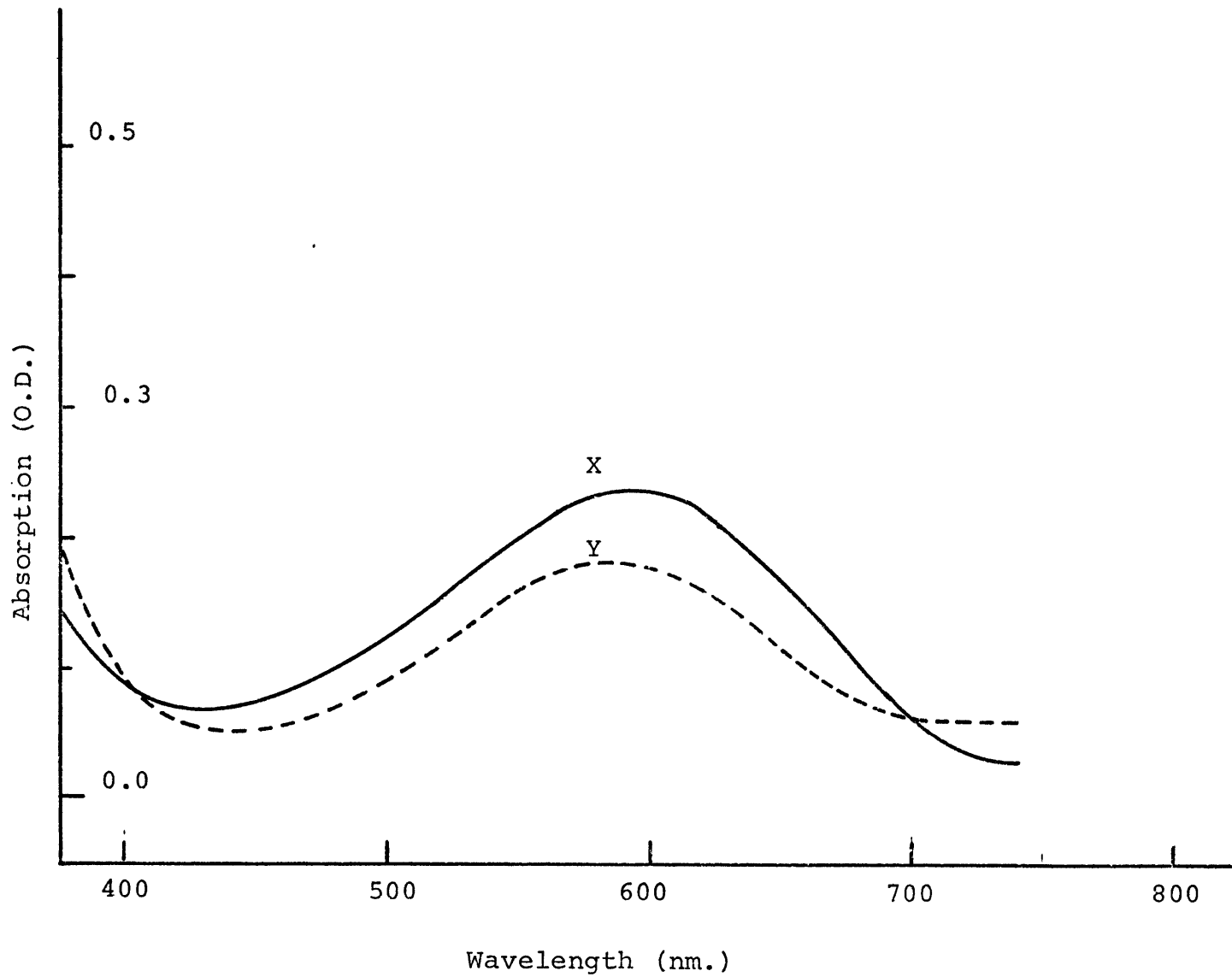
a



b

FIGURE VI-4

The polarized spectra of a gillespite single crystal mounted in the diamond cell such that the c-axis is perpendicular to the anvil faces. The spectral measurement was made when the pressure increased above 26 kb.. The two spectra may be related to two orientations as explained in the text.



anvil faces, and increasing the pressure just above 26 kb., the crystal also changes color from pale pink to pale blue. The polarized spectra of this crystal above the transition pressure consist of two superimposed spectra; one is a duplicate of that shown in Figure VI-1, and the other is similar to the "a" spectrum, but has different intensity (Figure IV-4). The latter could correspond to a third orientation designated here as "b".

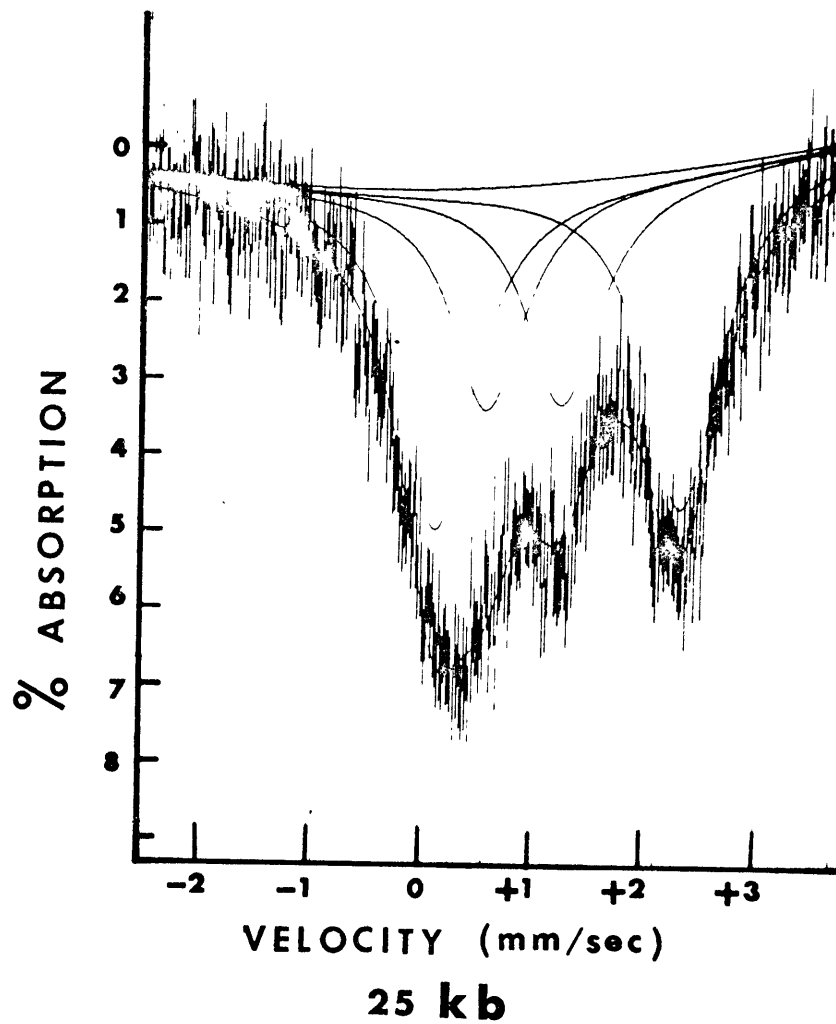
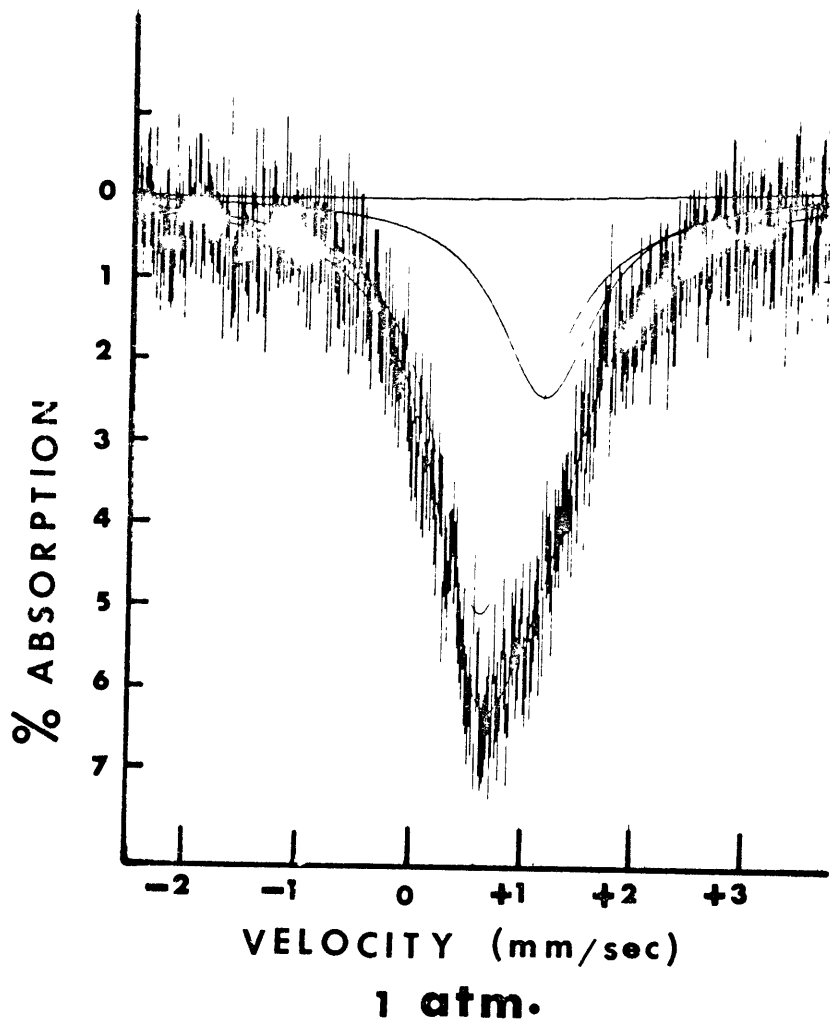
Further high pressure studies have been made on synthetic gillespite using the Mössbauer technique (Tossell and Vaughan, unpubl. data). The Mössbauer spectrum of gillespite at 1 atm. (Figure VI-5) consists of a quadrupole doublet with the splitting around 0.51 mm/sec. and the isomer shift 0.85 mm/sec.. Above the transition pressure, the quadrupole doublet of the low pressure phase has split into two doublets. The new doublets have the following parameters (based on stainless steel standard):

<u>Isomer Shift (mm/sec.)</u>	<u>Quadrupole Splitting (mm/sec.)</u>
Inner doublet 0.87	0.64
Outer doublet 1.13	2.02

It should be mentioned that the interpretation of the high pressure absorption and Mössbauer spectral data was made by Abu-Eid et al. (1973) as due principally to the change in the site symmetry of Fe^{2+} from square planar to a flattened tetrahedron. This interpretation will be explained further in the discussion. Moreover, high pressure single crystal x-ray studies have also provided further evidence for the structural nature of

FIGURE VI-5

Mössbauer spectra of synthetic gillespite at 1 atm. (a) and above the transition pressure (b) (Tossell and Vaughan, unpublished data).



the gillespite transition. Single crystal x-ray precession photographs obtained below and above the transition pressure (Abu-Eid and Hazen, 1975; Hazen and Abu-Eid, 1974) have also shown significant changes in the structure.

A crystal fragment of gillespite was oriented in the diamond anvil press such that the c-axis is perpendicular to the anvil faces. The pressure cell was mounted on a goniometer head which allows the crystal in the x-ray beam to be oriented and centered. The assembled pressure cell-goniometer head was then attached to an x-ray precession camera. Precession photographs were obtained at pressures below and above the transition pressure, which is identified from the color change red to blue. Figures VI-6 and VI-7 show the cone-axis x-ray photographs of gillespite recorded below and above the transition pressure 26 kb.. From these two photographs, it is apparent that the c-axis of the high pressure phase is approximately half of its value in the low pressure, red phase, i.e. in the h.p. phase the unit cell contains only one single tetrahedral layer instead of having a double layer as in the low-pressure phase. Furthermore, precession c-axis photographs were also obtained for the two phases. Figures VI-8,9 and 10 show the 0-level precession x-ray photographs of the low pressure and the high pressure polymorphs, respectively. From Figures VI-8,9, it is noticed that reflections with $h+k = 2n+1$ are extinct in the low pressure phase, indicating the presence of n- and c-glide planes. However, Figure VI - 10 shows that such reflections are present, which indicate that the n- and c-glide planes are

FIGURE VI-6

Cone-axis x-ray photograph of a gillespite single crystal oriented in the diamond cell such that the c-axis is perpendicular to the anvil faces. (This photo was recorded when the crystal was at low pressure (below 26 kb.).

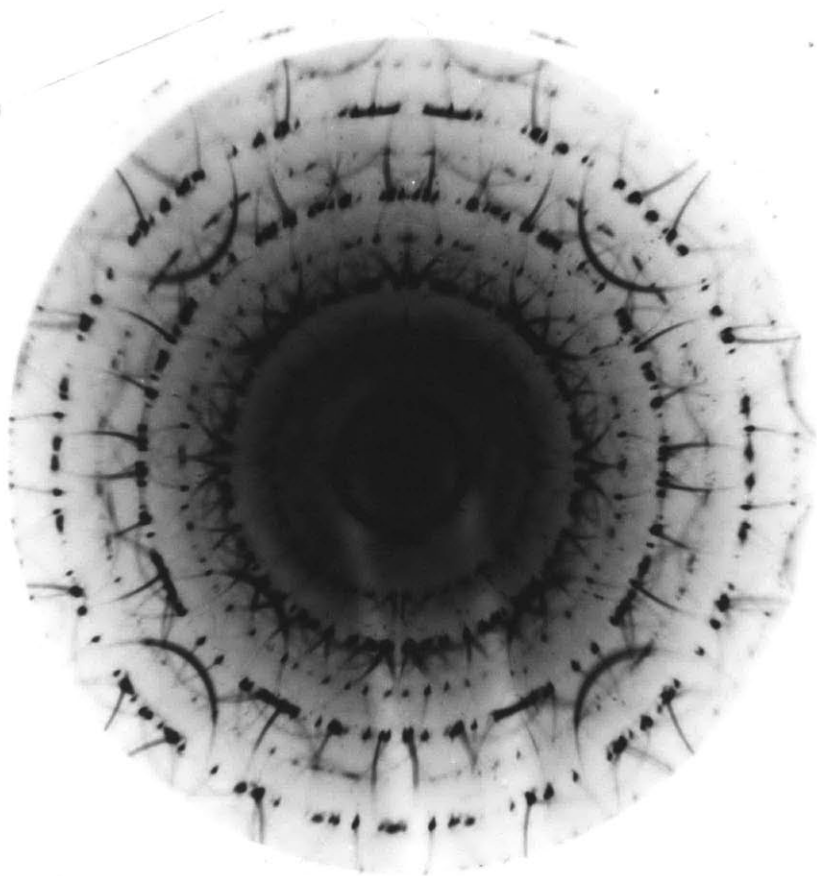


FIGURE VI-7

The cone-axis photograph of the same crystal
recorded above 26 kb..

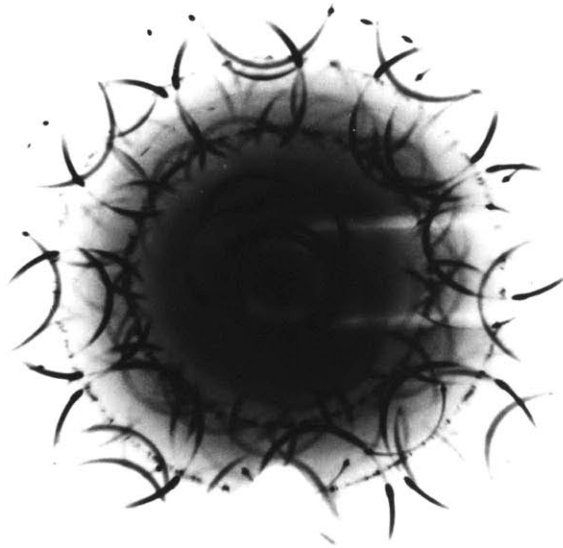
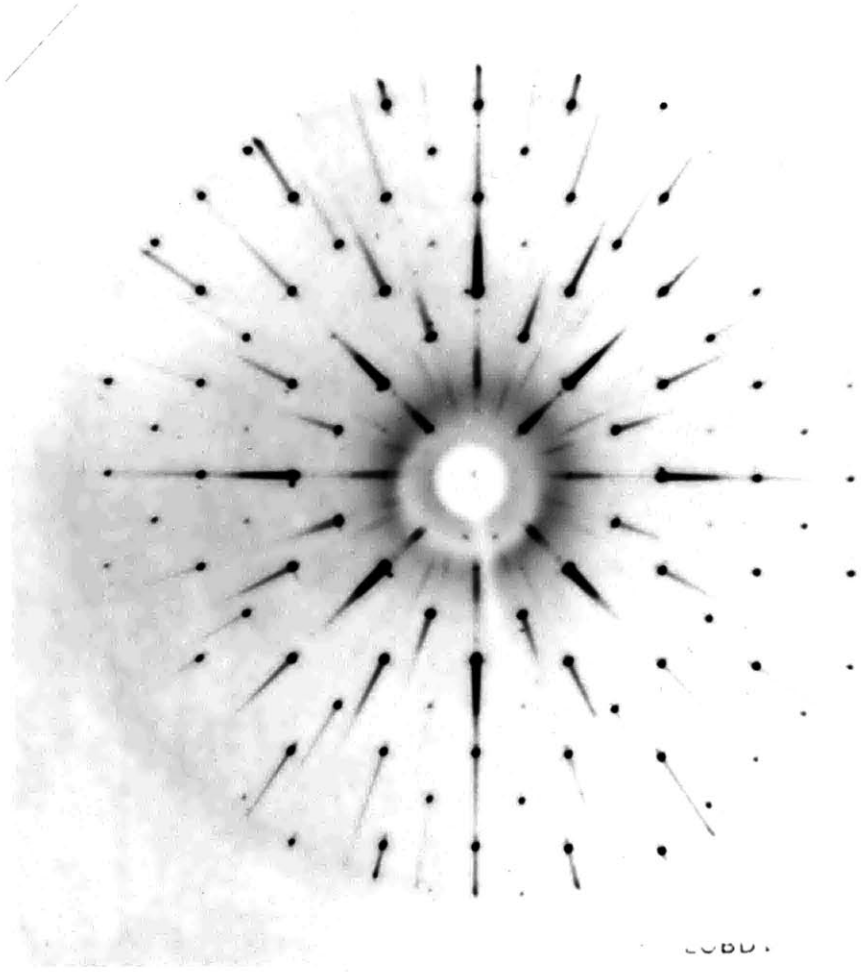


FIGURE VI-8

O-level precession x-ray photograph of a gillespite single crystal mounted on a goniometer head without the diamond cell.



COBB

FIGURE VI-9

O-level precession x-ray photograph recorded when the crystal was oriented inside the diamond cell and the pressure was below 26 kb..

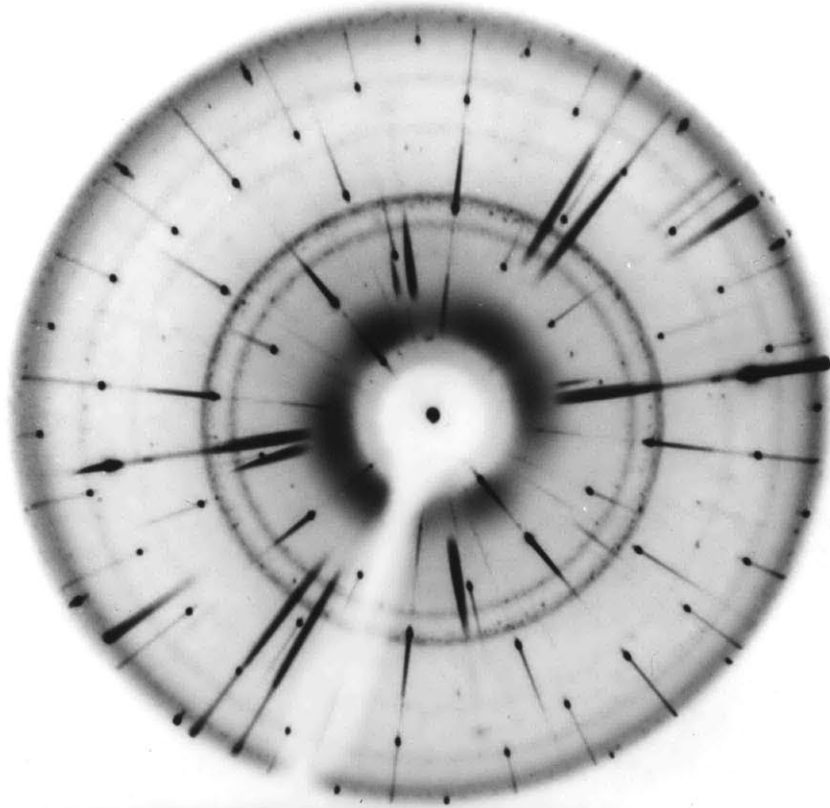
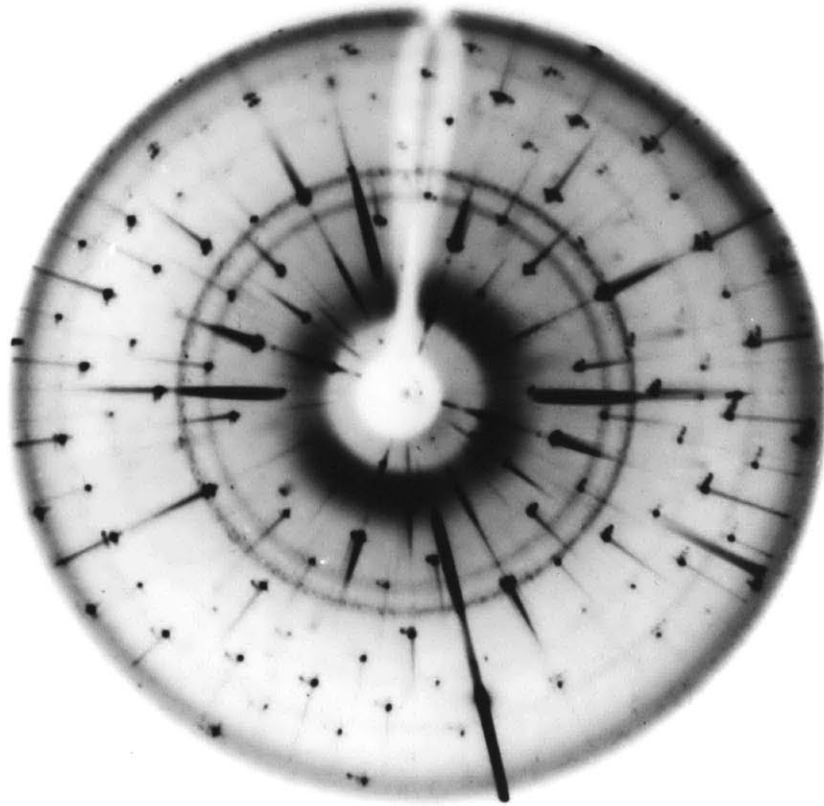


FIGURE VI-10

O-level x-ray photograph of the same crystal
subjected to pressure above 26 kb..



absent. Nevertheless, reflections with $h+k = 2n+1$ of the classes $h00$ and $0k0$ are extinct in both gillespite phases, as shown in the precession photographs, indicating the presence of screw axes (2_1) parallel to a and b axes in both phases.

From the above high pressure x-ray data and study of the distribution of diffraction intensity, Abu-Eid and Hazen (1974) and Hazen and Abu-Eid (1974) derived the following unit cell parameters, diffraction symbols, and space groups for the two phases:

	<u>a(A)</u>	<u>c(A)</u>	<u>Diffraction Symbol</u>	<u>Space Group</u>
Red Phase	7.04	16.08	4/mmmP-/ncc	P4/n2 ₁ /c2/c
Blue Phase	7.03	8.02	4/mmmP-/-2 ₁ -	P42 ₁ 2 or P $\bar{4}$ 2m

Both space groups, P42₁2 and P $\bar{4}$ 2m belong to the tetragonal system; however, the latter one is preferred in this interpretation since the Fe²⁺ site in this space group is a flattened tetrahedron which conforms with the interpretations of the high pressure spectral data, whereas in P42₁2 space group the Fe²⁺ site is a square planar.

Recently, Hazen and Burnham (1974) reported the detailed analysis of the high pressure phase in gillespite. In their study, they reported that the high pressure phase belongs to the orthorhombic space group, P2₁2₁2, with the unit cell parameters at $a=7.349$, $b=7.515$, $c=7.894\text{\AA}$, and $z=2$. In addition, the Fe²⁺ site in the high pressure phase was also reported to be flattened tetrahedron.

VI-2.3 Discussion

(a) The Pressure-Induced Spin-Transition Phenomena

The process of "high-spin" to "low-spin" pressure-induced transition of Fe^{2+} in minerals has many significant aspects relevant to the nature and composition of the earth's mantle. The most important of these aspects are the changes in the magnetic properties (paramagnetic to diamagnetic) and the prominent decrease in volume of phases bearing ferrous ions.

Fyfe (1960) predicted that spin-pairing of ferrous ions contained in fayalite may take place in the earth's mantle at a depth of the order of 1400 km. Burns (1969) has estimated the pressure at which "high-spin" to "low-spin" transitions may take place in the Fe^{2+} ions in various oxides and silicate phases, and Gaffney (1972) has discussed in some detail the effect of the "low-spin" Fe^{2+} on the composition of the lower mantle. In all of the previous reviews, no experimental evidence has been given for the formation of "low-spin" Fe^{2+} .

On the other hand, Strens (1966, 1969) discussed the nature and the geophysical significance of spin-pairing in minerals containing Fe^{2+} . Strens claimed that he observed spin-pairing transitions in gillespite occurring as a consequence of increasing the pressure up to about 25 kb.; the evidence he obtained for the spin-transition is the reversible color change (red to colorless) and the featureless spectrum of the high pressure form.

Strens' observations and interpretations do not conform with the spectral properties of the low-spin cation, because:

- 1) low-spin ferrous ions are expected to show new spectral fea-

tures different from those of the high-spin ions, rather than having featureless spectra. This is simply explained in the energy level diagrams shown in Figures VI-11a,b,c. Figure VI-a shows the energy level diagram of Fe^{2+} in the square planar site in gillespite. The ground state is $^5A_{1g}$, and the following electronic transitions are observed in the visible-near i.r. region*: $^5A_{1g} \rightarrow ^5B_{1g}$ and $^5A_{1g} \rightarrow ^5B_{2g}$.

With increasing pressure, the splittings between the energy levels will increase as a result of decreasing the cation-anion distances (Figure VI-11b). With the continuous increase in the splitting energy between the ground state and the higher energy excited state, the electronic excitation energies may then exceed the energy acquired from coupling the electrons in $^1B_{1g}$ and $^1B_{2g}$ levels with those in the 1E_g level; consequently, spin-pairing will take place.

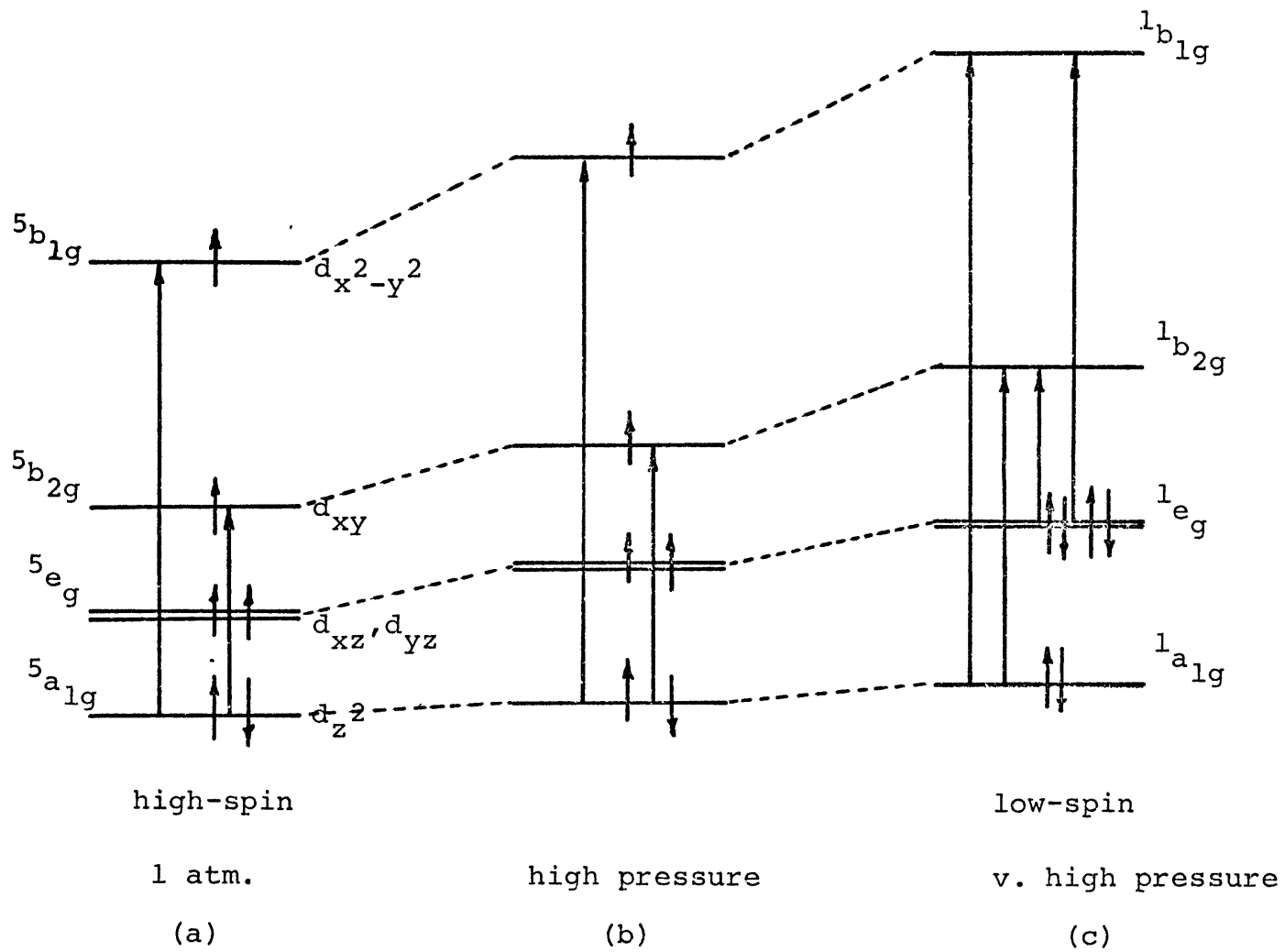
Up to this point, we are assuming that the site symmetry has not been changed; here, then, the low-spin Fe^{2+} will have the same energy levels, but the splitting energy is more than that of the high-spin Fe^{2+} .

As a consequence of coupling the electrons, the ground state is designated as $^1A_{1g}$, since the total angular momentum or the multiplicity of the term has been changed. The expected spin-allowed electronic transitions for the low-spin Fe^{2+} are:
 $^1A_{1g} \rightarrow ^1B_{1g}$, $^1A_{1g} \rightarrow ^1B_{2g}$, $^1E_g \rightarrow ^1B_{1g}$, and $^1E_g \rightarrow ^1B_{2g}$.

* Burns et al. (1966) reported another electronic transition, ($^5A_{1g} \rightarrow ^5E_g$), which occurs around 1000 cm^{-1} .

FIGURE VI-11

- (a) Energy level diagram of $\text{Fe}^{2+}_{\text{h.s.}}$ in the square planar site in gillespite.
- (b) Energy level diagram showing increases in the splitting energies as a result of decreasing cation-anion distances.
- (c) Energy level diagram of $\text{Fe}^{2+}_{\text{l.s.}}$ in the square planar site (not the new spin-allowed transitions).



From the energy level diagram shown in Figure VI-11c , it is obvious that Fe^{2+} ions in the low-spin state show spectral features at energies higher than those of the high-spin state, rather than having featureless spectra, as was reported by Strens (1966, 1969).

2) all of the reported low-spin ions are colored and give intense spectral bands related to the predicted spin-allowed transitions. In addition, these transitions occur at higher energies than those of the high-spin ions. As an example, CoF_6^{3-} is one of the spin-free Co^{3+} derivatives, and exhibits two bands at 10000 and 15000 cm^{-1} ; whereas, the majority of low-spin Co^{3+} compounds exhibit spectral features at higher energies than those of CoF_6^{3-} (Lever, 1968).

Lever (1968) also reported that the $\text{Co}(\text{H}_2\text{O})_6^{3+}$ ion which contains Co^{3+} in the low-spin state has two spin-allowed bands at energies 16500 and 24700 cm^{-1} ; these are related to the transitions ${}^1\text{A}_{1g} \rightarrow {}^1\text{T}_{1g}$ and ${}^1\text{A}_{1g} \rightarrow {}^1\text{T}_{2g}$, respectively. Further, $\text{Co}(\text{NH}_3)_6^{3+}$ also exhibits two bands at 21200 and 29550 cm^{-1} , related to the same electronic transitions.

In conclusion, it is predicted that low-spin Fe^{2+} will exhibit spectral bands at higher energies than those of high-spin Fe^{2+} . Furthermore, additional possible spectral features may also be observed at lower energies. It should also be mentioned that the above argument of the low-spin Fe^{2+} holds for both the triplet and singlet low-spin states.

(b) The Nature of the Gillespite Transition

From the above discussion, it is evident that if the phase transition is of the high-spin \rightarrow low-spin type, the electronic transitions ${}^1A_{1g} \rightarrow {}^1B_{1g}$ and ${}^1A_{2g} \rightarrow {}^1B_{2g}$ of the low-spin Fe^{2+} ion should occur at higher energies than those of the high-spin Fe^{2+} in gillespite, if the symmetry of the coordination polyhedron remains unchanged. Since none of the low-spin transition types were observed in the spectra of the high pressure phase and all spectral bands shifted abruptly to lower energies, it is most likely, then, that the d-energy levels have been disrupted suddenly and their energy values are changed as a consequence of rearranging the oxygen ligands around the central ion Fe^{2+} .

The energy level diagram that may correspond to the measured spectral bands of the high pressure blue phase is shown in Figure VI-12b.

Comparing these energy levels with those constructed from the 1 atm. spectra (Figure VI-12a), it is evident that the energy values of the d_{xz} and d_{yz} levels have increased significantly above the transition pressure, whereas the energies of other levels have either increased or decreased slightly. These changes in the energy levels are due mostly to puckering of the square planar site and displacing the oxygen atoms from the x-y plane into the x-z and y-z planes as illustrated in Figure VI-13.

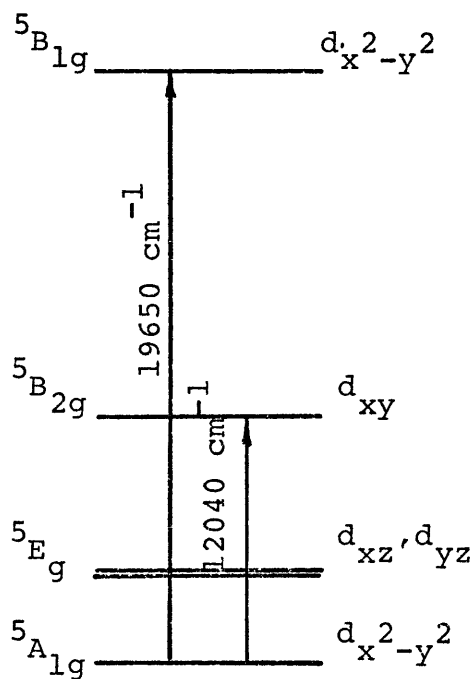
When the pressure was increased beyond 26 kb., crystal field bands shifted slowly to lower energies indicating that the rotation of the oxygen atoms toward the z-axis is increasing and the site symmetry of the ferrous ion is approaching the

FIGURE VI-12

- (a) Energy level diagram of Fe^{2+} in the square plane, D_{4h} , constructed from the spectral data obtained at normal pressure.
- (b) Energy level diagram constructed from the spectra measured above 26 kb. and shown in Figure VI-1(b). The new site symmetry is predicted to be D_2 .

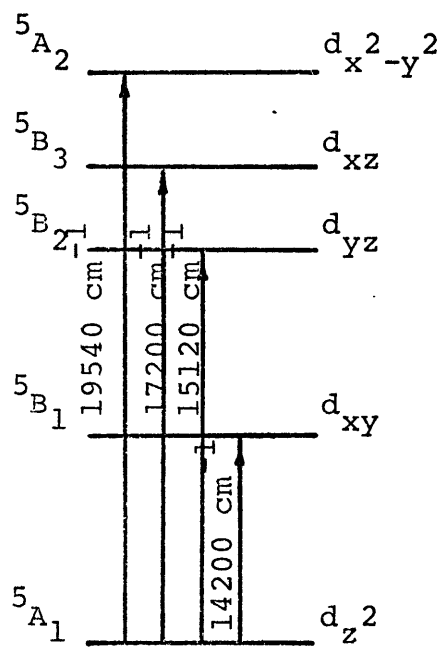
1 atm.

above 26 kb.



D_{4h}

(a)



D_2

(b)

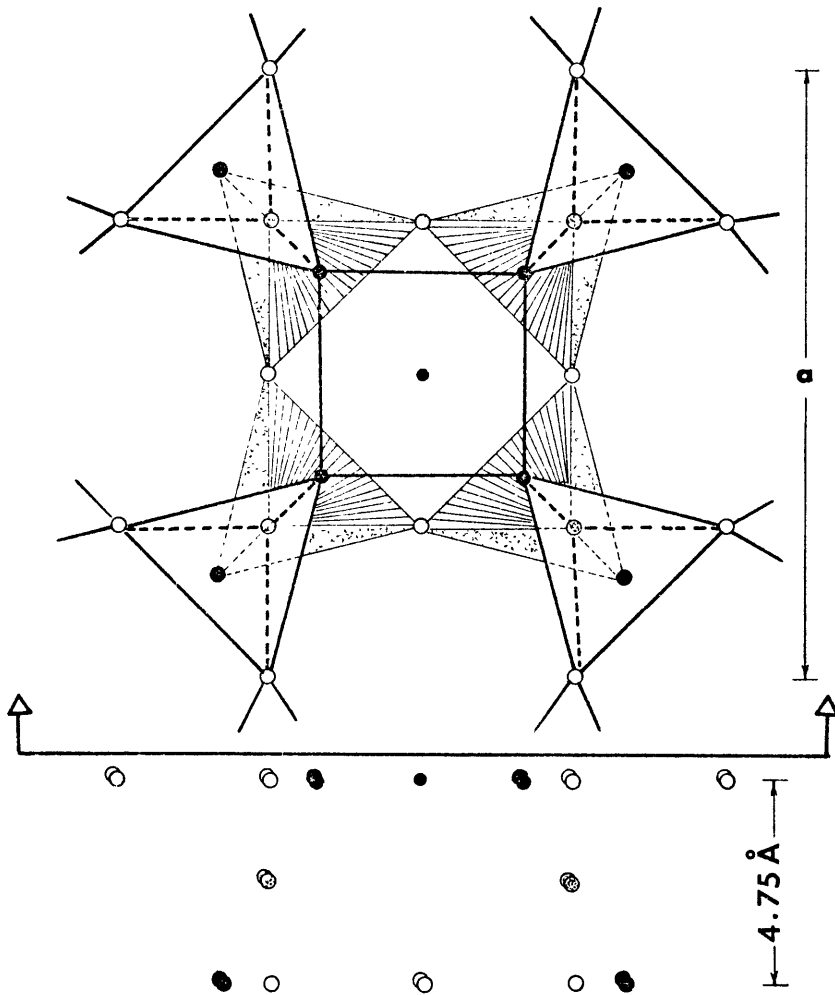
FIGURE VI-13

Two diagrams illustrating the sites of Fe^{2+} in the low pressure phase, which is square planar, and the high pressure phase, which is very distorted or flattened tetrahedra. The black circles are oxygen atoms at unshared corners of the tetrahedra; the blank circles are oxygens at corners shared by two tetrahedra at the same level, and the dotted circles are oxygens at corners shared by two tetrahedra at different levels. Notice the projection of ferrous and oxygen atoms parallel to (010). In the low pressure phase, the unshared oxygens occur in one plane perpendicular to the c-axis; meanwhile, above the transition pressure, the four oxygens are not located in the same plane. This is due to puckering of the square planar site and displacing the oxygen atoms from the x-y plane into the x-z and y-z planes.

- O_{III}
- ⊙ O_I
- O_{II}
- Fe

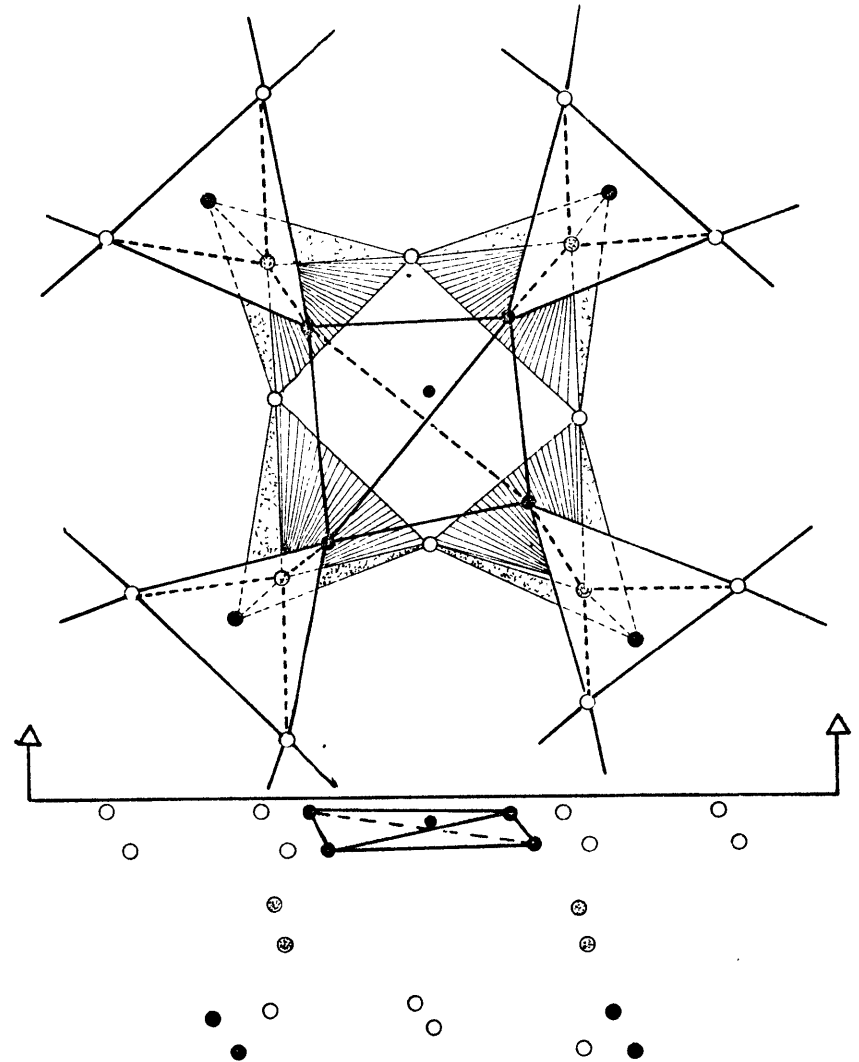
$a = 7.495 \text{ \AA}$

373



Fe In Square Planar Site

$c = 4.75 \text{ \AA}$



Fe In Very distorted Tetrahedral Site

regular tetrahedron. Here then, it is predicted that the low-spin transition in Fe^{2+} is unlikely to occur with increasing pressure above 26 kb., since the crystal field parameter, Δ , is decreasing rather than being increased as pressure increases. With increasing pressure up to about 80 kb., no significant changes have been observed in the spectra of the blue phase other than the slow red shift of Fe^{2+} bands.

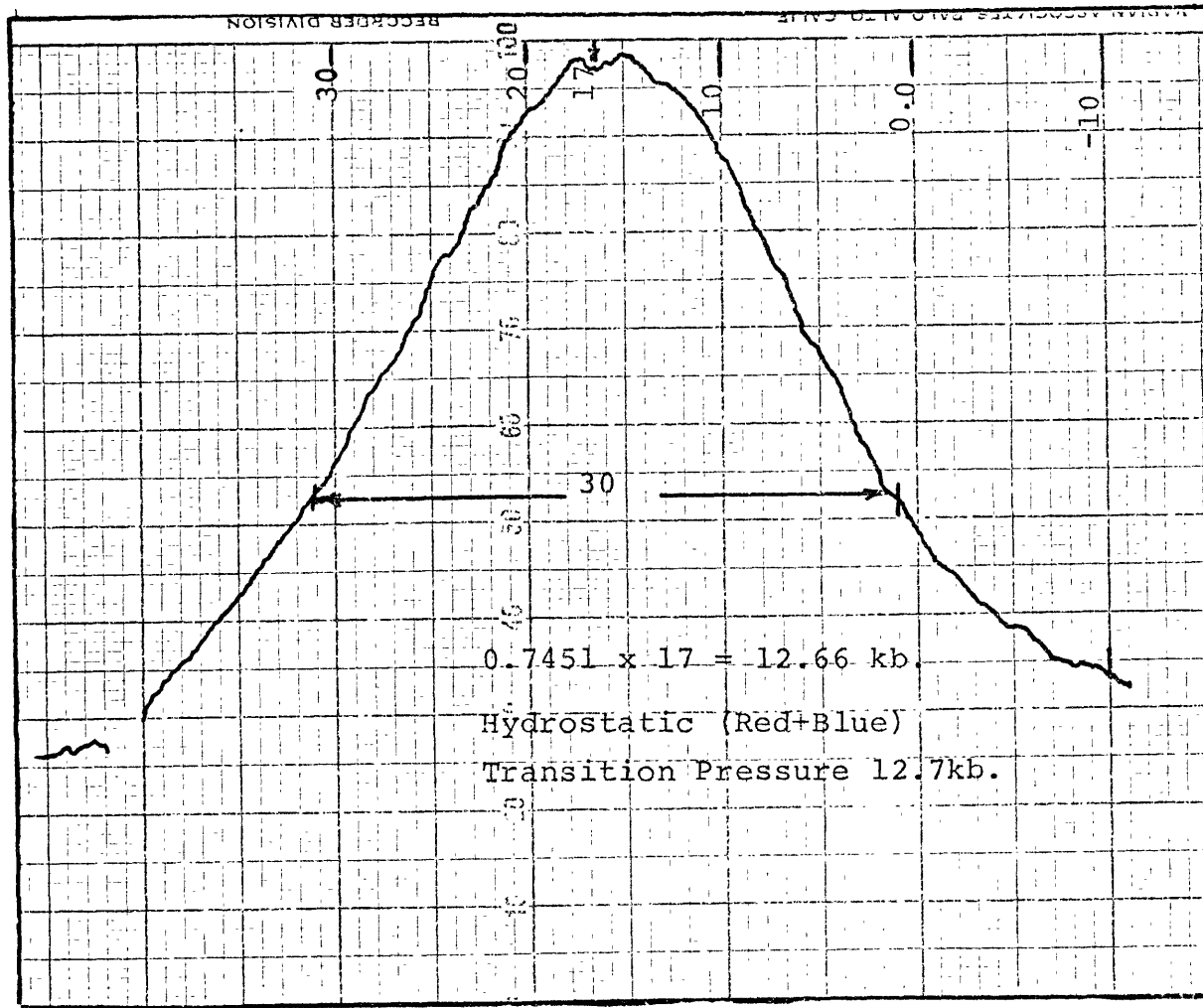
It is worth mentioning that by recycling the pressure back and forth on the same crystal and repeating measuring the transition pressure (using the ruby fluorescence line method, Forman et al., 1972), it was observed that the transformation takes place at progressively lower pressures than 26 kb.. Keeping the crystal under high pressure above 26 kb. for two weeks, then releasing the pressure to zero and increasing it again, led to the red-blue transformation taking place at about 12.6 kb.. The fluorescence spectrum of a ruby crystal fragment contained in the diamond cell at 12.6 kb. is shown in Figure VI-14 ; the width of the fluorescence band at this pressure also indicated the hydrostatic pressure condition in the cell.

It is obvious that there is some hysteresis in the reversible pressure transformation of gillespite, contrary to the prediction made by Hazen and Burnham (1974). The main factor that controls the hysteresis is the magnitude of the strain energy that can be stored in the hybrid crystals. It also depends on the degree of rotation of the oxygen atoms from their original positions.

From the above discussion, it is concluded that the nature

FIGURE VI-14

The fluorescence spectrum of a ruby crystal
fragment contained in the diamond cell at
12.6 kb..



of the gillespite transition is exclusively structural rather than being due to changes in the electronic structure of Fe^{2+} ; in addition, electron spin-pairing in Fe^{2+} is found to be unattainable in gillespite with increasing pressure up to 80 kb., which could be related to the continuous rotation of the oxygen atoms surrounding the ferrous ion. From the spectral data reported for gillespite phases and the optical observation of the changes of color and refractive indices at the transition pressure, it is apparent that the transition is reversible and a structural displacive type. The above results and interpretations have been obtained from the high pressure optical absorption and Mössbauer spectral techniques, and the structural nature of this transition have also been confirmed using the high pressure single crystal x-ray method (Abu-Eid and Hazen, 1974).

VI-3. Egyptian-Blue ($\text{BaCuSi}_4\text{O}_{10}$)

Egyptian-blue is an inorganic compound which has an intense blue color and a structure similar to that of gillespite. It contains Cu^{2+} ions in square planar coordination sites and the Cu-O interatomic distances are similar to those of Fe-O distances in gillespite (Pabst, 1959).

It has been selected for investigation in this project for two reasons: 1) it is isostructural with gillespite; thus, it may be an appropriate second example to demonstrate further the pressure-induced displacive transition observed in gillespite; 2) since it contains Cu^{2+} ions, then it will be suitable for

studies of the pressure-induced reduction process which was found (Wang and Drickamer, 1973) to occur in Cu(II) ions contained in square planar positions in organic complexes; 3) the Cu^{2+} energy levels are reciprocal to Fe^{2+} , so that all these transitions may be measured for the square planar ion in the visible-near i.r. region (see Clark and Burns, 1967).

The absorption spectrum of $\text{BaCuSi}_4\text{O}_{10}$ (Figure VI-15a) was measured at normal pressure by Clark and Burns (1967). It consists of a weak band (I) at 12900 cm^{-1} , and other two intense bands, (II) and (III), at 15800 and 18800 cm^{-1} . These bands were assigned by Clark and Burns (1967) to the following spin-allowed transitions in Cu^{2+} :

<u>Band Energy (cm^{-1})</u>	<u>Electronic Transition</u>
12900 (I)	${}^2B_{1g} \rightarrow {}^2B_{2g}$
15800 (II)	${}^2B_{1g} \rightarrow {}^2E_g$
18800 (III)	${}^2B_{1g} \rightarrow {}^2A_{1g}$

The energy level diagram shown in Figure VI-15b illustrates the assignments of these transitions.

In the present study, the spectra of $\text{BaCuSi}_4\text{O}_{10}$ were measured at different pressures. Figure (VI-16) shows the spectra measured at 1 atm., 50 kb., and 200 kb.. With increasing pressure, crystal field bands shifted to higher energies; the absorption maxima of the two bands at 12900 and 18800 cm^{-1} were unable to be located at elevated pressures due to their low intensities. However, the energy maximum of the band at 15800 cm^{-1} was determined accurately at various pressures.

At pressure around 50 kb., bands I and III became less in-

FIGURE VI-15

- (a) The absorption spectrum of $\text{BaCuSi}_4\text{O}_{10}$ measured at normal pressure (Clark and Burns, 1967).
- (b) Energy level diagram illustrating the assignments of the electronic transitions in Cu^{2+} in Egyptian-blue.

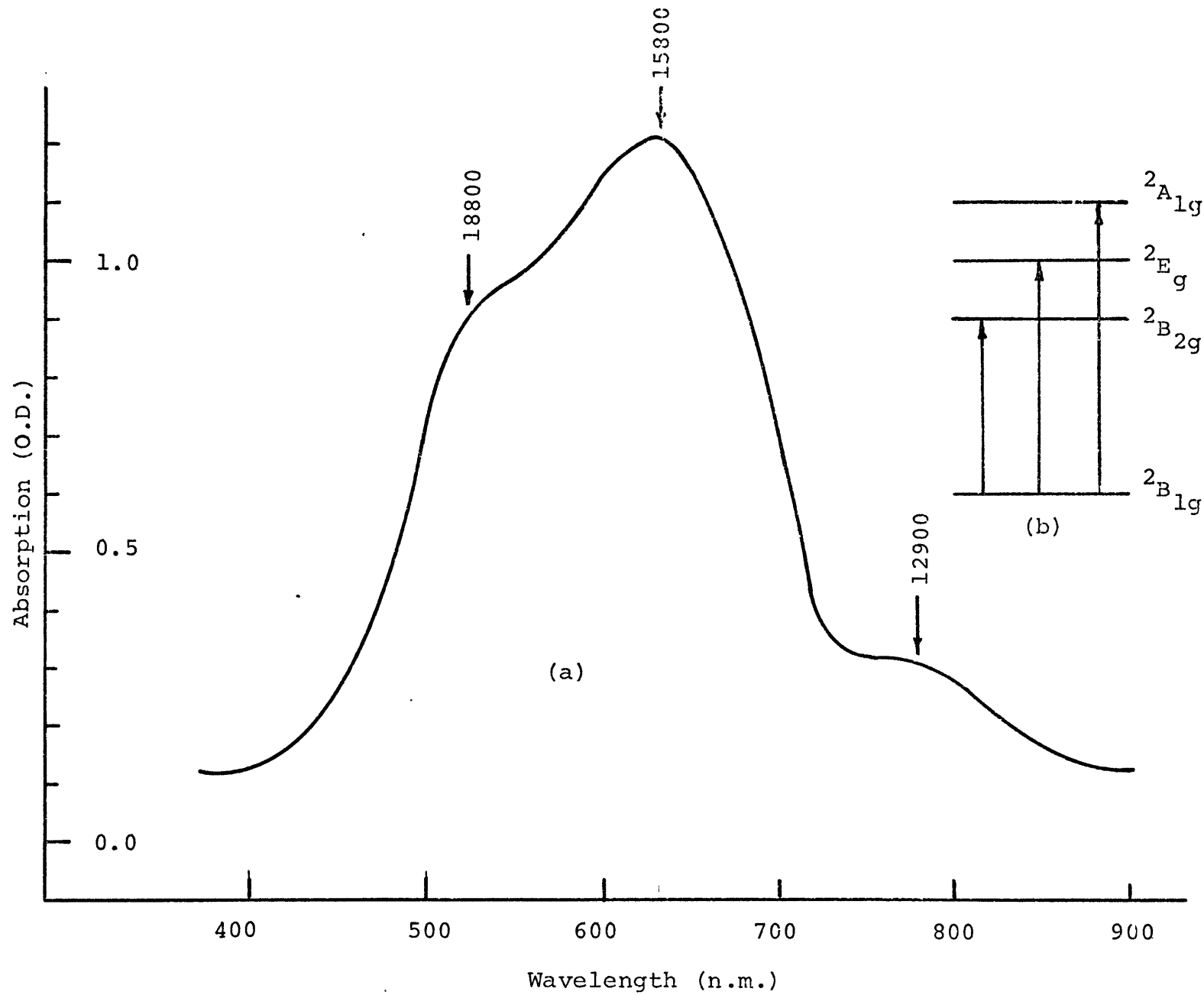
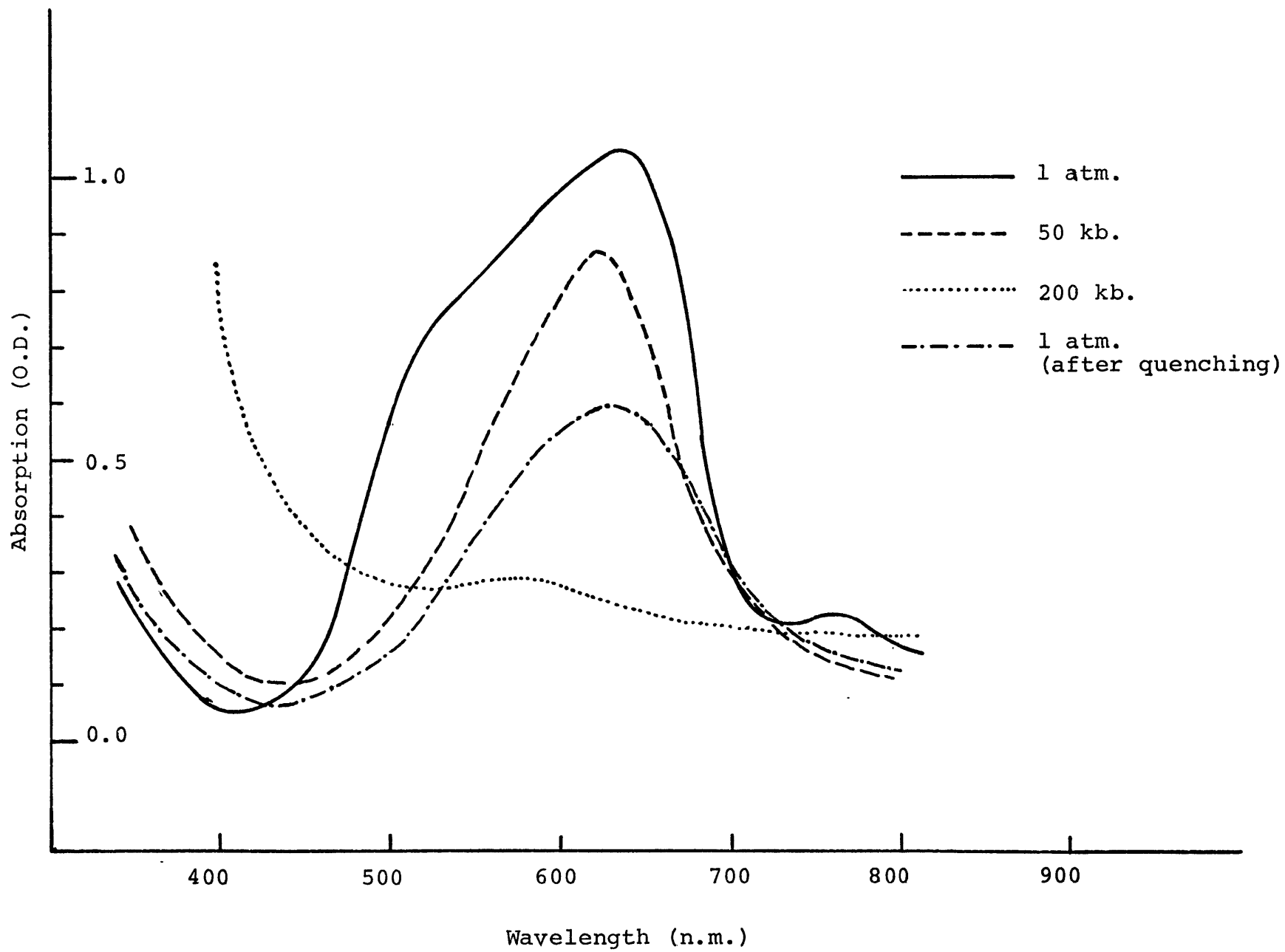


FIGURE VI-16

The spectra of $\text{BaCuSi}_4\text{O}_{10}$ measured at 1 atm., 50 kb., and 200 kb. and after releasing the pressure.



tense and could not be identified; band II decreased slightly in intensity and shifted from 15800 to 15950 cm^{-1} (Figure VI-16)

The absorption edge at about 23000 cm^{-1} was also observed to shift to lower energy. At pressure around 200 kb., band II decreased significantly in intensity (its intensity at 200 kb. is approximately 1/5th of its value at 1 atm.) and shifted to 16360 cm^{-1} . The absorption edge showed a tremendous increase in intensity and shifted further to lower energy.

It is difficult to predict from the high pressure spectra of $\text{BaCuSi}_4\text{O}_{10}$ whether there is a significant change in the site symmetry of Cu^{2+} or whether there is a displacive transition, since the two spectral bands, I and II, could not be resolved. Nevertheless, the tremendous decrease in crystal field band intensities and the substantial increase in the charge transfer (M-L or L-M) band intensity are taken as evidence of the reduction of Cu(II) and Cu(I) oxidation states, in accord with the findings of Wang and Drickamer (1973). The disappearance of crystal field bands is expected since Cu^{2+} ions have completely filled d-levels; thus, no crystal field transitions are expected to occur in this ion.

The color of the Egyptian-blue specimen was observed to show a continuous color change from blue to pale blue to colorless as pressure increases, indicating that amounts of Cu^+ ions increase with increasing pressure. It was noticed also that with decreasing pressure, the blue color starts to reappear and increases in intensity.

The spectrum of the Egyptian-blue sample, measured at nor-

mal pressure after it has been subjected to 200 kb., is shown in Figure VI-16 . It is similar to the spectrum obtained at 1 atm. before applying pressure on the sample. However, the bands are slightly less intense in the former, which may be related to some hysteresis in the pressure-induced reduction process.

The above results suggest that the reduction process is a continuous and reversible one. It involves the transfer of an electron from a non-bonding molecular orbital, of CuO_4^{6-} cluster, which belongs primarily to the oxygen ligands to the Cu^{2+} 3d-orbital. Similar results were obtained by Drickamer and co-workers from their high pressure studies of organic complexes containing Fe^{3+} and Cu^{2+} ions (Drickamer et al., 1970, 1972; Drickamer and Frank, 1972, 1973; Frank and Drickamer, 1972).

In conclusion, from the high pressure spectra of $\text{BaCuSi}_4\text{O}_{10}$, it is believed that electronic transitions in Cu^{2+} (pressure-induced reduction) occur in Cu^{2+} at pressures between 150-200 kb.. No evidence could be found for the displacive transformation of the structure observed in gillespite.

VI-4. Azurite $\text{Cu}_3(\text{CO}_3)_2(\text{OH})_2$

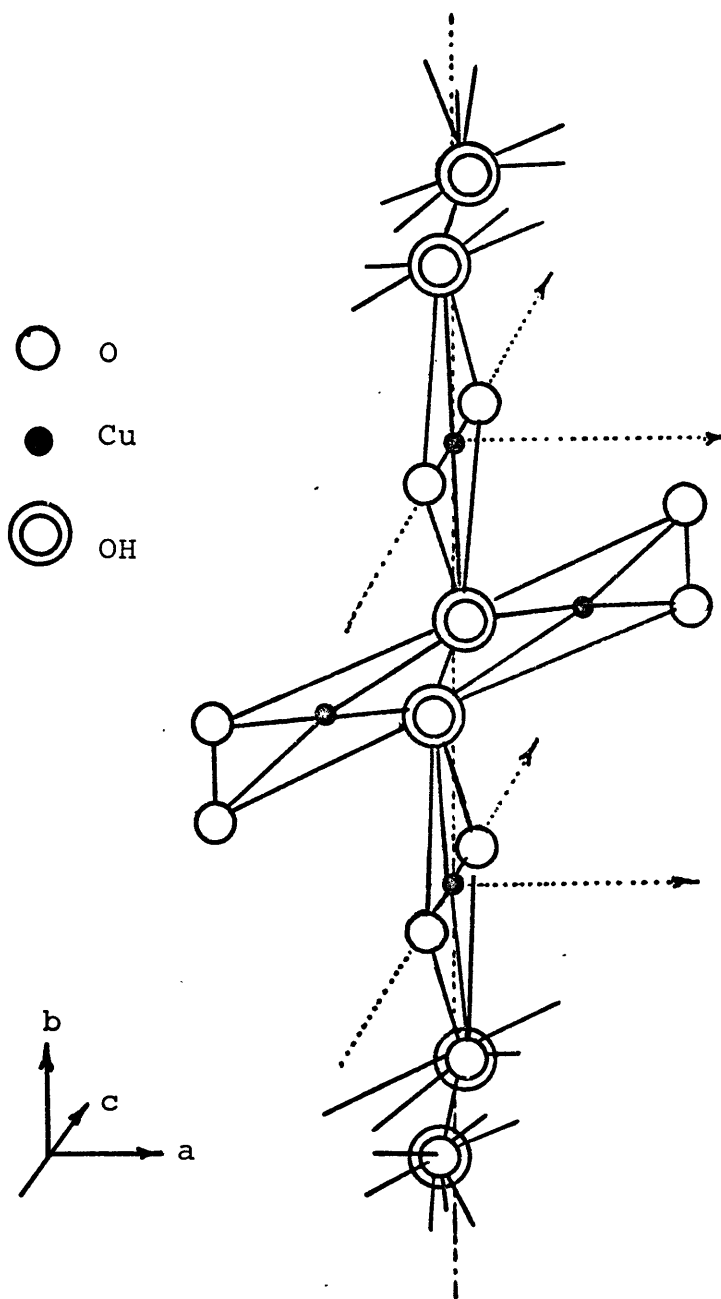
Azurite is a basic carbonate mineral which belongs to the space group $P2_1/c$ and has an intense blue color. The crystal structure was determined by Brasseur (1932) and refined by Gattow and Zemann (1958). The Cu^{2+} ions are contained in two crystallographic distinct positions denoted by Cu_I and Cu_{II} .

The Cu_I atom is coordinated to two OH groups and two oxygen atoms in a square planar site (Figure VI-17). The Cu_I - OH and Cu_I - O interatomic distances are 1.98\AA and 1.88\AA , respectively. Further, there are other two oxygens, each of which are at a distance 2.75\AA from the Cu_I atom; since these two oxygens are at large distances from the copper atom, they are not considered as taking part in the Cu-coordination polyhedron. The Cu_{II} atom is also coordinated immediately to two OH groups and two oxygens (Figure VI-17). The interatomic distances are Cu_{II} -OH = 2.04\AA ; Cu_{II} -OH^{II} = 1.99\AA ; Cu_{II} -O^{III} = 1.92\AA ; and Cu_{II} -O^{II} = 2.01\AA . Moreover, there are two oxygen atoms at distances 2.38\AA and 2.83\AA from the Cu_{II} atom. Gattow and Zemann (1958) considered the Cu_{II} site as a square plane, whereas Povarennykl (1972) considered the site as a square pyramid, i.e. he assumed that the oxygen at 2.38\AA as coordinated to the Cu_{II} atom. The Cu_I and Cu_{II} sites share corners to form chains of square planes extended parallel to the b-axis; in addition, each Cu_{II} site shares one of its edges with another Cu_{II} polyhedron (Figure VI-17).

Apart from the diffuse reflectance study reported by Hunt and Salisbury (1971), no spectral data were reported previously for azurite. Hunt and Salisbury (1971) showed one broad spectral feature at 0.8μ (12500 cm^{-1}) which they assigned to the crystal field transition in Cu^{2+} in octahedral site. Other bands were also observed at 1.4μ (4250 cm^{-1}) and 2.5μ (4000 cm^{-1}). These bands were assigned by the above authors to OH, H_2O , or CO_3 vibrational frequencies.

FIGURE VI-17

The site symmetries and coordinates of Cu_I and Cu_{II} atoms in azurite (from Gattow and Zemann, 1958).



In the present study, the absorption spectra of azurite single crystals were measured at 1 atm. in the i.r. and visible regions. The spectra of azurite single crystals, mounted in the diamond cell, were also measured at elevated pressures. Figure

VI-18a shows the spectrum of azurite crystals mounted in the diamond cell at approximately normal pressure. It consists of a broad and intense absorption envelope covering the energy region 13000-20000 cm^{-1} and a sharp intense absorption peak at 25310 cm^{-1} . Two absorption bands were fitted under the broad absorption profile, and the absorption maxima of the two bands were located at 16130 and 14700 cm^{-1} . The three absorption features at energies 14700, 16130, and 25310 cm^{-1} indicate a distortion in the site symmetry of Cu^{2+} ; the site symmetry is considered here to be approximately D_{4h} , the energy level diagrams for Cu^{2+} are shown for both O_h and D_{4h} symmetries Figure VI-19.

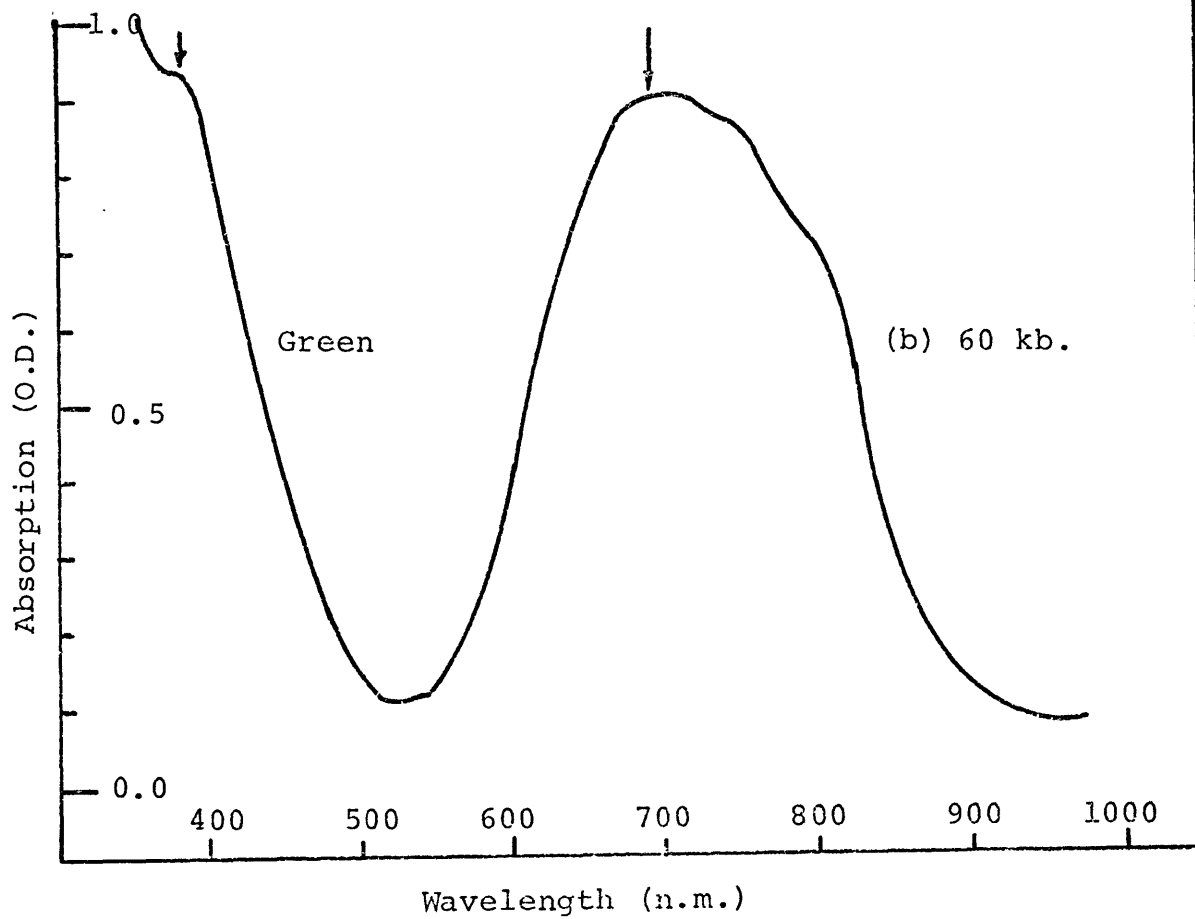
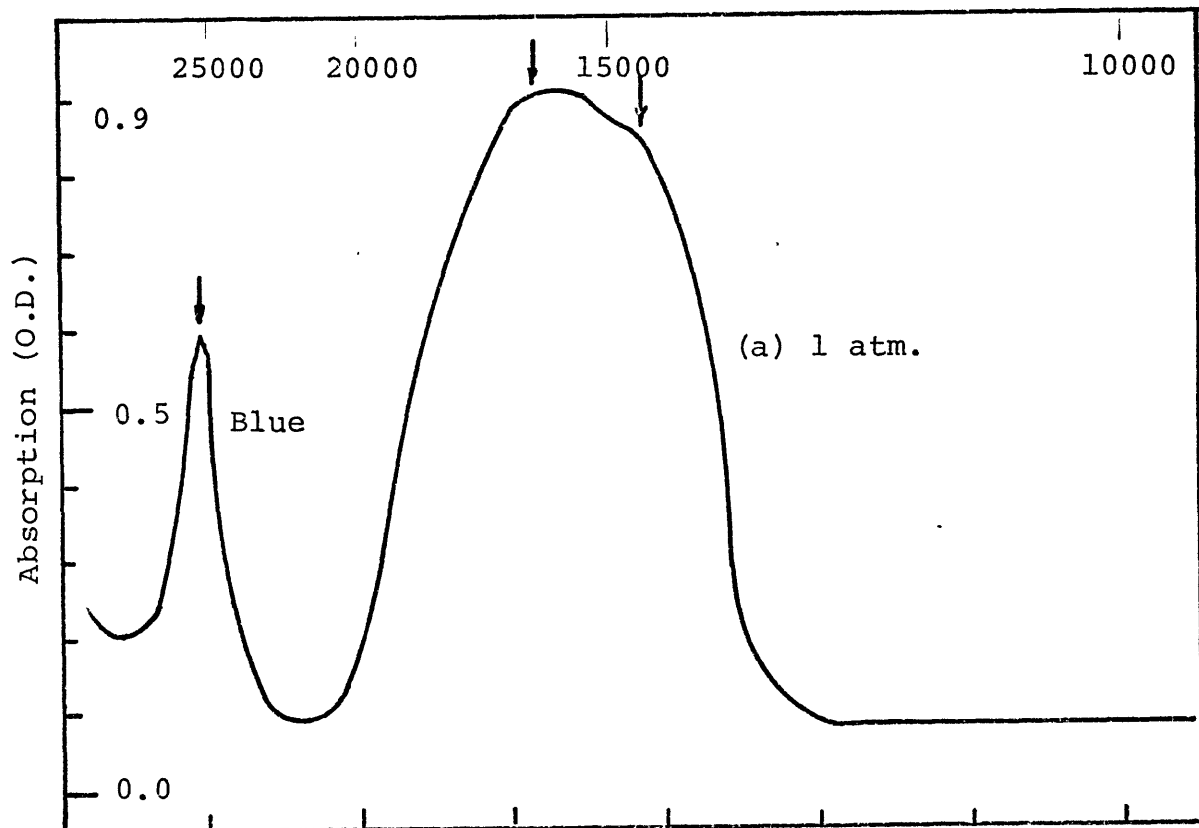
The band at 14700 cm^{-1} is assigned to the electronic transition ${}^2B_{1g} \rightarrow {}^2B_{2g}$, and the band at 16130 cm^{-1} is assigned to ${}^2B_{1g} \rightarrow {}^2E_g$. The remaining band at 25310 cm^{-1} is assigned to ${}^2B_{1g} \rightarrow {}^2A_{1g}$ transition.

Another important spectral feature is the intense absorption of M-L or L-M charge transfer (absorption edge) which starts at 23800 cm^{-1} . Although the band at 25310 cm^{-1} overlaps on the absorption edge, it is not obscured due to its large intensity and sharpness. The blue color in azurite arises due to the transmission of light in the blue-spectral region 19250-

FIGURE VI-18

- (a) Absorption spectrum of azurite crystal in the diamond cell at approximately normal pressure (the crystal exhibits an intense blue color).
- (b) The spectrum of azurite crystal above 60 kb. Note the shift of spectral bands to lower energies (the color at this pressure changes to green).

Wave number (cm^{-1})



23800 cm^{-1} as shown in the spectrum (Figure VI-18a).

With increasing pressure, spectral bands shifted to higher energies as a consequence of decreasing Cu-ligand interatomic distances. However, at pressure around 60 kb., the color changed abruptly from blue to green. The spectrum measured above the transition pressure (Figure VI-18b) consisted of a broad and intense absorption profile which covered the energy region 12000-18000 cm^{-1} . Two spectral bands were fitted under this absorption envelope at energies 13300 and 15000 cm^{-1} . The sharp band at 25310 cm^{-1} in the 1 atm. spectrum shifted slightly to higher energy as pressure increased to 60 kb. (about 200 cm^{-1}), and the absorption edge showed a substantial low-energy shift. As a consequence of the red shifts of both the absorption edge and the absorption envelope, the transmission window at 60 kb. occurred in the green spectral region 17500-21500 cm^{-1} ; this shift explains the change in color from blue to green. It should be mentioned that after releasing the pressure, the color of azurite remained green, and the spectrum measured after quenching is similar to that measured at 60 kb..

The above high pressure spectral data indicated an irreversible phase change in azurite which may be of the first order type. It is interpreted from the high pressure spectrum that the coordination number of Cu^{2+} ion may have increased from four to five or possibly to six as a consequence of shortening the interatomic distances between Cu^{2+} and the remaining next nearest oxygen atoms neighbors. It also may be due to kinking of the $\text{Cu}(\text{O},\text{OH})_4$ polyhedral chain, i.e. the bond angles $\text{Cu}_I\text{-OH-}$

Cu_I and/or $\text{O}_{\text{Cu}_{II}}-\text{OH}-\text{O}_{\text{Cu}_{II}}$ may have decreased significantly.

Malachite, $[\text{Cu}_2(\text{OH})_2\text{CO}_3]$, is a copper carbonate mineral which also has a green color. Thus, it may be useful to compare the structural and spectral features of malachite with those of the high pressure azurite form. Malachite contains the copper atoms in two sites viz. Cu_I and Cu_{II} ; the Cu_I atom is surrounded by two oxygens and two OH^- ions in approximately a square planar symmetry. The Cu_I -ligand interatomic distances are: $\text{Cu}_I\text{-O1} = 1.987$; $\text{Cu}_I\text{-O2} = 2.071$; $\text{Cu}_I\text{-OHI} = 1.899$; and $\text{Cu}_I\text{-OH2} = 1.915\text{\AA}$; in addition, there are two oxygen atoms at a greater distance (2.520 and 3.630\AA) which may be considered as coordinated to the Cu_I atom. Here, then, the Cu_I site may be envisaged as an elongated octahedron.

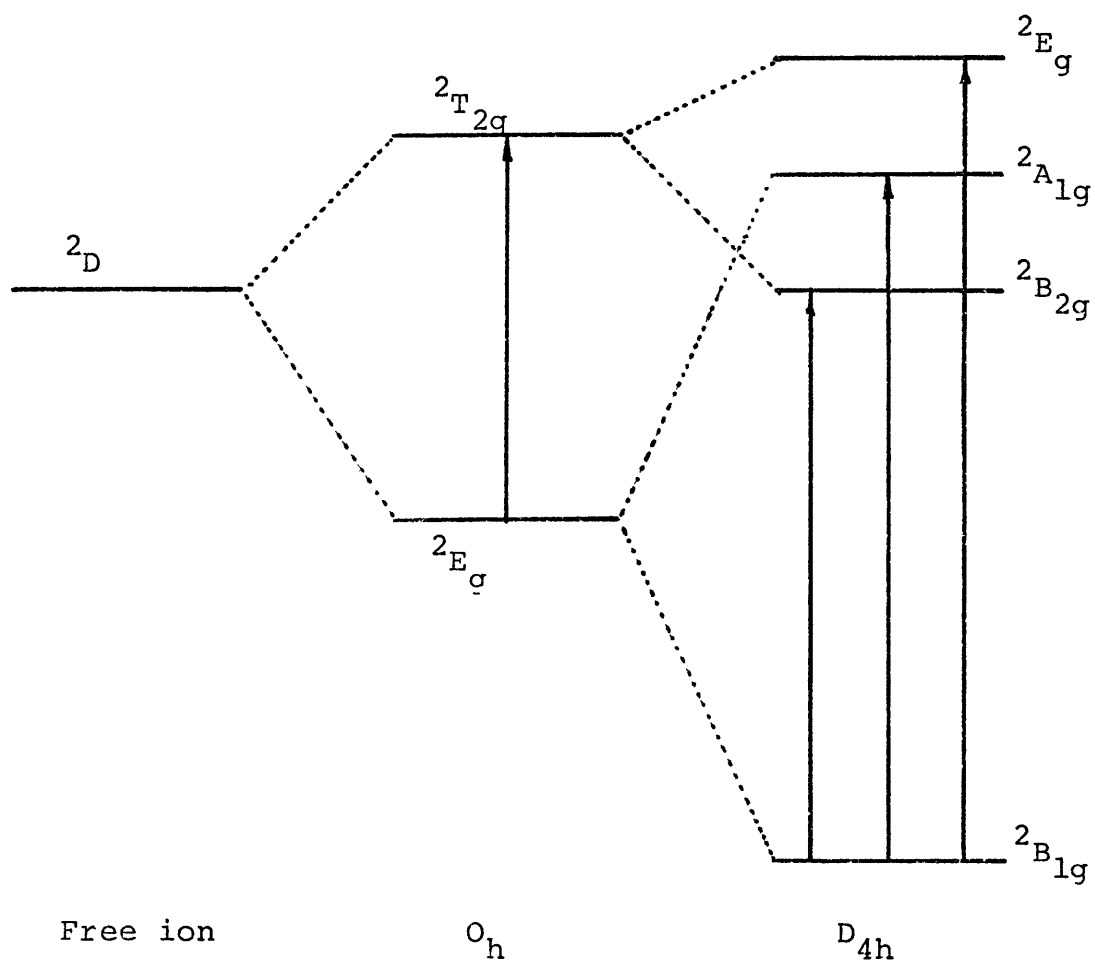
The Cu_{II} atom is also coordinated immediately to two OH groups and two oxygen atoms in a square planar site with the Cu_{II} -ligand distances are: $\text{Cu-O2} = 2.116$; $\text{Cu-O3} = 2.042$; $\text{Cu-OH1} = 1.924$; and $\text{Cu-OH2} = 1.922\text{\AA}$. Moreover, there are two other hydroxyl groups at distances 2.362 and 2.353\AA , which may also be coordinated to the Cu_{II} atoms. Thus, the Cu_{II} position may be considered as a six-fold coordination site.

The absorption spectrum of malachite at normal pressure was reported by Lakshman and Reddy (1973). It consists of a broad spectral feature which has a maximum absorption at 11919 cm^{-1} and the other prominent spectral band at 20166 cm^{-1} . Two other weak absorption bands at energies 16482 and 18160 were also observed in malachite spectrum.

Comparing the spectrum of malachite with that of the high

FIGURE VI-19

Energy level diagram of Cu^{2+} in O_h and D_{4h} symmetries.



pressure form of azurite, the spectral bands at 11919, 16482, and 20166 cm^{-1} in malachite spectrum may correspond to the two broad spectral features at 13300 and 15000 cm^{-1} and the sharp band at 25310 cm^{-1} , observed in the high pressure spectra of azurite. The difference in the energy values of spectral bands in the spectra of malachite and the green-azurite and the disappearance of the band at 18160 cm^{-1} in the spectra of azurite may be due to the difference in the site symmetries and the interatomic distances.

Although it is safe to assume an increase in the coordination number of Cu atoms in azurite above 60 kb., the nature of the blue-green azurite transition is still uncertain. It is obvious, however, that this transition is a structural type rather than electronic, and that the copper ion is still in the divalent oxidation state at this pressure, as indicated from the high pressure spectra. For the deep knowledge of the nature of this transition, and the interatomic distances of the high pressure form, single crystal high pressure x-ray studies are warranted.

Chapter VII

DISCUSSION

VII-1. Energy Shifts of Spectral Bands with Pressure

It was previously believed that crystal field bands show high energy shifts with increasing pressure. This prediction was based on the assumption that most crystal field transitions are dependent on Δ_0 or $10Dq$, which varies as $1/R^5$ and the pressure influence would, naturally, decrease R.

The present study is an attempt to investigate more carefully the pressure influence on the various types of crystal field transitions, and then to understand the relationship between the energy of each transition and the parameters $10Dq$, B, and C.

From the experimental results presented in Chapter IV, it is evident that the spin-allowed transitions, dependent mainly on $10Dq$, shift significantly to higher energies as pressure increases. These transitions include those of Ti^{3+} [${}^2T_{2g} \rightarrow {}^2E_g$]; Cr^{3+} [${}^4A_{1g} \rightarrow {}^4T_{2g}(F)$, ${}^4T_{1g}(F)$, ${}^4T_{1g}(P)$]; Mn^{3+} [${}^5E_g \rightarrow {}^5E_g$]; Fe^{2+} [${}^5T_{2g} \rightarrow {}^5E_g$]; Co^{2+} [${}^4T_{1g}(F) \rightarrow {}^4T_{2g}(F)$, ${}^4A_{1g}(F)$, ${}^4T_{1g}(P)$], and Cu^{2+} [${}^2E_g \rightarrow {}^2T_{2g}$].

The shift to higher energy of each transition at elevated pressure is an indication of a consistent increase in $10Dq$ value, due to shortening M-L distances. However, the magnitude of this shift depends on other factors such as the site compressibility of each cation, the regularity or distortion of the site, and the structure of the mineral phase.

In the case of olivine, one of the spectral bands for the M_1 site shifted to higher energy with pressure, and the other to lower energy. However, in spite of the opposite energy shift of the two bands, there appears to be a net increase in $10Dq$. The decrease in the energy separation between these two bands with pressure indicates that the M_1 site is getting more regular.

The change of the polyhedral distortions towards more regular octahedra in fayalite have also been demonstrated by Huggins (1974) using the high pressure Mössbauer technique. The high pressure spectral results of olivine are useful for understanding the nature and mechanism of olivine→spinel transitions, which will be discussed in the forthcoming pages.

The abrupt low-energy shift of crystal field bands for Fe^{2+} in gillespite and Cu^{2+} in azurite was presented in Chapter VI. From such shifts in the spectral features, a reversible displacive structural transition in gillespite was identified in which the site symmetry of Fe^{2+} changed from a square plane to a distorted, flattened, tetrahedron. Azurite, however, showed an irreversible phase change in which the coordination number of the site was predicted to increase, and the site symmetry to change significantly at pressure around 60 kb..

Apart from the absorption bands in olivine, gillespite, and azurite, the remaining spectral bands corresponding to the spin-allowed transitions in Ti^{3+} , Cr^{3+} , Mn^{3+} , Fe^{2+} , Co^{2+} , and Cu^{2+} in silicate minerals showed continuous high energy shifts with increasing pressure.

The rates of these shifts vary from one band to another in the spectrum of each transition metal ion. This variation is related to three factors: 1) the degree of shortening of each M-L interatomic distance relative to the mean M-L bond distance; 2) the geometry of the transition metal ion site which also involves the L-L interatomic distances; and 3) the position of the transition metal atom and the ligand atoms relative to each other and then relative to the crystallographic axes x, y, and z.

Furthermore, any discontinuous change in the rate of band energy shift may indicate a disruption in the site symmetry of the transition metal ion and suggest a phase change in the bulk mineral phase.

In addition to the spin-allowed transitions which are dependent only on $10Dq$ parameter, there are other spectral features which correspond to the spin-forbidden transitions. The energies of these are dependent mostly on Racah parameters, B and C, and to a lesser extent on $10Dq$. Table (II-1. a,b,c) summarizes the energies of these transitions in various transition metal ions.

Absorption bands dependent only on Racah parameters are expected to shift slightly to lower energies, since the values of both B and C are predicted to decrease with decreasing M-L distances (Minomura and Drickamer, 1961). Zahner and Drickamer (1961) had shown that there is a decrease of about 20 cm^{-1} in the value of B for Ni^{2+} in MgO , with increasing pressure over 140 kb.

In the present study, a decrease of 6 cm^{-1} is found for Cr^{3+} ions in uvarovite as the pressure increases to about 100 kb.. A further piece of evidence for the slight changes of B values in silicate minerals is the undetectable energy shifts of Fe^{3+} bands in andradite, which are directly related to B and C, and the negligible shift of the spin-forbidden bands of Fe^{2+} ions in olivine and pyroxenes, which are dependent to a large extent on B and C values. From the above results, it is safe to assume that the energies of those crystal field bands which are dependent on B and C parameters will at most decrease slightly.

Charge transfer bands, on the other hand, should show a negative energy (red) shift accompanied by significant increases in width and intensity with increasing pressure.

The slow red shift of the absorption edge in all the investigated silicate minerals, which has been related to L-M or M-L charge transfer, is consistent with the prediction based on molecular orbital and band theory models. However, the huge low energy shift of the absorption edge, observed in the spectra of crocoite, vanadinite, and potassium permanganate, may be due to other processes which will be discussed in detail later in this chapter.

Suchan and Drickamer (1959) and Suchan et al. (1959) have reported the red shift of the absorption edges in many halide compounds, and related the shifts to closing gaps between the conduction and valence bands. They also found that the pressure required to eliminate the gap of all iodide compounds is below 30 kb..

Recently, Mao and Bell (1972a,b) found that above 100 kb., the absorption edge of olivine shifts abruptly with pressure into the near infrared region with simultaneous exponential increase in electrical conductivity. Although the abrupt shift was not explained, it will be discussed in some detail in section VII-6.

M-M charge transfer bands that arise from an electron hopping between Fe^{2+} and Fe^{3+} ions shift slowly to lower energies with an increase in their widths and intensities as pressure increases. These trends have been observed in the C.T. spectra of fayalite, orthoferrosilite, blue-omphacite, glaucophane, and vivianite. The increase in intensities of M-M charge transfer bands in the first four minerals, with increasing pressure up to 50 kb., is about 20-50% of their values at 1 atm.. This increase in intensity is related to the increase in the probability of electron transfer between the two neighboring transition metal ions. Nevertheless, the tremendous increase in $Fe^{2+}-Fe^{3+}$ C.T. bands in vivianite at pressure around 300 kb. (Mao, 1974) may be an indication of significant changes in the atomic structure of the bulk mineral phase or in the electronic structure of the transition metal ion, or both.

VII-2. The Degree of Covalency and Racah Parameter B at Elevated Pressures

The degree of covalency of the metal-ligand bond is indicated by obtaining the ratio of the electronic repulsion parameter B in the complex, to that of the free cation, B_0 . In the

free metal ion, the interelectronic repulsion integrals are approximately proportional to the average reciprocal radius, $\langle r^{-1} \rangle_{3d}$, of the partly filled 3d shell (König, 1971). B and C values in transition metal compounds have been found to be lower than their values in the free transition metal ions. This decrease in B is attributed to an expanded radial distribution of d electrons in the complex (König, 1971). The covalency parameter, $\beta = B/B_0$, known as the nephelauxetic parameter, is of two types: first, a parameter type related to central field covalency which arises from screening the nuclear charge of the cation by the ligands (Lever, 1968; König, 1971) and designated by β_{35}^* ; and second, a parameter related to the symmetry restricted covalency which arises due to delocalization of d electrons onto the ligands and designated as β_{33} and β_{55} .

Fortunately, the B value for Cr^{3+} , which is determined from ν_1 and ν_2 transitions (equation IV-10), is related to the first type of covalency, i.e. it depends on both orbitals, e_g and t_{2g} , and is not restricted only to one type of orbital (Reiner, 1969).

The B value depends on many factors such as the nature of the ligands surrounding the central ion, the M-L interatomic distances, and the relative concentration of chromium ions in the structure.

* The repulsion parameters containing e_g or (γ_3) orbitals, only, are designated as β_{33} , and those with t_{2g} of (γ_5) are given as β_{55} ; whereas integrals containing both e_g and t_{2g} orbitals are designated as β_{35} (Reiner, 1969).

Reiner (1969) reported that Δ_o and B values for $\text{Cr}_x\text{Al}_{2-x}\text{O}_3$ mixed crystal series vary with the concentration of Cr^{3+} ions. Reiner found that both Δ_o and B values decrease with increasing x. The decrease in Δ_o is easily explained because the Cr^{3+} site is getting larger with increasing x. However, the decrease in B may be due to an increase in the degree of delocalization of d-electrons onto the ligands as the chromium content increases. This is reflected in the higher electronegativity of Cr^{3+} relative to Al^{3+} .

B value is expected to decrease with decreasing the M-L interatomic distance due to the increase in the degree of the metal-ligand orbital overlap which then causes an increase in the radius of the partly filled 3d shell.

In this study, the degree of covalency has been examined in various minerals and correlated with the average Cr-O distances. Burns (1974) has listed the energies of ν_1 and ν_2 transitions in Cr^{3+} ions contained in a suite of natural minerals. Burns also listed the average M-O distances in these minerals to obtain CFS and CFSE parameters. From the energy values of ν_1 and ν_2 transitions, B values were obtained for Cr^{3+} ions in those minerals. Figure (VII-1) shows the trend of energy change in B values with the change in Cr-O distances. From Figure (VII-1) it is apparent that there is a slight decrease in B value as M-O distance decreases. However, some minerals fall far away from this trend; these are: epidote, tremolite, tourmaline, and beryl. These minerals have substantially larger B values relative to the remaining minerals. Studying carefully the nature

of ligands surrounding the Cr^{3+} ions in such minerals, it is observed that the Cr^{3+} ion is surrounded by 4 oxygens and two OH^- ions, whereas in other minerals, it is surrounded by 6 oxygens. The large B value in the hydroxyl-bearing minerals is then related to replacing two oxygens by two OH^- ions. Since the OH^- ion has one negative electron charge less than O^{2-} , it is expected to have a smaller electron density than O^{2-} to overlap onto the Cr^{3+} d-orbitals. Consequently, when the Cr^{3+} cation is coordinated to OH^- ions, the radius of the partly filled 3d shell is expected to be smaller than the case when Cr^{3+} is coordinated only to oxygens; thus, B values should be larger.

It is also observed in Figure (VII-1) that Cr^{3+} in eskolaite (Cr_2O_3) has a very low B value. This is in fact expected since the chromium content is very large (Reiner, 1969).

With increasing pressure, the M-L interatomic distances will decrease; consequently, a decrease in B value should be expected.

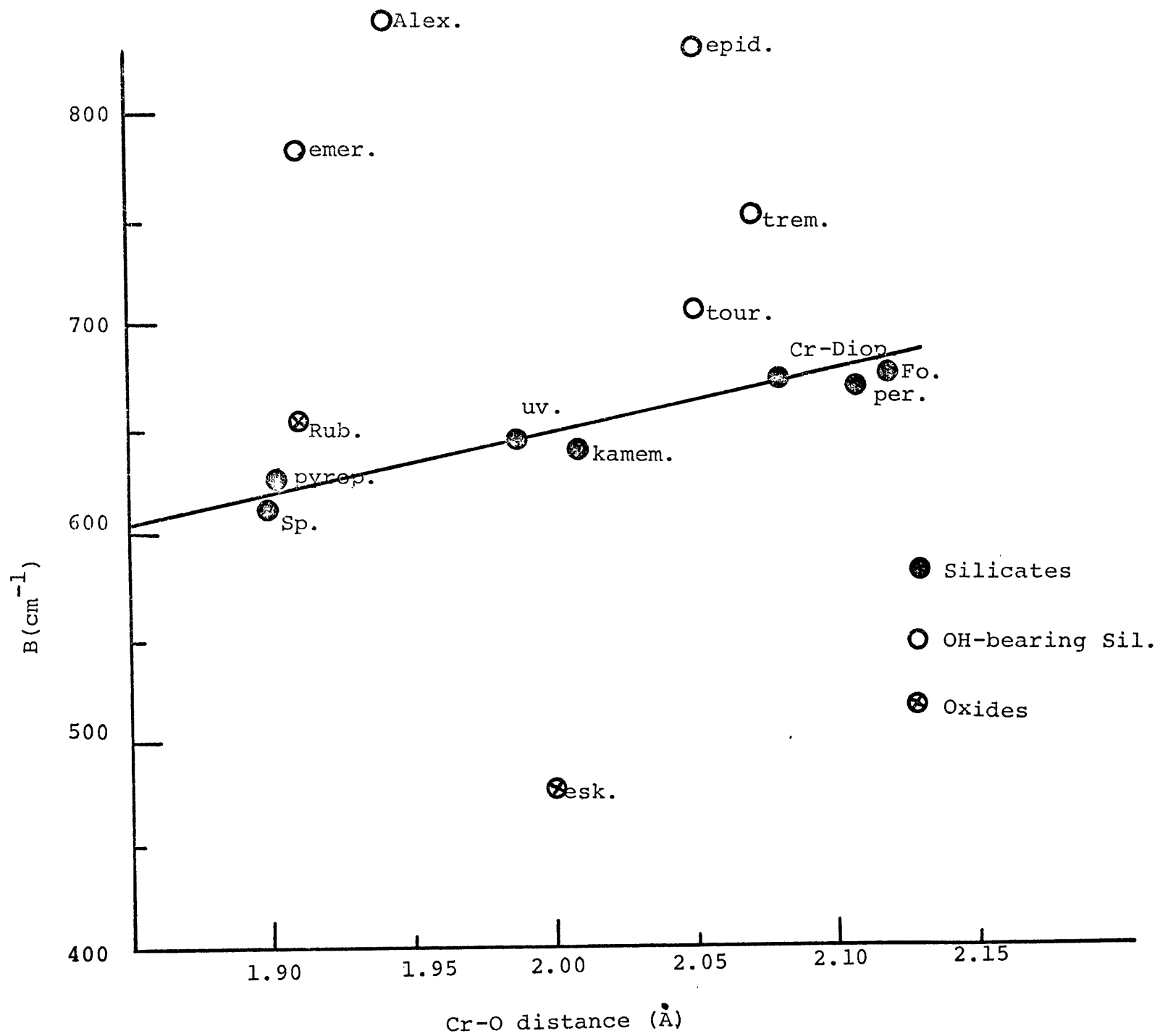
The slope of the line shown in Figure (VII-1) indicates that the rate of B change with shortening Cr-O distance is about $50 \text{ cm}^{-1}/0.1\text{\AA}$. The change in Cr-O distance at elevated pressure may be roughly estimated from 10Dq values obtained at these pressures.

From the energy values of Δ_p (10Dq at high pressure) and Δ_o (10Dq at 1 atm.) for Cr^{3+} , which were given in section IV-4.3, and considering the equivalence, II-7, the following relationship was derived:

FIGURE VII-1

Variation of B value with Cr-O distance in a suite of chromium minerals. The B value for each mineral was calculated from the energies of ν_1 and ν_2 transitions tabulated by Burns (1974b):

<u>notation</u>	<u>mineral name</u>
epid	epidote
alex	alexandrite
emer	emerald
trem	tremolite
tour	tourmaline
Cr-diop	Cr-diopside
Fo	fosterite
per	periclase
kam	kamemerite
uv	uvarovite
rub	ruby
pype	pyrope
sp	spinel
esk	eskolite



$$[\Delta_o/\Delta_p] = [(Cr-O)_p/(Cr-O)_o]^5 \quad (1)$$

considering the average Cr-O distance in uvarovite at normal pressure as 1.986Å; $\Delta_o \equiv 16667 \text{ cm}^{-1}$; $\Delta_{95 \text{ kb.}} \equiv 17007$; and $\Delta_{197 \text{ kb.}} \equiv 17668 \text{ cm}^{-1}$, then the average Cr-O distance decreases then by about 0.01 and 0.014Å at these pressures. Considering this decrease and the slope of the line shown in Figure (VII-1) it appears that the value B will decrease at 95 and 197 kb. by 5 cm^{-1} and 10 cm^{-1} . These changes in B value are in good agreement with those obtained in section IV-4.3, namely 7 cm^{-1} and 12 cm^{-1} . It is evident then from the experimental results obtained in section IV-4.3 and the argument presented above, that B value decreases very slightly with increasing pressure and decreasing M-O distances.

A further indication of the slight decrease in B stems from the high pressure studies of the spectra of Fe^{3+} ions in silicate minerals. These minerals are blue-omphacite, andradite, Fe^{3+} -epidote, and glaucophane.

Fe^{3+} in these minerals has many spin-forbidden absorption bands; the most intense of these bands is the band related to the transition, ${}^6A_{1g} \rightarrow {}^4A_{1g}(G), {}^4E_g(G)$. The energy of this band is equivalent to $10B + 5C$. At elevated pressures, no detectable energy shifts have been observed in this band in each of these minerals. However, this shift was estimated from the high pressure spectra to be about 100 cm^{-1} in 50 kb. Assuming that $C=4B$, then the energy of this transition will be $30 B$. Consequently, the change in B value in 50 kb. should be about 3.3

cm^{-1} . This energy change in B value is also consistent with the above argument and the results obtained for Cr^{3+} in uvarovite.

Another piece of evidence of the slight negative change in B value with decreasing M-O distances is the undetectable energy shift of Fe^{2+} spin-forbidden bands. In all of the silicate minerals containing substantial amounts of Fe^{2+} , there is a sharp conspicuous peak which occurs at about 19800 cm^{-1} . This band was assigned in Chapter IV to the transition, ${}^5\text{T}_{2g} \rightarrow {}^3\text{T}_{1g}$ or ${}^5\text{T}_{2g} \rightarrow {}^3\text{T}_{2g}$. The energies of both transitions, (Table II-1), are proportional to the energies of B and $10Dq$. Undetectable energy shifts with pressure are observed in these transitions because the trends of the pressure-induced energy changes for B and $10Dq$ are in opposite directions.

From the above discussion, it is apparent that changes in the degree of covalency of the Cr-O, Fe^{3+} -O, and Fe^{2+} -O bonds with increasing pressure up to 200 kb. are very small. This implies that the ionic model for the M-O bond in silicates still holds in the earth's mantle. It is expected, then, that changes in the structure such as phase transitions or disproportionation to oxide components may take place before any significant changes in the ionic character of the M-O bond occur.

It should be mentioned that the nature of the chemical bond in the oxides assumed to occur in the lower mantle is most likely to be of metallic character. The increase in the electrical conductivities of $(\text{Mg,Fe})_2\text{SiO}_4$ polymorphs at pressure above 100 kb. (Mao, 1973) and the shifts of their absorption edges to low-

er energies may be related to increases in the metallic character of these phases. Such changes may be an intermediate stage that takes place before the disproportionation of $(\text{Mg,Fe})_2\text{SiO}_4$ phases to their oxide components occur.

VII-3. Site Compressibilities from 10Dq Values

In Chapter II it was mentioned (equation II-7) that 10Dq is related to the average M-L distance, R, as: $10Dq \propto R^{-5}$. Consider: $10Dq \equiv E$ and $R \equiv (V)^{1/3}$. Where E is the energy and V is the volume of the polyhedron, it follows then that:

$$E \propto V^{-5/3} \quad (2)$$

Differentiating with respect to V will give $dE/dV \equiv -5/3V^{-8/3}$, and then using the relation (2), the following relation is obtained:

$$dE/dP = 5/3(E/K) \quad (3)$$

where K is the bulk modulus of the t.m. polyhedron.

The above equation has been used by Abu-Eid (1974), Shankland et al. (1974), and Huggins (1974) to calculate the bulk moduli of transition metal ion polyhedra in silicate minerals. However, Shankland et al. (1974) assumed that E is equivalent to the energy value of the Fe^{2+} band at 10000 cm^{-1} , and found that:

$$dE/dP = 1.3 E/K \quad (4)$$

where he considered K as the bulk modulus of the whole mineral phase. It should be mentioned that the relationship given in (4) which was derived from the experimental data by Shankland et al. is quantitatively inaccurate, simply because the energy

of the crystal field band at 10000 cm^{-1} is related to the volume of the polyhedron containing the transition metal ion rather than to the volume of the bulk mineral, i.e. E is related to K of the site rather than to that of the bulk mineral phase.

Further, the E value should correspond directly to the energy value of $10Dq$ parameter, rather than to the energy of a single crystal field band. This is because Fe^{2+} ions are mostly contained in more than one site which are usually distorted. Thus, they will give rise to more than one crystal field band; the energy of each could be a portion of the energy value of $10Dq$. Consequently, energy level diagrams have to be constructed, as illustrated in Chapter IV, and then the $10Dq$ parameter could be evaluated from these diagrams. Using equation (3) and constructing energy level diagrams from the high pressure spectral data presented earlier in Chapter IV, K could be estimated easily. As an example, the crystal field splitting parameter, $10Dq$, in piemontite increases about 1642 cm^{-1} over 197 kb.. This increase is due mostly to shortening metal-ligand interatomic distances, and then decreasing the volume of Mn^{3+} polyhedron by about 7%.

The estimated bulk modulus of the Mn^{3+} polyhedron is about 2.7 Mb. Comparing this value with the bulk modulus of the mineral phase which is about 1.074 Mb (Simmons and Wang, 1971), it is concluded that the Mn^{3+} octahedral site is relatively less compressible suggesting that the calcium polyhedra take up most of the volume. Similarly, the K value for the Cr^{3+} polyhedron

in uvarovite was calculated at 177 kb., using equation (3) and the data reported in Chapter IV, this is found to be 4.91 Mb. The K value for the Cr^{3+} site suggests also that the calcium, 8-fold, coordination site is the most compressible polyhedron in the garnet structure.

In the case of pyroxenes (orthoferrosilite and bronzite), the bulk moduli of the M1 and M2 site were calculated to be 0.69 and 0.45 Mb, respectively. Comparing these two values with K of the bulk mineral which is about 1.061 Mb, it is evident that the M1 and M2 octahedral sites are substantially more compressible than the silicon tetrahedral site. It is also noticed that the M2 site is more compressible than the M1 site. This is in fact expected, since the M2 site is relatively larger and more distorted than the M1 site.

In fayalite, K was calculated for the M1 site from the spectra measured at 40 kb.; it is found to be 0.755 Mb. This value is significantly less than the K value of the bulk mineral (1.32 Mb). This indicates that the M1, and presumably the M2 sites are rather compressible and any changes in the olivine structure at elevated pressure should correspond mostly to changes in the M1 and M2 sites.

Calculating the bulk moduli of the cations' sites at various pressures could be very useful for extending the bulk modulus volume relationships. Anderson (1969) and Anderson and Anderson (1970) have shown that for compounds of constant mean atomic weight, the relationship:

$$KV = \text{const.} \quad (4)$$

holds. The constant in equation (4) was given for any oxide as $0.157Z_c Z_a e^2$, where Z_c and Z_a are the cation and anion charges, respectively, and e is the electronic charge. Considering the relation given in (4) and the value of this constant, Huggins (1974) suggested that this relationship may also apply to the individual polyhedra of the cations in the bulk mineral structure. This relation for the individual polyhedron may also be given as:

$$K_{\text{pol}} = Z_c Z_a e^2 K/V_{\text{pol}}. \quad (5)$$

For most silicate minerals, oxygen is the anion coordinating the cations. Then, the two parameters, Z_c and V_{pol} , become the most significant factors. V_{pol} depends mostly on the coordination number and the degree of distortion or regularity of the site. Consequently, Huggins (1974) suggested the following order of site compressibility, β_{pol} :

$$\beta_{\text{Fe}^{3+}(\text{IV})} < \beta_{\text{Fe}^{3+}(\text{VI})} < \beta_{\text{Fe}^{2+}(\text{VI})} < \beta_{\text{Fe}^{2+}(\text{VIII})}.$$

Huggins did not consider the distortion factor. However, it appears from the high pressure spectral data that the more distorted sites are more compressible than the regular ones.

It was mentioned above that the K values for Cr^{3+} and Mn^{3+} sites are significantly larger than those for the bulk mineral phases, suggesting that those sites are rather incompressible. The negligible energy change of B values for Fe^{3+} cations in andradite, blue-omphacite, epidote, and glaucophane may also be related to the negligible changes in M-O distances and thus the volumes of the polyhedra containing Fe^{3+} ions. Furthermore, the

relatively slow energy shift of spectral bands related to Fe^{2+} and Co^{2+} in tetrahedral sites may be due to the small tetrahedral volume which then increases the value of K as given in equation (5).

Tischer and Drickamer (1962) investigated the local symmetries and compressibilities of some transition elements in several silicate and phosphate glasses. They found that the tetrahedral sites are less compressible than the bulk glass and that Co^{2+} and Ni^{2+} tend to transfer from the tetrahedral to the octahedral site. These could be significant to predict the nature of the high pressure polymorphs that may occur in the mantle.

VII-4. Crystal Field Stabilization Energies (CFSE)

The crystal field stabilization energy of a transition metal ion is the resultant energy acquired by the electrons in the five d-orbitals relative to the baricenter of gravity. As an example, Fe^{2+} has d^6 electrons; considering an octahedral array of ligands surrounding the central ion, the electrons will be distributed between t_{2g} and e_g levels (Figure VII-2a). Each electron in the e_g level will be destabilized by $3/5\Delta_o$, whereas each electron in the t_{2g} level will be stabilized by $2/5\Delta_o$ relative to the baricenter of energy; the net resultant stabilization energy then will be:

$$4(2/5\Delta_o) - 2(3/5\Delta_o) = 2/5\Delta_o.$$

The above approach has been used by many authors (Dunn, et al. 1965; Cotton, 1963; Figgis, 1966; Lever, 1966) and used to cor-

relate the degree of stabilities of transition metal ions contained in sites of different symmetries in various inorganic complexes.

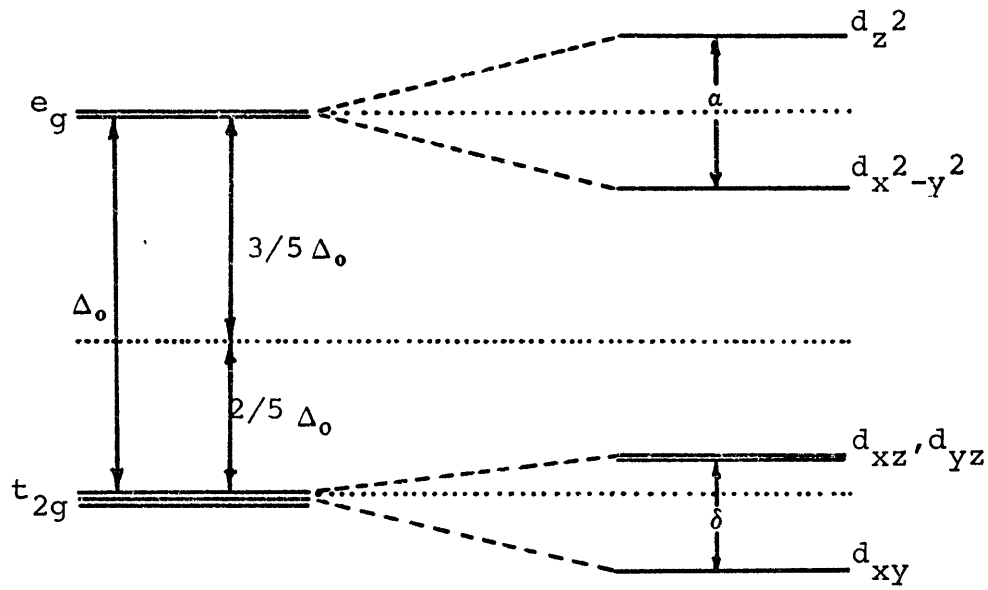
The CFSE parameter has also been used to estimate the site population and ordering of transition metal ions in silicate minerals (Burns, 1969, 1970). The usage of CFSE parameter in minerals required careful treatments since the t.m. ions are usually contained in distorted and/or multiple sites. Thus, d-levels will split further causing an increase in the CFSE parameter as a result of this distortion. Figure VII-2b shows the energy levels of Fe^{2+} in an octahedral site compressed along the z-axis. From this figure it is apparent that the 6th d-electron in the d_{xy} level acquired a stabilization energy of $2/3 \delta$, where δ is the energy separation between d_{xy} level and (d_{xz}, d_{yz}) levels.

To calculate the CFSE parameter in a distorted site, it is essential then to establish an energy level diagram in which the energy separation between each level is known.

In many instances, evaluation of CFSE parameters have been in error due to two factors: first, inaccurate assignments of crystal field bands to the appropriate energy levels or to the appropriate site, e.g. Runciman et al. (1974a,b). Second, the incomplete information on the magnitude of energy separation between the lower levels, e.g. t_{2g} levels in Figure (VII-2b). The energy separations between the lower levels correspond to energies in the far-infrared region which are difficult to measure. Huggins (1974) and Huggins and Abu-Eid (1974) adopted

FIGURE VII-2

- (a) Splitting of the d-energy levels in regular octahedron and distribution of the six d-electrons.
- (b) Energy levels of Fe^{2+} in an octahedral site compressed along the z-axis.



VII-2a

VII-2b

Ingall's model (1964) and used the high temperature Mössbauer data to calculate the magnitude of energy separations between the lower d-levels of ferrous iron in some silicate minerals. Huggins and Abu-Eid (1974) determined accurately the CFSE parameter at 1 atm. for almandine and orthoferrosilite; this parameter was also calculated accurately for fayalite, and melilite using both optical absorption and Mössbauer spectral data (Chapter IV).

The high temperature Mössbauer method could be used to determine the energy separation between the low-energy d-levels of ferrous ion only, and could not be used for other cations such as Cr^{3+} and Mn^{3+} . Fortunately, Cr^{3+} is contained in a fairly regular octahedral site in uvarovite and only the energies of the higher two levels are required to be obtained; those are determined from the energy values of the absorption bands usually occurring in the visible region. The CFSE parameter of Mn^{3+} ($3d^4$) could also be determined from the measured crystal field bands, as it was explained in Chapter IV.

With increasing pressure, the crystal field splitting parameter, Δ_o , will increase; this implies that the CFSE will also increase. As a consequence of this, ions with large CFSE values are expected to be enriched at depths in the earth relative to those cations of small CFSE. Further, if the crystal field splitting parameter, $10Dq$, increases significantly with pressure to become larger than the pairing energy, then the electrons which were in the upper e_g levels can couple with

electrons in the t_{2g} levels to obtain a lower energy configuration. This coupling of the electrons in the t_{2g} level, caused by Δ_p exceeding the pairing energy is known as spin-pairing, or alternatively, a high spin-low spin transition (Fyfe, 1960; Strens, 1969; Burns, 1969). The spin-pairing phenomenon was discussed in Chapter IV and will be discussed further in the next section.

The crystal field stabilization energies of Mn^{3+} in piemontite were calculated at various pressures from the energy level diagrams constructed at each pressure. Figure IV-34 shows the variation of CFSE versus pressure. From this figure is obvious that the CFSE parameter increases by about 1100 cm^{-1} (3.3 K.cal.) with increasing pressure up to 197 kb.. This pressure-induced increase of the stabilization energy of Mn^{3+} suggests that Mn^{3+} is stable at elevated pressures.

When a sufficient pressure is applied such that CFSE becomes large enough and exceeds the energy required to couple the electron in the high energy level into the lowest energy d-level, then Mn^{3+} may undergo a high spin-low spin transition. The pressure at which this transition may take place could not be evaluated. However, the low-spin Mn^{3+} cation may be identified from three, new, spin-allowed transitions expected to be observed at higher energies than those of the high-spin Mn^{3+} cation. Instead of the spin-pairing process, the reduction of the Mn^{3+} cation to lower oxidation state may take place before the spin-pairing occurs. In fact, Gibbon et al. (1974) reported the reduction of Mn^{3+} to Mn^{2+} in rhodonite where the sample was

subjected to a shock pressure of about 496 kb..

The crystal field stabilization energy of Cr^{3+} ions in uvarovite was also estimated at 1 atm., 95 and 177 kb. from the spectral data reported in Chapter IV. The CFSE parameter ($3/5 \Delta_o$) of Cr^{3+} increases by about 6% with increasing pressure up to 177 kb.. Burns (1974) suggested, from the CFSE data of various minerals, that the order of Cr^{3+} enrichment in the upper mantle is: spinel > garnet > pyroxene > olivine.

The above results indicate that CFSE parameter for Cr^{3+} increases substantially with pressure, suggesting that Cr^{3+} will be enriched in phases that induce large CFSE values. Consequently, the high pressure spectral data agrees with Burns' prediction.

The CFSE parameters at elevated pressures were also evaluated for the Fe^{2+} cation contained in orthoferrosilite, olivine, and almandine. In orthoferrosilite, Fe^{2+} is contained in M1 and M2 sites; from the results obtained in section IV-2.1, it appears that the M1 and M2 sites have similar CFSE energy values (11.45 and 11.48 K.cal., respectively) at 1 atm., indicating that Fe^{2+} should be distributed randomly between the two sites. At pressure around 20 kb., the CFSE increases for both sites. However, it increases significantly for the M1 site more than the M2; the CFSE values at this pressure for M1 and M2 sites are 12.08 and 11.63 K.cal., respectively. This trend of CFSE increase suggests that the ferrous iron preferentially occupies the M1 site at elevated pressures.

In olivine (fayalite), the CFSE parameter was determined accurately at normal pressure by coupling the absorption spectra with the high temperature Mössbauer data. It was found that the CFSE parameters for both the M1 and M2 sites are similar (11.85 and 11.95 K.cal.). This also indicates that Fe^{2+} may be randomly distributed between the two sites in olivine. At elevated pressure, the CFSE parameter increased for both sites. However, the magnitude of this increase could not be determined accurately, due to the lack of data for the energies of the lower d-levels at those pressures.

The crystal field stabilization energy parameters obtained at elevated pressures are significant in predicting the fractionation and distribution of transition metals between mineral phases in the mantle. Ringwood (1970, 1973) proposed various structure types in the earth's mantle in which the coordination numbers of the cations and the densities of those polymorphs are increased. The stabilization energies of transition metal ions in these structures were discussed by Burns (1974a,b) and Gaffney (1973).

Ringwood (1973) suggested the following polymorphic transitions in the mantle:

<u>Structural Transition</u>	<u>C.N.</u>	<u>Depth, Km.</u>	<u>Pressure, Kb.</u>
Olivine - spinel	6	400 Km.	130 kb.
Spinel - Sr_2PbO_4	7	650 Km.	230 kb.
Sr_2PbO_4 - $CaFe_2O_4$ or	8	1050 Km.	400 kb.
K_2NiF_4	9	1250 Km.	

The crystal field stabilization energy of spinel was determined experimentally from the spectra of fayalite, which was transformed to the spinel structure (Mao and Bell, 1973); this was estimated as $2/5(11000) = 4400 \text{ cm}^{-1}$ (12 K.cal.). Gaffney (1974) calculated the CFSE values in Sr_2PbO_4 and CaFe_2O_4 structures to be 6610 cm^{-1} (18.9 K.cal.) and 3530 cm^{-1} (10.1 K.cal.), respectively.

Syono et al. (1971) discussed the influence of the ferrous iron crystal field stabilization energy on the olivine→spinel transformation. They observed that synthetic olivines containing transition metal ions, such as Fe^{2+} , Co^{2+} , and Ni^{2+} transform at lower pressure than those containing other cations such as Zn^{2+} and Mg^{2+} . Consequently, they related this phenomenon to energy contributions from the CFSE of the transition metal ions. Mao and Bell (1973) calculated that the CFSE lowers the transformation pressure at 1000°C by 98 Kb..

The arguments of the influences of CFSE parameter on the energies of phase transitions in the earth's mantle are yet inconclusive. This is due to two factors: First, the occurrences of structures such as Sr_2PbO_4 and CaFe_2O_4 in the earth's mantle are not well established. Recent laboratory studies by Bassett and Ming (1972), Kumazawa et al. (1974), and Ming and Bassett (1975) demonstrated that the post-spinel phases in the Mg_2SiO_4 - Fe_2SiO_4 system are simple oxides: periclase (MgO) and stishovite (SiO_2) structure types. If this is the case in the lower mantle, then the arguments about the CFSE parameter in structures such

as Sr_2PbO_4 and CaFe_2O_4 may not be of great importance to mantle mineralogy.

Second, the arguments given by Bell and Mao (1973) and Syono et al. (1971) are based on the olivine composition of fayalite rather than $(\text{Mg}_{0.88}\text{Fe}_{0.12})_2\text{SiO}_4$, as was suggested by Ringwood (1970). Considering the latter composition for olivine in the upper mantle will decrease significantly the effect of CFSE on the transition pressure.

VII-5. Pressure-Induced Reduction

Pressure-induced reduction of ferric ions in many organic and inorganic complexes has been reported (Drickamer and Frank, 1973) to occur at a wide range of pressure, depending on the type of the ligands surrounding the metal ion and the nature of the complex. Recently, Wang and Drickamer (1973) have reported that pressure-induced reduction could also take place in copper complexes, and the reduction of Cu^{2+} to Cu^+ took place at pressure around 118 kb.. Further, reduction of ferric ions in amphiboles (magnesian riebeckite) have been demonstrated by Burns et al. (1972) using high pressure Mössbauer techniques. Furthermore, Gibbons et al. (1973), from their shock pressure experiments on Mn^{3+} in rhodonite, observed irreversible pressure-induced reduction of Mn^{3+} in a sample which had been shocked to 496 kb.. They related the reduction of the trivalent manganese ions to the presence of water in the rhodonite structure.

The main evidence of pressure-induced reduction was obtained from either high pressure optical absorption or high pressure

Mössbauer studies (Drickamer et al., 1972; Drickamer and Frank, 1973). Since the present study is mostly concerned with the optical absorption method, our attention will be focused on the evidence of reduction drawn from absorption spectral measurements.

The process of reduction involves an electron transfer from an orbital of mostly ligand character to another orbital of primarily metal character. This process has been defined earlier as ligand-to-metal charge transfer. The reduction process could be approached theoretically by performing an analysis which relates the parameters of the L→M charge transfer bands (their widths, intensities, energies) to the probability of thermal transfer (Drickamer et al., 1972; Drickamer and Frank, 1973).

The analogy with the thermal transfer may be expressed in the relation given by Drickamer et al. (1972):

$$E_{th} = h\nu_{max} - [(\delta E)_{1/2}^2 (\omega/\omega')^2] / 16KT \ln 2 \quad (6)$$

where E_{th} is the difference in energy between the bottom of the ground state and excited state potential wells, ν_{max} is the frequency of the maximum absorption peak, $(\delta E)_{1/2}$ is the half width of the peak, and ω and ω' are the force constants of the ground and excited states, respectively. The reduction process may take place when E_{th} approaches to zero, and then the excited state becomes more stable at higher pressures.

Considering the relation given above (6), E_{th} will decrease if $h\nu_{max}$ decreases and $(\delta E)_{1/2}$ increases, assuming that ω and ω' are constants.

In this study, no evidence has been observed for reduction of Ti^{3+} , Fe^{3+} , Mn^{3+} , and Cr^{3+} in silicate minerals up to 200 kb.. This conclusion is made since no new crystal field transitions that may be related to lower oxidation states have been observed, and the tails of the L→M charge transfer bands shift slowly to lower energies.

On the other hand, the high pressure spectra of crocoite (Cr^{6+}), vanadinite (V^{5+}), potassium permanganate (Mn^{7+}), and Egyptian-blue (Cu^{2+}) showed unusual changes at certain pressures. The L→M charge transfer bands of O-Cr, O-V, O-Mn, and O-Cu shifted rapidly to lower energies at elevated pressures with a huge increase in their widths and intensities. The pressure-induced red shift of the absorption edge was substantially more drastic in the first three minerals.

The rapid low energy shift and increase in the half width of the charge transfer band could be a manifestation of a large decrease in the thermal energy gap between the ground state (e.g. Cr^{6+}) and the excited state (Cr of lower oxidation state and oxidized ligands). As a consequence of the consistent decrease in this energy gap, the electronic configuration of Cr of the lower oxidation state and oxidized ligands could well be more stable at high pressure than Cr^{6+} surrounded by the regular ligands.

Reducing Cr^{6+} (d^0), V^{5+} (d^0), Mn^{7+} (d^0), and Cu^{2+} (d^9) to their lower oxidation states will introduce at least one electron into the d-level of each cation. If this is the case, it

is expected that new spectral features would be observed which are related to crystal field transitions in the high pressure spectra of the reduced chromium, vanadium, and manganese cations. Conversely, introducing an electron in the d-level of Cu^{2+} cations will produce completely filled d-shells and then no crystal field transitions are expected to be observed in the spectra of Cu^{2+} ions, i.e. disappearance of the crystal field spectra, and hence color, of Cu^{2+} is expected at the pressure-induced $\text{Cu}^{2+} \rightarrow \text{Cu}^+$ transition. This condition is actually observed in the high pressure spectra of Egyptian-blue, although crystal field bands did not disappear completely. On the other hand, the rapid low-energy shifts of the absorption edges of V^{5+} , Cr^{6+} , and Mn^{7+} probably have masked any possible crystal field transitions expected to be observed in the visible-near infrared region.

Alternatively, the rapid low energy shift of the absorption edge may be due to closing the energy gap between conduction and valence bands, which then causes an increase in the metallic character of the solid subjected to high pressure. Further, significant changes in the structure could also be partially responsible for the pressure-induced red shift of the absorption edge.

It was mentioned earlier that Mao and Bell (1972) also observed rapid low-energy shifts of the absorption edges in olivine and spinel at pressures above 100 kb.. It is not yet known whether this phenomenon observed in olivine and spinel is

the same as the one observed in crocoite, vanadinite, and KMnO_4 , or it is related to another type of electronic process.

An explanation was given in section V-4.5 for the causes of the tremendous increase in the absorption edge intensity, and its rapid low energy shift with pressure. In the forthcoming discussion, the pressure-induced reduction phenomenon will be explained more specifically in cations of d^0 , d^9 , and d^5 electronic configurations.

In the energy level diagram constructed for the CrO_4^{--} ion (Figure V-7), it appears that an electron transferred from the non-bonding $1t_1$ ligand level to the metal level $2e$, which is relatively stable in the latter level at elevated pressure due to decreasing the energy separation between the two levels. If we assume now that this electron is stable in the $2e$ level, then the new electronic configuration of the metal ion will be d^1 and the most likely transition that may take place is $2e \rightarrow 7t_2$. When this transition occurs another electron may be transferred from $1t_1$ to $2e$ level, and then the metal ion will have d^2 configuration. The probability of electron transfer may also increase with decreasing the energy gap between $1t_1$ and $2e$ levels, and then the absorption edge related to $L \rightarrow M$ electron transfer will increase in intensity and shift to lower energy. Since pressure is expected to decrease this energy gap as it was expected, then several low oxidation states such as Cr(V) , Cr(IV) , Cr(III) may be formed at elevated pressure. The $1t_1 \rightarrow 2e$ transition is designated as $L \rightarrow M$ transition and the $2e \rightarrow 7t_2$ corresponds to the crystal field transition (C.F.). The VO_4^{--} and MnO_4^-

ionic clusters have similar energy levels to CrO_4^{--} . Then, the only electronic transition that occurs in these ions at 1 atm. is the L→M transition. Nevertheless, at elevated pressures they may give rise to C.F. transitions. The rapid low-energy shift of the absorption edge is related then to enhancing electron transfer between the ligand orbital $1t_1$ and the metal orbital $2e$ with a simultaneous pressure-induced reduction process as a result of stabilizing one, or more, electrons in the metal orbitals $2e$ or $7t_2$. It should be mentioned that electron transfer (M→L) from the metal orbital $7t_2$ to the ligand orbital $8t_2$ is unlikely to occur since the latter orbital is at substantially higher energy. However, if M→L electron transfer occurs, then the electron transferred from the d-level to the anti-bonding, π^* , level will be substituted by another electron from the $1t_1$ orbital or the lower levels.

In the case of the Cu^{2+} (d^9) ion, the reduction process may take place by means of two simultaneous transitions, namely crystal field and L-M transitions, respectively. In the C.F. transition, an electron is transferred from ${}^2B_{1g}$ to ${}^2A_{1g}$ level (Figure VI-15); consequently, the upper d-level will be completely filled and the lower level, ${}^2B_{1g}$, will be half filled. The C.F. transition is then followed by L-M electron transfer from the non-bonding ligand orbitals to the ${}^2B_{1g}$ d-level, thus, completing the reduction process and forming a completely filled d^{10} shell. The probability of L-M electron transfer is relatively low since an energy must be expended to overcome the pairing energy of the electrons in the ${}^2B_{1g}$ level. It is then

predicted that reduction of Cu^{2+} may take place at higher pressures than Cr^{6+} , V^{5+} , and Mn^{7+} ions. This prediction conforms with the results obtained in Chapter VI. It should be noticed also that the probability of electron transfer, M-L or L-M, after the reduction process will be very low, since the d-shell is completely filled. As a result of this, the charge transfer absorption edge is not expected to increase drastically in intensity, which is consistent with the experimental observation.

On the other hand, the reduction process in Fe^{3+} (d^5) is expected to be more difficult to obtain than Cr^{6+} and Cu^{2+} ions. This is related to two factors:

- 1) There are no C.F. spin-allowed transitions in Fe^{3+} which cause an excitation of an electron from the low-energy d-level to the highest energy level. The probability of L-M electron transfer then will be low, and introducing an electron to the d-shell is unlikely to occur at low pressures.
- 2) To obtain the low oxidation state, Fe^{2+} at substantially high energy is required to transfer an electron from the non-bonding ligand orbitals to one of the d-levels, and then to couple the transferred electron with the electron occupying that d-level. It is also possible that the reduction process may occur through two processes, namely, spin-forbidden transition in d-levels, and then L-M transition. Whatever the mechanism of reduction of Fe^{3+} is, it is expected to require a tremendous amount of energy to couple and/or uncouple the electrons in the d-energy levels. It is expected then that the pressure-induced reduction in Fe^{3+} will take place at pressures much more than those pressures

necessary to induced reduction in Cr^{6+} , V^{5+} , Mn^{7+} , and Cu^{2+} . Nevertheless, the reduction of Fe^{3+} may be facilitated when there are neighboring atoms that can easily donate electrons, i.e. of small electron affinity, such as nitrogen and hydrogen atoms. On the basis of the above discussion, it is believed that reduction of Fe^{3+} ions may occur at very high pressures (possibly more than 300 kb) when it is coordinated to oxygen atoms. However, these pressures may be lowered by having a neighboring electron donor such as N or H atoms. This explains why the pressure-induced reduction of Fe^{3+} was obtained easily in organic complexes (Drickamer and Frank, 1973), whereas it was hard to induce in silicate minerals with increasing pressure up to 200 kb (Huggins, 1974).

VII-6. Pressure-Induced Spin-Pairing

The "high-spin" to "low-spin" pressure-induced transition phenomenon in Fe^{2+} was discussed in section VI-2.3. In addition, it was demonstrated in Chapter VI that spin transition of Fe^{2+} in gillespite does not occur with increasing pressures up to 80 kb.. Instead, a structural displacive transition took place at about 26 kb; in the new structure, the ferrous ion site changed from a square planar to a distorted flattened tetrahedron. Increasing the pressure further above 26 kb., and measuring the spectra, it was interpreted from the spectra measured at these pressures that the site continuously changes to become more regular tetrahedral. Since crystal field bands shift to lower energies, the crystal field splitting parameter decreases

due to changing the site symmetry. Consequently, gillespite should not be used as a model to study the pressure-induced spin transition.

Griffith (1966) reported that the ground states of the high-spin and low-spin Fe^{2+} in octahedral symmetry (${}^5\text{T}_{2g}$ and ${}^1\text{A}_{1g}$, respectively) may become equal in energy when:

$$2\Delta_p = 5B + 8C \quad (7)$$

where Δ_p is the pairing energy. Strens (1969) estimated Δ_p , based on many assumptions, as 12000 cm^{-1} .

In the present discussion, the spin-pairing energy will be estimated roughly from two sources of information; 1) from Tanabe and Sugano (1954a,b) and Berkes (1968) energy level diagrams which show the energies of the levels of a d^n system, in B units, plotted against $10Dq$ in B units, also; 2) from the rate of energy change of a certain d-level with pressure, as determined from the pressure-induced energy shifts of crystal field bands.

The transition metal ions that are expected to have low-spin electronic states in octahedral coordination are those with d^4 , d^5 , d^6 , and d^7 configurations; these correspond to Mn^{3+} , Fe^{3+} , Fe^{2+} , and Co^{3+} cations. Since the Fe^{3+} ion does not have spin-allowed transitions, variations of $10Dq$ with pressure could not be obtained at this stage. In addition, since the Co^{2+} ion is contained in a tetrahedral site in lusakite, estimations of the rates of energy shifts of crystal field bands corresponding to Cu^{2+} in octahedral sites are unattainable. Consequently, the pressure-induced spin transition will be discussed for Mn^{3+} and

Fe²⁺ cations only.

Figures (VII-3 a,b) show the energy levels of the spin-allowed transitions for Mn³⁺ and Fe²⁺ cations. These diagrams were constructed by Berkes (1968) and are similar to those of Tanabe and Sugano diagrams (1954a,b). Berkes' diagrams were used in this study because the B values used in constructing them are similar to those of Mn³⁺ and Fe²⁺ ions contained in natural minerals. These B values are:

d^n	Cation	$B(\text{cm}^{-1})$
d^4	Mn ³⁺	965
d^6	Fe ²⁺	917

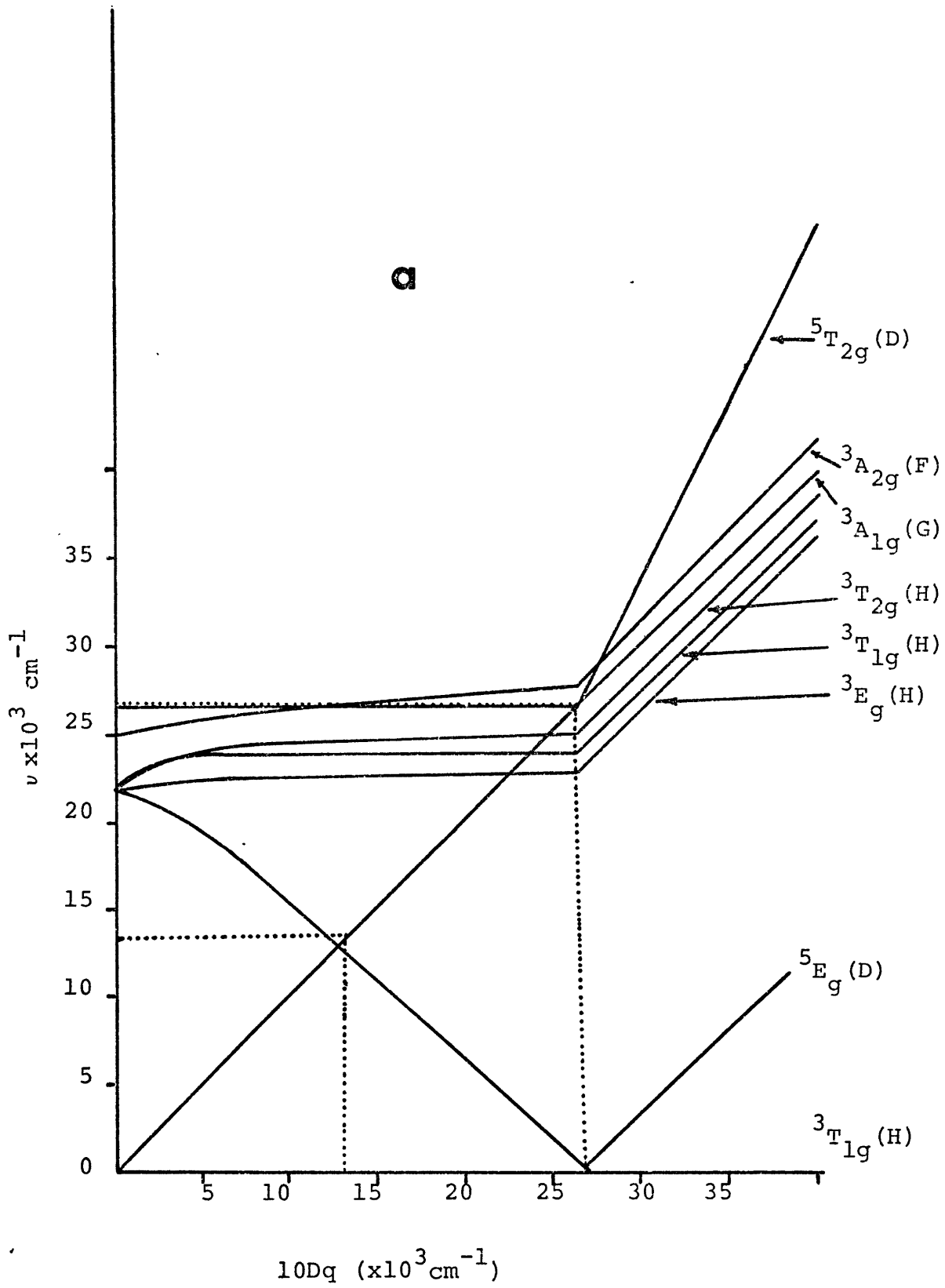
Considering Mn³⁺ in the regular octahedral site, the energy of the spin-allowed transition, ${}^5E_{1g} \rightarrow {}^5T_{2g}$ (Figure VII-a), is equivalent to $10Dq$. The energy values of $10Dq$ for Mn³⁺ were obtained at 1 atm. and 197 kb. (Chapter IV). These values are 13450 and 15092 cm^{-1} , respectively. The high-spin \rightarrow low-spin transition in Mn³⁺ may occur when the energy of the transition, ${}^5E_g \rightarrow {}^5T_{2g}$, has a minimum value of 26670 cm^{-1} (Figure VII-a), i.e. an energy increase of 13220 cm^{-1} in $10Dq$ is necessary to achieve the low-spin state of Mn³⁺. Since $10Dq$ changes by about 1642 cm^{-1} in 197 kb., then the spin transition in the Mn³⁺ ion may occur at pressure around 1590 kb..

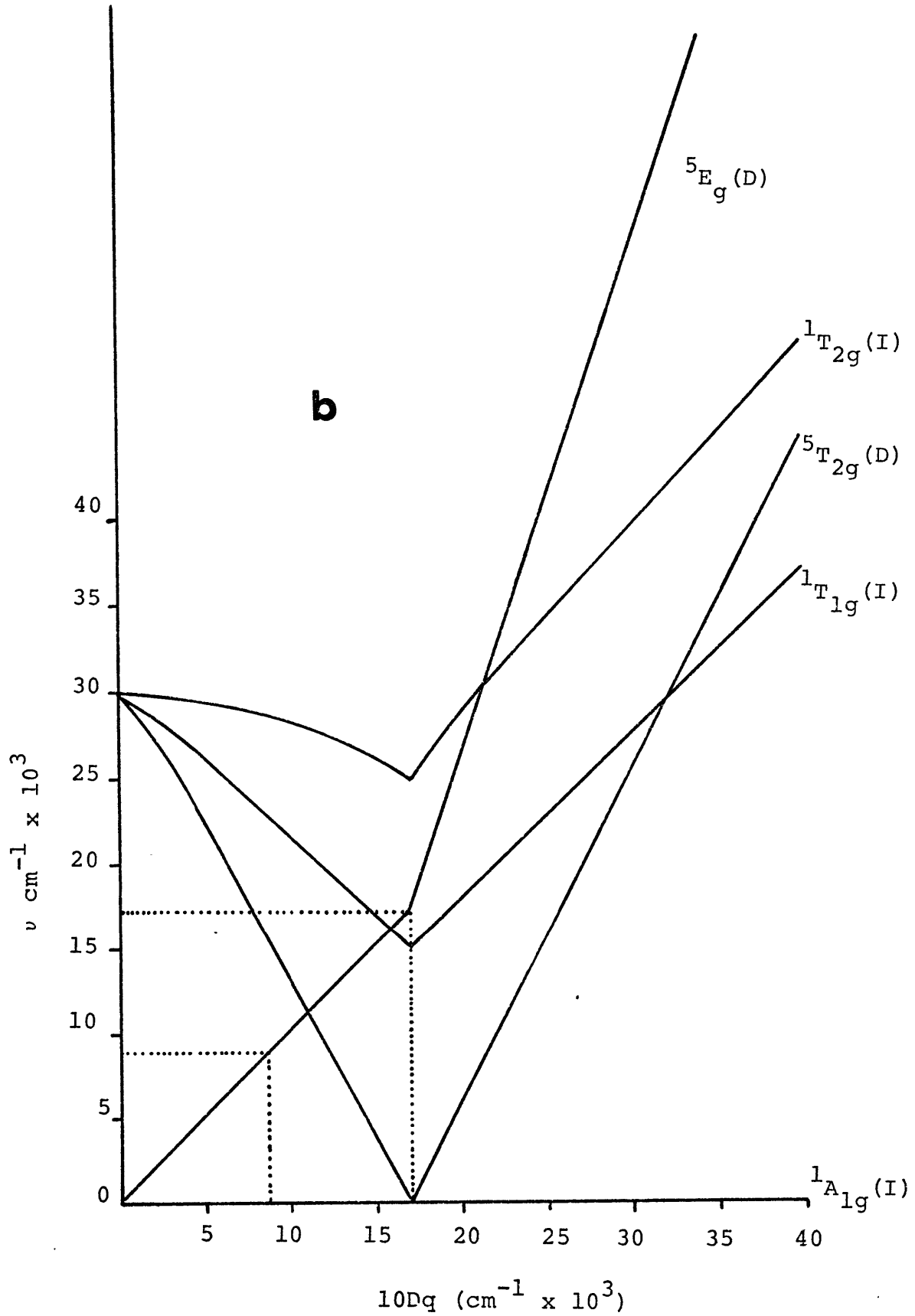
In the case of the Fe²⁺ ion in octahedral site, the same procedure will be followed to estimate the h.s. \rightarrow l.s. transition pressure. The high pressure spectral data of Fe²⁺ in pyroxene will be used to estimate the rate of energy change in

FIGURE VII-3

- (a) Energy level diagram showing the spin-allowed transitions in $\text{Mn}^{3+} (d^4)$ and the energy limit of the ${}^5E_g \rightarrow {}^5T_{2g}$ transition required for the spin transition in Mn^{3+} [modified from Berkes, J.S., 1968]*.
- (b) Energy level diagram showing the spin-allowed transitions in Fe^{2+} h.s. and the spin-allowed transitions in Fe^{2+} l.s.. Note the maximum energy that the ${}^5T_{2g} \rightarrow {}^5E_g$ should have to obtain the low-spin state of Fe^{2+} [modified from Berkes, J.S., 1968]*.

* [Berkes, J.S. (1968) energy level diagrams for transition metal ions in cubic crystal field. MRL, Monograph No. 2, Material Res. Lab., Penn. State Univ. (1968)].





10Dq with pressure. The 10Dq values obtained at 1 atm. and 20 kb. for Fe^{2+} in orthoferrosilite are 7735* and 8194* cm^{-1} , respectively. Using the energy level diagram, shown in Figure IV-6, it appears that, in order for the $\text{Fe}^{2+}_{\text{h.s.}} \rightarrow \text{Fe}^{2+}_{\text{l.s.}}$ transition to occur, the transition, ${}^5\text{T}_{2g} \rightarrow {}^5\text{E}_g$, (which is equivalent to 10Dq) should have an energy value of 17000 cm^{-1} . Then an increase of 9266 cm^{-1} in 10Dq value is required to achieve the low-spin state of Fe^{2+} in orthoferrosilite. Considering the rate of energy change in 10Dq with pressure, the $\text{Fe}^{2+}_{\text{h.s.}} \rightarrow \text{Fe}^{2+}_{\text{l.s.}}$ transition in pyroxene may occur at pressure around 400 kb.. Following the above method and using the high pressure spectral data of olivine and bronzite, the high-spin \rightarrow low-spin transition pressures of Fe^{2+} in these minerals are estimated to be about 850 and 720 kb., respectively. Considering an average energy shift of 10 $\text{cm}^{-1}/\text{kb.}$ for spinel, the spin transition of Fe^{2+} in this structure may occur at pressure around 600 kb.

Although the above estimates are only approximate, it appears that spin-pairing of ferrous ion is unlikely to occur in the upper mantle or in the transition zone. However, it is most likely to occur in the deep region of the lower mantle or at the mantle-core boundary. If this is the case, it is very well reasonable to assume a low-spin state of Fe^{2+} in the magnesio-wüstite [(Mg,Fe)O] phase.

The wüstite (FeO) phase has a structure similar to that of

* These values are the average 10Dq values, $(10\text{Dq M1} + 10\text{Dq M2})/2$, obtained at 1 atm. and 20 kb..

NaCl, in which the Fe and O atoms are at alternate corners of a set of cubes (Bragg et al, 1965), i.e. the Fe^{2+} ion is surrounded by 6-oxygens having an octahedral symmetry.

Assuming a low-spin state of the Fe^{2+} ion in wüstite, the following spin-allowed transitions in $\text{Fe}^{2+}_{\text{l.s.}}$ are likely to occur:

<u>Transition</u>	<u>Estimated Energy (cm⁻¹)</u>
${}^1\text{A}_{1g} \rightarrow {}^1\text{T}_{1g}$	16000
${}^1\text{A}_{1g} \rightarrow {}^1\text{T}_{2g}$	24000
${}^1\text{A}_{1g}(\text{I}) \rightarrow {}^1\text{A}_{1g}(\text{G})$	32000

The influence of the absorptions related to the above transitions on the radiative heat transfer in the lower mantle may not be significant, since the absorption edge for the FeO phase is expected to cover all of the visible and most of the infrared spectral regions. Nevertheless, the pressure-induced spin-pairing of Fe^{2+} in the lower mantle is an extremely important geophysical phenomenon. The consequences of the $\text{Fe}^{2+}_{\text{h.s.}} \rightarrow \text{Fe}^{2+}_{\text{l.s.}}$ transition have been discussed by Strens (1969), Burns (1969, 1970), Gaffney (1973), and Gaffney and Anderson (1973).

These consequences are:

1) The low-spin Fe^{2+} ionic radius is 0.16Å smaller than that of the high-spin Fe^{2+} (Shannon and Prewitt, 1969); thus, when the $\text{Fe}^{2+}_{\text{l.s.}}$ ion is coordinated to oxygen atoms in wüstite (FeO), the density of the $[\text{Fe}^{2+}_{\text{l.s.}}\text{O}]$ phase, 7.55 gm/cm³, is expected to be 28% denser than the $[\text{Fe}^{2+}_{\text{h.s.}}\text{O}]$ phase. The increase in

density may be related to the observed seismic discontinuity at a depth of about 1050 km. in the earth.

2) The low-spin Fe^{2+} ion may not form a solid solution with Mg, due to the smaller ionic radius of the former, 0.61\AA . Thus, an extra phase may be expected to exist in the lower mantle. If this is the case, the chemical homogeneity of the mantle may be changed since the low-spin ferrous iron will be enriched in the lower mantle.

3) Forming low-spin Fe^{2+} in the lower mantle provides an explanation for the inconsistency between the seismic data of the lower mantle and the pyrolite model assumed by Ringwood (1970).

4) The low-spin Fe^{2+} will affect significantly the magnetic properties of the lower mantle. This is due to the transition of Fe^{2+} from paramagnetic to diamagnetic, as a consequence of coupling all the electrons in the Fe^{2+} d-shell.

In summary, Fe^{2+} in gillespite should not be considered as a good model to study the spin-pairing phenomenon since its structure is unstable at elevated pressures. The results on gillespite, obtained in Chapter VI, should not negate the occurrence of low-spin Fe^{2+} phase in the lower mantle.

The high pressure spectral data indicate that low-spin transition of Fe^{2+} in pyroxenes and olivines may occur at pressures around 400 to 850 kb.. At these pressures, it is unlikely to have pyroxene or olivine structures; however, denser polymorphs or mixed oxides (MgO , FeO , SiO_2) may be predominant at such depths in the earth. It is very likely then, that the low-spin transition in Fe^{2+} will occur after the disproportionation

of the dense (Fe,Mg) silicate polymorphs.

VII-7. The Trend of the Pressure-Induced Changes in the Structures of Silicate Minerals

The high pressure spectral technique could be used for predictions of structural changes that may occur in natural minerals at great depths in the earth. Such predictions could be derived from the energy level diagrams constructed at elevated pressure, which provide information on the polyhedral symmetries of the transition metal ion.

The high pressure spectra of gillespite have been used successfully to predict the structure of a new high pressure polymorph (Abu-Eid et al., 1973), which was determined recently using a high pressure single crystal x-ray method (Hazen and Abu-Eid, 1974; Burnham and Hazen, 1974). Further predictions of pressure-induced structural changes in azurite, vivianite, KMnO_4 , crocoite, and vanadinite have been made from their high pressure spectral data (see Chapters V and VII). The proposed new structures for those minerals have not yet been verified using other techniques such as x-ray studies.

In the course of this study, no significant changes have been noticed in the high pressure spectra of many silicate minerals as pressure increased up to 200 kb., indicating that drastic changes in their structures may not occur at these pressures. Nevertheless, the trend of changing the polyhedral symmetries and M-O distances with pressure may elucidate any incipient changes in the structure before the transition to a new struc-

tural type occurs.

It is well known that structural transformations occur as a consequence of significant changes in the interatomic bond distances (M-M, M-O, and O-O) and the bond angles. Furthermore, it is also known that the degree of shortening or stretching of each type of bond depends on the magnitude of its strength (Burnham, 1966).

Using the high pressure spectral data of silicate minerals and the above mentioned principles, predictions of pressure-induced changes in their structure were made from the energy level diagrams constructed at elevated pressures for Fe^{2+} in orthoferrosilite and bronzite. It was shown that the M2 site is more compressible than the M1 site. In addition, the longer M-O bond distances in each site have been shortened substantially more than the shorter ones. Furthermore, the comparison of the bulk moduli of the M1 and M2 polyhedra with the bulk modulus of the mineral phase indicated that the M1 and M2 sites take up most of the compression. The same trend has been observed from the high pressure spectra of olivine, i.e. the M1 and M2 octahedra are more compressible than the SiO_4 tetrahedra, and the relatively long M-O distances are shortened more than the short ones.

From the above discussion and the results obtained, it may be concluded that compression of minerals containing only octahedral and tetrahedral sites may produce more regular octahedra with substantially smaller volumes; the SiO_4 tetrahedra however

are predicted to be the least compressible polyhedra in the structures. It should be mentioned also that the non-bridging oxygens may change their atomic positions easily with compression of the bulk mineral, whereas bridging oxygens may change their bond angles (e.g. Si-O-Si) without significant variations in their atomic positions (Hazen and Burnham, 1974).

In garnet and epidote, however, the volume change in the transition metal ions' polyhedra ($\Delta V_{\text{pol.}}$) relative to the bulk mineral (ΔV) was not as large as ($\Delta V_{\text{pol.}}$) observed in pyroxenes and olivine. The relative small compressibilities of Cr^{3+} and Mn^{3+} sites in uvarovite and epidote were related to the large compressibility of the calcium, 8-fold coordination, site.

It was also noticed that the tetrahedral sites containing transition metal ions have substantially lower compressibilities than the octahedra. In addition, the 4-fold square planar site in gillespite proved to be unstable at elevated pressures, changing to a very distorted tetrahedron.

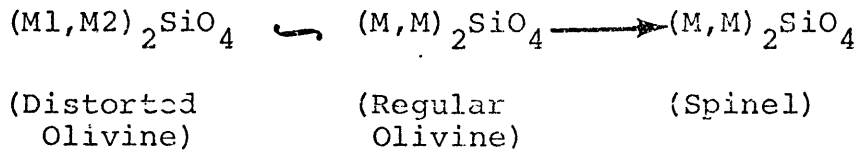
The structural polymorphic transitions that may occur in silicate minerals at pressure up to 300 kb. were presented by Ringwood in his classic review of the constitution of the earth's mantle (Ringwood, 1970). Ringwood and Major (1970) demonstrated that olivine [$(\text{Mg}_{0.8}\text{Fe}_{0.2})_2\text{SiO}_4$] transforms into β -spinel structure at pressure around 130 kb. and 1000°C. Further, Ringwood (1970) reported also that the germanium analogies of pyroxenes disproportionated into spinel ($\beta\text{Mg}_2\text{SiO}_4$) and stishovite (SiO_2). He also proposed the transformation of pyroxenes to garnet structure and the possibility of recombina-

tion of spinel and stishovite to form ilmenite structure. Furthermore, Ringwood (1970) suggested also the disproportionation of garnets into perovskite structure (CaSiO_3) and corundum.

It should be mentioned that the olivine-spinel transformation is now very well established and has been well demonstrated in many laboratories (Ringwood and Major, 1970; Kawai et al., 1966, 1970; Akimoto and Fujisawe, 1966; Akimoto and Ida, 1966). On the other hand, many of the remaining possible structural transformations in silicates, suggested by Ringwood, have not been demonstrated yet experimentally. Disproportionation of spinel into MgO , FeO , and SiO_2 oxides was reported by many authors (Bassett and Takahashi, 1970; Mao and Bell, 1971; Bassett and Ming, 1972; Kumazawa et al., 1974; Akimoto, 1974).

More recently, Ming and Bassett (private communication) also observed the disproportionation of orthoferrosilite into wustite and stishovite. Since the stoichiometry of the disproportionation reaction demonstrated in the laboratory may not simulate the earth's mantle P and T conditions, then the polymorphic transitions suggested by Ringwood may need to be reconsidered.

It was discussed in Chapter IV that the M1 site in olivine becomes more regular at elevated pressures and the two sites, M1 and M2, may become indistinguishable. These results indicate that there is a possibility of having an intermediate phase before the spinel phase is obtained, i.e. the transformation may occur as:



where the signs \curvearrowright and \longrightarrow stand for continuous and discontinuous transitions, respectively.

The formation of the regular olivine phase could be significant for understanding the mechanism and kinetics of olivine-spinel transformation and hence deep earthquake predictions. It should be mentioned that it is unlikely that the spinel be in the inverse-spinel form, since this requires an increase in the coordination number of the silicon, and as we discussed above, the silicon tetrahedra does not respond to the compression. It is suggested also in the present study that the post-spinel phases suggested by Ringwood may be metastable phases, or they may form after the disproportionation. This prediction was made because the formation of Sr_2PbO_4 structure may require a break in the Si-O bonds. However, since the Si-O bond is stronger (more covalent) than the M-O bond, it is then expected that the Fe-O bond breaks first. When the Fe-O bond is broken, the silicon becomes coordinated with other two oxygens forming stishovite structure. In addition, ferrous iron prefers to occupy the octahedral site since the CFSE is higher in this site. Thus, Fe will be coordinated with 6-oxygens forming a structure similar to that of NaCl.

In pyroxenes, however, the calcium will play an important role. The pyroxenes having significant amounts of calcium are more likely to transform to the garnet structure rather than to

spinel $(\text{Ca},\text{Mg})_2\text{SiO}_4$ and stishovite (SiO_2) . Since the calcium site is more highly compressible, it either increases in coordination number or stays the same. It is also unlikely that calcium will occupy the small octahedral site in spinel structure. It is predicted then that pyroxenes containing appreciable amounts of calcium may transform to the garnet structure. On the other hand, pyroxenes of composition $(\text{Mg},\text{Fe})\text{SiO}_3$ may well be disproportionated into spinel $[(\text{Mg},\text{Fe})_2\text{SiO}_4]$ and stishovite (SiO_2) and spinel then may disproportionate further into oxides.

Transformation of garnets will also depend on the calcium content. Calcic garnets are predicted to disproportionate to perovskite structure (CaSiO_3) and corundum, since the calcium cation will be contained in 8-fold coordination site in perovskite. Pyrope and almandine garnet, on the other hand, may transform to the ilmenite structure $(\text{Fe},\text{Mg})\text{SiO}_3$ and corundum.

In summary, in predicting trends of structural transformations, site compressibilities should be taken into consideration, since one site may be more compressible than another and thus influence the trend of the transformation. The tetrahedral sites are the least compressible polyhedra, whereas calcium 8-fold coordination sites are the most compressible ones; consequently, the calcium content could be an important parameter determining the trend of structural changes. It is suggested that the post spinel phases proposed by Ringwood may be metastable phases which cannot be formed under current experimental conditions.

VII-8. Absorption Spectra and Radiative Heat Transfer

There are two major processes responsible for absorption of radiation in the earth's mantle. First, the process of crystal field absorption, and second, the charge transfer absorption. To understand the nature of such absorptions at depths in the earth, it is essential to know the pressure and temperature conditions at such depths, and the nature and composition of the earth's mantle materials. It is also a prerequisite to understand the effects of both pressure and temperature on such kinds of absorption.

The mantle of the earth consists, in general, of three zones: the upper mantle region where the temperature ranges from 1,000-1,750°K, and the maximum pressure is estimated to be about 250 kb. (Ringwood, 1966, 1970). The dominant mineral phases in that region are believed to be olivine, pyroxenes, and garnets with some amphiboles. In general, the effect of pressure on the spectra of mineral phases in this zone is to shift crystal field bands to higher energies and charge transfer bands to lower energies. Considering the results presented earlier in this thesis, and those of Mao and Bell (1972a,b), the energy regions in which olivines and pyroxenes absorb considerably occur at energies between 4500-12000 cm^{-1} and above 25000 cm^{-1} . With increasing pressure, the window in the region 12000-25000 cm^{-1} may become narrower due to a shift of crystal field bands to higher energies, and ligand-metal charge transfer bands to lower energies. Although the temperature factor will broaden spectral bands (C.F.) towards the infrared region, the pressure factor

could be the dominant one. In the transition zone of the lower mantle, it is difficult to interpret the nature of absorption since the composition and the structure of the earth's materials in these two zones are not well established yet. Ringwood (1970) assumes a pyrolite model for the mantle, in the region 700-1050 K (240-400 kb.) where the predominant phases are: 55% $(\text{Mg,Fe})\text{SiO}_4$ with strontium plumbate structure; 36% $(\text{Mg,Fe,Cr,Al})(\text{Si,Al})\text{O}_3$ with ilmenite structure; 6.5% CaSiO_3 with perovskite structure; and 2.5% NaAlSiO_4 with calcium ferrite structure. The crystal field effects in these types of phases have been discussed by Gaffney (1972), where he reported that the radiative transfer will be unimportant in the mantle between 650 and 1050 km., but may be significant when $(\text{Mg,Fe})\text{SiO}_4$ occurs in the calcium ferrite structure below 1050 km..

Conversely in Gaffney's discussion, there are two points of view that have not been considered. First, the abrupt red shift of the absorption edge in olivine and spinel which was observed to start at 100 kb. and be more prominent at pressure around 200 kb. (Mao and Bell, 1972). Second, the structure and composition of mantle minerals in the transition zone may have another model different from that of Ringwood's, as it was discussed in the previous section.

Considering Bassett and Ming (1972) and Akimoto's (1974) experimental results, the transition zone may be assumed to consist of a mixture of MgO , FeO , and SiO_2 oxides. If this is the case, the predictions of absorption and transfer of radiation in the earth's mantle have to be reviewed.

Mao (1973) has measured the optical absorption of magnesio-wustite ($\text{Wu}_{22}\text{-Fe}_{78}$) at pressures up to 310 kb.. The most important factors observed in the spectra are the crystal field absorption of Fe^{2+} and the ligand-metal charge transfer which starts at about 22000 cm^{-1} . The crystal field band of Fe^{2+} shifts slowly to higher energy, whereas the absorption edge starts to shift rapidly to lower energy at pressure around 165 kb.. At more elevated pressures, the absorption becomes more intense and the absorption edge block severely more than 75% of the radiative energy (Mao, 1973). Mao has assumed that the phonon transfer is the major mechanism responsible for thermal conductivity in the lower mantle. On the other hand, considering the mixture of MgO , FeO , and SiO_2 oxides, the latter will be as a window to transfer the radiative heat.

REFERENCES

- Abu-Eid, R.M., Mao, H.K., and Burns, R.G. (1973) Polarized absorption spectra of gillespite at high pressure, Ann. Rept. Geophys. Lab., Year Book 72, 564-567.
- Abu-Eid, R.M., Burns, R.G., and Mao, H.K. (1973) A blue high pressure phase for gillespite, EOS Trans. A.G.U. (abstract), 54, 498.
- Abu-Eid, R.M. (1974) Effect of pressure on crystal field and charge transfer bands, EOS Trans. A.G.U. (abstract), 55, 463.
- Abu-Eid, R.M. (1975a) Absorption spectra of transition metal-bearing minerals at high pressures, Chapter in: Petrophysics: The Physics and Chemistry of Minerals and Rocks (ed. R.G.J. Strens) in press. (J.Wiley & Sons)
- Abu-Eid, R.M. and Hazen, R.M. (1975b) Evidence for structural change in gillespite at 25 kilobars, (abstract) In: Petrophysics: The Physics and Chemistry of Minerals and Rocks (ed. R.G.J. Strens) in press. (J. Wiley & Sons)
- Ahrens, T.J. and Graham, E.K. (1972) A shock-induced phase change in iron-silicate garnet, Earth Planet. Sci. Lett., 14, 87-90.
- Akimoto, S. (1974) High-pressure crystal chemistry of orthosilicates and the formation of the mantle transition zone, In: Petrophysics: The Physics and Chemistry of Minerals and Rocks (ed. R.G.J. Strens) in press (J. Wiley & Sons).
- Akimoto, S. and Ida, Y. (1966) High pressure synthesis of Mg_2SiO_4 spinel, Earth Planet. Sci. Lett., 1, 358-359.

- Akimoto, S. and Sato, Y. (1968) High-pressure transformation in Co_2SiO_4 olivine and some geophysical implications, *Phys. Earth Planet. Int.*, 1, 498-504.
- Akimoto, S. and Fujisawa, H. (1968) Olivine-spinel solid solution equilibria in the system Mg_2SiO_4 - Fe_2SiO_4 , *J. Geophys. Res.*, 73, 1467-1479.
- Anderson, D.L. (1969) Bulk modulus - density systematics. *J. Geophys. Res.*, 74, 3857-
- Anderson, D.L. and Anderson, O.L. (1970) The bulk modulus - volume relationship for oxides, *J. Geophys. Res.*, 75, 3494-3500.
- Appleman, D.E. (1966) Crystal chemistry of the pyroxenes, Short Course Lecture Notes on: Chain Silicates, pp. 1-26, American Geological Institute, Washington, D.C..
- Ballhausen, C.J. (1954) Studies of absorption spectra II: Theory of copper (II) spectra, *Dan. Mat. Fys. Medd.*, 29, no. 4, 1-18.
- Ballhausen, C.J. (1962) An Introduction to Ligand Field Theory (McGraw-Hill, New York).
- Bancroft, G.M. (1967) Quantitative estimates of site populations in an amphibole by the Mössbauer effect, *Phys. Lett.*, 26A, 17-18.
- Bancroft, G.M., Maddock, A.G., and Burns, R.G. (1967) Application of the Mössbauer effect to silicate mineralogy: 1. Iron silicate of known crystal structure, *Geochim. Cosmochim. Acta*, 31, 2219-2246.
- Bancroft, G.M., Burns, R.G., and Stone, A.J. (1968) Applications

- of the Mössbauer effect to silicate mineralogy. II. Iron silicates of unknown and complex crystal structures, *Geochem. Cosmochim. Acta*, 32, 547-559.
- Bancroft, G.M. and Burns, R.G. (1969) Mössbauer and absorption spectral study of alkali amphiboles, *Mineral. Soc. Amer., Spec. Pap.*, 2, 137-148.
- Bancroft, G.M., Williams, P.G., and Essene, E.J. (1969) Mössbauer spectra of omphacites, *Mineral. Soc. Amer., Spec. Pap.*, 2, 54-65.
- Bancroft, G.M. (1974) Mössbauer Spectroscopy: An Introduction for Inorganic Chemists and Geochemists (McGraw-Hill, England).
- Bassett, W.A. and Takahashi, T. (1965) Silver iodide polymorphs, *Amer. Mineral.*, 50, 1576-1594.
- Bassett, W.A., Takahashi, T., and Stook, P.W. (1967) X-ray diffraction and optical observations on crystalline solids up to 300 kb, *Review Sci. Instr.*, 38, 37-42.
- Bassett, W.A. and Ming, L-C. (1972) Disproportionation of Fe_2SiO_4 to $2\text{FeO} + \text{SiO}_2$ at pressures up to 250 kbar. and temperature up to 3000°C, *Phys. Earth Planet. Int.*, 6, 154-160.
- Bassett, W.A. (1974) The application of the diamond anvil cell to geophysical and geochemical problems, Crosby Lecture Series, Dept. Earth & Planetary Sciences, M.I.T., Feb.-April, 1974.
- Bell, P.M. and Mao, H.K. (1972a) Crystal-field effects of iron and titanium in selected grains of Apollo 12, 14, and 15

- rocks, glasses, and fine fractions, Proc. 3rd Lunar Sci. Conf., Suppl. 3, Geochim. Cosmochim. Acta, 1, 545-553.
- Bell, P.M. and Mao, H.K. (1972b) Crystal field studies of lunar samples, Ann. Rept. Geophys. Lab., Year Book 71, 480-489.
- Bell, P.M. and Mao, H.K. (1972c) Apparatus for the measurement of crystal field spectra of single crystals, Ann. Rept. Geophys. Lab., Year Book 71, 608-611.
- Bell, P.M., Mao, H.K., and Rossman, G.R. (1974) Absorption spectroscopy of ionic and molecular units in crystals and glasses, In: Infrared and Raman Spectroscopy of Lunar and Terrestrial Materials (ed. C. Karr, Jr.; Academic Press).
- Birle, J.D., Gibbs, G.V., Moore, P.B., and Smith, J.V. (1968) Crystal structures of natural olivines, Amer. Mineral., 53, 807-824.
- Bragg, W.H. and Bragg, W.L. (1916) X-rays and Crystal Structure, (G. Bell & Sons, London) 169 pp.
- Bragg, W.L. and Brown, G.B. (1926) Die Struktur des Olivines, Zeits. Krist., 63, 538.
- Bragg, W.L., Claringbull, G.F., and Taylor, W.H. (1965) The Crystalline State, Vol. IV (ed. L. Bragg; Cornell Univ. Press).
- Brasseur, H. (1932) The crystal structure of azurite, Zeits. Krist., 82, 195.
- Bridgman, P.W. (1963) General outlook on the field of high pressure research, Chapter 1, In: Solids Under Pressure, (ed. W. Paul and D.M. Warchauner; McGraw-Hill, New York).

- Brown, G.E. and Wechsler, B.A. (1973) Crystallography of pigeonite from basaltic vitrophyre 15597, Proc. 4th Lunar Sci. Conf., Suppl. 4, Geochim. Cosmochim. Acta, 1, 887-900, Pergamon Press.
- Buerger, M.J. (1957) Chapter in: Phase Transformations In Solids (Ed. R. Smoluchowski; J. Wiley & Sons, New York).
- Buerger, M.J. (1971) Phase transformations, Kirsystallographia, 16, 1084-1096.
- Burnham, C.W. (1966) Ferrosilite, Ann. Rept. Geophys. Lab., Year Book 65, 285-290.
- Burns, R.G. (1965) Electronic spectra of silicate minerals. Applications of Crystal Field Theory to Aspects of Geochemistry, Ph.D. Diss., Univ. of California, Berkeley.
- Burns, R.G. (1966) Origin of optical pleochroism in orthopyroxenes, Mineral. Mag., 35, 715-719.
- Burns, R.G. and Strens, R.G.J. (1966) Infrared study of the hydroxyl band in clinoamphiboles, Science, 153, 890-892.
- Burns, R.G., Clark, M.G., and Stone, A.J. (1966) Vibronic polarization in the electronic spectra of gillespite, a mineral containing iron(II) in square planar coordination. Inorg. Chem., 5, 1268-1272.
- Burns, R.G. and Strens, R.G.J. (1967) Structural interpretation of polarized absorption spectra of the Al-Fe-Mn-Cr epidotes Mineral. Mag., 36, 204-206.
- Burns, R.G. and Prentice, F.J. (1968) Distribution of iron cations in the crocidolite structure, Amer. Mineral., 53, 770-776.

- Burns, R.G. (1969b) Site preferences of transition metal ions in silicate crystal structures, *Chem. Geol.*, 5, 275-283.
- Burns, R.G. (1969a) Optical absorption in silicates, pp. 191-211 in: The Application of Modern Physics to the Earth and Planetary Interiors (ed. S.K. Runcorn; J. Wiley & sons, London).
- Burns, R.G. (1970b) Crystal field spectra and evidence of cation ordering in olivine mineral, *Amer. Mineral.*, 55, 1608-1632.
- Burns, R.G. (1970a) Mineralogical Applications of Crystal Field Theory, Cambridge Univ. Press, England.
- Burns, R.G. (1972) Mixed valencies and site occupancies of iron in silicate minerals from Mössbauer spectroscopy, *Canad. Spectroscopy*, 17, no. 2, 51-59.
- Burns, R.G., Tossell, J.A., and Vaughan, D.J. (1972a) Pressure-induced reduction of a ferric amphibole, *Nature Phys. Sci.*, 240, 33-35.
- Burns, R.G., Abu-Eid, R.M., and Huggins, F.E. (1972b) Crystal field spectra of lunar pyroxenes, *Proc. 3rd Lunar Sci. Conf., Geochim. Cosmochim. Acta, Suppl. 3*, 1, 533-543, MIT Press.
- Burns, R.G., Abu-Eid, R.M., and Huggins, F.E. (1972c) Crystal field spectra of lunar silicates, (abstract) In: *Lunar Science III* (ed. C. Watkins), pp. 108-109, Lunar Science Institute Contr. No. 88.
- Burns, R.G., Huggins, F.E., and Abu-Eid, R.M. (1972d) Polarized

absorption spectra of single crystals of lunar pyroxenes and olivines, *The Moon*, 4, 93-102.

Burns, R.G., Vaughan, D.J., Abu-Eid, R.M., Witner, M. and Morawski, A., (1973) Spectral evidence for Cr^{3+} , Ti^{3+} , and Fe^{2+} rather than Cr^{2+} , and Fe^{3+} in lunar ferromagnesian silicates, *Proc. 4th Lunar Sci. Conf., Suppl. 4, Geochim. Cosmochim. Acta*, 1, 983-994.

Burns, R.G. and Huggins, F.E. (1973) Visible region absorption spectra of Ti^{3+} fassaite from the Allende meteorite: A discussion, *Amer. Mineral.*, 58, 955-961.

Burns, R.G. and Vaughan, D.J. (1974) Polarized electronic spectra, Chapter in: Infrared and Raman Spectroscopy of Lunar and Terrestrial Minerals (ed. C. Karr, Jr.; Academic Press) in press.

Burns, R.G. (1974c) Partitioning of transition metals in mineral structures of the mantle, In: Petrophysics: The Physics and Chemistry of Minerals and Rocks (ed. R.G.J. Strens; J. Wiley & Sons, London) in press.

Burns, R.G. (1974b) Crystal field effects in chromium and its partitioning in the mantle, Paper presented at the Conference on Chromium, Geophys. Lab., Washington D.C., Jan. 6-7, 1974.

Burns, R.G. (1974a) The polarized spectra of iron in silicates: Olivine. A discussion of neglected contributions from Fe^{2+} ions in M(1) sites, *Amer. Mineral.*, 59, 625-629.

Clark, C.D., Ditchbure, R.W., and Dyer, H.B. (1956) The absorp-

- tion spectra of natural and irradiated diamonds, Proc. Royal Soc. London, A 234, 363-381.
- Clark, M.G. and Burns, R.G. (1967) Electronic spectra of Cu^{2+} and Fe^{2+} square planar coordination by oxygen in $\text{BaXSi}_4\text{O}_{10}$, J. Chem. Soc. (A), 1034-1038.
- Clark, J.R., Appleman, D.E., and Papike, J.J. (1969) Crystal-chemical characterization of clinopyroxenes based on eight new structure refinements, Mineral. Soc. Amer., Spec. Pap., 2, 31-50.
- Clark, J.R. and Papike, J.J. (1968a) Crystal-chemical characterization of omphacites, Amer. Mineral., 53, 840-868.
- Colloti, G., Conti, L., and Zocchi, M. (1959) The structure of the orthorhombic modification of lead chromate, PbCrO_4 , Acta. Cryst., 12, 416.
- Cotton, F.A. and Wilkinson, G. (1966) Advanced Inorganic Chemistry (J. Wiley & Sons, New York).
- Cotton, F.A. (1971) Chemical Applications of Group Theory (J. Wiley & Sons, New York).
- Dollase, W.A. (1968) Refinement and comparison of the structures of zoisite and clinozoisite, Amer. Mineral., 53, 1882-1898.
- Dollase, W.A. (1969) Crystal structure and cation ordering of piemontite, Amer. Mineral., 54, 710-717.
- Decker, D.L. (1965) Equation of state of NaCl and its use as a pressure gauge in high-pressure research, J. Appl. Phys., 36, 157-161.

- Decker, D.L. (1966) Equation of state of sodium chloride, J. Appl. Phys., 37, 5012-5014.
- Dowty, E., Ross, M., and Cuttita, F. (1972) Fe²⁺-Mg site distribution in Apollo 12021 clinopyroxenes: Evidence for bias in Mössbauer measurements, and relation of ordering to exsolution, Proc. 3rd Lunar Sci. Conf., Suppl. 3, Geochim. Cosmochim. Acta, 1, 481-492, MIT Press.
- Dowty, E. and Clark, J.R. (1973a) Crystal-structure refinement and optical properties of Ti³⁺ fassaite from Allende meteorite, Amer. Mineral., 58, 230-242.
- Dowty, E. and Clark, J.R. (1973b) Crystal-structure refinement and optical properties of Ti³⁺ fassaite from Allende meteorite: Reply, Amer. Mineral., 58, 962-964.
- Drickamer, H.G. and Frank, C.W. (1973) Electronic Transitions and the High Pressure Chemistry and Physics of Solids (Chapman and Hall, London).
- Drickamer, H.G. (1965) The effect of high pressure on the electronic structure of solids, Solid State Phys., 17, 1-133.
- Drickamer, H.G., Lewis, Jr., G.K., and Fung, S.C. (1969) The oxidation state of iron at high pressure, Science, 163, 885-890.
- Drickamer, H.G., Vaughan, R.W., and Lewis, Jr., G.K. (1969a) The effect of high pressure on the oxidation state of iron, Comm. Sol. State Phys., 1, 163-167.
- Drickamer, H.G., Frank, C.W., and Slichter, C.P. (1972) Optical vs. thermal transitions in solids at high pressures, Proc. Nat. Acad. Sci., 69, 933-937.

- Dunn, T.M., McClure, D.S., and Pearson, R.G. (1965) Some Aspects of Crystal Field Theory (Harper and Row, New York).
- Evans, R.C. (1966) An Introduction to Crystal Chemistry (Cambridge Univ. Press, London).
- Faye, G.H., Manning, P.G., and Nickel, E.H. (1968) The polarized optical absorption spectra of tourmaline, cordierite, chloritoid, and vivianite: ferrous-ferric electronic interactions as a source of pleochroism, *Amer. Mineral.*, 53, 1174-1200.
- Faye, G.H. (1968) The optical absorption spectra of iron in six-coordinate sites in chlorite, biotite, phlogopite, and vivianite. Some aspects of the pleochroism in the sheet silicates, *Canad. Mineral.*, 9, 403-425.
- Figgis, B.N. (1966) Introduction to Ligand Fields (J. Wiley & Sons, New York).
- Finger, L.W. (1970) Fe/Mg ordering in olivines, *Ann. Rept. Geophys. Lab., Year Book 69*, 302-305.
- Finger, L.W. (1971) Fe/Mg ordering in an olivine: a comparison of x-ray and Mössbauer results, (abstract), *Geol. Soc. Amer.*, 3, 310.
- Forman, R.A., Piermarini, G.J., Barnett, J.D., and Black, S. (1972) Pressure measurement made by utilization of Ruby Sharp-Line Luminescence, *Science*, 176, 284-285.
- Fukas, Y., Mizutani, H., and Uyeda, S. (1968) Optical absorption spectra at high temperatures and radiative thermal conductivity of olivines, *Phys. Earth Planet. Int.*, 1, 57-62.

- Fyfe, W.S. (1960) The possibility of d-electron coupling in olivine at high pressures, *Geochim. Cosmochim. Acta*, 19, 141-143.
- Frank, C.W. and Drickamer, H.G. (1972) The effect of pressure on the electronic structure of twelve β -diketone complexes, *J. Chem. Phys.*, 56, 3551-3565.
- Gaffney, E.S. (1972a) Crystal Field Effects in Mantle Minerals, Ph.D. Thesis, California Institute of Technology, Pasadena, California.
- Gaffney, E.S. (1972b) Crystal-field effects in mantle minerals, *Phys. Earth Planet. Int.*, 6, 385-390.
- Gaffney, E.S. and Anderson, D.L. (1973) Effect of low-spin Fe^{2+} on the composition of the lower mantle, *J. Geophys. Res.*, 78, 7005-7014.
- Gattow, V.G. and Zemann, J. (1958) Neubestimmung der Kristallstruktur von Azurit, $\text{Cu}_3(\text{OH})_2(\text{CO}_3)_2$, *Acta Cryst.*, 11, 866-872.
- Geller, S. (1967) Crystal chemistry of the garnets, *Z. Kristallogr.*, 125, 1-47.
- Ghose, S. (1965) Mg^{2+} - Fe^{2+} order in an orthopyroxene $\text{Mg}_{0.93}\text{Fe}_{1.07}\text{Si}_2\text{O}_6$, *Zeit. Krist.*, 122, 81-99.
- Gibbons, R.V., Ahrens, T.J., and Rossman, G.R. (1974) A spectrographic interpretation of the shock produced color change in rhodonite (MnSiO_3): the shock-induced reduction of Mn (III) to Mn (II), *Amer. Mineral.*, 59, 177-182.
- Gibbs, G.V. and Smith, J.V. (1965) Refinement of the crystal structure of synthetic pyrope, *Amer. Mineral.*, 50,

2023-2039.

- Griffith, J.S. (1964) The Theory of Transition Metal Ions, 1st ed. (Cambridge Univ. Press, London).
- Hafner, S.S., Virgo, D., and Warburton, D. (1971) Cation distributions and cooling history of clinopyroxenes from Oceanus Procellarum, Proc. 2nd Lunar Sci. Conf., Geochim. Cosmochim. Acta, Suppl. 2, 1, 91-108, MIT Press.
- Hanisch, K. (1966) Zur Kenntniss der Kristallstruktur von Staurolith, Neues Jahrb. Mineral., Monatsh., 362-366.
- Hanke, K. and Zemann, J. (1963) Verfeinerung der Kristallstruktur von Olivin, Naturwissenschaften, 3, 91-92.
- Hazen, R.M. and Abu-Eid, R.M. (1974) Crystallography of the displacive high pressure gillespite phase transformation, (abstract), Trans. A.G.U., 55, 463.
- Hazen, R.M. and Burnham, C.W. (1974) The crystal structure of gillespite I and II: a structure determination, Amer. Mineral., 59, 1166-1176.
- Heide, H.G. and Boll-Dornberger, K. (1955) Die Struktur des Dioptase, $\text{Cu}_6(\text{Si}_6\text{O}_{18}) \cdot 6\text{H}_2\text{O}$, Acta Cryst., 8, 425-430.
- Holt, S. and Ballhausen, C.J. (1967) Theor. Chim. Acta, 7, 313-
- Huggins, F.E. (1974) Mössbauer studies of iron minerals under pressures of up to 200 kilobars, Ph.D. Thesis, M.I.T., Cambridge, Mass.
- Huggins, F.E. and Abu-Eid, R.M. (1974) Reassessment of crystal

- field splitting parameters, Δ , and stabilization energies, CFSE, for ferrous silicates, (abstract), Geol. Soc. Amer., 1974 Ann. Meet., 6, no. 7, 803.
- Hunt, G.R. and Salisbury, J.W. (1971) Visible and near-infrared spectra of minerals and rocks: II. Carbonates, Modern Geology, 2, 23-30.
- Hush, N.J. (1967) Intervalence-transfer absorption, Part 2. Theoretical consideration and spectroscopic data, Prog. Inorg. Chem., 8, 391-444.
- Hush, N.J. (1968) Homogeneous and heterogeneous optical and thermal electron transfer, Electrochimica Acta, 13, 1005-1023.
- Hutchings, T.M. (1964) Point-charge calculations of energy levels of magnetic ions in crystalline electric field, Solid State Phys., 16, 227-273.
- Ilse, F.E. and Hartmann, H. (1951a)
Z. Phys. Chem., 197, 239-
- Ilse, F.E. and Hartmann, H. (1951b)
Z. Naturforschg., 62, 751.
- Ingalls, R. (1964) Electric-field gradient tensor in ferrous compounds, Phys. Rev., 133A, 787-795.
- Ito, K., Endo, J., and Kawai, N. (1971) Olivine-spinel transformation in a natural forsterite, Phys. Earth Planet. Int., 4, 425-428.

- Ito, T., Morimoto, N. and Sadanaga, R. (1954) On the structure of epidote, *Acta Cryst.*, 7, 53-59.
- Jackson, J.W. and Waxman, M. (1963) High Pressure Measurement (ed. Giardini and Lloyd; Butterworth, Washington), pp. 39-58.
- Johnson, K.H. (1973) Scattered wave theory of the chemical bond, *Adv. Quant. Chem.*, 7, 143-185.
- Kamb, B. (1968) Structural basis of the olivine-spinel stability relation, *Amer. Mineral.*, 53, 1439-1455.
- Kawai, N., Endo, S., and Sakata, S. (1966) Synthesis of Mg_2SiO_4 with spinel structure, *Proc. Japan. Acad.*, 42, 626-628.
- Kawai, N. Endo, S., and Ito, K. (1970) Split sphere high pressure vessel and phase equilibrium relation in the system Mg_2SiO_4 - Fe_2SiO_4 , *Phys. Earth Planet. Ints.*, 3, 182-185.
- Kennedy, G.C. (1957)
Chapter in: Phase Transformations In Solids (ed. R. Smoluchowski; J. Wiley & Sons, New York).
- Kinsland, G.L..(1974) Yield Strength Under Confining Pressures to 300 Kb. in the Diamond Anvil Cell, Ph.D. Thesis, Univ. of Rochester, Rochester, New York.
- König, E. (1971) The nephelauxetic effect: calculation and accuracy of interatomic repulsion parameters in cubic high-spin d^2 , d^3 , d^7 , and d^8 systems, In: Structure and Bonding, vol. 9, (Springer-Verlag, New York) pp. 175-211.
- Kumazawa, M., Sawamoto, H., Ohtani, E., and Masaki, K. (1974)

- Postspinel phase of forsterite and evolution of the earth's mantle, *Nature*, 247, 356-358.
- Lakshman, S.V.J. and Reddy, B.J. (1973) Optical absorption spectra of Cu^{2+} in chalcantite and malachite, *Canad. Mineral.*, 12, 207-210.
- Lever, A.B.P. (1968) Inorganic Electronic Spectroscopy (Elsevier Publ.; Amsterdam).
- Lippincott, E.R. and Duecker, H.C. (1964) Pressure distribution measurements in fixed-anvil high-pressure cells, *Science*, 146, 1119-
- Littler, J.G.F. and Williams, R.J.P. (1965) Electrical and optical properties of crocidolite and some other iron compounds, *J. Chem. Soc.*, 6368-6371.
- Loeffler, B.M., Burns, R.G., Tossell, J.A., Vaughan, D.J., and Johnson, K.H. (1974) Charge transfer in lunar material. Interpretation of uv-visible spectral properties of the moon, In: Proc. 5th Lunar Sci. Conf., *Geochim. Cosmochim. Acta*, Suppl. 5, vol. 3,
- Lyubutin, I.S. and Dodokin, A.P. (1971a) Temperature dependence of the Mössbauer effect for tetrahedral iron atoms in garnets, *Sov. Phys. Cryst. (trans.)*, 15, 936-938.
- Lyubutin, I.S. and Dodokin, A.P. (1971b) Temperature dependence of the Mössbauer effect for Fe^{2+} in dodecahedral coordination in garnets, *Sov. Phys. Cryst. (trans.)*, 15, 1091-1092.
- Mao, H.K. and Bell, P.M. (1973a) A study of charge-transfer and crystal-field spectra of iron and titanium in synthetic

- "basalt" glass as a function of P_{O_2} , Ann. Rept. Geophys. Lab., Year Book 72, 629-631.
- Mao, H.K. and Bell, P.M. (1973b) Polarized crystal field spectra of microparticles of the moon, In: Analytical Methods Developed for Application to Lunar Samples Analyses, ASTM STP 539, 100-119, Amer. Soc. for Testing and Materials.
- Mao, H.K. and Bell, P.M. (1973c) Crystal field stabilization of the olivine-spinel transition, Ann. Rept. Geophys. Lab., Year Book 72, 527-528.
- Mao, H.K. and Bell, P.M. (1971) Crystal-field spectra, Ann. Rept Geophys. Lab., Year Book 70, 207-215.
- Mao, H.K. and Bell, P.M. (1972a) Interpretation of the pressure effect on the optical absorption bands of natural fayalite to 20 kb., Ann. Rept. Geophys. Lab., Year Book 71, 524-527.
- Mao, H.K. and Bell, P.M. (1972b) Electrical conductivity and the red shift of absorption in olivine and spinel at high pressure, Science, 176, 403-406.
- Mao, H.K. (1967) The Pressure Dependence of the Lattice Parameters and Volume of Ferromagnesian Spinel, and its Implications to the Earth's Mantle, Ph.D. Thesis, Univ. of Rochester, Rochester, New York.
- Mao, H.K. (1973) Electrical and optical properties of the olivine series at high pressure. Observation of optical absorption and electrical conductivity in magnesio-wustite at high pressures. Thermal and electrical properties of the earth's mantle, Ann. Rept. Geophys. Lab., Year Book 72,

552-564.

- Mao, H.K. (1975) Charge-transfer processes at high pressure, In: Petrophysics: The Physics and Chemistry of Rocks and Minerals (Ed. R.G.J. Strens; J. Wiley & Sons) in press.
- Manning, P.G. (1967a) The optical absorption spectra of garnets, almandine-pyrope, pyrope, and spessartine and some structural interpretations of mineralogical significance, Canad. Mineral., 9, 237-251.
- Manning, P.G. (1967b) The optical absorption spectra of some andradites and the identification of the ${}^6A_1 \rightarrow {}^4A_1, {}^4E(G)$ transition in octahedrally bonded Fe^{3+} , Canad. J. Earth Sci., 4, 1039-1047.
- Manning, P.G. (1969a) Optical absorption spectra of chromium-bearing tourmaline, black tourmaline, and buergerite, Canad. Mineral., 10, 57-70.
- Manning, P.G. (1969b) On the origin of colour and pleochroism of astrophyllite and brown clintonite, Canad. Mineral., 9, 663.
- Manning, P.G. (1969c) An optical absorption study of the origin of colour and pleochroism in pink and brown tourmalines, Canad. Mineral., 9, part 5, 678-690.
- Manning, P.G. (1970) Racah parameters and their relationship to lengths and covalencies of Mn^{2+} and Fe^{3+} oxygen bonds in silicates, Canad. Mineral., 10, 677-688.
- Manning, P.G. (1972) Optical absorption spectra of Fe^{3+} in octahedral and tetrahedral sites in natural garnets, Canad. Mineral., 11, 826-839.

McClure, D.S. (1959) Electronic spectra of molecules and ions in crystals, *Solid State Phys.*, vol. 9, 399-525.

McClure, D.S. (1962)

J. Chem. Phys., 36, 2757-

Merrill, L. (1973) Crystallographic studies of the metastable high pressure phases of calcium carbonate, $\text{CaCO}_3(\text{II})$ and $\text{CaCO}_3(\text{III})$, Ph.D. Thesis, Univ. of Rochester, Rochester, New York.

Merrill, L. and Bassett, W.A. (1974) Miniature diamond anvils pressure cell for single crystal x-ray diffraction studies, *Rev. Sci. Instrum.*, 45, 290-294.

Ming, L. and Bassett, W.A. (1975) The postspinel phase in the $\text{Mg}_2\text{SiO}_4\text{-Fe}_2\text{SiO}_4$ system, *Science*, 187, 66-68.

Minomura, S. and Drickamer, H.G. (1961) Effect of the pressure on the spectra of transition metal ions in MgO and Al_2O_3 , *J. Chem. Phys.*, 35, 903-907.

Mooney, R.C. (1931) The crystal structure of potassium permanganate, *Phys. Review*, 37, 1306-1310.

Moore, R.K. and White, W.B. (1971) Intervalence electron transfer effect in the spectra of the melanite garnets, *Amer. Mineral.*, 56, 826-849.

Moore, R.K. and White, W.B. (1972) Electronic spectra of transition metal ions in silicate garnets, *Canad. Mineral.*, 11, 791-811.

Mori, H. and Ito, T. (1950) The structure of vivianite and symplectite, *Acta Cryst.*, 3, 1.

- Newnham, R.E. and De Haan, Y.M. (1962) Refinement of the α -Al₂O₃, Ti₂O₃, V₂O₃, and Cr₂O₃ structures, Zeits. Kristallogr., 117S, 235-237.
- Newnham, R.E. and Santoro, R.P. (1967) Magnetic and optical properties of diopside, Phys. State Solids, 19, K87-K90.
- Novak, G.A. and Gibbs, G.V. (1971) The crystal chemistry of the silicate garnets, Amer. Mineral., 56, 791-825.
- Oeldrug, D. (1971) Absorption spectra and ligand field parameters of tetragonal 3d-transition metal fluorides, Structure and Bonding, 9, 1-26 (Springer-Verlag, New York).
- Orgel, L. (1966) An Introduction to Transition-Metal Chemistry: Ligand-Field Theory (Methuen, London) 2nd edition.
- Pabst, A. (1943) Crystal structure of gillespite, BaFeSi₄O₁₀, Amer. Mineral., 28, 372-390.
- Pabst, A. (1959) The crystal structure of Egyptian-blue, Acta Cryst., 12, 733.
- Papike, J.J. and Clark, J.R. (1968) The crystal structure and cation distribution of glaucophane, Amer. Mineral., 1156-1173.
- Parson, R.W. and Drickamer, H.G. (1958) Effect of pressure on the spectra of certain transition metal complexes, J. Chem. Phys., 29, 930-937.
- Peacor, D.R. and Niizeki, N. (1963) The redetermination and refinement of the crystal structure of rhodonite (Mn,Ca) SiO₃, Zeit. Kristallogr., 119S, 98-116.
- Phillips, G.S.P. and Williams, R.J.P. (1966) Inorganic Chemistry (Oxford Univ. Press) Vol. 2.

- Piermarini, G.J., Block, S., and Barnett, J.D. (1973) Hydrostatic limits in liquids and solids to 100 kbar, *J. Appl. Phys.*, 44, 5377-5382.
- Prewitt, C.T., Brown, G.E., and Papike, J.J. (1971) Apollo 12 clinopyroxenes: high temperature x-ray diffraction studies, *Proc. 2nd Lunar Sci. Conf.*, 1, 59-68, MIT Press.
- Prewitt, C.T., Shannon, R.D., and White, W.B. (1972) Synthesis of a pyroxene containing trivalent titanium, *Contr. Mineral. Petrol.*, no. 1715, 845/1-6.
- Pitt, G.D. and Tozer, D.C. (1970a) Optical absorption measurements on natural and synthetic ferromagnesian minerals subjected to high pressures, *Phys. Earth Planet. Ints.*, 2, 179-188.
- Pitt, G.D. and Tozer, D.C. (1970b) Radiative heat transfer in dense media and some other ferromagnesian minerals under typical upper mantle conditions, *Phys. Earth Planet. Ints.*, 2, 189-199.
- Poole, C.P. Jr. (1964) The optical spectra and color of chromium containing solids, *J. Phys. Chem. Solids*, 25, 1169-1182, Pergamon Press.
- Povarennykh, A.S. (1972) Crystal Chemical Classification of Minerals, vol. 1 and 2 (translated from Russian) (Plenum Press, New York).
- Quareni, S. and De Pieri, R. (1964) Two-dimensional refinement of the structure of crocoite, $PbCrO_4$, *Rend. Soc. Min. Ital.* 20, 232.

- Quarenì, S. and De Pieri, R. (1965) A three-dimensional refinement of the structure of crocoite, PbCrO_4 , *Acta Cryst.*, 19, 287-289.
- Raal, F.A. (1959) A strong absorption system in type I diamonds, *Proc. Phys. Soc. London*, 74, 647-649.
- Racah, G. (1942a) Theory of complex spectra I, *Phys. Review*, 61, 186-198.
- Racah, G. (1942b) Theory of complex spectra II, *Phys. Review*, 62, 438-462.
- Racah, G. (1943) Theory of complex spectra III, *Phys. Review*, 63, 367-382.
- Racah, G. (1949) Theory of complex spectra IV, *Phys. Review*, 76, 1352-1362.
- Reiner, D. (1969) Ligand field spectroscopy and chemical bonding in Cr^{3+} -containing oxidic solids, In: Structure and Bonding, vol. 6 (Springer-Verlag, New York) p. 30-51.
- Ringwood, A.W. (1966) The composition and origin of the earth, In: Advances in Earth Science (ed. P.M. Hurley), (MIT Press, Cambridge, Mass).
- Ringwood, A.E. (1970) Phase transformation and the constitution of the mantle, *Phys. Earth Planet. Ints.*, 3, 109-155.
- Ringwood, A.E. and Searbrook, M. (1963) *J. Geophys. Res.*, 68, 4601-
- Ringwood, A.E., Reid, A.F., and Wadsley, A.D. (1967) High pressure transformation of alkali aluminosilicates and aluminogermanates, *Earth Planet. Sci. Lett.*, 3, 38-40.

- Ringwood, A.E. and Reid, A.F. (1968) High pressure polymorphs of olivines: the K_2NiF_4 type, *Earth Planet. Sci. Lett.*, 5, 67-70.
- Ringwood, A.E. and Major, A. (1970) The system Mg_2SiO_4 - Fe_2SiO_4 at high pressures and temperatures, *Phys. Earth. Planet. Int.*, 3, 89-108.
- Robbins, D.W. and Strens, R.G.J. (1968) Polarization-dependence and oscillator strengths of metal-metal charge transfer bands in iron(II,III) silicate minerals, *Chem. Communications*, 309, 508-509.
- Robbins, D.W. and Strens, R.G.J. (1972) Charge-transfer in ferromagnesian silicates: the polarized electronic spectra of trioctahedral micas, *Mineral. Mag.*, 38, 551-563.
- Robin, M.B. and Day, P. (1967) Mixed valence chemistry - a survey and classification, *Adv. Inorg. Chem.*, 10, 247-422.
- Runciman, W.A., Sengupta, D., and Marshall, M. (1973a) The polarized spectra of iron in silicates. I. enstatite, *Amer. Mineral.*, 58, 444-450.
- Runciman, W.A., Sengupta, D., and Gourley, J.T. (1973b) The polarized spectra of iron in silicates. II olivine, *Amer. Mineral.*, 58, 451-456.
- Runciman, W.A., Sengupta, D. (1974) The spectrum of Fe^{2+} in silicate garnets, *Amer. Mineral.*, 59, 563-566.
- Runciman, W.A., Sengupta, D., and Gourley, J.T. (1974) The polarized spectra of iron in silicates. II. olivine: A reply, *Amer. Mineral.*, 59, 630-631.

Schläfer, H.L. and Gotz, R. (1961) Über einen cyanokomplex des III - wertigen titans, Z. Anorg. Allgem. Chem., 309, 104-109.

Schläfer, H.L. (1962)

Proc. Symp. Theory Struct. Complex. Comp., Wroclau, Pergamon Press, p. 181.

Schairer, J.F. (1957)

Chapter in: Phase Transformations in Solids (ed. R. Smoluchowski; J. Wiley & Sons, New York)

Shankland, T.J. (1970) Pressure shift of infrared absorption bands in minerals and the effect on radiative heat transfer, J. Geophys. Res., 75, 409-413.

Shankland, T.J. (1972) Velocity-density systematics: derivation from Debye theory and the effect of ionic size, J. Geophys. Res., 77, 3750-3758.

Shankland, T.J., Duba, A.G., and Woronow, A. (1974) Pressure shifts of optical absorption bands in iron-bearing garnet, spinel, olivine, pyroxene, and periclase, J. Geophys. Res., 79, 3273-3282.

Shannon, R.D. and Prewitt, C.T. (1969) Effective ionic radii in oxides and fluorides, Acta Cryst., B25, 925-946.

Shenoy, G.K., Kalvius, G.M., and Hafner, S.S. (1969) Magnetic behavior of the FeSiO_3 - MgSiO_3 orthopyroxene system from NGR in ^{57}Fe , J. Appl. Phys., 40, 1314-1316.

- Simmons, G. and Wang, H. (1971) Single crystal elastic constants and calculated aggregate properties, A handbook, MIT Press, Cambridge, Mass.
- Smith, J.V. (1968) The crystal structure of staurolite, Amer. Mineral., 53, 1139-1155.
- Smith, J.V. (1953) Reexamination of the crystal structure of melilite, Amer. Mineral., 38, 643-661.
- Smoluchowski, R. (1957) Phase Transformation in Solids (J. Wiley & Sons, New York).
- Smyth, J.R. (1973) An orthopyroxene structure up to 850°C, Amer. Mineral., 58, 836-848.
- Stephens, D.R. and Drickamer, H.G. (1961) Effect of pressure on the spectra of certain complexes of Cu^{2+} , Co^{2+} , and Fe^{2+} , J. Chem. Phys., 35, 424-426.
- Strens, R.G.J. (1966) Pressure-induced spin-pairing in gillespite, $\text{BaFe(II)Si}_4\text{O}_{10}$, Chem. Comm.,
- Strens, R.G.J. (1969) The nature and geophysical importance of spin-pairing in minerals of iron(II), In: Applications of Modern Physics to the Earth and Planetary Interiors (S.K. Runcorn, ed.; J. Wiley & Sons, London) pp. 213-220.
- Suchan, H.L. and Drickamer, H.G. (1959) The effect of pressure on the absorption edge of certain molecular compounds, J. Phys. Chem. Solids, 11, 111-114.
- Suchan, H.L., Wiederhorn, S., and Drickamer, H.G. (1959) Effect of pressure on the absorption edges of certain elements, J. Chem. Phys., 31, 355-357.

- Sung, C-M., Abu-Eid, R.M., and Burns, R.G. (1974) Ti^{3+}/Ti^{4+} ratios in lunar pyroxenes: implications to depth of origin of mare basalt magma, Proc. 5th Lunar Sci. Conf., Suppl. 5, Geochim. Cosmochim. Acta, 1, 717-726.
- Süsse, V.P. (1967) Verfeinerung der kristallstruktur des malachits, $Cu_2(OH)_2CO_3$, Acta Cryst., 22, 146-151.
- Syono, Y., Tokonami, M., and Matsui, Y. (1971) Crystal field effect on the olivine-spinel transformation, Phys. Earth Planet. Ints., 4, 347-352.
- Takeda, H. and Ridely, W.I. (1972) Crystallography and chemical trends of orthopyroxene - pigeonite from rock 14310 and coarse fine 12033, Proc. 3rd Lunar Sci. Conf, Suppl. 3, Geochim. Cosmochim. Acta, 1, 423-430, MIT Press.
- Takeda, Y. and Sugano, S. (1954a) On the absorption spectra of complex ions II, J. Phys. Soc. Japan, 9, 753-763.
- Tanabe, Y. and Sugano, S. (1954b) On the absorption spectra of complex ions II, J. Phys. Soc. Japan, 9, 766-779.
- Tandon, S.P. and Gupta, J.P. (1970) Diffuse reflectance spectrum of ferric oxide, Spectroscopy Letters, 3, 297-301.
- Tischer, R.E. and Drickamer, H.G. (1962) Use of pressure to investigate local symmetry and compressibility in glass, J. Chem. Phys., 37, 1554-1562.
- Tossell, J.A., Vaughan, D.J., and Johnson, K.H. (1973) The electronic structure of ferric iron octahedrally coordinated to oxygen: a fundamental polyhedral unit of iron-bearing oxide and silicate minerals, Nature (Phys. Sci.), 244,

42-45.

- Tossell, J.A., Vaughan, D.J., and Johnson, K.H. (1974) The electronic structure of rutile, wustite, and hematite from molecular orbital calculations, *Amer. Mineral.*, 59, 319-334.
- Townsend, M.G. and Faye, G.H. (1970) Polarized electronic absorption spectrum of vivianite, *Phys. Stat. Sol.*, 38, K57-K60.
- Trotter, J. and Barnes, W.H. (1958) The structure of vanadinite, *Canad. Mineral.*, 6, part 2, 161-173.
- Van Valkenberg, A. (1965) Visual observation of single crystal transitions under true hydrostatic pressures up to 40 k bar, *Conference Internationale sur-les Hautes Pressions, Le Creusot, Saone-et-Loire, France 2 au 6 Aout*.
- Vratny, F. and Kokalas, J.J. (1962) The reflectance spectra of metallic oxides in the 300 to 1000 millimicron region, *Appl. Spectrosc.*, 16, 176-184.
- Wang, P.J. and Drickamer, H.G. (1974) The reduction of Cu(II) at high pressure, *J. Chem. Phys.*, 59, 713-717.
- Weaver, J.S., Takahashi, T., and Bassett, W.A. (1968) Calculation of the P-V relation for sodium chloride up to 300 kilobars at 25°C, *Symposium on Accurate Characterization of the High-Pressure Environment, NBS, Gaithersberg, Md., Oct. 14-18*, pp. 189-199.
- Weir, C.E., Block, S., and Piermarini, G.J. (1965) Single crystal x-ray diffraction at high pressures, *J. Res. Nat.*

- Bur. Stand., 69C, 279-281.
- Weir, C.E., Piermarini, G.J., and Block, S. (1969) Instrumentation for single crystal x-ray diffraction at high pressures, *Rev. Sci. Instruments*, 40, 1133-1136.
- Wenk, H.R. and Raymond, K.N. (1971) Crystal structure refinements of four magnesium-rich olivines, *Geol. Soc. Amer., Abstr.*, 3, 748-749.
- Whipple, E.R. (1973) Quantitative Mössbauer Spectra and Chemistry of Iron, Ph.D. Thesis, MIT, Cambridge, Mass.
- White, W.E. and Keester, K.L. (1966) Optical absorption spectra of iron in the rock-forming silicates, *Amer. Mineral.*, 51, 774-791.
- White, W.B. and Moore, R.K. (1972) Interpretation of the spin-allowed bands of Fe^{2+} in silicate garnets, *Amer. Mineral.*, 57, 1692-1710.
- Whittaker, E.J. (1949) The structure of Bolivian crocidolite, *Acta Cryst.*, 2, 312-317.
- Willis, B.T. and Rooksby, H.P. (1952) Crystal structure and anti-ferromagnetism in hematite, *Proc. Phys. Soc. London*, B65, 950-954.
- Wolfsberg, M. and Holmholz, L. (1952) The electronic structure of the tetrahedral ions MnO_4^- , CrO_4^{--} , and ClO_4^- , *J. Chem. Phys.*, 20, 837-843.
- Wood, B.J. and Strens, R.G.J. (1972) Calculation of crystal-field splitting in distorted coordination polyhedra: spectra and thermodynamic properties of minerals, *Mineral. Mag.*, 38, 909-917.

Zahner, J.C. and Drickamer, H.G. (1961) Effect of pressure on crystal-field energy and covalency in octahedral complexes of Ni^{2+} , Cu^{2+} , and Mn^{2+} , J. Chem. Phys., 35, 1483-1490.

VITA

The author was born on February 5, 1946, in Jaffa, Palestine. He enrolled at Alexandria University in 1964 and received a B.Sc. degree (with honours) in Geology and Chemistry in June, 1968. After graduation he worked for the Ministry of Education in Kuwait for one year and then came to the United States in June, 1969. He worked for over one year for Charles T. Main Engineering Co., Boston as a Geologist and then entered the Graduate School at M.I.T., in September, 1970. During his study at M.I.T. he has held either research assistantships or teaching assistantships for the academic years 1971-1974. He is the author or co-author of about 19 publications and he is a member of the following societies:

Geological Society of America
Mineralogical Society of America
American Geophysical Union
Mineralogical Association of Canada
American Association of Petroleum Geologists
Arab Physical Society
American Association For the Advancement of Science
The Society of Sigma XI
listed in Who's Who in the East, 1975

The author was recently wedded , on September 28, 1974, to Maria Letizia Uttaro of Arlington, Massachusetts. He has accepted an appointment as an Assistant Professor at Pahlavi University, Iran, starting January 21, 1975.